RATE SENSITIVE BEHAVIOR OF CEMENT PASTE AND MORTAR IN COMPRESSION

by

Shraddhakar Harsh
Zhenjia Shen
David Darwin

A Report on Research Sponsored by
THE AIR FORCE OFFICE OF SCIENTIFIC RESEARCH
Research Grant
AFOSR-85-0194

UNIVERSITY OF KANSAS
LAWRENCE, KANSAS
March 1989

SECURITY CLASSIFICATION OF THIS PAGE

REPORT DOCUMENTATION PAGE

1a. REPORT SECURITY CLASSIFICATION Unclassified	1b. RESTRICTIVE MARKINGS
2a. SECURITY CLASSIFICATION AUTHORITY	3. DISTRIBUTION/AVAILABILITY OF REPORT Approved for Public Release; distribution is unlimited
2b. DECLASSIFICATION/DOWNGRADING SCHEDULE	
4. PERFORMING ORGANIZATION REPORT NUMBER(S)	5. MONITORING ORGANIZATION REPORT NUMBER(S)
6a. NAME OF PERFORMING ORGANIZATION University of Kansas Center for Research, Inc. 6b. OFFICE SYMBOL *(If applicable)*	7a. NAME OF MONITORING ORGANIZATION Air Force Office of Scientific Research
6c. ADDRESS *(City, State, and ZIP Code)* Lawrence, KS 66045	7b. ADDRESS *(City, State, and ZIP Code)* AFSOR/NA Bolling Air Force Base Washington, DC 20332
8a. NAME OF FUNDING/SPONSORING ORGANIZATION 8b. OFFICE SYMBOL *(If applicable)*	9. PROCUREMENT INSTRUMENT IDENTIFICATION NUMBER AFOSR-85-0194
8c. ADDRESS *(City, State, and ZIP Code)*	10. SOURCE OF FUNDING NUMBERS

PROGRAM ELEMENT NO.	PROJECT NO.	TASK NO.	WORK UNIT ACCESSION NO.
61102F	2302	C2	

11. TITLE *(Include Security Classification)*
Strain-Rate Sensitive Behavior of Cement Paste and Mortar in Compression

12. PERSONAL AUTHOR(S)
Harsh, Shraddhakar, Zhenjia, Shen, and Darwin, David

13a. TYPE OF REPORT	13b. TIME COVERED	14. DATE OF REPORT *(Year, Month, Day)*	15. PAGE COUNT
Final	FROM 850401 TO 890331	890420	290

16. SUPPLEMENTARY NOTATION

17. COSATI CODES			18. SUBJECT TERMS *(Continue on reverse if necessary and identify by block number)*
FIELD	GROUP	SUB-GROUP	cement pastes; composite moduli; compression; concrete; creep strain; effective bulk modulus; hydrostatic stress; mortars; modulus of elasticity; Poisson's ratio; pore fluid movement; pore shape; sand content; self-consistent model; strain at peak stress; strain rate; strain-rate sensitivity; strength; stress-strain curve.

19. ABSTRACT *(Continue on reverse if necessary and identify by block number)*

The strain-rate sensitivity of the cement paste and mortar constituents of concrete is studied both experimentally and analytically. Cement paste and mortar specimens are loaded in compression using seven strain rates, ranging from 0.3 to 300,000 microstrain/sec. Water-cement ratios of 0.3, 0.4, and 0.5 are used. Specimens are loaded to 15,000 microstrain, 27 to 29 days after casting. Strain-rate sensitivity is measured in terms of the initial modulus of elasticity, Poisson's ratio, and stress and strain at failure.

An analytical model of a porous solid is developed to study and simulate the rate sensitive behavior of the materials. The model consists of spherical grains and saturated spheroidal pores in communication with unsaturated regions. Movement of pore fluid results in a strain-rate sensitive response to load. The model is used to duplicate the strain-rate sensitive elastic moduli and to simulate basic creeip strains of cement paste.

The initial elastic moduli at low stresses and the strength of cement paste and mortar increase by 7 percent and 15 percent, respectively, with every order of magnitude increase in strain rate. Poisson's ratio is more strain-rate sensitive as strain increases. The strain at the maximum stress is the greatest for the lowest strain rate. With increase in strain rate, the strain at the maximum stress first increases and than decreases.

To simulate the strain-rate sensitivity of cement paste, the analytical model requires the representative pore shape to be a flat oblate spheroid. The model duplicates the strain-rate sensitive initial elastic moduli of cement paste, and explains most of the nonlinearity of the stress-strain curve at low stresses. The model closely simulates the short-term basic creep strains under low sustained stresses. In the long-term, the analytical creep strains are expected to be lower than the experimental values due to continued hydration, and maturation creep, which are not included in the model.

20. DISTRIBUTION/AVAILABILITY OF ABSTRACT	21. ABSTRACT SECURITY CLASSIFICATION
☒ UNCLASSIFIED/UNLIMITED ☐ SAME AS RPT. ☐ DTIC USERS	

22a. NAME OF RESPONSIBLE INDIVIDUAL	22b. TELEPHONE *(Include Area Code)*	22c. OFFICE SYMBOL
Dr. Spencer T. Wu	(202) 767-6962	AFOSR/NA

DD FORM 1473, 84 MAR 83 APR edition may be used until exhausted. All other editions are obsolete.

SECURITY CLASSIFICATION OF THIS PAGE

★U.S. Government Printing Office: 1985—507-047

ACKNOWLEDGEMENTS

This report is based on a thesis submitted by Shraddhakar Harsh to the Department of Civil Engineering at the University of Kansas in partial fulfillment of the requirements for the Ph.D. degree.

The research was supported by the Air Force Office of Scientific Research under grant AFSOR-85-0194.

Cement was donated by Ash Grove Cement Company. Numerical calculations were performed on the Harris 800 and 1200 computer systems operated by the Computer Aided Engineering Laboratory at the University of Kansas.

TABLE OF CONTENTS (continued)

LIST OF TABLES

LIST OF TABLES (continued)

LIST OF FIGURES

LIST OF FIGURES (continued)

LIST OF FIGURES (continued)

LIST OF FIGURES (continued)

LIST OF FIGURES (continued)

LIST OF FIGURES (continued)

LIST OF FIGURES (continued)

CHAPTER 1

INTRODUCTION

1.1 General

Concrete exhibits uniquely nonlinear and strain-rate sensitive behavior in compression. The degree of nonlinearity decreases with an increase in strain rate (38, 45, 77-79). Concrete structures are sometimes subjected to high strain rates due to impact, tornado, earthquake, etc. (76). Analysis of such structures should be based on an understanding of the behavior of concrete at high strain rates, since the use of material properties at low strain rates can result in misleading conclusions. Thus, there is a need to investigate the stress-strain behavior of concrete as a function of strain rate.

Most of the effort in this respect has been experimental in nature: to observe the variation in strength for a range of applied strain rates and find an expression that defines the relationship between the two (2, 30, 38, 45, 61, 99). While this experimental effort is essential, it is only by understanding the physical processes at the microscopic level that one can completely explain the macroscopic behavior of concrete.

The strain-rate sensitive behavior of concrete and its constituent materials has been studied since the early part of this century. The early research showed that concrete, like other structural materials, shows higher tensile (98, 99), flexural (30, 31, 33, 39, 86, 93), and compressive (1, 2, 15, 23, 24, 25, 38, 46, 58, 59,

64, 68, 73, 74, 75, 79, 84) strengths at higher strain rates. What sets concrete apart from most other structural materials, e.g. steel, is that its initial elastic modulus increases with strain rate as well (2, 15, 38, 45, 57, 90).

For concrete, strain rate also appears to have an effect on the strain corresponding to the peak stress, but the results have been contradictory. While some studies have found the strain at maximum stress to increase slightly with increasing strain rate, others have found it to decrease, and still others have found it to remain almost constant with increasing strain rate. The effects of degree of saturation, water to cement ratio, and aggregate properties on the rate sensitivity have also been studied (5, 18, 28, 28, 34, 38, 46, 73, 96, 99). In general, it has been observed that the degree of saturation (presence of free water) is one of the most important influencing factors in the rate sensitive behavior (46).

Since 1970, several attempts have been made to model the rate sensitive behavior of concrete and its constituents. Fracture mechanics principles (92, 97, 99), thermohydraulic flow (94), stochastic theory (55), rheology (39, 57), creep law (9, 10), and continuous damage concepts (79, 80) have been used in these models. They have been able to explain or approximately simulate some aspects of the rate sensitive behavior. Still, many questions remain unanswered.

Effort has also been made to observe the difference in the extent of microcracking (at 30x) with increasing strain rates (24).

Recently, Attiogbe and Darwin (6, 7, 8, 21) have used submicroscopic cracking (at 1250x) data to help explain the nonlinear and strain-rate sensitive behavior of cement paste and mortar.

The present study aims to observe and explain the strain-rate sensitive behavior of cement paste and mortar. Specimens will be loaded at different strain rates in uniaxial compression to observe the rate sensitivity of the materials. An analytical model will be developed to explain the rate sensitivity of the elastic moduli, at low stresses, and the role of pore water in the stress-strain behavior of these materials.

1.2 Background

A considerable number of studies have been done on the strain-rate sensitive behavior of concrete since the first such work done by Abrams (1) in 1917. In the majority of the cases, the sensitivity of compressive strength to strain rate was studied (1, 2, 15, 23, 34, 46, 58, 59, 64, 73, 74, 79, 84). The rate sensitivity of tensile strength (51, 92, 97-99), modulus of rupture (52, 53, 78, 79), modulus of elasticity (5, 15, 38, 45, 57), strain at maximum stress (2, 15, 25, 81, 90), concrete-to-reinforcing bar bond strength (32, 33, 52, 78, 88), and shear strength (52) also have been investigated. In most cases, these properties show significant increases with each order of magnitude increase in strain or stress rate.

Researchers have studied the behavior of concrete as a function of both strain rate (2, 5, 15, 25, 32, 44, 53) and stress rate (5,

46, 84, 96-99). Strictly speaking, sensitivity to stress rate is not equivalent to sensitivity to strain rate because of the nonlinear stress-strain curve of concrete. However, the results can be grouped together for approximate comparisons since it takes an order of magnitude increase in stress or strain rate to observe a significant change in the behavior of concrete. In this study, involving consideration of deformation at the microscopic level, strain rate is used, in preference to stress rate.

In most investigations, the rate sensitivity of concrete has been measured in terms of its compressive strength. Generally, the rate of increase in compressive strength up to a moderate strain rate, 0.001/sec, is approximately linear with an increase in the logarithm of the strain rate. In a majority of cases, a 7-15% increase in compressive strength is observed with each order of magnitude increase in strain rate. At higher strain rates, there is no general agreement. While some investigators have found the linear relation to be maintained up to strain rates as high as 800/sec (53, 82), others have found it to become concave upwards (5), and still other found it to become concave downwards (77, 79, 80, 90).

In the design of most concrete structures, it is assumed that concrete does not possess any tensile strength. However, in some concrete structures, such as piles, a compressive stress pulse can rebound as a tensile stress pulse. Hence, the rate sensitivity of concrete tensile strength has drawn some interest (51, 92, 97-99).

Tensile strength appears to be slightly more strain-rate sensitive than compressive strength (77, 79).

The effect of strain rate on the elastic modulus has been studied by a number of researchers (2, 15, 38, 45, 51, 57, 90). Moduli used for comparison have included (i) the secant modulus at a fraction, e.g. 45%, of the maximum stress (2, 15, 45), (ii) the secant modulus at a small strain, e.g. 0.001 (38, 90), and (iii) the initial tangent modulus (57, 90). In general, the elastic modulus shows more sensitivity when the upper point for its secant value calculations is moved higher on the stress-strain curve (38, 45, 90). With an increase in strain rate, the initial part of the stress-strain curve becomes less and less nonlinear (38, 45, 77, 78, 79). And since the nonlinearity before the maximum stress is thought to be strongly influenced by microcracking, it has been suggested that at a given strain the amount of microcracking before the maximum stress should be less at higher strain rates (33, 78). However, to the contrary, experiments have found that the amount of microcracking is higher at a given strain at higher strain rates (6, 7, 8, 21, 24).

A few studies measured the effect of strain rate on the Poisson's ratio, ν. Dhir and Sangha (23) observed that under compressive loading, ν increases with strain rate. However, Takeda and Tachikawa (81) found that it does so only below about 80% of the maximum stress. For stresses higher than about 80% of the maximum, the Poisson's ratio decreases with strain rate. Suaris and Shah (80),

using an analytical model, supported the findings of Takeda and Tachikawa (81) at the maximum stress.

The strain at the maximum stress, ε_p, both in tension and in compression, has generally been found to vary with strain rate. In some cases, ε_p has been found to increase (5, 81, 90), while in other cases it has been found to decrease (15, 25, 69) or remain almost constant with strain rate (38, 45). Generally, when ε_p was found to increase with strain rate, the experiments were done at higher strain rates. In three related studies Zielinsky (97, 98) and Zielinski et. al (99) noted that as the stress rate in tension was increased, the strain at the maximum stress first decreased then increased.

Several factors have been found to influence the rate sensitivity of concrete. In compression, concrete is significantly more strain-rate sensitive if wet than if dry (23, 46). In general, weaker concretes appear to be more strain-rate sensitive than stronger concretes (5, 18, 28, 38, 96, 99). Concretes made of angular, rough and less stiff aggregates are more strain-rate sensitive than concretes made of round, smoother, and stiffer aggregates, respectively (34, 73). As suggested by Mainstone (52), the temperature of concrete at the time of test may also influence the effects of strain rate, but this aspect has yet to be studied. Kaplan (46) performed an extensive study of factors influencing the strain-rate sensitivity of concrete. He made the general observation that all

factors that change the microstructural nature of cement paste, mortar, or concrete (moisture content, age, curing, and mix proportions) also influence their rate sensitivity.

Although a number of researchers have recognized the presence and the important role that microcracks play in the strain-rate sensitivity of concrete (21, 34, 46, 71, 77, 97, 99), the amount of experimental work done in this respect has been limited. Dhir and Sangha (24) observed that the amount of matrix microcracking (at 30x) in mortar seems to increase with strain rate, while the amount of bond cracking remains almost constant. Attiogbe and Darwin (6, 7, 8, 21) found that the amount of submicroscopic cracking (1200x) is higher for monotonic loading than for sustained loading to the same strain. The sustained loading took about fifteen times longer to reach each strain level.

1.3 Previous Work Related to This Study

The discussion in the previous section shows that, in spite of the large number of studies of the rate sensitive behavior of concrete, few studies have considered the physical processes responsible for that behavior. A few investigators, however, have considered these processes.

Dhir and Sangha (23, 24) investigated the strain-rate sensitivity of concrete in compression. 2 in. x 5 in. cylindrical specimens were cored out of 6 in. cubes 28 days after casting. The cores were kept in a "laboratory environment" for ten additional

weeks, causing a large reduction in the amount of free water present in the concrete. The cores were then tested in uniaxial compression using strain rates ranging from 0.05 to 2500 microstrain/sec. For all specimens tested below 250 microstrain/sec, the maximum stress was virtually the same. An increase in the strain rate from 250 to 2500 microstrain/sec increased the maximum stress by less than 5%. This contradicts the results of other investigators (1, 2, 5, 15, 25, 38, 46, 58, 73), who observed a 7-15% increase in strength with each order of magnitude increase in strain rate. The most significant difference between Dhir and Sangha's procedures (23) and those of the previous investigators was that Dhir and Sangha allowed the specimens to dry for ten weeks, while others either did not allow any air drying, or did so for only a few days. Dhir and Sangha (23) concluded that the effect of strain rate on the maximum compressive stress diminishes as the degree of air curing is increased. They (23, 24) also observed that as the strain rate increases, (i) the amount of mortar microcracking (30x) on "sections corresponding to maximum stress" increases while the amount of bond microcracking remains almost constant, and (ii) the Poisson's ratio increases.

Zielinsky (97), Zielinsky and Reinhardt (98) and Zielinsky et. al (99), in related investigations, studied the rate sensitivity of concrete in tension. Concrete and mortar specimens were tested in uniaxial tension at increasing stress rates up to 31.5×10^3 MPa/sec (4570 ksi/sec) using a Split-Hopkinson-Bar. An increase of 5 orders of magnitude in loading rate (from 0.1 to 3.0×10^4 MPa/sec) resulted

in a 33 to 134% increase in tensile strength for various types of concretes. It was observed that at the lowest loading rate (0.1 MPa/sec), fracture planes passed under aggregate particles, while at higher loading rates ($3.0x10^3$ or $3.0x10^4$ MPa/sec), fracture planes passed through many aggregate particles. For the higher stress rates, the cracks were straighter, and there was a tendency towards a larger number of microcracks. In most cases, failure occurred due to the growth of a single macrocrack in the central section of the specimen. But, at the higher loading rates, two of the specimens developed two macrocracks each at the time of failure, causing them to break into three parts. Based on these observations it was concluded that at higher stress rates, (i) the higher stresses at fracture were due to the propagation of cracks through shorter paths of higher resistance, and (ii) the higher strains at fracture were due to greater amount of microcracking and macrocracking. An analytical model was developed (97) to simulate the rate sensitive behavior of concrete in tension. The model treats concrete as an idealized material consisting of spherical aggregate particles embedded in an otherwise homogenous cement paste matrix. The rate sensitivity of the fracture stress is simulated by relating it to the fracture energies associated with propagation of cracks through the matrix, aggregate particles, and the matrix-aggregate interface.

In 1980, Kaplan (46) investigated the influence of free water, age, and curing conditions on the relationship between strength and stress rate for concrete, mortar, and cement paste. He observed that

the moisture content at the time of testing is one of the most important factors in the rate sensitivity of these three related materials. Age and curing conditions also influence load-rate sensitivity, since they also change the internal structure of the materials. Since he conducted all of the experiments in load control, specimens tested at the same load rate but with different strengths experienced different strain rates. Still, as discussed earlier, his results can be compared, at least qualitatively, with similar tests under strain control.

Kaplan dried the specimens in an oven at 105°C for 1 to 24 hours to study the influence of free water. The higher the amount of free water at the time of testing, the greater was the rate sensitivity of these materials. To study the influence of age on the rate sensitive behavior of cement paste when not subjected to drying, Kaplan tested specimens at various stress rates up to 49 MPa/sec, 2 to 29 days after casting. The younger specimens (2 to 8 days old) showed less rate sensitivity below about 1 MPa/sec (6.89 ksi/sec), after which there was a steep rise in the sensitivity, causing the average rate sensitivity of the younger specimens loaded over the full range of strain rate, 0.001 to 49 MPa/sec (0.007 to 338 ksi/sec), to be higher than the older specimens (15 or 29 days old). Age had a similar effect on mortar and concrete specimens, except the younger specimens (2 to 3 days old) showed insignificant rate sensitivity even up to the maximum stress rate (49 MPa/sec). The rate sensitivities of water-cured, humidity-chamber cured, and air-cured cement paste

specimens, all saturated at the time of testing, were compared. The water-cured specimens exhibited an approximately linear relation between maximum stress and logarithm of stress rate. Specimens with the other two curing conditions had a nonlinear, concave downwards, relation between these two variables. The air cured specimens had the most nonlinear relation, very similar to that of the young (2 to 8 days old) specimens, between maximum stress and logarithm of stress rate.

Kaplan explained the influence of age and curing conditions on compressive strength based on the viscous, time-dependent movement of free water in the pores and channels of the materials. Specimens with smaller pores and channels (water-cured and older specimens) develop higher pore-water pressure, while those with larger pores and channels (air-cured and younger specimens) build up the pressure only when the loading rates are sufficiently high. He also observed that if a fraction (20%) of the total load was applied at a slower rate (0.0034 MPa/sec (0.023 ksi/sec)) and the balance applied at a higher rate (49.05 MPa/sec (338 ksi/sec)), the resulting maximum stress was higher than if all of the stress had been applied monotonically at the higher rate. Kaplan felt that the improvement in strength was due to a more uniform distribution of pore fluid and stable positioning of some crystals when part of the load is applied at a slower loading rate.

In 1979, Wu (94) developed a computational model that considered the time-dependent flow of fluid from narrow gel spaces to capillary

pores so that the time-dependent behavior of concrete under impulsive loading could be estimated. The time-dependent flow was treated as a two dimensional problem and was divided into transient flow, with a boundary layer effect, and thermohydraulic flow. The total amount of discharge volume was calculated by integrating the fluid flow expression over the gel pore width. This volume was then used in an expression which could provide an upper bound on the time-dependent strain.

1.4 Object and Scope

The present study investigates the stress-strain behavior of cement paste and mortar at various strain rates. An analytical model is developed which considers the time-dependent movement of pore water to explain the rate sensitive behavior of these materials.

Cement paste and mortar specimens with water-cement ratios of 0.3, 0.4, and 0.5 are subjected to uniaxial compression at strain rates of 0.3, 3, 30, 300, 3000, 30,000, and 300,000 microstrain/sec. An Instron closed-loop servo-hydraulic testing system is used for the tests. The tests provide complete stress-strain curves at the chosen strain rates. Strain-rate sensitivity is measured in terms of the initial modulus of elasticity, the maximum compressive stress, and the strain at the maximum stress. Rate sensitivities are compared for different water-cement ratios and between cement paste and mortar.

A strain-rate sensitive analytical model is developed to provide a better understanding of the physical processes involved in the behavior of porous solids, such as cement paste, mortar, and concrete at different strain rates. A nearly saturated porous solid is modeled as a composite consisting of isotropically distributed saturated spheroidal pores and solid spherical grains. The solid phase is considered to be insensitive to loading rate. Under load, the flow of the pore fluid between the saturated pores and unsaturated regions is considered to develop expressions for rate sensitive effective moduli of the pores. The effective bulk modulus of a saturated pore, for a given average strain on the porous solid, depends on the volume of fluid that flows between the pore and an unsaturated region. Thus, the more restricted the communication of the pore fluid and the higher the strain rate, the higher the effective bulk modulus of the pore. The effective bulk moduli of the pores and the moduli of the solid phase are used in a self-consistent manner to estimate the composite moduli of the porous solid. The rate sensitive nature of the moduli of the saturated pores causes the composite to be rate sensitive as well. The applicability of the model is demonstrated using test results for cement paste.

The equations and procedures of the strain-rate sensitive model are modified to simulate creep of a porous solid under sustained loading. The properties of the pore fluid and the pore structure of the porous solid are assumed constant to obtain the analytical creep strains (both longitudinal and transverse) as functions of time. The

parameters of the model are calibrated using strain-rate sensitive moduli of cement paste. Analytical creep response is compared with experimental short-term and long-term creep of cement paste.

CHAPTER 2

EXPERIMENTAL INVESTIGATION

2.1 Introduction

The strain-rate sensitive behavior of concrete has been under investigation for several decades (1). The rate sensitivity has generally been measured in terms of the strength, the modulus of elasticity, or the strain at the maximum stress in compression. Sometimes it has also been measured in terms of the Poisson's ratio, the tensile strength or the flexural strength. In this experimental investigation, the rate sensitivity of cement paste and the mortar in compression is measured in terms of the maximum stress, the strain at maximum stress, the initial elastic modulus, and the initial Poisson's ratio.

In most studies, concrete compressive strength has been observed to increase approximately linearly with every order of magnitude increase in strain rate up to moderate strain rates, e.g. up to 1000 microstrain/sec. Generally, the increase has been 7 to 15 percent with each order of magnitude increase in strain rate or stress rate (1, 23, 28, 64, 68, 84, 96). In a few cases, however, the increase has been considerably less (59, 90) or insignificant (23, 73). At higher than moderate strain rates (e.g. higher than 1000 microstrain/sec), there has been less agreement among various studies. Some have observed that the linear relation is maintained up to strain rates as high as 8×10^{8} microstrain/sec (82), while

others have found the relation to become concave upwards (77, 79, 80, 90) and others have found it to become concave downwards (5, 15) with increasing strain rates

The modulus of elasticity, while less sensitive than strength (2, 15, 45) has also been found to increase with strain rate. The modulus of elasticity is calculated as either the initial tangent modulus or the secant modulus at a small strain or stress. With increasing strain rate, the initial part of the stress-strain curve becomes steeper and less nonlinear. Since nonlinearity is associated with microcracking, it has been suggested that the amount of microcracking at a given strain should be less at higher strain rates (33, 78). However, to the contrary, experiments have found the amount of microcracking to be significantly higher at higher strain rates (6, 21, 23, 24).

The effect of strain rate on the Poisson's ratio of concrete has not been investigated extensively (23, 24, 81). Dhir and Sangha (23, 24) observed that Poisson's ratio increases significantly with strain rate. Takeda and Tachikawa (81) found that it does so only below about 80 percent of the maximum stress. After that, it decreases with strain rate.

There is little agreement among researchers on the rate sensitive behavior of strain at the maximum stress. Some have found it to increase (51, 81, 90), while others have found it to remain almost constant (38, 45) or even decrease (15, 23, 69) with increasing

strain rate. Generally, in cases when it was found to increase, the tests were done at higher strain rates.

In spite of the considerable number of studies on the rate sensitivity of concrete and its constituents, there are significant disagreements. The disagreements can sometimes be attributed to changes in test conditions, such as the moisture content of specimens, the curing conditions, or the range of strain rates used. Thus, for example, the insignificant increase in compressive strength with increasing strain rate observed by Dhir and Sangha was most likely due to the low moisture content of their specimens caused by storage in air for ten weeks.

The purpose of this study is to help improve the knowledge of concrete by studying the rate sensitive response of its constituents, cement paste and mortar. The study is aimed at gathering basic information on the response of fully saturated materials, that is materials that are not affected by drying. A study of the materials in the saturated state, while not universally applicable to all concrete, directly applies to a large percentage of concrete structures which remain saturated at depth. Compressive stress-strain response is measured in terms of the peak stress, f_p, the strain corresponding to the peak stress, ε_p, post peak strain corresponding to 90% of the maximum stress, ε_{pp}, the initial modulus of elasticity, E_i, and the initial Poisson's ratio, ν_i. Material response is compared based on strain rate, $\dot{\varepsilon}$, water-cement ratio, W/C, and sand-cement ratio, S/C.

In chapter 3, the data gathered are used in calibrating a rate sensitive model.

2.2 Materials

Cement: Type I cement, Ashgrove brand, with the following composition was used: tricalcium silicate = 51.1%, dicalcium silicate = 22.3%, tetracalcium aluminoferrite = 9.5%, and tricalcium aluminate = 7%.

Fine Aggregate: The fine aggregate was Kansas river sand consisting mainly of quartz, with 10-15% chert. Larger particles contained some limestone and dolomite. Fineness modulus = 2.91, bulk specific gravity (saturated surface dry) = 2.61, absorption = 0.79%. Source: Kansas River, Lawrence, Kansas. The sand was passed through a No. 4 sieve before use.

Mix Proportions: Three water-cement ratios (W/C), 0.3, 0.4, and 0.5, were used for cement paste and mortar. Concrete mixes were designed in order to obtain the sand-cement ratio (S/C) for one mortar, mortar A, for each water-cement ratio (W/C). For W/C = 0.4 and 0.5, a second mortar, mortar B, was used to evaluate the effect of a change in S/C upon the response. The mortar (A) with W/C = 0.3 had S/C = 0.97. For W/C = 0.4, mortar A had S/C = 1.59 and mortar B had S/C = 1.97. For W/C = 0.5, mortar A had S/C = 1.29 and mortar B had S/C = 2.28.

2.3 Test Procedure

2.3.1 Test specimen

Prismatic test specimens, 1 in. square by 5 in., were prepared. The sand was oven dried at 105°C for a twenty-four hour period prior to batching. It was then cooled to room temperature and soaked in part of the mix water. The mix water was increased to account for the absorption of the sand. The constituents were mixed according to ASTM C 305-80 (3) except the sand was presoaked.

Each batch consisted of twelve specimens cast vertically in two steel molds (Fig. 2.1). The molds were oiled prior to the casting and the joints were sealed with modeling clay to prevent loss of moisture. The molds were filled in three equal layers. For W/C = 0.5, each layer was hand rodded twenty-five times using a one-quarter in. diameter steel rod. For W/C = 0.3 and 0.4, the molds were bolted to a vibrating table with a frequency of 60 cycles/sec and an amplitude of 0.006 in. Each layer was vibrated for 2.5 minutes for W/C = 0.3 and 2 minutes for W/C = 0.4. After consolidation, the molds were sealed at the top.

During the first twenty-four hours, the molds were stored in the laboratory in a horizontal position to reduce the effects of bleeding. The specimens were then removed from the molds and stored in lime-saturated water until the time of test.

Prior to testing, the specimens were shortened to 3 in. by removing equal portions from each end using a high-speed masonry saw. Special care was taken to keep the sawed surfaces square with the

length of the specimen. Each specimen was wrapped in plastic to avoid the loss of moisture during testing.

2.3.2 Loading system

All tests were done in strain control mode using a 110,000 pound capacity closed-loop servo-hydraulic Instron testing machine (Model No. 1334). The specimens were placed between flat, nonrotating platens using the following procedure. A layer of freshly mixed high strength gypsum cement (Hydrostone) was placed on the bottom platen. The specimen was gently pressed on it. Another layer of Hydrostone was placed on the top of the specimen. The bottom platen was raised slowly, bringing the top layer in contact with the top platen. The specimen was twisted gently by hand a few times as the bottom platen was further raised allowing the Hydrostone to squeeze out between specimen ends and the platens. Using this procedure, Hydrostone layers less than 0.01 in. thick were obtained at each end of the specimen. The Hydrostone layers were allowed to dry for at least 30 minutes before loading the specimen.

2.3.3 Stress and strain measurements

A pair of Schaevitz Linear Variable Differential Transformers (LVDT's), Model No. 050 MP, were used to measure the average axial strain (Fig. 2.2), and to serve as the controlling transducers for the closed-loop testing machine. The LVDT's had a range of 0.05 in. and a sensitivity of 0.005 in./volt. The LVDT's were clamped to the bottom platen at equal distances from opposite faces of the specimen. The LVDT core rods were attached to the top platen and were held

parallel to the specimen's longitudinal axis. The two LVDT's provided the average longitudinal strain for the total height of the specimen. Two MTS extensometers, Model No. 532.11B-20, were used either as comparison transducers for longitudinal strain or for measuring the average lateral strain.

For the first several specimens, the extensometers were used as comparison transducers for longitudinal strain. One-inch gage extenders were attached to the fixed legs of the extensometers to enable measurements to be made over the middle 2 in. of a specimen. A cyanoacrylate adhesive and rubber bands were used to attach the extensometers on two opposite faces of a specimen. Up to 20% of the maximum stress, the strain measured with the LVDT's (over the total height (3 in.) of the specimen) was within 0.5% of the strain measured with the extensometers (over the middle 2 in. of the specimen). Between 20% and 90% of the maximum stress, the average strain measured with the LVDT's was within 2% (lower) of the average strain measured with the extensometers. At stresses higher than 90% of the maximum stress, the LVDT readings stayed slightly below (2 to 5%) those of the extensometers. At the maximum stress and on the descending part of stress-strain curve, the readings using the extensometers became unreliable as the extensometers detached from the specimen surface due to cracking. Ahmad and Shah (2) compared the strain measured with various transducers and gage lengths on concrete specimens. They concluded that the measurement of strain over the total height of the specimen, using LVDT's, provides a "fair

average" of strain values measured over various fractions of the specimen height, using strain gages and compressometers. In this study, the strain measured over the total height (3 in.) of the specimen tended to be smaller than the strain measured over the middle 2 in. of the specimen for high stress levels. This happens because of the restraint at the ends of the specimens, especially at higher stress levels, caused by a triaxial state of compression which consequently reduces the axial deformation in these regions.

For the remaining specimens, only LVDT's were used to measure longitudinal strain, and the extensometers were used, without the extenders, to measure the average lateral strain at the middle of the specimen height. As before, a cyanoacrylate adhesive and rubber bands were used to attach the extensometers on two opposite faces of a specimen to measure the average lateral deformation at the mid-height of the specimen. An Instron load cell, Model 3156-115, with a 110,000 pound capacity was used to measure axial force.

The average signal from the LVDT's lagged behind the signal from the load cell by 1.17 milliseconds. The load cell signal, in turn, lagged behind the extensometer signal by 0.6 millisecond. These time lags were accounted during data reduction. Thus, for example, while plotting the stress-strain curves at a strain rate of 300,000 microstrain/sec, the LVDT strain values were shifted backwards by 14 readings to match with the stress values.

2.3.4 High speed data acquisition

A Hewlett-Packard Measurement Plotting System, Model No. 7090A, was used to acquire the experimental stress-strain data. This system can simultaneously scan up to 1000 readings on each of its three transducer channels over a period that may range from 0.03 sec. to 24 hr. Following a test, the data was transferred to a Hewlett-Packard desktop computer, Model No. 9825T, for analysis and storage. The data was later transferred to a Harris 1200 computer.

2.4 Scope of Tests

The specimens were strained in compression to 15,000 microstrain, ensuring data from the descending as well as the ascending portions of the stress-strain curve at all strain rates. The specimens were loaded at seven strain rates ranging from 0.3 microstrain/sec (3.0×10^{-7}/sec) to over 300,000 microstrain/sec (3.0×10^{-1}/sec) using the Instron testing machine. Successive strain rates were separated by a factor of 10 (one order of magnitude). At the slowest strain rate a specimen failed in about 12 hours, while at the fastest strain it failed in 0.03 sec. These strain rates and test durations compare to a typical compression test for concrete, which is made at a strain rate of 15 microstrain/sec and takes about 2 minutes. The highest strain rates used in the tests are comparable to strain rates that occur in a helicopter crash (76).

In the data that follow, three strain rates are shown: the average strain rate from zero stress to the peak stress, $\dot{\varepsilon}_{0-100}$, the

average strain rate from 5 percent to 20 percent of the peak stress, $\dot{\varepsilon}_{5-20}$, and the average strain rate from 50 percent (point A in Fig. 2.3) to 99 percent of the peak stress (on the descending portion of stress-strain curve, point B in Fig. 2.3), $\dot{\varepsilon}_{50-99}$. While $\dot{\varepsilon}_{5-20}$ controls the initial response of the materials, $\dot{\varepsilon}_{50-99}$ controls the response near the peak.

Virtually constant strain rates were obtained during loading up to nominal strain rate of 300 microstrain/sec. At higher rates of loading, the initial response of the machine, up to about 30% of the strength, was dependent on the stiffness of the material. At a nominal strain rate of 3000 microstrain/sec, the initial response of the testing machine was higher than the desired strain rate, the stiffer the material the greater was the $\dot{\varepsilon}_{5-20}$. Thus, $\dot{\varepsilon}_{5-20}$ was up to 36% higher than $\dot{\varepsilon}_{0-100}$ (for mortar A, W/C = 0.5, Table 2.9).

At a nominal strain rate of 30,000 microstrain/sec, the initial response of the machine was either lower or higher than the desired strain rate depending on whether the initial modulus of elasticity (see section 2.5.5) was less than or greater than 4.0×10^6, respectively. Thus, $\dot{\varepsilon}_{5-20}$ was higher (up to 27%) than $\dot{\varepsilon}_{0-100}$ for the three pastes and mortar B with W/C = 0.5. $\dot{\varepsilon}_{5-20}$ was lower (up to 19%) than $\dot{\varepsilon}_{0-100}$ for the mortars, except for mortar B with W/C = 0.5.

At a nominal strain rate of 300,000 microstrain/sec the initial response was always lower than the desired strain rate. The greater the initial modulus of elasticity for a material (Table 2.9), the lower was the $\dot{\varepsilon}_{5-20}$. The strain rate stabilized at about 30% of the

compressive strength. $\dot{\varepsilon}_{50-99}$ was consistently higher (up to 95%) than $\dot{\varepsilon}_{0-100}$ for the materials. Fig. 2.3 shows a typical strain versus time plot at a nominal strain rate of 300,000 microstrain/sec.

A total of 98 paste and 125 mortar specimens were tested. Major emphasis was placed on strain rates of 3, 3000, and 300,000 microstrain/sec. At least 2 and as many as 11 specimens of each material at each strain rate were tested to compare strength, initial modulus of elasticity, and strain at the peak stress at the seven strain rates. At least one and as many as 11 specimens of each material were tested at most strain rates to compare initial Poisson's ratios as a function of strain rate. Test results for individual cement paste and mortar specimens including materials, number of specimens, strain rates, strength, selected strains, initial modulus of elasticity, and initial Poisson's ratio, are given in Tables 2.1-2.8. Table 2.9 shows the average values at each strain rate for the data shown in Tables 2.1 through 2.8. Tables 2.10-2.17 show the average values of Poisson's ratio at various strain levels for each of the seven strain rates. Table 2.18 shows strain rates and the initial Poisson's ratio values for specimens tested exclusively to study the strain-rate sensitivity of Poisson's ratio.

2.5 Test Results

2.5.1 Stress-strain curves

Figs. 2.4-2.6 show typical stress-strain curves at the seven strain rates for cement paste with W/C = 0.3, 0.4, and 0.5. Figs.

2.7-2.11 show the same for mortars. These curves are plotted to a maximum strain of 15,000 microstrain, so that most of the descending portions can also be included. Oscillations after the peak stress in the stress-strain curves at higher strain rates are due to the limited stiffness of the load frame and the finite response time of the servo-hydraulic feed-back system.

A significant change in the stress-strain response of the materials with every order of magnitude increase in strain rate is clearly seen in these figures. For each material, as the strain rate is increased, both the initial slope and the peak stress increase, while the nonlinearity of the initial response decreases. The loss of stress after attaining the maximum value is more abrupt in pastes than in mortars. The strain at the peak stress is generally the greatest at the lowest strain rate (0.3 microstrain/sec). As the strain rate is increased, the strain at the peak stress first decreases and then increases. Similar variations have been observed by others (14, 15, 23, 47) for concrete and its constituents. There are some dissimilarities between the stress-strain response of cement paste and mortar. For example, the pastes are generally stronger than mortars with the same water-cement ratio. These differences are discussed in section 2.5.7. Specific aspects of the response of the materials as a function of strain rate are discussed in sections 2.5.3-2.5.6. A general discussion of the observations is provided in section 2.6.

2.5.2 Failure Mode

As the strain rate is increased, specimens failed more abruptly, with an increasing number of cracks and a louder cracking noise. This behavior was most evident for cement pastes with low water-cement ratios. At the highest strain rate, in excess of 300,000 microstrain/sec, paste specimens with W/C = 0.3 disintegrated into a large number fragments, which frequently flew out of the plastic cover. To protect the test equipment from the fragments, a thick cloth was tied around the platens of the testing machine before loading the specimen at high strain rates. Mortar specimens, especially those with high water-cement ratios, failed with comparatively less violence. At higher strain rates, mortar specimens generated particles of sand and paste in the failure regions. The failure cracks in cement paste were generally straighter, longer and cleaner than those in the mortar specimens. At higher strain rates, cracks were larger in number and straighter, and the specimens produced a larger number of fragments at failure than at lower strain rates. The sensitivity of the failure mode of concrete specimens to strain rate has been observed by others (5, 38).

2.5.3 Peak stress

Figs. 2.12 and 2.13 show the variation in the average peak stresses of cement pastes and mortars as a function of strain rate. The figures represent all specimens tested, except those tested specifically to study the rate sensitivity of Poisson's ratio. Each

data point represents the average of 2 to 11 specimens. The diverging lines with increasing strain rate indicate that the strength of the stronger materials is enhanced more by increasing strain rate than the strength of the weaker materials. Additional information can be obtained by normalizing the results with respect to the strength at a single strain rate. This is done in Fig. 2.14, in which all strength values shown in Figs. 2.12 and 2.13 are normalized with respect to the strength at 3 microstrain/sec. Fig. 2.14 indicates that with every order of magnitude increase in strain rate, the strength of saturated cement paste and mortar increases about 15 percent. This nearly linear increase in strength with each order of magnitude increase in strain rate does not appear to be a function of the type of material (paste or mortar) or the water-cement ratio, although the two highest strength pastes show the greatest increase in strength at the highest strain rate.

The fact that the effects of strain rate on strength are virtually the same for the materials tested indicates that the mechanisms that control the rate sensitive behavior of these materials are quite similar.

Figs. 2.12-2.14 and Table 2.9 indicate that, for the strain rates used in this study, for W/C = 0.5 the strength of cement paste is about the same (within 5%) as for mortar, for W/C = 0.4 the paste is slightly stronger (up to 6%) than mortar, and for W/C = 0.3 the paste is considerably (10% to 32%) stronger than mortar.

2.5.4 Strain at Peak Stress

Fig. 2.15 shows the variation in the average strain at the peak stress, ε_p, as a function of strain rate ($\dot{\varepsilon}_{50-99}$) for the materials. Fig. 2.16 shows the same for the average post peak strain at 90 percent of the peak stress, ε_{pp}. ε_{pp} is used because it provides a somewhat better measure of ductility than ε_p. For both materials, the nonmonotonic nature of ε_p and ε_{pp} is clearly shown in Figs. 2.15-2.16. Both ε_p and ε_{pp} first decrease and then increase with increasing strain rates. In each case, the slowest test rate (test duration = 12 hours) results in the highest value of ε_p, due to the effect of creep. As the strain rate increases, the creep effects decrease and ε_p decreases accordingly. With a further increase in strain rate, ε_p once again increases. This increase in ε_p is likely the result of limitations in crack velocity compared to the rate of loading. The influence of limited crack velocity on stress-strain behavior is discussed in section 2.6.

The effect of water-cement ratio on ductility (ε_{pp}) is illustrated in Fig. 2.17, where the average values of ε_{pp} are compared with water-cement ratio for each strain rate for the materials. Within the range of water-cement ratios used, there is a trend towards decreased strain capacity as the water-cement ratio is increased. For cement paste tested at 0.3 microstrain/sec and 3.0 microstrain/sec, the results do not follow the trend at the other strain rates. While at 0.3 microstrain/sec the decrease in ε_{pp} is nonmonotonic, at 3 microstrain/sec there is a slight increase in ε_{pp}

(from 7940 to 8061 microstrain) as the water-cement ratio is increased from 0.3 to 0.5.

A decrease in the strain at the maximum stress with an increase in water-cement ratio can be expected. For higher water-cement ratio material, the matrix is less stiff than that in the lower water-cement ratio materials. This makes the difference in the stiffness of the matrix and that of an inhomogeneity (e.g. an unhydrated cement particle or a sand grain) greater, causing higher intensity of interfacial cracking and resulting in lower strain capacities for the higher water-cement ratio materials.

2.5.5 Initial modulus of elasticity

In this study, the initial modulus of elasticity, E_i, is taken as the slope of the best fit line through stress-strain curve between 5 and 20 percent of the peak stress. This range is selected to remove the initial seating errors as a specimen is loaded, to allow a range wide enough to limit the effects of scatter, and to keep the upper limit at a value where the response is virtually linear. Fig. 2.18 shows that with increasing strain rate, the elastic moduli of the materials increase significantly. The relative changes in E_i are shown in Fig. 2.19, where the values shown in Fig. 2.18 are normalized with respect to the value at 3 microstrain/sec. The normalized results for all the materials lie within a narrow band, indicating that the effects of strain rate on E_i are similar for the materials. As with strength (Fig. 2.14), the overall rate sensitive behavior of the elastic moduli is approximately linear. The percentage increase

in E_i is approximately constant with each order of magnitude increase in strain rate. However, this increase in E_i (Fig. 2.19), is only about half of the corresponding increase in strength. The lower rate sensitivity of E_i compared to strength is consistent with similar observations in studies of concrete (2, 15, 45). For both cement paste and mortar, E_i increases by about 40 percent as the strain rate ($\dot{\varepsilon}_{5-20}$) increases from 0.3 microstrain/sec to about 150,000 microstrain/sec, or about 7 percent for each order of magnitude increase in strain rate. The results clearly show that the initial stiffness of each material increases considerably with increasing strain rate.

2.5.6 Poisson's ratio

Figs. 2.20 and 2.21 illustrate the variation in the average Poisson's ratios of the pastes and mortars, respectively, as a function of strain rate ($\dot{\varepsilon}_{5-20}$). The Poisson's ratio, ν_i, illustrated here is calculated at 20 percent of the strength. The data points shown represent 1 to 11 specimens. Some electrical noise in the transverse strain signal necessitated passing smooth curves through the transverse strain versus longitudinal strain plots. Fig. 2.22 compares the Poisson's ratios for paste and mortar and indicates that the values of Poisson's ratio fall within a narrow range for the materials, with the value of ν_i being, on the average, somewhat lower for mortar than cement paste. For example at strain rates ($\dot{\varepsilon}_{5-20}$) of 3, 3000, and about 150,000 microstrain/sec, the range of values of ν_i are 0.199 to 0.234, 0.227 to 0.270, and 0.262 to 0.281, respectively.

The strain-rate sensitivity of Poisson's ratio is about the same as that of the elastic modulus, about 7 percent for each order of magnitude increase in strain rate.

As stated earlier, very few studies have considered the rate sensitive behavior of Poisson's ratio (23, 24, 81). The magnitude of the increase in the initial Poisson's ratio observed in this study is consistent with the observations of Dhir and Sangha (23, 24) and Takeda and Tachikawa (81).

Fig. 2.23-2.25 show the variation in the Poisson's ratio as a function of strain for pastes with W/C = 0.3, 0.4 and 0.5, respectively, for strain rates from 0.3 microstrain/sec to 300,000 microstrain/sec. Figs. 2.26-2.30 do the same for the mortars. Values of Poisson's ratio were not obtained for the mortars at 0.3 microstrain/sec, mortar A with W/C = 0.4 at 3 and 300,000 microstrain/sec or mortar A with W/C = 0.5 at 300,000 microstrain/sec. The Poisson's ratios of the materials, except for pastes with W/C = 0.4 tested at the slowest strain rate (0.3 microstrain/sec), increase with increasing strain. For cement paste (Figs. 2.23-2.25), in general, the higher the strain rate, the greater the increase in the Poisson's ratio with increasing strain. For example, for paste with W/C = 0.5 tested at 0.3 microstrain/sec, the Poisson's ratio at 1000 microstrain is 0.191, while the value at 5000 microstrain is 0.205, or an increase of 7%. However, at 300,000 microstrain/sec, the Poisson's ratio increases by 34% from 0.294 at 1000 microstrain to 0.393 at 5000 microstrain. For mortars (Figs.

2.26-2.30), the increase in the Poisson's ratio with increasing strain is significantly greater than that for cement paste. This happens because of higher intensities of cracking in mortar at higher strain levels (6) due to the presence of sand. The increase in Poisson's ratio of the mortars, with an increase in strain, does not increase significantly (even decreases sometimes) with increase in strain rate. For example, for mortar A with W/C = 0.5 tested at 3 microstrain/sec, the Poisson's ratio at 500 microstrain/sec is 0.180 while the value at 2500 microstrain is 0.336, for an increase of 87%. For the same mortar tested at 300 microstrain/sec, the Poisson's ratio at 500 microstrain is 0.219, while the value at 2500 microstrain is 0.364, for an increase of 66%. The corresponding values of the Poisson's ratio of the same mortar at 300,000 microstrain/sec are 0.253 and 0.419, for an increase of 66%.

For pastes tested at the slowest strain rate (0.3 microstrain/sec), the Poisson's ratio does not change much with an increase in strain. For example, with an increase in strain from 1000 microstrain to 5000 microstrain, the Poisson's ratio of paste with W/C = 0.4 decreases by 4% (from 0.187 to 0.181). The Poisson's ratios of pastes with W/C = 0.3 and 0.5 increase by 15% (from 0.141 to 0.161) and 7% (from 0.191 to 0.205), respectively. At 0.3 microstrain/sec, the relative insensitivity of Poisson's ratio of the pastes to changes in strain is expected due to the effects of creep and the subsequent reduction in cracking (6). Under sustained loading (section 4.7.5), it is observed that the Poisson's ratio of

cement paste drops due to creep (6). At 0.3 microstrain/sec, creep effects are not dominant enough to result in a clear drop in the Poisson's ratio. However, if a strain rate one order of magnitude below 0.3 microstrain/sec were used, a drop in the Poisson's ratio would be expected. At higher strain rates, creep effects decrease, cracking increases, and Poisson's ratio increases significantly with an increase in strain.

For cement paste, in general, the strain-rate sensitivity of Poisson's ratio (the increase in Poisson's ratio with each order of magnitude increase in strain rate) increases with an increase in strain. For mortar, however, apart from scatter in the data, the strain-rate sensitivity of Poisson's ratio increases little with an increase in strain. This is reflected in the change in the strain-rate sensitivity of Poisson's ratio with strain. For example, the average strain-rate sensitivity of Poisson's ratio for paste at 1000 microstrain is about 9%, while the values at ε = 2500 and 5000 microstrain are about 13% and 17%, respectively (note the diverging Poisson's ratio versus strain curves, especially Fig. 2.24 and 2.25). The strain rate sensitivity of the Poisson's ratio of mortar at 500 microstrain is about 7%, while the value at 2500 microstrain is about 8% (compared to about 13% for the pastes) (Figs. 2.26-2.30).

In the above comparisons (Figs. 2.23-2.30), the upper limits for the strains (2500 to 4000 microstrain for mortars and 5000 to 6000 microstrain for cement paste) correspond to at least 85% of the strength of the materials. These comparisons clearly show that

Poisson's ratio increases with an increase in strain rate up to stress levels in excess of 85% of the material strength. This behavior differs from the observations of Takeda and Tachikawa for concrete specimens (81) that Poisson's ratio decreases with strain rate at stress levels higher than 80% of the strength. The comparisons with Takeda and Tachikawa are not exact, however, because unlike Takeda and Tachikawa, the Poisson's ratio values here are calculated as a function of strain and not of stress.

2.5.7 Effect of Sand Content

Sand increases the initial modulus of elasticity and reduces the strength and ductility of cement paste. As discussed by Attiogbe and Darwin (6), sand acts as stress raiser, thus increasing the local compressive and lateral tensile stresses within the material. The increase in local stresses reduces both strength and strain capacity. The addition of relatively stiffer sand particles to cement paste increases initial stiffness. Thus, mortars have higher initial elastic moduli than paste with the same water-cement ratio. At a given water-cement ratio, the mortar with the higher sand content (mortar B for W/C = 0.4 and mortar A for W/C = 0.5) has a higher initial elastic modulus than the mortar with the lower sand content. The effects of strain rate on strength and initial elastic moduli, E_i and ν_i, for both paste and mortar appear to be about the same, indicating that the controlling mechanisms are not greatly affected by either the water-cement ratio or sand content.

The effect of sand content on the rate sensitivity of strength is illustrated in Fig. 2.13. The results shown in Fig. 2.13 are also compared in Table 2.9. Aside from the scatter in the data, the different sand contents appear to have little effect on the influence of strain rate on relative strength gain.

The effect of sand content on the initial elastic modulus, E_i, is illustrated in Fig. 2.18. All mortars have a higher initial modulus than cement pastes of the same water-cement ratio. As stated earlier, the higher the sand content of mortar, the higher the initial modulus of elasticity. For W/C = 0.3, the ratio of E_i for mortar A to E_i for cement paste ranged from 1.307 to 1.494. Similarly, for W/C = 0.4 the ratio of E_i of mortar to E_i of paste ranged from 1.706 to 1.855 for mortar A (S/C = 1.59) and from 1.723 to 1.988 for mortar B (S/C = 1.97). For W/C = 0.5, the ratio of E_i of mortar to E_i of paste ranged from 1.622 to 1.906 for mortar B (S/C = 1.29) and from 1.960 to 2.206 for mortar A (S/C = 2.28).

Fig. 2.31 compares the ratio of ε_{pp} for each mortar to ε_{pp} for the cement paste with the same water-cement ratio as function of strain rate. The ratio may be considered to be a measure of the relative ductility of mortar with respect to cement paste. In all cases, the relative ductility is less than 1.0, indicating a reduction in the ductility of paste with the addition of sand. For mortars with the same water-cement ratio, the higher the sand content the lower the relative ductility. Fig. 2.31 indicates that the relative ductility of the mortars increases with strain rate. The

increase in relative ductility with strain rate is less pronounced for mortars with W/C = 0.5 than for the other mortars.

2.6 Discussion

The comparisons of sections 2.5.3-2.5.7 show that the rate sensitivities of the stress-strain behavior near failure, the initial modulus of elasticity, and the initial Poisson's ratio do not change with the strength. Thus the results differ from previous observations for concrete in which weaker concrete was observed to be more rate sensitive than stronger concrete (5, 18, 28, 38, 96, 99).

The differences in the stress-strain response near failure and the failure mode of cement paste and mortar with changes in strain rate can be explained by considering the growth and propagation of cracks in an inhomogeneous media subjected to increasing strain (92, 98).

In cement paste, the transition zones between the unhydrated cement particles and the hydration products are comparatively strong and are not usually sources of preexisting flaws. As a crack grows under increasing strain, it sooner or later meets a relatively stiffer unhydrated cement particle and is arrested, at least temporarily. If the applied strain rate is slow enough, the crack eventually grows around the inhomogeneity. However at higher strain rates, more and more such cracks find insufficient time to grow around the stiff inhomogeneities. At higher strain rates, two alternative processes are likely for each growing crack: (i) the crack is forced to grow through a stiffer zone, or (ii) the increased local stress intensity

is relieved by the initiation or growth of other cracks in the vicinity that have no hindrances. The former process causes an increased strength and a more violent failure mode; the latter process causes a larger number of shorter length cracks, in place of a smaller number of longer cracks, allowing higher strain capacity before failure (Fig. 2.15-2.17). These processes are intensified as the W/C is lowered, i.e. the number of unhydrated particles are increased, making cement paste with the lowest water-cement ratio fail most violently and have the highest strain and stress capacities.

In the case of mortar, the sand particle-matrix transition zones are very weak compared to both the matrix and sand particles. In addition, these transition zones contain preexisting flaws created by bleed water that has collected below the sand particles. The growing cracks, even at higher strain rates, find enough weak links, in the form of the preexisting flaws at the sand-matrix interface, to grow without being forced through the stiffer sand particles. Thus, the failure mode of mortar specimens, especially those with higher water-cement ratios, is less violent than paste specimens. As mentioned in section 2.5.7, the stiffer sand particles raise the local stress intensities, as well as provide weak zones for the preexisting flaws to grow into cracks, resulting in lower stress and strain capacities than the paste specimens. At high strain rates, the presence of inhomogeneities, both sand and unhydrated cement particles, do provide for some crack arrest, causing both the peak stress and the strain at the peak stress to increase, though by lesser magnitudes than in the

case of paste specimens. The smallest increase in relative ductility with increasing strain rate occurs in the case of mortars with the highest water-cement ratio (W/C = 0.5) (Fig. 2.31). This is expected since these mortars have the highest density of flaws due to bleed water.

While the rate sensitivity of stress-strain response near failure can be related to the initiation and growth of cracks, the same cannot be said for the rate sensitivity of the initial moduli, E_i and ν_i. Very little cracking occurs at the strain levels at which E_i and ν_i are calculated (6), yet these parameters are significantly rate sensitive, indicating that another mechanism, in all likelihood moisture movement, plays an important role in the initial response of the materials. The experimental results also indicate that the concept of "strain-rate independent material moduli" is not correct. In chapter 3, a micromechanics viscoelastic model is developed to study and simulate the strain-rate sensitivity of the initial moduli. The model considers viscous and rate dependent flow of pore water to determine the effective bulk moduli of water saturated pores. Paste is modeled as a composite consisting of spheroidal pores and spherical solid grains. A self-consistent scheme is used to determine the overall composite moduli. Since the effective bulk moduli of the pores are strain-rate dependent, they make the response of the composite strain-rate dependent as well. The model closely matches the experimental variation in the initial moduli as a function of strain rate.

2.7 Summary of Observations

1. The stress-strain curves of cement paste and mortar are nonlinear up to a nominal strain rate of 300,000 microstrain/sec.
2. The nonlinearity of stress-strain curves for cement paste and mortar decreases with increasing strain rate.
3. Specimens fail more violently as the strain rate is increased. In general, at higher strain rates failure cracks are straighter and greater in number than at the lower strain rates.
4. For a given water-cement ratio, cement paste specimens have a higher peak stress than mortar specimens. The loss of stress after the peak is more abrupt in cement paste than in mortar.
5. The compressive strength, initial modulus of elasticity, and initial Poisson's ratio of cement paste and mortar increase approximately linearly with each order of magnitude increase in strain rate. Strength is about twice as rate sensitive as the initial modulus of elasticity and Poisson's ratio.
6. The relative increases in strength, initial modulus of elasticity, and Poisson's ratio with each order of magnitude increase in strain rate are about the same for cement paste and mortar with W/C = 0.3, 0.4 and 0.5.

7. The strain at the peak stress varies in a nonmonotonic manner with strain rate. Its value is greatest at the slowest strain rate, 0.3 microstrain/sec, used. With increasing strain rate, it first decreases then increases.
8. Within the range of water-cement ratios considered, the materials tend to have lower strain capacities at higher water-cement ratios.
9. The Poisson's ratio of the materials, except pastes tested at 0.3 microstrain/sec, increase significantly with increased strain. The increase in Poisson's ratio with increased strain is greater for mortar than that for cement paste.
10. The increase in Poisson's ratio of the materials with an order of magnitude increase in strain rate is greater at higher strains that at lower strains. This is more so for paste than for mortar. This higher strain-rate sensitivity is observed for Poisson's ratio up to 5000 microstrain for paste and 2500 microstrain for mortar.
11. The introduction of sand lowers the strain capacity of cement paste. At a given water-cement ratio, cement paste has a higher strain at the peak stress than does mortar. For mortars, the lower the sand content, the higher strain at the peak stress.
12. The introduction of sand increases the initial modulus of elasticity of cement paste. Within the ranges considered,

the higher the sand content, the higher the initial modulus of elasticity.

13. The differences in the values of the peak stress, the strain at the peak stress, and Poisson's ratio for cement paste and mortar can be explained by the growth and propagation of cracks in the materials.

14. The strain-rate sensitivity of the initial moduli of the materials, at strains where very little cracking is expected, strongly indicates the importance of moisture movement in the strain-rate sensitivity of the moduli.

CHAPTER 3

STRAIN RATE SENSITIVE MODEL FOR A NEARLY SATURATED POROUS SOLID

3.1 Introduction

The strain-rate sensitivity of cement paste, mortar, and concrete has been studied since the early part of this century (1). These materials, like other structural materials, show increased tensile (95, 96), flexural (30, 31, 33, 86, 95), and compressive (1, 2, 15, 23, 24, 25, 38, 46, 58, 59, 64, 68, 73, 74, 75, 79, 84) strengths at higher strain rates. What sets them apart from most other structural materials, such as steel, is that their moduli of elasticity are sensitive to strain rate as well (2, 15, 38, 45, 51, 57, 90). The degree of saturation at the time of testing seems to be the most important factor influencing the rate sensitive behavior. The higher the water content, the greater the strain-rate sensitivity (46). A self-consistent model is developed here to estimate the effective modulus of elasticity and Poisson's ratio of a nearly saturated porous solid as functions of strain rate and pore structure.

A porous solid, such as hardened cement paste, can be viewed as a composite consisting of a distribution of pores of various shapes and sizes embedded in a solid matrix. The overall moduli of such a composite are dependent upon the shapes and the moduli of the pores and the solid grains. When a porous solid is nearly saturated (a term which will be defined more precisely later), most of the pores

are filled with a fluid. If the porosity is significant, the saturated pores are generally connected with the unsaturated pores. For the purpose of this development, an "unsaturated pore" is a pore in which the fluid, if any, will develop no appreciable stress when the material is stressed. An unsaturated pore may serve as a source or a sink for pore fluid (tension or compression). The connection between a saturated and an unsaturated pore is represented by a circular orifice.

Under axial stress the pores tend to change in volume, resulting in a hydrostatic stress in the pore fluid and a flow through the orifice. For a given strain rate and pore dimensions, the response of a saturated pore depends on the orifice dimension. When the orifice cross section approaches zero, or its length approaches infinity, the pore behaves as though it were isolated and its effective bulk modulus, K_f^*, is the same as the bulk modulus of the fluid, K_f, it contains (Note: The shear modulus of the pore fluid is taken as zero, and will not be considered). As the orifice cross section is increased, or its length is decreased, the pore fluid is able to escape through it more easily, making the effective modulus, K_f^*, smaller and the material more compliant (19).

Similarly, if the applied strain rate, $\dot{\varepsilon}$, is varied, keeping the geometry of the orifice relative the pore constant, a corresponding variation in K_f^* can be observed. When $\dot{\varepsilon}$ approaches zero, the pore fluid gets enough time to escape, and there is negligible hydrostatic stress buildup, thus K_f^* approaches zero. As the strain rate, $\dot{\varepsilon}$, is

increased there is less and less time for the fluid to escape through the orifice causing the response of the pore to be stiffer, i.e., causing the effective bulk modulus of the pore, K_f^*, to increase, until it approaches the bulk modulus of the pore fluid, K_f. With a further increase in strain rate, the pore responds like an isolated pore.

Thus, the effective bulk modulus of a saturated pore, K_f^*, depends both on the applied strain rate and the geometry of the orifice relative to the pore. The higher the strain rate and the smaller diameter of the orifice, the higher the effective bulk modulus of the pore.

If the effective bulk moduli of the pores, K_f^*, and moduli of solid grains are known, the composite moduli can be determined using a self-consistent scheme. Four general approaches have been used to determine effective moduli of composites. Approaches that consider the shapes of the pores also require the pores to be isotropically distributed. A few studies have compared the theoretical values of composite moduli, determined with these approaches, with experimental values (22, 48). The four approaches used for determining the composite moduli are briefly compared next. In section 3.5 they are discussed in more detail.

In the bounding approach, used by Paul (62) and Hashin and Shtrikman (37), expressions are obtained for conservative upper and lower bound values for the composite moduli. Hashin and Shtrikman's

(62) expressions provide much tighter bounds than those provided by Paul's (62) expressions.

Eshelby (27), one of the pioneers of rigorous perturbation theory, considered the perturbation in elastic energy due to an ellipsoidal inclusion in an otherwise uniform stress field. The composite moduli expressions are then obtained by arithmetically summing the perturbations due to all inclusions. Eshelby neglected any interactions between the inclusions, and the resulting expressions, though exact, work well only for very low concentrations of inclusions.

The static self-consistent approach of Budiansky (16), Hill (43), and Wu (95) works well up to significantly high concentrations of inclusions (91). In this approach, Eshelby's results are used, and the interactions among the inclusions are approximated by replacing the real matrix with an effective matrix having the moduli of the composite. In some cases, this approach has been shown to give unreasonable estimates for the composite moduli (16, 36, 40, 62, 102). The unreasonable estimates have led to some modifications of the approach. These aspects of the static self consistent approach are discussed in section 3.5.

The elastic wave scattering approach (50) estimates the elastic moduli of a composite by considering the scattering of an elastic wave from a representative sphere of the composite and equating that to the scattering from an equal size sphere of the effective medium, i.e., a medium having the moduli of the composite. Berryman (11, 12)

has shown that his self-consistent procedure, using a modification of the elastic wave scattering approach, provides reasonable estimates of the overall moduli of solids with fluid inclusions. His results are used in the rate-sensitive model developed here.

3.2 Overview of the Model

In the strain-rate sensitive model presented in the next few sections, a nearly saturated porous solid is modeled as consisting of isotropically distributed saturated spheroidal pores and spherical grains (13, 49). Each saturated pore is assumed to be connected to an unsaturated pore or region via a circular cylindrical orifice. The hydrostatic stress within a pore, $\sigma_f(t)$, which is surrounded by the effective medium whose moduli depend on the response of all pores, is expressed as a function of the geometry of the pore and the orifice, the properties of the saturating liquid, the applied strain, and the strain rate. For the purposes of this development, the strain rate is constant. The effective bulk modulus of a pore, K_f^*, is then a function of $\sigma_f(t)$, the bulk modulus of the fluid, K_f, and the relative geometry of the pore and the orifice. The effective bulk moduli of pores with various orifice sizes are determined and used along with the moduli of the solid phase in a self-consistent manner to estimate the overall moduli of the porous solid. Rate sensitive composite moduli are compared with the corresponding experimental results.

3.3 Hydrostatic Stress in Pore Fluid, $\sigma_f(t)$

In this section, expressions for the hydrostatic stress in the pore fluid, $\sigma_f(t)$, for a porous material under axial strain are obtained. A differential equation in $\sigma_f(t)$ is obtained by equating the rate of change of the volume of the pore fluid to that of the pore containing it. The differential equation is solved for two cases. Case I is applicable for small strains when the volume of the orifice flow is negligible compared to the volume of the pore. Case II does not have this restriction. For case I a closed-form expression for $\sigma_f(t)$ is obtained after simplifying the differential equation in $\sigma_f(t)$ to a first order linear differential equation. For case II a closed-form solution is not possible. Hence, values of $\sigma_f(t)$ are successively calculated at selected times, starting with the initial condition $\sigma_f(t) = 0$ at $t = 0$.

3.3.1 Derivation of Differential Equation in $\sigma_f(t)$

Consider a saturated spheroidal pore surrounded by a homogeneous isotropic medium subjected to uniform stress away from the pore. The pore is connected to an unsaturated region in the medium via a circular cylindrical orifice. The orifice is very small in comparison with the pore, so that its interference with the latter's strain field is negligible. The unsaturated pore, or regions in the case of cement paste, can arise due to self desiccation or evaporation. Each unsaturated region can be connected to more than one saturated pore via smaller cylindrical pores or orifices. The total volume of the

unsaturated regions is considered to remain constant with time and thus does not enter the calculations.

When the surrounding medium is subjected to a uniform average strain, the magnitude of the hydrostatic stress of the pore fluid, $\sigma_f(t)$, is a function of the relative geometry of the pore and the orifice, the properties of pore fluid and the strain rate. Similarly, the rate of flow through the orifice, $q_{or}(t)$, is a function of the same variables. In fact, the two, e.g., $\sigma_f(t)$ and $q_{or}(t)$ are interdependent. The higher the strain rate, the less the time for the fluid to flow, and the higher the value of $\sigma_f(t)$. Since the pore surface always remains in contact with the pore fluid, the rate of change of volume of the pore fluid at time t must be equal to the rate of change of the volume of the pore itself at time t, or

$$\frac{\Delta V_{fluid}(t)}{\Delta t} = \frac{\Delta V_{pore}(t)}{\Delta t} \tag{3.1}$$

The left hand side of Eq. 3.1 is the sum of the rate of change of volume of the fluid due to pressure in it $\left(\frac{\Delta V_{fp}(t)}{\Delta t}\right)$ and the rate of flow of fluid through the orifice $\left(q_{or}(t)\right)$. The right hand side is the sum of the rate of change of volume of empty pore under the external strain $\left(\frac{\Delta V_{pe}(t)}{\Delta t}\right)$ and the rate of change of volume of the pore due to the pressure in the fluid $\left(\frac{\Delta V_{pp}(t)}{\Delta t}\right)$. Thus, Eq. 3.1 can be written in incremental form as:

$$\frac{\Delta V_{fp}(t)}{\Delta t} + q_{or}(t) = \frac{\Delta V_{pe}(t)}{\Delta t} + \frac{\Delta V_{pp}(t)}{\Delta t} \qquad (3.2)$$

The form of Eq. 3.2 has to be changed so that an expression for the hydrostatic stress in the pore fluid, $\sigma_f(t)$, can be obtained. In order to do that, the numerators and the denominators of the first term in the left hand side, and first and second terms in the right hand side are multiplied by $V(t)\Delta\sigma_f(t)$, $\Delta\varepsilon(t)$ and $V_i\Delta\sigma_f(t)$, respectively. In which $V(t)$ is the volume of pore at time t, $\Delta\sigma_f(t)$ is the change in the hydrostatic stress in the pore fluid in time Δt at time t, $\Delta\varepsilon(t)$ is the change in the average strain applied on the material containing the pore in time Δt at time t, and V_i is the initial volume of the pore. After these multiplications, and some rearrangement, Eq. 3.2 can be written as:

$$\left(\frac{1}{\dfrac{\Delta\sigma_f(t)}{\Delta V_{fp}(t)/V(t)}}\right)V(t)\frac{\Delta\sigma_f(t)}{\Delta t} + q_{or}(t) = \left(\frac{\Delta V_{pe}(t)}{\Delta\varepsilon(t)}\right)\frac{\Delta\varepsilon(t)}{\Delta t}$$

$$+ \left(\frac{\Delta V_{pp}(t)/V_i}{\Delta\sigma_f(t)}\right)V_i\frac{\Delta\sigma_f(t)}{\Delta t} \qquad (3.3)$$

The denominator of the term inside the parenthesis on the left hand side of Eq. 3.3 is the expression for the bulk modulus of the pore fluid, K_f.

$$K_f = \frac{\Delta\sigma_f(t)}{\Delta V_{fp}(t)/V(t)} \tag{3.4}$$

The term inside the first parenthesis, on the right hand side of Eq. 3.3, is the change in the volume the of the pore per unit average applied strain on the material containing the pore, v^*, or

$$v^* = \frac{\Delta V_{pe}(t)}{\Delta\varepsilon(t)} \tag{3.5}$$

v^* can be expressed in terms of pore geometry, pore orientation, ψ, and moduli of the material surrounding the pore. ψ is defined as the angle between the polar semiaxis of the pore and the horizontal plane. The expression for v^* is quite complex and is derived in Appendix A. The term inside the last parenthesis in Eq. 3.3 is the fractional volume change of the pore per unit internal hydrostatic stress (in pore fluid) or pore compressibility (101), C_{pp}

$$C_{pp} = - \frac{\Delta V_{pp}(t)/V_i}{\Delta\sigma_f(t)} \tag{3.6}$$

C_{pp} can be expressed as a function of the pore geometry and the moduli of the material surrounding the pore. Such expressions are given in Appendix B.

Substituting Eqs. 3.4-3.6 into Eq. 3.3 and changing the equation to differential form gives:

$$\frac{1}{K_f}V(t)\dot{\sigma}_f(t) + q_{or}(t) = v^*\dot{\varepsilon} - C_{pp}V_i\dot{\sigma}_f(t) \tag{3.7}$$

in which the dot represents derivative with respect to time. $\dot{\varepsilon}$ is the applied strain rate and assumed constant for this derivation. In Appendix C, the following expression for the rate of flow of pore fluid through orifice, $q_{or}(t)$, at time t is derived:

$$q_{or}(t) = \left(\frac{\pi d^4}{64\mu h}\right)\sigma_f(t) \tag{3.8}$$

in which, d is the diameter of the orifice, h is the length of the orifice, and μ is the viscosity of the pore fluid. Eq. 3.8 shows that $q_{or}(t)$ is a function of $\sigma_f(t)$. To solve Eq. 3.7 for $\sigma_f(t)$, Eq. 3.8 must be substituted for $q_{or}(t)$ in Eq. 3.7. After the substitution, Eq. 3.7 becomes:

$$\frac{1}{K_f}V(t)\dot{\sigma}_f(t) + \left(\frac{\pi d^4}{64\mu h}\right)\sigma_f(t) = v^*\dot{\varepsilon} - C_{pp}V_i\dot{\sigma}_f(t) \tag{3.9}$$

Also, in Eq. 3.9 for t = T,

$$V(T) = V_i + \int_o^T q_{or}(t)dt \tag{3.10}$$

If $V_i >> \int_o^T q_{or}(t)dt$ which is true if the applied strain on the matrix is small, then V(T) can be replaced by V_i and Eq. 3.9 becomes a simple first order linear differential equation whose closed-form solution can be obtained easily. If such a replacement can not be made, then Eq. 3.9 must be solved numerically. These two cases are considered next.

3.3.2 Case I $V(T) = V_i$

In this case, Eq. 3.9 can be rewritten as

$$A\dot{\sigma}_f(t) + B\sigma_f(t) = C \tag{3.11}$$

in which $A = V_i(\frac{1}{K_f} + C_{pp})$, $B = \pi d^4/64\mu h$, and $C = v^*\dot{\varepsilon}$ are not functions of time. Eq. 3.11 is a first order linear differential equation satisfying the initial condition

$$\sigma_f(t) = 0 \text{ at } t = 0 \tag{3.12}$$

The general solution of Eq. 3.11 is the linear combination of (i) a particular solution and (ii) a homogeneous solution. Since the right hand side is a constant, the particular solution will have the form

$$\zeta(t) = M \tag{3.13}$$

in which M is a constant. Substituting Eq. 3.13 into Eq. 3.11, M = C/B, thus

$$\zeta(t) = C/B \tag{3.14}$$

The homogeneous equation corresponding to Eq. 3.11 is

$$A\dot{\sigma}_f(t) + B\sigma_f(t) = 0 \tag{3.15}$$

with the characteristic equation

$$A\beta + B = 0 \tag{3.16}$$

Eq. 3.16 has a root of $\beta = -B/A$. Hence the solution of the homogeneous equation (Eq. 3.15) is

$$\sigma_f(t) = e^{-\frac{B}{A}t} \tag{3.17}$$

The general solution of Eq. 3.11 is

$$\sigma_f(t) = \frac{C}{B} + Ee^{-\frac{B}{A}t} \tag{3.18}$$

To satisfy the initial condition (Eq. 3.12),

$$E = -\frac{C}{B} \tag{3.19}$$

Hence, the general solution of Eq. 3.11 is

$$\sigma_f(t) = \frac{C}{B}(1 - e^{-\frac{B}{A}t})$$

or

$$\sigma_f(t) = C_1(1 - e^{-C_2 t}) \tag{3.20}$$

in which

$$C_1 = \frac{C}{B} = \frac{64\mu h v^* \varepsilon}{\pi d^4} \tag{3.21}$$

and

$$C_2 = \frac{B}{A} = \frac{\pi d^4}{64\mu h V_i (\frac{1}{K_f} + C_{pp})} \tag{3.22}$$

At this point an important parameter, the characteristic volume ratio, R_{cv}, is introduced.

$$R_{cv} = \frac{\pi d^4}{h V_i} \tag{3.23}$$

in which, $\pi d^4/h$ represents the geometry of the orifice and has units of volume, and V_i is the initial volume of the pore. The characteristic volume ratio, R_{cv}, represents the geometry of the orifice relative to the pore. A higher R_{cv} corresponds to a greater ease of

flow through the orifice and a softer response of the pore, i.e., the pore has a lower effective bulk modulus, K_f^*, than a pore with a lower R_{cv}. The dependence of K_f^* on R_{cv} (see examples in section 3.4) shows that the former does not simply depend on the absolute dimensions of the orifice, but rather on the dimensions of the orifice relative to the pore.

3.3.3 Case II $V(T) \neq V_i$

In this case, the total flow through the orifice is not negligible compared to the initial volume of the pore, V_i. Substituting Eq. 3.10 into Eq. 3.9 and rearranging gives

$$\left(\frac{V_i}{K_f} + \frac{\int_o^T q_{or}(t)dt}{K_f} + V_i C_{pp}\right) \frac{d\sigma_f(t)}{dt} + \frac{\pi d^4}{64\mu h}\,\sigma_f(t) = v^* \dot{\varepsilon} T \qquad (3.24)$$

Integrating Eq. 3.24 for $0 \leq t \leq T$ and substituting for q_{or} using Eq. 3.8 gives

$$\left(\frac{V_i}{K_f} + \frac{\frac{\pi d^4}{64\mu h}\int_o^T \sigma_f(t)dt}{K_f} + V_i C_{pp}\right)\sigma_f(T) + \frac{\pi d^4}{64\mu h}\int_o^T \sigma_f(t)dt = v^* \dot{\varepsilon} T \qquad (3.25)$$

or

$$\left(\frac{V_i}{K_f} + V_i C_{pp}\right)\sigma_f(T) + \left(1 + \frac{\sigma_f(T)}{K_f}\right)\frac{\pi d^4}{64\mu h}\int_o^T \sigma_f(t)dt = v^* \dot{\varepsilon} T \qquad (3.26)$$

in which $\dot{\varepsilon}T$ is the external strain on the at $t = T$. Replacing T by t_i and the integral by the corresponding sum in Eq. 3.26,

$$\left(\frac{V_i}{K_f}+V_i C_{pp}\right)\sigma_f(t_i) + \left(1+\frac{\sigma_f(t_i)}{K_f}\right)\frac{\pi d^4}{64\mu h}\sum_{j=1}^{j=i}\sigma_f(t_j)\Delta t - v^*\dot{\varepsilon}t_i = 0 \quad (3.27)$$

Expanding the second term, Eq. 3.27 becomes

$$V_i\left(\frac{1}{K_f} + C_{pp}\right)\sigma_f(t_i) + \frac{\pi d^4}{64\mu h}\sum_{j=1}^{j=i}\sigma_f(t_j)\Delta t + \frac{\pi d^4}{64\mu h}\left(\frac{\sigma_f(t_i)}{K_f}\right)\sum_{j=1}^{j=i}\sigma_f(t_j)\Delta t - v^*\dot{\varepsilon}t_i = 0 \quad (3.28)$$

Taking the i^{th} terms out of the two summations

$$V_i\left(\frac{1}{K_f} + C_{pp}\right)\sigma_f(t_i) + \frac{\pi d^4}{64\mu h}\left\{\sigma_f(t_i)\Delta t + \sum_{j=1}^{j=i-1}\sigma_f(t_j)\Delta t\right\} + \frac{\pi d^4}{64\mu h}\left\{\frac{(\sigma_f(t_i))^2\Delta t}{K_f} + \frac{\sigma_f(t_i)}{K_f}\sum_{j=1}^{j=i-1}\sigma_f(t_j)\Delta t\right\} - v^*\dot{\varepsilon}t_i = 0 \quad (3.29)$$

Rearranging to get a quadratic equation in $\sigma_f(t_i)$

$$\frac{\pi d^4\Delta t}{64\mu h}(\sigma_f(t_i))^2 + \left\{V_i\left(\frac{1}{K_f}+C_{pp}\right)+\frac{\pi d^4\Delta t}{64\mu h}+\frac{\pi d^4}{64\mu h K_f}\sum_{j=1}^{j=i-1}\sigma_f(t_j)\Delta t\right\}\sigma_f(t_i) + \frac{\pi d^4}{64\mu h}\sum_{j=1}^{j=i-1}\sigma_{ftj}\Delta t - v^*\dot{\varepsilon}t_i = 0 \quad (3.30)$$

Eq. 3.30 can be further simplified by dividing by V_i throughout and replacing $\frac{\pi d^4}{nV_i}$ by R_{cv} (Eq. 3.23)

$$\frac{R_{cv}\Delta t}{64\mu}(\sigma_f(t_i))^2 + \{\frac{1}{K_f} + C_{pp} + \frac{R_{cv}\Delta t}{64\mu} + \frac{R_{cv}}{64\mu K_f}\sum_{j=1}^{j=i-1}\sigma_f(t_j)\Delta t\}\sigma_f(t_i)$$

$$+ \frac{R_{cv}}{64\mu}\sum_{j=1}^{j=i}\sigma_f(t_j)\Delta t - \frac{v^*\dot{\varepsilon}t_i}{V_i} = 0 \qquad (3.31)$$

This is a quadratic equation in $\sigma_f(t_i)$ of the form

$$A_3(\sigma_f(t_i))^2 + B_3(\sigma_f(t_i)) + C_3 = 0 \qquad (3.32)$$

in which

$$A_3 = \frac{R_{cv}\Delta t}{64\mu} \qquad (3.33)$$

$$B_3 = \frac{1}{K_f} + C_{pp} + \frac{R_{cv}\Delta t}{64\mu} + \frac{R_{cv}}{64\mu K_f}\sum_{j=1}^{j=i-1}\sigma_f(t_j)\Delta t \qquad (3.34)$$

and $$C_3 = \frac{R_{cv}}{64\mu}\sum_{j=1}^{j=i}\sigma_f(t_j)\Delta t - \frac{v^*\dot{\varepsilon}t_i}{V_i} \qquad (3.35)$$

Eq. 3.32 has a root of

$$\sigma_f(T) = \sigma_f(t_i) = \frac{-B_3 + \sqrt{B_3^2 - 4A_3C_3}}{2A_3} \qquad (3.36)$$

Determination of $\sigma_f(t_i)$ using Eq. 3.36 requires the knowledge of all $\sigma_f(t_j)$ $1 \leq j \leq i - 1$. Since the initial condition is known, $\sigma_f(t_j) = 0$ at $t = 0$, $\sigma_f(t_1)$ can be calculated using Eqs. 3.33-3.36. Proceeding in this manner, the successive values of $\sigma_f(t_j)$ can be calculated.

3.3.4 Numerical Examples

To study the behavior of the hydrostatic stress in pore fluid as function of strain rate for various shapes and orientations of pore, a few numerical examples are used. The properties used are: characteristic volume ratio, $R_{cv} = 6 \times 10^{-13}$, viscosity of fluid, $\mu = 1.5 \times 10^{-7}$ psi-sec, bulk modulus of fluid $K_f = 3.25 \times 10^5$psi, shear modulus of fluid $G_f = 0$ (note the fluid is water), elastic modulus of the solid phase $E_s = 1 \times 10^7$psi and Poisson's ratio for solid phase, $\nu_s = 0.3$. Strain rate range $= 1 \times 10^{-1}$ to 1×10^6 microstrain/sec, and strain $\varepsilon = 1000$ microstrain corresponding to $t = T$, are used. For all calculations the exact expressions (Case II, i.e. $V(T) \neq V_i$) are used.

Fig. 3.1 shows the variation in the hydrostatic stress in the pore fluid, $\sigma_f(T)$, as a function of strain rate for an oblate spheroidal shape with aspect ratio $r = 0.02$. The aspect ratio of a pore, r, is calculated as the ratio of the polar semiaxis to the equatorial semiaxis. The pores are oriented with an angle $\psi = 0°$, 30°, 45°, 60°, 75° and 90°. ψ is the angle between the polar semiaxis and the horizontal plane. Figs. 3.2 and 3.3 show the corresponding results for spherical ($r = 1$) and prolate spheroidal (r

= 10) pores. For all r and ψ, $\sigma_f(T)$ first increases with $\dot{\varepsilon}$ and then becomes virtually constant. The $\dot{\varepsilon}$ at which $\sigma_f(T)$ becomes constant depends on R_{cv}.

Oblate spheroidal pores (r = 0.02) show a greater variation in $\sigma_f(T)$ as a function of orientation (Fig. 3.1) than prolate spheroidal pores (Fig. 3.3). For oblate spheroidal pores, at all strain rates, $\sigma_f(T)$ decreases with increasing ψ, while for prolate pores, $\sigma_f(T)$ increases with increasing ψ. Orientation is, of course, not a factor for spherical pores.

Fig. 3.4 shows the variation in the ratio of the orifice flow volume to pore volume as a function of strain rate, $\dot{\varepsilon}$, for materials with isotropic pore orientations and pore aspect ratios, r, in the range 0.02 to 20.0. To find the total volume of orifice flow, for a nearly saturated porous solid with isotropic pore orientations, eighteen pore orientations $\psi = \psi_j$ at an interval of 5^o were considered. Orifice flow volumes at these values of ψ were calculated using Eq. 3.8 and a weighted sum obtained. The weight at any orientation ($\psi = \psi_j$) of $\int_{\psi_j-2.5}^{\psi_j+2.5} \sin\psi d\psi$ was used to represent the equal number of pores at each spatial angle.

As shown in Fig. 3.4, for each r the orifice flow volume is at the maximum at the lowest strain rate. As $\dot{\varepsilon}$ is increased, the orifice flow volume decreases, slowly at first, then at increasing rates. The rate of decrease in the orifice flow volume slows down

before the orifice flow volume approaches zero. With a further increase in strain rate, the orifice flow volume essentially remains at zero for ε = 1000 microstrain. By decreasing the strain rate below a certain value, in this case 1 x 10^1 microstrain/sec, the orifice flow volume remains at the maximum value. Fig. 3.4 also shows that the flatter the pore (lower r), the greater the orifice flow volume. For the lowest r considered here (0.02), the orifice flow volume stays below 2% of the pore volume at ε = 1000 microstrain. A change in the characteristic volume ratio, R_{cv}, does not change the maximum and the minimum (zero) values of the orifice flow volume, but it does shift the range of $\dot{\varepsilon}$ over which the change from the maximum to the minimum occurs. For example, increasing R_{cv} increases the strain rates at which the transition from the maximum to the minimum value of the orifice flow volume occurs. With the shift, the ratio of the two strain rates remains the same.

The meaning of the term "nearly saturated" now becomes clear. The empty volume of unsaturated pores must be able to accomodate the orifice flow volume. This fraction of the total volume of the saturated pores is obviously small for practical cases, but does depend on pore geometry, strain and strain rate.

3.4 Effective Bulk Modulus of a Saturated Pore, K_f^*

3.4.1 General Expression for K_f^*

The effective bulk modulus of the saturated pore considered in the previous section can be written as

$$K_f^* = \frac{\sigma_f(T)}{\varepsilon_v(T)} \tag{3.37}$$

in which $\sigma_f(T)$ is the hydrostatic stress in the pore fluid at time T and $\varepsilon_v(T)$ is the ratio of the total volume change due to the compressibility of the pore fluid ($\Delta V_c(T)$) and the flow of the pore fluid through the orifice ($\Delta V_o(T)$), divided by the initial volume of the pore (V_i). Thus,

$$K_f^* = \frac{\sigma_f(T)}{\frac{\Delta V_c(T)}{V_i} + \frac{\Delta V_o(T)}{V_i}} \tag{3.38}$$

If $\Delta V_o(T) = 0$, Eq. 3.38 reduces to $K_f^* = K_f$, i.e. the effective bulk modulus of the pore is equal to the bulk modulus of the pore fluid. This happens when the pore is completely isolated, i.e., the orifice is absent. Also, when the strain rate is very high, or the orifice diameter is small, K_f^* approaches K_f. On the other hand, when the strain rate is very low or when the orifice diameter is big so that there is practically no hydrostatic stress in the pore fluid, K_f^* approaches zero. Thus, for all cases $0 \leq K_f^* \leq K_f$.

In Eq. 3.38, using the definition of the bulk modulus of the pore fluid, K_f

$$K_f = \frac{\sigma_f(T)}{\Delta V_c(T)/V(T)} \tag{3.39}$$

$$\text{or} \quad \Delta V_c(T) = \frac{\sigma_f(T)V(T)}{K_f} \tag{3.40}$$

Also, integrating Eq. 3.8 between $0 \leq t \leq T$,

$$\Delta V_o(T) = \frac{\pi d^4}{64\mu h} \int_o^T \sigma_f(t)dt \tag{3.41}$$

Substituting Eqs. 3.39 and 3.41 in Eq. 3.38,

$$K_f^* = \frac{\sigma_f(T)}{\frac{V(T)\sigma_f(T)}{V_i K_f} + \frac{\pi d^4}{64\mu h V_i} \int_o^T \sigma_f(t)dt} \tag{3.42}$$

As in the previous section, two cases can be considered depending on the magnitude of the flow through the orifice. If $V_i >> \int_o^T q_{or}(t)dt$, then $V(T) \approx V_i$.

3.4.2 Case I $V(T) \approx V_i$

In this case, Eq. 3.42 can be written as

$$K_f^* = \frac{\sigma_f(T)}{\frac{\sigma_f(T)}{K_f} + \frac{\pi d^4}{64\mu h V_i} \int_o^T \sigma_f(t)dt} \tag{3.43}$$

As mentioned in the introduction (section 3.1), the self-consistent equations for estimating the strain-rate sensitive moduli

of a porous solid (section 3.6) require that pores with given moduli have isotropic orientation. In other words, for given orifice and pore geometry, the effective moduli of a pore should remain the same as the pore orientation, ψ, is changed. It was observed in section 3.3 that the hydrostatic stress in the pore fluid, $\sigma_f(T)$, is very sensitive to pore orientation, ψ, (Figs. 3.1-3.3). Since $\sigma_f(T)$ appears in Eq. 3.43, it is not obvious whether the effective bulk modulus of a saturated pore, K_f^*, is a function of pore orientation, ψ, or not. A few substitutions and rearrangements will be made in Eq. 3.43 to show that K_f^* is not a function of ψ for case I ($V(T) \approx V_i$). Using Eq. 3.20 for $\sigma_f(t)$, the integral in the denominator of Eq. 3.43 is

$$\int_0^T \sigma_f(t)dt = C_1 T - \frac{\sigma_f(T)}{C_2} \tag{3.44}$$

Substituting Eq. 3.44 into Eq. 3.43,

$$K_f^* = \frac{\sigma_f(T)}{\frac{\sigma_f(T)}{K_f} + \frac{\pi d^4 C_1 T}{64\mu h V_i} - \frac{\pi d^4 \sigma_f(T)}{64\mu h V_i C_2}} \tag{3.45}$$

Dividing the numerator and the denominator by $\sigma_f(T)$ and then substituting Eq. 3.20 with $t = T$ for $\sigma_f(T)$ into Eq. 3.45, gives

$$K_f^* = \frac{1}{\frac{1}{K_f} + \frac{\pi d^4 T}{64\mu h V_i (1 - e^{-C_2 T})} - \frac{\pi d^4}{64\mu h V_i C_2}} \tag{3.46}$$

Substitutions of Eq. 3.22 for C_2 and Eq. 3.23 for the characteristic volume ratio, R_{cv}, into Eq. 3.46, gives:

$$K_f^* = \left\{ \frac{R_{cv} T}{64\mu\left(1 - e^{-\left(\frac{R_{cv} T}{64\mu(1/K_f + C_{pp})}\right)}\right)} - C_{pp} \right\}^{-1} \tag{3.47}$$

Eq. 3.47 shows that for $V_i >> \int_o^T q_{or}(t)dt$ (Case I), the effective bulk modulus of a saturated pore, K_f^*, is a function of: the characteristic volume ratio, R_{cv}, the viscosity, μ, and bulk modulus, K_f, of the pore fluid, the compressibility of the pore, C_{pp}, and the time, T. Of these, the properties of the pore fluid, μ and K_f are clearly not functions of pore orientation, ψ. R_{cv} is a function of the dimensions of pore and orifice and thus not a function of ψ. C_{pp}, the compressibility of a pore, is also not a function of ψ. Thus, all the parameters on which K_f^* depends are not functions of the pore orientation, making K_f^* independent of ψ.

3.4.3 Case II $V_T \neq V_i$

Substituting Eqs. 3.8 for flow through orifice, q_{or}, and Eq. 3.10 for the volume of the pore at time T, V(T), into Eq. 3.42 and simplifying gives

$$K_f^* = \frac{\sigma_f(T)}{\frac{\sigma_f(T)}{K_f} + \left(1 + \frac{\sigma_f(T)}{K_f}\right) \frac{\pi d^4}{64\mu h V_i} \int_o^T \sigma_f(t)dt} \tag{3.48}$$

In Eq. 3.48, dividing both the numerator and the denominator by $\sigma_f(t)$ and substituting R_{cv} for $\pi d^4/hV_i$ (Eq. 3.23) gives,

$$K_f^* = \frac{1}{\frac{1}{K_f} + \left(\frac{1}{\sigma_f(T)} + \frac{1}{K_f}\right) \frac{R_{cv}}{64\mu} \int_o^T \sigma_f(t)dt} \tag{3.49}$$

For case I, it was clearly shown that K_f^* is not a function of ψ. For case II, however, a closed form expression for K_f^* cannot be obtained, because Eq. 3.36 cannot be substituted for $\sigma_f(T)$. Eq. 3.36 involves the summation of a large number of values of $\sigma_f(t)$ at $t < T$ which are successively calculated. In this case, numerical examples are used to illustrate the extent to which K_f^* depends on ψ. These examples show that for typical strains (below 1000 microstrain) and a relatively flat pore shape ($r = 0.04$), the variation in K_f^* is within 0.5% for a change in ψ from 0° to 90°. Only at very high strains (e.g., greater than 10,000 microstrain) do values of K_f^* differ more than 5%. For such high strains, self-consistent equations that do not assume an isotropic orientation of inclusions are required to estimate the composite moduli.

3.4.4 Numerical Examples

In the following examples, changes in the effective bulk modulus of a saturated pore, K_f^*, are studied as a function of (i) pore orientation, ψ, (ii) characteristic volume ratio, R_{cv}, and (iii) pore aspect ratio, r. For the examples, the expressions based on case II (Eq. 3.36 and 3.49) are used. A comparison will also be made using case I. The following constituent properties are used: Elastic modulus of solid phase $E_s = 6 \times 10^6$ psi, Poisson's ratio of solid phase $\nu_s = 0.25$, and pore fluid properties are the same as those in section 3.3.

3.4.4.1 K_f^* versus ψ

To study the variation in K_f^* as a function of ψ, comparisons are made using r = 0.04, $\dot{\varepsilon}$ = 1, 4, 10, 40, 100, 400, 1000, and 4000 microstrain/sec, and ε = 1000, 2000, 5000, and 10,000 microstrain. The comparisons show that K_f^* is mildly dependent upon orientation, but that the dependence is significant only at high strains and only at certain strain rates.

Fig. 3.5 shows the variation in K_f^* at ε = 10,000 microstrain (the highest strain considered) for each strain rate, as ψ is increased from 0° to 90°. Although not readily apparent from Fig. 3.5, K_f^* varies up to 4.9% as a function of orientation. The variations become more apparent if normalized to values of K_f^* at $\psi = 0^\circ$. Fig. 3.6 shows the results of Fig. 3.5 normalized to K_f^* at $\psi = 0^\circ$. At the lowest strain rate ($\dot{\varepsilon}$ = 1 microstrain/sec), the variation in K_f^* with ψ is insignificant (only 0.15%). With an increase in strain rate,

the variations in K_f^* become more noticeable and reach a maximum of 4.9% at $\dot{\varepsilon}$ = 40 and 100 microstrain/sec. With a further increase in $\dot{\varepsilon}$, the variations in K_f^* become smaller, and insignificant as $\dot{\varepsilon}$ reaches 4000 microstrain/sec. Fig. 3.6 clearly shows that the variations in K_f^* are significant only at the intermediate strain rates. The insignificant variation (below 0.3%) in K_f^* at the extreme strain rates (1 and 4000 microstrain/sec) is expected since K_f^* approaches its limiting values of 0 and K_f, respectively, at these strain rates. For strain rates outside this range, K_f^* is effectively independent of orientation, even at large strains.

The effects of strain rate on the mild orientation sensitive behavior of the effective bulk modulus of a pore at high strains (10,000 microstrain) can be explained using Eq. 3.49. In Eq. 3.49, $\sigma_f(T)$ and the integral of $\sigma_f(t)$ with respect to time are the two variables that change with ψ and $\dot{\varepsilon}$. These variables appear in the second term in the denominator of Eq. 3.49, e.g. in $\left(\frac{1}{\sigma_f(T)} + \frac{1}{K_f}\right) \frac{R_{cv}}{64\mu}$ $\int_o^T \sigma_f(t)dt$. $\sigma_f(T)$ and $\int_o^T \sigma_f(t)dt$ have opposing influences on the mild orientation sensitive behavior of K_f^*. At higher strain rates, the increase in $\sigma_f(T)$ that causes K_f^* to become sensitive to ψ is counteracted by the decrease in the integral. Figs. 3.7 and 3.8 show the variations in $\sigma_f(T)$ and $\int_o^T \sigma_f(t)dt$ as functions of ψ, for ε = 10,000 microstrain and the strain rates used for Figs. 3.5 and 3.6. As Fig. 3.7 shows, at a very slow strain rate (e.g. 1 microstrain/sec) the value of hydrostatic stress in the pore fluid, $\sigma_f(T)$, is negligible.

$1/\sigma_f(T)$ becomes large, making K_f^* approach zero. This happens at all orientations, i.e., K_f^* does not depend on ψ at very slow $\dot{\varepsilon}$. As $\dot{\varepsilon}$ is increased, $\sigma_f(T)$ increases and its orientation sensitivity (Fig. 3.7) translates into a mild orientation sensitivity for K_f^*. As Fig. 3.8 shows, increasing $\dot{\varepsilon}$ has the opposite effect on the integral. As $\dot{\varepsilon}$ is increased, the value of the integral becomes smaller and smaller until it becomes negligible compared to its value at the lowest strain rate (at 1 microstrain/sec). Up to intermediate strain rates (e.g. 40 and 100 microstrain/sec in the above example) the reduction in the magnitude of the integral is not large enough to nullify the orientation sensitive influence of $\sigma_f(t)$. However, at higher strain rates (e.g. 4000 microstrain/sec in the comparison), as T approaches zero, the value of the integral becomes negligible, causing K_f^* to approach K_f.

To check that the orientation sensitivity indeed becomes negligible for smaller strains, normalized values of K_f^* at $\psi = 45^\circ$ and 90° are compared at ε = 1000, 2000, 5000, and 10,000 microstrain in Table 3.1. As expected, the larger the strain, the larger the variation in K_f^*. At $\psi = 45^\circ$, the maximum normalized values of K_f^* are 1.003, 1.005, 1.013, and 1.023, and at $\psi = 90^\circ$ the maximum normalized values are 1.005, 1.011, 1.026 and 1.049, for ε = 1000, 2000, 5000 and 10,000 microstrain, respectively. The comparisons in Table 3.1 show that for each strain, the maximum normalized value of K_f^* occurs at a different strain rate. The higher the strain, the higher the strain rate at which the maximum variation in K_f^* occurs. For the study of

cement paste at low stresses discussed later in this chapter, calculations typically are made for strains below 1000 microstrain. Thus, the variations in K_f^* with ψ are less than 0.5%. The use of a self-consistent scheme which assumes that pores are isotropic in K_f^* is therefore reasonable. In fact, this 0.5% variation holds for the flatest pore ($r = 0.04$) used to model cement paste. For pores which are less oblate, the effect of orientation is even lower.

3.4.4.2 K_f^* versus R_{cv}

Fig. 3.9 shows the variation of K_f^* at $\varepsilon = 1000$ microstrain as a function of strain rate for $R_{cv} = 6 \times 10^{-13}$ and 6×10^{-9}, and $r = 0.02$, 1.0, and 10.0. Strain rates in the range of 1×10^{-1} to 7×10^{6} microstrain/sec are used. For both values of R_{cv}, at the lowest strain rate K_f^* is close to zero. As $\dot{\varepsilon}$ is increased, K_f^* increases slowly at first and then at increasing rates. With further increases in $\dot{\varepsilon}$, the increase in K_f^* slows before approaching 3.25×10^5 psi, the bulk modulus of the pore fluid, K_f. The strain rate at which K_f^* approaches K_f increases with increasing R_{cv}. Physically this means that for a higher value of R_{cv}, as fluid passes more easily through the orifice, it takes a higher strain rate for the pore to respond like one without an orifice.

Fig. 3.10 shows the variation in K_f^* as R_{cv} is increased from 1×10^{-15} to 1×10^{-10} for $\dot{\varepsilon} = 1$, 10 and 100 microstrain/sec. The shapes of the K_f^* versus R_{cv} curves for all three strain rates are identical. For a low value of R_{cv}, it is difficult for the pore fluid to pass

through the orifice, and K_f^* approaches K_f for all three strain rates. With increasing R_{cv}, K_f^* decreases until it approaches zero.

3.4.4.3 K_f^* versus r

Fig. 3.11 shows that the effective bulk modulus of a pore, K_f^*, decreases as the aspect ratio, r, increases from 0.02 to 20.0 ($\psi = 0^o$ and 90^o, $R_{cv} = 6 \times 10^{-13}$, $\dot{\varepsilon} = 2$ microstrain/sec and $\varepsilon = 1000$ microstrain). K_f^* is the highest at the lowest value of r (flat oblate spheroidal pore). K_f^* reaches a minimum as r is increased to 1 (spherical pore), after which it increases slightly.

Fig. 3.12 compares the variation in K_f^* as a function of r for cases I and II at $\psi = 0^o$, $\dot{\varepsilon} = 2$ microstrain/sec and $\varepsilon = 1000$ microstrain. Fig. 3.12 verifies that for small strains the values of K_f^* are practically the same for cases I and II (within 0.5% in this case). Since case I is an approximation for case II, the latter is used in all calculations except for this comparison (Fig. 3.12), and in section 3.7.1, where the expressions for case I are used to discuss the influence of pore size on the composite response.

3.5 Determination of the Effective Moduli of a Composite

Once the elastic moduli of its constituents are obtained, several procedures can be used to determine the effective moduli of a multiphase composite. Generally, one of the following four approaches is used in developing such a procedure: (i) bounding approach, (ii) perturbation approach, (iii) static self-consistent approach, and (iv) elastic wave scattering approach. Sometimes the

expressions developed using two approaches are identical (12, 49) or they produce identical results for a limiting geometry or concentration. Watt et al. (91), Hashin (36), and Cleary et al. (20) present excellent reviews of the available work on this issue. Following is a brief discussion of the four types of approaches:

3.5.1 Bounding Approach

Reuss (67) and Voigt (87), in separate studies, developed simple expressions to estimate the effective moduli of polycrystalline aggregates. These are known as the "series" and "parallel" models. In the first, all crystals of a polycrystalline aggregate are assumed to have the same stress; in the second, they are assumed to have the same strain. When applied to multiphase composites, these two methods generate strain and stress discontinuities at the boundaries of the inclusions, respectively, unless the differences in the constituents' moduli are negligible. Later, Paul (63) derived these series and parallel expressions for composites and appropriately called them the lower and upper bounds, respectively. Paul's expressions can be written as (42):

$$M_R^* = \left(\sum_{i=1}^{n} \frac{C_i}{M_i} \right)^{-1} \leq M^* \leq \sum_{i=1}^{n} C_i M_i = M_V^* \qquad (3.50)$$

in which C_i is the volume concentration of ith phase, M_i is the shear

or bulk modulus of ith phase, M^* is the shear or bulk modulus of composite, M_R^* is the Reuss estimate of M^*, and M_V^* is the Voigt estimate of M^*.

To provide a better estimate than the Reuss and Voigt expressions, Hill (41) suggested that either the arithmetic $(M_R^* + M_V^*)/2$ or geometric $\sqrt{M_R^* * M_V^*}$ averages of Reuss and Voigt moduli be used.

Using variational principles, Hashin and Shtrikman (37) derived tighter bounds than Paul (63). There seems to be general agreement that any reasonable estimate of the effective moduli of a composite must be within the Hashin-Shtrikman bounds (11, 12, 36, 91), at least up to moderate concentrations of the inclusions. In fact, for some composites, the Hashin-Shtrikman bounds are so close that either one of them can be used in engineering applications (12). From the general Hashin-Shtrikman expressions for the lower bounds on moduli (K^- and G^-) of an n phase composite, the following lower bounds on the bulk and shear moduli of a two phase composite can be obtained:

$$K_{HS}^- = K_1 + \frac{C_2}{1/(K_2 - K_1) + 3C_1/(3K_1 + 4G_1)}$$

and (3.51)

$$G_{HS}^- = G_1 + \frac{C_2}{1/(G_2 - G_1) + 6C_1(K_1 + 2G_1)/5G_1(3K_1 + 4G_1)}$$

in which, subscripts 1 and 2 refer to phases 1 and 2 of the composite, respectively and K_i, G_i, and C_i are the bulk moduli, shear moduli, and phase concentrations, respectively. $K_1 < K_2$ and $G_1 < G_2$.

The upper bounds (K^+ and G^+) can be obtained by interchanging subscripts 1 and 2. The Hashin-Shtrikman bounds do not consider the shapes of the inclusions. This, however, is done to some extent by Miller (56). Miller provides tighter bounds for the overall bulk modulus of a composite than Hashin and Shtrikman (37). Miller bounds are provided for the overall bulk modulus of materials having a single shape for all phases and for materials having multiple shapes for the phases. Miller bounds on the shear modulus are not available, and the bounds on the bulk modulus apply to a restricted class of material termed "cell materials" (56). For equal phase concentrations, of a two phase composite, the Miller bounds become independent of inclusion shape (12).

3.5.2 Perturbation Approach

This is the most direct and rigorous approach, but its application is limited. In the most well-known method, developed by Eshelby (27), the perturbation or change in elastic energy due to an ellipsoidal inclusion in an otherwise uniformly stressed specimen is considered. The total change in elastic energy of the specimen is then obtained by simply multiplying the inclusion energy by the number of inclusions. Clearly, no interaction among the strain fields of the inhomogeneities is assumed in this approach and thus the results, although exact, are valid only for small concentrations of inhomogeneities. Although this approach does not have a direct application in determination of the effective moduli of most composites, it provides the basis for the most commonly used static

self-consistent approach (16, 43, 95). Also, because the expressions developed with this approach are exact, they provide a check of validity for the static self-consistent approach in the limiting case of very low concentrations of inclusions.

3.5.3 Static Self-Consistent Approach

This is the most well-known approach for the determination of the effective moduli of composites with significantly high concentrations of the inclusions. In this approach, the interaction among the inclusions is approximately accounted for by finding the elastic strain energy of an isolated inclusion in a homogeneous matrix which has the overall properties of the composite. Thus, this approach is similar to the previous approach, except now the real matrix has been replaced by the effective matrix with yet unknown moduli. The earliest procedures considered only spherical inclusions (16, 43), later general spheroidal inclusions at random orientations were added (95). The resulting expression has to be solved numerically by an iterative scheme because the calculation of inclusion strain energy includes the elastic moduli of the composite, which are not known to begin with. In the case of a cracked solid (17), crack energies which are expressed in terms of the stress intensity factors at the crack tip, are considered in place of the inclusion strain energy.

There has been some criticism of the static self-consistent approach (36, 38, 62, 100) and modifications have been suggested. One of the most common criticisms is that it overestimates the effect of

inclusions on the overall elastic moduli. Using Wu's (95) self consistent expressions, Zimmerman (100) has shown that the effective bulk modulus of glass with 50 percent porosity is zero, while the experiments showed it to be about one-fourth of the modulus of the solid glass matrix. In the static self-consistent procedure of Wu (95), one of the phases of a multiphase composite is treated as the matrix and the others are treated as the inclusion phases. As a result, there are n estimates for the composite moduli depending on which phase of the n phase composite is treated as the matrix. The self-consistent embedding procedure of Korringa et. al (49) treats all phases equally, and provides unique and satisfactory estimates for moduli of fluid filled composites.

3.5.4 Elastic Wave Scattering Approach

Kuster and Toksoz (50) derived expressions for the effective moduli of an n phase composite for the propagation of elastic waves whose wave lengths are much longer than the size of the spheroidal inclusions. The expressions for the effective moduli were obtained by equating the scattering of the elastic waves from a spherical region consisting of the actual macrohomogeneous composite with that from a similar region consisting of the effective material, i.e. a material with the yet to be found moduli. Kuster and Toksoz (50) assumed no interaction between inclusions, and their expressions are expected to work well only up to $c/\alpha \leq 1$, in which c is the volume fraction of the inclusions and α is the ratio of the smaller to larger axis of the spheroidal inclusions. Notice, $\alpha = r$ for oblate

spheroidal and spherical ($r \leq 1$) pores, and $\alpha = 1/r$ for prolate spheroidal ($r > 1$) pores. Thus, the more nonspherical the pore shape, the smaller the volume fraction of inclusions up to which the expressions work well. For only spherical inclusions the expressions work well up to any concentration of pores. For an n phase composite, the Kuster and Toksoz (50) expressions provide n estimates for the composite moduli by alternatively treating one of the phases as the matrix and the others as inclusions. For a two phase composite with spherical grains, it is shown (11, 12) that the two estimates, obtained by switching the roles of the matrix and the inclusions, are identical to the two Hashin-Shtrikman bounds. For needle and disk shaped inclusions, the Hashin-Shtrikman bounds are violated even at small volume fractions. Berryman (11, 12) extended the work of Kuster and Toksoz by modifying their approach and by incorporating self-consistency. His expressions which treat all phases equally are not limited by c/α and fall between the Hashin-Shrikman bounds for all shapes and concentrations of phases.

Berryman (11, 12) considered the scattering from a spherical region surrounded by a uniform medium. The surrounding medium's moduli can be varied as desired. The spherical scattering region is assumed to be made of the same constituents, in the same proportions, as the n phase composite. Berryman (11, 12) derived the self-consistent expressions for the composite moduli by imposing the condition that the net scattering from the embedded spherical scattering region would vanish if the moduli of the surrounding medium

match those of the composite. The resulting expressions for the composite moduli are symmetrical in all phases, i.e. do not treat one of the constituents as the matrix and others as the inclusions. Berryman's expressions (12) for the effective moduli of an n phase composite are identical to those of Korringa et al. (49) who used the static self-consistent approach for porous rocks. Berryman derived the following equations for the estimation of effective bulk, K^*, and shear G^*, moduli :

$$\sum_{j=1}^{m} C_j (K_j - K^*) P^{*j} = 0 \qquad (3.52a)$$

$$\sum_{j=1}^{m} C_j (G_j - G^*) Q^{*j} = 0 \qquad (3.52b)$$

P^{*j} and Q^{*j} are coefficients that relate the uniform applied strain field with the strain field at a spheroidal inclusion. Expressions for P^{*j} and Q^{*j} are given in Appendix D. C_j, K_j, and G_j are the volume concentration, bulk modulus, and shear modulus of the jth phase of the m phase composite. In this study, Berryman's expressions are used to formulate a self-consistent procedure for estimating the strain-rate sensitive moduli of a nearly saturated porous solid.

3.6 Self-Consistent Procedure for Finding Composite Moduli

Eq. 3.52 of the previous section leads to the following iteration scheme to determine the effective bulk and shear moduli of a porous solid.

$$K^*_{n+1} = \frac{\sum_{j=1}^{m} C_j K_j (P^{*j})_n}{\sum_{j=1}^{m} C_j (P^{*j})_n} \tag{3.53a}$$

$$G^*_{n+1} = \frac{\sum_{j=1}^{m} C_j G_j (Q^{*j})_n}{\sum_{j=1}^{m} C_j (Q^{*j})_n} \tag{3.53b}$$

in which K^*_{n+1} and G^*_{n+1} are the estimated value of the composite bulk and shear moduli, respectively, at the end of n+1 iterations. C_j and K_j, $1 \leq j \leq m$, are the same as defined for Eq. 3.52. $(P^{*j})_n$ and $(Q^{*j})_n$ are the estimated values of those variables, as given in Appendix D, at the end of n iterations. For obtaining the effective moduli of the pores, K^*_f (or the K_i corresponding to the pores), initial estimates of the composite moduli, K^*_1 and G^*_1, are needed. Since, the overall response of a composite consisting of a solid phase and fluid inclusions is softer than the solid phase, K^*_1 and G^*_1 are set equal to fractions of the solid phase moduli, K_s and G_s, respectively. The iteration scheme of Eq. 3.53 is started with K^*_1

and G_1^* as the initial estimates for K^* and G^*, respectively, and continued until two successive estimates of K^* and G^* (i.e., K_{n+1}^*, G_{n+1}^* and K_n^*, G_n^*) fall within a reasonable tolerance. For general self-consistency, it is necessary to use the converged values of the composite moduli, K^* and G^*, in the calculations of K_i of the pores. Thus, the iteration scheme may have to be repeated unless K_1^* and G_1^* are close enough to the converged values of K^* and G^*, respectively.

3.6.1 Solution Procedure

The following procedure is used to calculate the effective bulk and shear moduli for a given strain rate, and strain level.

1. Make an initial estimate of the effective composite bulk and shear moduli, K_1^* and G_1^*, e.g., set them equal to fractions of the moduli of the solid phase, K_s, G_s, respectively.
2. Calculate the hydrostatic stress of the pore fluid, $\sigma_f(t)$, at the desired strain level (Eq. 3.36) using the characteristic volume ratio, R_{cv}, the aspect ratio of the pores, r, and the current effective moduli of the porous solid.
3. Find the effective bulk moduli of the pores, K_f^*, using R_{cv} and r and the values of $\sigma_f(t)$ calculated in step 2. The effective shear moduli of the pores are always zero.
4. Using Eq. 3.53 iteratively, find the improved estimates of the overall composite moduli until two successive pairs of estimates fall within the desired tolerance. Tolerances of

$1 \times 10^{-6} K^*$ and $1 \times 10^{-6} G^*$ can be used for checking the convergence of bulk and shear moduli, respectively.

5. If the initially estimated moduli at step 1, K_1^* and G_1^*, are not within small tolerances, e.g., $1 \times 10^{-3} K^*$ and $1 \times 10^{-3} G^*$, respectively, of the corresponding converged values at the end of step 4, then return to step 2 using the results of step 4 as the new values of K_1^* and G_1^*.

After determining the effective bulk and shear moduli, the corresponding elastic moduli, E_i^* and Poissons's ratio, ν_i^*, can be obtained using standard elasticity relationships.

3.7. Factors Influencing Rate-Sensitive Composite Moduli, E_i^* and ν_i^*

3.7.1 Influence of Pore Size

As discussed in section 3.5, the overall moduli of a composite are functions of the moduli of the constituent phases. In the rate-sensitive model developed here, the solid phase moduli, K_s and G_s, are assumed to be insensitive to strain rate. Thus, the rate sensitivity of the model originates from the rate sensitivity of the bulk moduli of the pores. To determine if the rate sensitive response depends on pore size it will be sufficient to investigate if the effective bulk modulus of a pore, K_f^*, depends on pore size.

Since it has been shown in section 3.4 that Case I ($V_T \approx V_i$) provides practically the same values of K_f^* as Case II ($V_t \neq V_i$), the former, Eq. 3.47, can be used to discuss the effect of pore size on K_f^*. Eq. 3.47 shows that K_f^* is a function of R_{cv}, μ, K_f, C_{pp} and T.

Appendix B shows that C_{pp} depends only on the shape of the pore and the moduli of the solid phase. Therefore, the only term that needs consideration for the present investigation of the pore size effect is R_{cv}. From Eq. 3.23,

$$R_{cv} = \frac{\pi d^4}{hV_i} \tag{3.54}$$

Now, if while varying the size of a pore we keep the relative size of the orifice constant, the following variables can be defined for the orifice geometry.

$$R_d = d/D \tag{3.55}$$

and $$R_h = h/D$$

in which D is the diameter of a sphere with the same volume as the pore. Substituting Eq. 3.55 into Eq. 3.54,

$$R_{cv} = \frac{\pi R_d^4 D^4}{R_h(D\pi/6)D^3} \tag{3.56}$$

or

$$R_{cv} = \frac{6R_d^4}{R_h} \tag{3.57}$$

Thus, if R_d and R_h, representing the geometry of the orifice relative to the pore, are kept the same while varying the size of the pore, K_f^*

will remain the same as the pore and orifice change size. This means that E_i^* and ν_i^* do not depend on the size of the pores. However, the size of pores cannot be increased indefinitely. Pores must be small enough to maintain the macroisotropic and macrohomogeneous nature of the porous solid.

3.7.2 Effect of Pore Shape, r

In this model, the pores are considered to have a spheroidal shape. The solid matrix is considered to be made up of spherical grains. By varying the pore aspect ratio, r, the pores can be made prolate spheroidal ($r > 1$), spherical ($r = 1$), and oblate spheroidal ($r < 1$) shaped.

For the examples given in this and the next two sections, the constituent properties, except as noted, are: Elastic modulus of the solid phase, $E_s = 11.55 \times 10^6$ psi, Poisson's ratio of the solid phase, $\nu_s = 0.417$, porosity = 40%, bulk modulus of the pore fluid, $K_f = 3.25 \times 10^5$ psi, shear modulus of the pore fluid $G_f = 0$, viscosity of the pore fluid, $\mu = 1.5 \times 10^{-7}$, and pore aspect ratio, $r = 0.0795$. Sixteen characteristic volume ratios, R_{cv}, are selected. They are geometrically equally spaced in the range of 3.75×10^{-18} and 1.24×10^{-4}. Geometrically equal spacing of the R_{cv} values is necessary to have a linear moduli versus logarithmic strain rate response. To have the sixteen R_{cv} values geometrically equally spaced, $R_{cv}(n) = R_{cv}(1)(1 + F_1)^{n-1}$, $1 \leq n \leq 16$, and $F_1 = 7.97$. The constituent properties used correspond to a porous solid, designated as PS.5P, which duplicates the experimental strain-rate sensitive elastic

modulus and Poisson's ratio data for cement paste with W/C = 0.5 (section 3.8.2.1).

In this section, to study the influence of pore shape on the rate sensitivity of the analytically predicted composite moduli, E_i^* and ν_i^*, r = 0.06, 0.08, 0.10, 0.20, 1.0, 3.0, and 20.0 are used in place of the fixed values of r for PS.5P. Other properties are the same as those of PS.5P.

Figs. 3.13 and 3.14 show the influence of pore shape on the rate sensitivity of the composite elastic modulus, E_i^*, and composite Poisson's ratio ν_i^*, respectively. The flatter pores make the composite response more rate sensitive than do the spherical or prolate spheroidal ones. The rate sensitivity of a composite with prolate spheroidal, needle-like, pores is in between those with oblate spheroidal, crack like, and spherical pores. In this example, for r = 0.06, 0.08, 0.10, 0.20, 1.0, 3.0, and 20.0 the rate sensitivities of E_i^* are 29.3%, 9%, 4.9%, 1.0%, 0.15%, 0.20%, and 0.25% per decade change in strain rate, respectively. The corresponding rate sensitivities of ν_i^* are 9.0%, 6.2%, 4.6%, 1.7%, 0.50%, 0.60%, and 0.70% per decade change in strain rate.

Berryman (12) has shown that inclusion shape has very little effect on the composite response if the moduli of the inclusions and the matrix are not too different. As the difference between the moduli is increased, the composite response becomes more sensitive to the shape of the inclusions. The influence of inclusion shape on the composite response can be explained by considering the case of empty

R_{cv} means either a bigger orifice diameter or a smaller orifice length. In any case, a higher R_{cv} makes it easier for the fluid to flow through the orifice and requires a higher strain rate to see a significant value of K_f^*. The rate sensitivity of E_i^* and ν_i^* can be studied for single or multiple values of R_{cv}.

3.7.4.1 Materials with a Single Value of R_{cv}

Figs. 3.19 and 3.20 illustrate the rate sensitivity of E_i^* and ν_i^* for two composites in which the pores have a single value of R_{cv}, 4.86×10^{-11} or 7.78×10^{-10}. The other properties are the same as those of PS.5P (section 3.7.2). The shapes of the E_i^* versus $\dot{\varepsilon}$ and ν_i^* versus $\dot{\varepsilon}$ curves are the same for both composites. At very low strain rates, e.g., below 1 microstrain/sec, E_i^* and ν_i^* are constant. This represents the case when the effective bulk modulus of the pore, K_f^*, approaches zero. At very high strain rates, the two curves coincide once again. In this case K_f^* approaches K_f. At intermediate rates, K_f^* is lower for composite with $R_{cv} = 7.78 \times 10^{-10}$ than for $R_{cv} = 4.86 \times 10^{-11}$ because the fluid faces less resistance leaving the pore if the orifice is wider or shorter. As pointed out in section 3.3 (Eq. 3.23), a higher value of R_{cv} causes a softer overall response, except at extreme strain rates where either $K_f^* \to 0$ ($\dot{\varepsilon} \to 0$) or $K_f^* \to K_f$ ($\dot{\varepsilon} \to \infty$).

3.7.4.2 Materials with Multiple Values of R_{cv}

For cement paste, the experimental moduli, E_i and ν_i, versus logarithm of strain rate relations are almost linear. The unrealistic shapes shown in Figs. 3.19 and 3.20 arise from the unrealistic

assumption of a single R_{cv} value. Unlike the idealized materials of the previous section, real porous materials have many combinations of pores and orifices which results in multiple values of R_{cv}. Figs. 3.21 and 3.22 show that as the number of R_{cv} values is increased, the E_i^* and ν_i^* versus log $\dot{\varepsilon}$ relations become more and more linear. To obtain a linear increase in moduli with increasing logarithm of strain rate, it is not only necessary to have multiple values of R_{cv}, but it is also necessary to have values of R_{cv} that are not clustered around one value. To simulate the experimental results, the range of strain rates for which the experimental response is linear dictates the range of the R_{cv} values; the wider the experimental linearity, the wider must be the range of R_{cv} values. In this example (Figs. 3.21 and 3.22), the values of R_{cv} are geometrically equally spaced between 3.75×10^{-18} and 1.24×10^{-4}.

The moduli versus logarithm of strain rate relations shown in Figs. 3.21 and 3.22 eventually become insensitive to strain rate if strain rates outside the range considered are used. Figs. 3.23a and 3.23b show the elastic modulus and the Poisson's ratio, E_i^* and ν_i^*, versus strain rate relations, respectively, for strain rates in the range 1×10^{-7} to 1×10^{12} microstrain/sec. As expected, both relations become insensitive to strain rate beyond a certain strain rate range (in this case 3×10^{-7} to 3×10^{10} microstrain/sec). As stated earlier, the range of the strain rates for which the response remains rate sensitive depends on the range of R_{cv} used. In real materials, the range of pore sizes which governs the range of R_{cv} is finite.

Hence, according to the model, the response of a porous material must become insensitive to strain rate, if extreme strain rates are used.

3.7.5 Dry Material

In a dry porous material, the pore fluid is air which has a negligible bulk modulus, $K_a \cong 0$. Thus, $0 \leq K_f^* \leq K_a$. Whatever the upper limit of K_f^*, it can be achieved only at very high strain rates because the viscosity of air is much lower than that of a liquid. The model is not strain-rate sensitive for dry specimens.

3.8 Simulation of Experimental Results for Cement Paste

In this section the self-consistent model is used to duplicate experimental moduli, E_i and ν_i, versus $\dot{\varepsilon}$ relationships for cement paste. Several numerical examples are presented to demonstrate how the model is able to match experimental results. Knowledge gained in section 3.7 is used in developing the following procedure.

3.8.1 Procedure

The procedure begins with the selection of a representative pore shape, r, (i.e. one value for all pores) and values of the characteristic volume ratio, R_{cv}. A set of rate insensitive solid phase moduli, K_s and G_s, are selected and initial estimates of the composite moduli, K_1^* and G_1^* (see Eq. 3.53), are made so that the values of the effective bulk moduli of the pore, K_f^*, can be obtained at a selected strain rate. Using these moduli, the composite moduli of the porous solid, K^* and G^*, are iteratively calculated using Eq. 3.53 until convergence is achieved. To ensure that K_f^* is accurate,

this procedure is repeated unless K_1^* and G_1^* match well with the converged values of K^* and G^*. The process is repeated by varying K_s and G_s until the converged moduli match with the experimental values. Once such a match is obtained, the moduli of the solid phase are not changed, and the composite moduli are calculated at other strain rates.

After calculating the composite moduli, E_i^* and ν_i^*, at various strain rates, the results are plotted and compared with the experimental values. The analytical response is varied to match the experimental results by varying one or more of the following: (i) the number of R_{cv} values, (ii) the range of R_{cv} values, and (iii) the pore aspect ratio, r. Increasing the number of R_{cv} values increases the linearity of the composite moduli versus logarithm of strain rate relation. Increasing the upper limit of the range of R_{cv} values increases the upper limit of the strain-rate range for which the response is rate sensitive. Similarly, decreasing the lower limit of the range of R_{cv} values decreases the lower limit of the strain-rate range for which the response is rate sensitive. By reducing the aspect ratio of the pores the response can be made more rate sensitive. Reduction of the aspect ratio, r, also makes the response softer (section 3.3.7.2), i.e., lower composite moduli. Changes in R_{cv} or r require that the iterative solution for K^* and G^* be repeated.

An increase in the range of R_{cv} values, to some extent, reduces the rate sensitivity of the moduli. While the analytical strain-rate

sensitivity can be reduced by either increasing r or by increasing the range of R_{cv} values selected, section 3.8.2.3 shows that a unique set of constituent properties is needed to duplicate the rate sensitive experimental moduli.

3.8.2 Numerical Examples

In this section, examples are presented to compare the analytical moduli and stress-strain behavior with the experimental results for cement paste with W/C = 0.3, 0.4 and 0.5. The analytical results are obtained considering three nearly saturated porous solids, PS.3P, PS.4P and PS.5P.

As discussed in chapter 2, the experimental elastic modulus, E_i, of a specimen is calculated as the slope of the least squares fit line through the stress-strain plot in the range of 5% to 20% of its strength. The experimental Poissons's ratio, ν_i, of a specimen is calculated at 20% of the strength. For each material, the stress levels at which the analytical moduli, E_i^* and ν_i^*, are calculated are obtained as follows. The equation of the least squares straight line for the experimental average strength versus logarithm of strain rate data (Table 2.2) is obtained. However, the estimated strength at any strain rate is not allowed to be lower than 4000 psi. From this equation, the maximum stress for each strain rate is obtained. E_i^* represents the secant modulus at 20% of the strength (Reminder: K_f^* is based on the hydrostatic stress in the pore fluid and the total volume change of the pore at 20% of the strength). As shown in Figs.

3.24-3.26, the range of strain rates used for the analytical results includes the range of the experimental results.

3.8.2.1 Constituent Properties

The equivalent porous solids, PS.3P, PS.4P and PS.5P, have porosities of 30%, 35%, and 40% which are approximately equal to the total porosities in pastes with W/C = 0.3, 0.4, and 0.5 at 75% hydration (72). The procedure of section 3.8.1 is used to determine the constituent properties of these porous solids such that they duplicate the strain-rate sensitive moduli of cement pastes with W/C = 0.3, 0.4 and 0.5, respectively. The constituent properties of PS.3P, PS.4P and PS.5P are: r = 0.0377, 0.0572, 0.0795, E_s = 15.23 x 10^6 psi, 11.971 x 10^6 psi, 11.55 x 10^6 psi, and ν_s = 0.425, 0.420, 0.417, respectively. For each porous solid, sixteen R_{cv} values geometrically equally spaced in a range given below are used. The ranges of R_{cv} are: for PS.3P from 1.81 x 10^{-18} to 2.58 x 10^{-4}, for PS.4P from 2.34 x 10^{-19} to 1.99 x 10^{-3}, and for PS.5P from 3.75 x 10^{-18} to 1.24 x 10^{-4}.

A comparison of these ranges of R_{cv} shows that PS.5P, the porous solid representing the highest water-cement ratio (0.5) paste, has the narrowest range of R_{cv}. PS.4P, representing the next lower water-cement ratio (0.4) paste has a range of R_{cv} that is 257 times wider than that of PS.5P. PS.3P, which represents the paste with the lowest water-cement ratio (0.3), however, has an R_{cv} range that is only 4 times wider than that of PS.5P. The nonmonotonic nature of the increase in the width of the range of R_{cv} with decrease in the

water-cement ratio is a consequence of the aberrant nature of the rate sensitivity of paste with W/C = 0.4. As pointed out in Chapter 2, paste with W/C = 0.4 has rate sensitivity, both in terms of E_i and ν_i, that is lower than those of the pastes with W/C = 0.3 and 0.5. Although, the widening of the range of R_{cv} with the increase in water-cement ratio is clearly not monotonic in this comparison, there is a trend towards a wider range of R_{cv} for a porous solid that represents a lower water-cement ratio paste. This is expected, since less space is available for the hydration products to grow in pastes with low water-cement ratios (72), causing finer pore sizes and a wider range of R_{cv} than in pastes with high water-cement ratios.

3.8.2.2 E_i^* versus $\dot{\varepsilon}$

Figs. 3.24a, 3.25a and 3.26a compare the elastic moduli, E_i^*, of PS.3P, PS.4P and PS.5P with the experimental values, E_i, at several strain rates for cement pastes with W/C's of 0.3, 0.4, and 0.5, respectively, tested 27 to 29 days after casting. Each experimental value shown in these figures is the average of at least 2 specimens. For W/C = 0.3 and 0.5 and strain rates of 3, 3000, and about 170,000 microstrain/sec, at least 10 specimens were tested. Figs. 3.24a, 3.25a, and 3.26a demonstrate that the analytical E_i^* versus log $\dot{\varepsilon}$ relations closely match the experimental relations for the three pastes. The E_i^* - log $\dot{\varepsilon}$ relations are linear except near the lowest and the highest strain rates considered, where they tend to decrease in slope. This is consistent with the earlier observation (section

3.7.4.2) that at very high or very low strain rates, the moduli eventually become insensitive to strain rate.

3.8.2.3 ν_i^* versus $\dot{\varepsilon}$

Figs. 3.24b, 3.25b and 3.26b compare the experimental and analytical Poisson's ratios, ν_i^* and ν_i, at several strain rates for W/C of 0.3, 0.4, and 0.5, respectively. The results shown in these figures come from the same calculations that produce the results shown in Figs. 3.24a, 3.25a and 3.26a. In Figs. 3.24b, 3.25b and 3.26b, each experimental value is obtained by averaging ν_i for at least two specimens. For W/C = 0.3 and $\dot{\varepsilon}$ = 3, 3000, and 170,000 microstrain/sec at least 10 specimens are used.

As shown in Figs. 3.24b, 3.25b and 3.26b, the experimental Poisson's ratio versus strain rate data for W/C = 0.3, 0.4 and 0.5 pastes have more scatter than the corresponding data for the elastic moduli. There was some noise in the electrical signal of the transverse gages used on the specimens which required the data to be smoothed. Like the analytical versus experimental elastic moduli comparisons of section 3.8.2.1, the ν_i^* versus log $\dot{\varepsilon}$ relations for the three pastes match well with the experimental relations. Similarly, the ν_i^* versus log $\dot{\varepsilon}$ relations are linear except near the extreme strain rate.

3.8.2.4 Variability of Constituent Properties

It was pointed out in section 3.8.1 that the analytical rate sensitivities of the composite moduli can be decreased by either increasing the pore aspect ratio, r, or by widening the range of R_{cv}.

It is therefore conceivable that one could duplicate a given set of strain-rate sensitive moduli using an alternative porous solid(s) which has a wider range of R_{cv} values but a smaller effective aspect ratio, r.

In the following example, an attempt is made to find the constituent properties of such an alternative porous solid (now referred to as PS.5P') for PS.5P. The process of finding the constituent properties of PS.5P' is started with those of PS.5P, and involves widening the range of R_{cv}, followed by estimation of r, and the solid phase moduli, E_s and ν_s. The estimation of r, E_s and ν_s is an iterative process which is continued until the experimental elastic moduli, E_i, are duplicated (as they did for PS.5P), and the differences in the rate sensitive Poisson's ratios of PS.5P' and the experimental values are minimized. In the following example (Figs. 3.27-3.29) the steps of the iterative process are shown as if the values of the constituent properties of PS.5P' are found in a single iteration. This can happen only by chance. Constituent properties of PS.5P and PS.5P' are also used in section 4.7.7 to compare long term creep strains. As the following example demonstrates, while the elastic moduli of PS.5P and PS.5P' match, the rate sensitivity of the Poisson's ratio, ν_i^*, of PS.5P' is lower than that of PS.5P; primarily because a change in r changes the rate sensitivity of E_i^* to a greater extent than that of ν_i^*.

Fig. 3.24 compares the analytical strain-rate sensitive moduli, E_i^* and ν_i^*, of PS.5P with the experimental values, E_i and ν_i. Both

the analytical and the experimental results represent 7.3% and 4.9% increases in E^* and ν^*, respectively, with a decade increase in strain rate. Fig. 3.27 makes a similar comparison after the range of R_{cv} is widened 100 times (from 3.75×10^{-18} - 1.24×10^{-4} to 3.75×10^{-19} - 1.24×10^{-3}). The rate sensitivities of E_i^* and ν_i^* have now reduced to 6.2% and 4.2%, respectively.

Next, the aspect ratio, r, is decreased from 0.0795 (for PS.5P) to 0.0752, so that the rate sensitivity of the analytical elastic modulus, E_i^*, could be increased and brought closer to the experimental value. In the process, the rate sensitivity of ν_i^* also increases to some extent. As Fig. 3.28 shows, with the smaller r of 0.0752 (versus 0.0795 in Fig. 3.27) the rate sensitivities of E_i^* and ν_i^* increase to 7.8% and 4.7%, respectively (versus 6.2% and 4.2% in Fig. 3.27). Clearly, the decrease in r has increased the rate sensitivity of E_i^* to a considerably greater extent than that of ν_i^*. However, the decrease in r has also decreased the magnitudes of E_i^* and ν_i^*.

Finally, to minimize the differences in the magnitudes of the analytical and the experimental moduli, the solid phase moduli, E_s and ν_s, are increased to 12.8×10^6 psi and 0.443, respectively. The last change in the constituent properties enables the analytical elastic moduli to match the experimental values, minimizes the differences between the analytical Poisson's ratios and the experimental values, and thus, provides the constituent properties of PS.5P'. Fig. 3.29 compares the analytical rate sensitive moduli using PS.5P' with the experimental values. While the rate sensitive elastic

moduli, E_i^*, of PS.5P' are identical to that of the experimental elastic moduli, E_i, (and that of E_i^* of PS.5P), the same is not true for ν_i^*. The rate sensitivity of the Poisson's ratio, ν_i^*, of PS.5P' is 4.5% per decade change in strain rate which is 10% lower than the experimental value of 4.9% (and that of PS.5P).

Using this procedure, constituent properties of several porous solids like PS.5P' can be found if only the elastic moduli have to be matched, i.e. starting the procedure by widening (or narrowing) the range of R_{cv} to a different extent than the two orders of magnitude used here. A similar procedure can be used to find the constituent properties of yet another porous solid that would match Poisson's ratio values for paste with W/C = 0.5 (or those of PS.5P); but then the former's elastic moduli would not match with the latter's. It is possible to have more than one porous solid that can duplicate experimental rate sensitivity of one of the moduli, but the same is not true for both the moduli. Thus, the constituent properties of PS.5P are unique. PS.5P' represents a material, if it exists, whose rate sensitive elastic moduli values are identical to those of paste with W/C = 0.5, but whose Poisson's ratio values are not quite the same (and 10% less rate sensitive) as those of PS.5P.

PS.5P' has a range of R_{cv} values that is two orders of magnitude wider (with smaller r) than that of PS.5P, but the rate sensitivity of the former's Poisson's ratio is only 10% less than the latter's. This indicates the properties of the equivalent porous solids are highly sensitive to small errors in the measurement of the moduli.

3.8.2.5 Stress-Strain Plots

Fig. 3.30 compares analytical and experimental stress-strain curves for paste with W/C = 0.5 loaded at 3 microstrain/sec and 300,000 microstrain/sec. The experimental stress-strain curves are for specimens 6-1/P-0.5/2 and 6-2/P-0.5/7 (Table 2.3) which had strengths of 6,260 psi and 10,330 psi, respectively. Experimental "initial slope" lines are also shown. These lines are the least squares straight lines through the experimental stress-strain values between stresses corresponding to 5% and 20% of the respective strengths. The analytical stress-strain curves are obtained by using the constituent properties of porous solid PS.5P (section 3.8.2.3) with the exception of the solid phase moduli, E_s and ν_s. E_s and ν_s are selected so that the analytical initial composite moduli, E_i^* and ν_i^*, match the experimental initial moduli, E_i and ν_i, for specimens X_1 and Y_1. Thus, E_s = 10.89 x 10^6 and 10.85 x 10^6 psi and ν_s = 0.38 and 0.40 were used for two analytical curves.

As shown in Fig. 3.30, the analytical curves are nonlinear for both strain rates. However, they are much less nonlinear than the experimental curves. For low stresses, e.g. up to 30% of the strength, both the analytical and the experimental stress-strain curves are very close to linear and match closely. At higher stresses the nonlinear strains, i.e. the values of strain after subtracting the strains corresponding to the respective "initial slope" line, of each curve increase. However, with an increase in stress, the nonlinear strains for the analytical curves become smaller and

smaller fractions of the experimental values. For example, at 3 microstrain/sec and stress levels of 40% and 60% of the strength, the analytical nonlinear strains are 60% and 27% of the experimental values of 70 and 288 microstrain, respectively. For 300,000 microstrain/sec curves, the two values are 57% and 30% of the experimental values of 86 and 278 microstrain, respectively. The lower degree of nonlinearity for the analytical curves, especially at higher stresses, is not surprising since the model does not consider cracking (6).

3.9 Pore Shape in Cement Paste

This study shows that pores in cement paste must be flat (oblate spheroids in this model) in order to duplicate the observed variation in elastic moduli as a function of strain rate. Although the shapes of the pores have been limited to spheroids in the current model, the results provide strong evidence that typical voids in hydrated cement paste deviates markedly from the circular cylinders commonly assumed in conventional porosimetry, and capillary condensation techniques. These new observations in no way take away from the applicability of those pore measurement techniques, but they do provide additional insight ito the nature of the structure of cement paste.

CHAPTER 4

USE OF THE RATE-SENSITIVE MODEL TO SIMULATE CREEP

4.1 Introduction

In the derivation of the equations for the strain-rate sensitive model (Chapter 3), a porous specimen loaded at a constant strain rate was considered. In this chapter, the equations and procedures are modified for a material undergoing creep at a constant stress (or stress-strength ratio). The basic physical phenomena, the viscous, time dependent flow of pore fluid, is the same.

Attiogbe and Darwin (6), in their study of submicroscopic cracking of cement paste and mortar, found that a substantial portion of the inelastic deformation under a sustained load was caused by factors other than submicroscopic cracking. Terry and Darwin's (83) sustained load tests show that cement paste exhibits significant inelastic deformation at a stress-strength ratio as low as 0.2. Since very little cracking is present at such low stress levels, Terry and Darwin's (83) results suggest that pore fluid movement plays an important role in the inelastic deformation. In this chapter, the rate-sensitive model is used to estimate the amount of inelastic deformation that can be attributed to the flow of pore fluid under sustained load.

As discussed in section 3.1, a porous solid, such as cement paste, can be viewed as a composite consisting of pores of various

shapes and sizes embedded in a solid matrix. The moduli of the composite are dependent upon the geometric and material properties of the pores and the matrix. In the rate-sensitive model, communication between saturated and unsaturated pores occurs through cylindrical orifices. The overall moduli of the isotropic porous solid, K^* and ν^*, depend on the moduli of the solid phase (not affected by the loading rate or stress history) and the effective bulk moduli of the pores (Note: the shear moduli of the pores are always zero, and will not be considered). The effective bulk modulus of a pore, K_f^*, is not, in general, the same as the bulk modulus of the pore fluid, K_f. Only when the orifice diameter is zero (i.e. the pore is completely isolated) does $K_f^* = K_f$, irrespective of the stress history. If the material properties are constant, K_f^* for a pore with a finite orifice diameter depends on the loading rate and the geometry of the orifice relative to the pore. For such cases K_f^* lies between 0 and K_f(section 3.1). K_f^* increases with an increase in the loading rate, an increase the length of the orifice, and a decrease in the diameter of the orifice.

In a creep test, as the stress is raised quickly, typically in a few seconds, very little flow occurs through the orifices. As the applied stress is held constant and the fluid flows through the orifices, the effective bulk moduli of the pores drop, resulting in a decrease in stiffness and an increase in the longitudinal and lateral strains with time.

4.2 Overview of the Model

As developed in Chapter 3, the rate-sensitive model represents a porous material as consisting of spheroidal pores surrounded by a homogeneous isotropic medium made up of spherical grains. The spheroidal pores are oriented isotropically. Each pore is assumed to be connected to an unsaturated region via an orifice. At any instant, the hydrostatic stress within a pore (really the hydrostatic stress within the pore fluid, $\sigma_f(t)$), which is surrounded by the effective medium whose moduli depend on the hydrostatic stress in all of all the pores, is expressed as a function of the relative geometry of the pore and the orifice, the properties of the pore fluid, the moduli of the surrounding medium, and the applied stress rate. The time-dependent effective modulus of a pore, K_f^*, is a function of $\sigma_f(t)$, and the deformation of the pore. The values of K_f^*, along with the moduli of the solid phase, K_s and ν_s, are used in a self-consistent manner to obtain the composite moduli of a porous solid as a function of time.

4.3 Hydrostatic Stress in Pore Fluid, $\sigma_f(t)$

In this section, an expression is developed for the hydrostatic stress in the pore fluid, $\sigma_f(t)$, for a porous material subjected to a stress history of the type normally used in a creep test. A differential equation in $\sigma_f(t)$ is obtained by equating the rate of change of the volume of the pore fluid to that of the pore. The differential equation involves an integral of $\sigma_f(t)$. A closed form

solution for $\sigma_f(t)$ cannot be found, and thus, a numerical procedure is used to find values of $\sigma_f(t)$ at selected times.

4.3.1 Derivation of Differential Equation in $\sigma_f(t)$

Consider a saturated spheroidal pore surrounded by a homogeneous isotropic medium subjected to uniform stress. The pore is connected to an unsaturated region via an orifice. Following the argument of section 3.3, the rate of change of the volume of the pore fluid must be equal to the rate of change of volume of the pore itself, or

$$\frac{\Delta V_{fluid}(t)}{\Delta t} = \frac{\Delta V_{pore}(t)}{\Delta t} \tag{4.1}$$

The left hand side of Eq. 4.1 is the sum of the rate of change of volume of the fluid due to pressure in it $\left(\frac{\Delta V_{fp}(t)}{\Delta t}\right)$ and the rate of flow of fluid through the orifice $\left(q_{or}(t)\right)$. The right hand side is the sum of the rate of change of volume of an empty pore under the external loading $\left(\frac{\Delta V_{pe}(t)}{\Delta t}\right)$ and the rate of change of volume of the pore due to the pressure in the fluid $\left(\frac{\Delta V_{pp}(t)}{\Delta t}\right)$. Thus, Eq. 4.1 can be written in incremental form as:

$$\frac{\Delta V_{fp}(t)}{\Delta t} + q_{or}(t) = \frac{\Delta V_{pe}(t)}{\Delta t} + \frac{\Delta V_{pp}(t)}{\Delta t} \tag{4.2}$$

The form of Eq. 4.2 has to be modified to obtain an expression for the hydrostatic stress in the pore fluid, $\sigma_f(t)$. To do that, the

numerators and the denominators of the first term in the left hand side, and the first and the second terms in the right hand side are multiplied by $V(t)\Delta\sigma_f(t)$, $\Delta\sigma(t)$ and $V_i\Delta\sigma_f(t)$, respectively. $V(t)$ is the volume of pore at time t, $\Delta\sigma_f(t)$ is the change in the hydrostatic stress in the pore fluid in time Δt at time t, $\Delta\sigma(t)$ is the change in the average stress applied on the material containing the pore in time Δt at time t, and V_i is the initial volume of the pore. After these multiplications, and some rearrangement, Eq. 4.2 can be written as:

$$\left(\frac{1}{\dfrac{\Delta\sigma_f(t)}{\Delta V_{fp}(t)/V(t)}} \right) V(t) \frac{\Delta\sigma_f(t)}{\Delta t} + q_{or}(t) = \left(\frac{\Delta V_{pe}(t)}{\Delta\sigma(t)} \right) \frac{\Delta\sigma(t)}{\Delta t}$$

$$+ \left(\frac{\Delta V_{pp}(t)/V_i}{\Delta\sigma_f(t)} \right) V_i \frac{\Delta\sigma_f(t)}{\Delta t} \qquad (4.3)$$

The denominator of the first term inside the parenthesis in Eq. 4.3 is the expression for the bulk modulus of the pore fluid, K_f.

$$K_f = \frac{\Delta\sigma_f(t)}{\Delta V_{fp}(t)/V(t)} \qquad (4.4)$$

The term inside the first parenthesis on the right hand side of Eq. 4.3 is the change in the volume of the pore per unit average applied

strain on the material containing the pore, v^*, divided by the elastic modulus of the surrounding medium, E^*.

$$\frac{v^*}{E^*} = \frac{\Delta V_{pe}(t)}{\Delta\sigma(t)} \tag{4.5}$$

v^* can be expressed in terms of pore geometry, pore orientation, ψ, and the moduli of the material surrounding the pore. ψ is defined as the angle between the polar semiaxis of the pore and the horizontal plane. The expression for v^* is quite complex and is derived in Appendix A. The term inside the last parenthesis in Eq. 4.3 is the fractional volume change of the pore per unit internal hydrostatic stress (in pore fluid) or pore compressibility (101), C_{pp}

$$C_{pp} = - \frac{\Delta V_{pp}(t)/V_i}{\Delta\sigma_f(t)} \tag{4.6}$$

C_{pp} can be expressed as a function of the pore geometry and the moduli of the material surrounding the pore. Such expressions are given in Appendix B.

Substituting Eqs. 4.4-4.6 into Eq. 4.3 and changing the equation to differential form gives:

$$\frac{1}{K_f}V(t)\dot{\sigma}_f(t) + q_{or}(t) = v^*\dot{\sigma}/E^* - C_{pp}V_i\dot{\sigma}_f(t) \tag{4.7}$$

in which the dot represents the derivative with respect to time. $\dot{\sigma}$ is the applied stress rate and assumed constant for this derivation. In Appendix C, the following expression for the rate of flow of pore fluid through the orifice, $q_{or}(t)$, is derived:

$$q_{or}(t) = \left(\frac{\pi d^4}{64\mu h}\right)\sigma_f(t) \tag{4.8}$$

in which, d is the diameter of the orifice, h is the length of the orifice, and μ is the viscosity of the pore fluid. Also, in Eq. 4.4 for $t = T$,

$$V(T) = V_i + \int_o^T q_{or}(t)dt \tag{4.9}$$

Eqs. 4.8 and 4.9 show that $q_{or}(t)$ and $V(T)$ are functions of $\sigma_f(t)$. To solve Eq. 4.7 for $\sigma_f(t)$, $q_{or}(t)$ and $V(T)$ must be replaced by Eqs. 4.8 and 4.9, respectively, in Eq. 4.7. After these substitutions and some rearrangement Eq. 4.7 becomes

$$\left(\frac{V_i}{K_f} + \frac{\pi d^4}{64\mu h K_f}\int_o^T \sigma_f(t)dt + V_i C_{pp}\right)\frac{d\sigma_f(t)}{dt}$$

$$+ \frac{\pi d^4}{64\mu h}\sigma_f(t) = (v^*/E^*)\frac{d\sigma(t)}{dt} \tag{4.10}$$

4.3.2 Numerical Procedure to Find Values of $\sigma_f(t)$

Eq. 4.10 is a differential equation in $\sigma_f(t)$ for which a closed form solution cannot be found because it also involves an integral of $\sigma_f(t)$. Hence, a numerical procedure is used to find values of $\sigma_f(t)$ at selected times. To do that, first both sides of Eq. 4.10 are integrated with respect to time. In the resulting expression, the integrals of $\sigma_f(t)$ are replaced by the equivalent sums to obtain a quadratic equation in $\sigma_f(t)$. The roots of the quadratic equation are found at selected times starting with the initial condition $\sigma_f(t) = 0$ at $t = 0$.

Integrating Eq. 4.10 with respect to time over the range $t_a \leq t \leq t_b = T$, gives

$$\left(\frac{V_i}{K_f} + \frac{\pi d^4}{64\mu h K_f}\int_o^T \sigma_f(t)dt + V_i C_{pp}\right)\left(\sigma_f(t_b) - \sigma_f(t_a)\right)$$

$$+ \frac{\pi d^4}{64\mu h}\int_{t_a}^{t_b} \sigma_f(t)dt = v^*\left(\sigma(t_b) - \sigma(t_a)\right)/E^* \qquad (4.11)$$

Replacing the integrals in Eq. 4.11 by the corresponding sums using the trapezoidal rule

$$\left(\frac{V_i}{K_f} + \frac{\pi d^4}{64\mu h K_f}\sum_{j=1}^{n-1}\left\{\frac{\sigma_f(t_j)+\sigma_f(t_{j+1})}{2}\right\}\Delta t_j + V_i C_{pp}\right)\left(\sigma_f(t_b) - \sigma_f(t_a)\right)$$

$$+ \frac{\pi d^4}{64\mu h}\left(\frac{\sigma_f(t_a) + \sigma_f(t_b)}{2}\right)\Delta t_a - v^*\left(\sigma(t_b) - \sigma(t_a)\right)/E^* = 0 \qquad (4.12)$$

in which $\Delta t_j = t_{j+1} - t_j$, $j = 1,2,\ldots n-1$ and $\Delta t_a = t_b - t_a$. In Eq. 4.12, note that the time interval can always be selected so that $t_n = t_b$ and $t_{n-1} = t_a$. Thus, $\sigma_f(t_b) = \sigma_f(t_n)$, $\sigma_f(t_a) = \sigma_f(t_{n-1})$, $\Delta t_a = \Delta t_{n-1}$, $\sigma(t_b) = \sigma(t_n)$, and $\sigma(t_a) = \sigma(t_{n-1})$. Making these substitutions in Eq. 4.12,

$$\left(\frac{V_i}{K_f} + \frac{\pi d^4}{64\mu h K_f} \sum_{j=1}^{n-1} \left\{\frac{\sigma_f(t_j)}{2} + \frac{\sigma_f(t_{j+1})}{2}\right\}\Delta t_j + V_i C_{pp}\right)\left(\sigma_f(t_n) - \sigma_f(t_{n-1})\right)$$

$$+ \frac{\pi d^4}{64\mu h}\left(\frac{\sigma_f(t_{n-1}) + \sigma_f(t_n)}{2}\right)\Delta t_{n-1} - v^*\left(\sigma(t_n) - \sigma(t_{n-1})\right)/E^* = 0 \quad (4.13)$$

Bringing the first and the last terms out of the summation,

$$\left(\frac{V_i}{K_f} + \frac{\pi d^4}{64\mu h K_f}\left\{\left(\frac{\sigma_f(t_1)}{2} + \frac{\sigma_f(t_2)}{2}\right)\Delta t_1 + \sum_{j=2}^{n-2}\left(\frac{\sigma_f(t_j)}{2} + \frac{\sigma_f(t_{j+1})}{2}\right)\Delta t_j\right.\right.$$

$$\left.\left. + \left(\frac{\sigma_f(t_{n-1})}{2} + \frac{\sigma_f(t_n)}{2}\right)\Delta t_{n-1}\right\} + V_i C_{pp}\right)\left(\sigma_f(t_n) - \sigma_f(t_{n-1})\right) \quad (4.14)$$

$$+ \frac{\pi d^4}{64\mu h}\left(\frac{\sigma_f(t_{n-1}) + \sigma_f(t_n)}{2}\right)\Delta t_{n-1} - v^*\left(\sigma(t_n) - \sigma(t_{n-1})\right)/E^* = 0$$

Substituting $\sigma_f(t_1) = 0$ (initial condition) and $\frac{\Delta t_{j-1} + \Delta t_j}{2} = \Delta t_{avgj}$, Eq. 4.14 can be written as

$$\left(\frac{V_i}{K_f} + \frac{\pi d^4}{64\mu h K_f}\left\{\sum_{j=1}^{n-1}\sigma_f(t_j)\Delta t_{avgj} + \frac{\sigma_f(t_n)\Delta t_{n-1}}{2}\right\} + V_i C_{pp}\right)\left(\sigma_f(t_n) - \sigma_f(t_{n-1})\right)$$

$$+ \frac{\pi d^4}{64\mu h}\left(\frac{\sigma_f(t_{n-1}) + \sigma_f(t_n)}{2}\right)\Delta t_{n-1} - v^*\left(\sigma(t_n)-\sigma(t_{n-1})\right)/E^* = 0 \tag{4.15}$$

The characteristic volume ratio, R_{cv}, defined by Eq. 3.21, is now introduced into Eq. 4.15.

$$R_{cv} = \frac{\pi d^4}{hV_i} \tag{4.16}$$

Substituting Eq. 4.16 into Eq. 4.15 and simplifying gives

$$A_1\{\sigma_f(t_n)\}^2 + B_1\{\sigma_f(t_n)\} + C_1 = 0 \tag{4.17}$$

in which,

$$A_1 = \frac{V_i R_{cv}\Delta t_{n-1}}{128\mu K_f} \tag{4.18}$$

$$B_1 = \frac{V_i}{K_f} + V_i C_{pp} + \frac{V_i R_{cv}}{64\mu K_f}\sum_{j=1}^{n-1}\sigma_f(t_j)\Delta t_{avgj} - \frac{V_i R_{cv}\Delta t_{n-1}}{128\mu K_f}\sigma_f(t_{n-1}) + \frac{V_i R_{cv}\Delta t_{n-1}}{128\mu} \tag{4.19}$$

$$C_1 = -(v^*/E^*)\left(\sigma(t_n) - \sigma(t_{n-1})\right) + \left\{\frac{V_i R_{cv}\Delta t_{n-1}}{128\mu} - \frac{V_i}{K_f} - V_i C_{pp} - \frac{V_i R_{cv}}{64\mu K_f}\sum_{j=1}^{n-1}\sigma_f(t_j)\Delta t_{avgj}\right\}\sigma_f(t_{n-1}) \tag{4.20}$$

Eq. 4.17 is a quadratic equation in $\sigma_f(t_n)$ with a root

$$\sigma_f(t_n) = \frac{-B_1 + \sqrt{B_1^2 - 4A_1C_1}}{2A_1} \tag{4.21}$$

Note, calculations for $\sigma_f(t_n)$ require the knowledge of $\sigma_f(t_j)$, j = 1,2...n-1. The process of finding $\sigma_f(t_n)$ is initiated by first finding $\sigma_f(t_2)$ (Note: $\sigma_f(t_1) = 0$ is the initial condition) and then sequentially finding $\sigma_f(t_j)$, j = 3,4,...n. Since creep strain is known to increase at slower and slower rates with time, the calculation efficiency can be improved by gradually increasing the time intervals, Δt_j, during the sustained loading.

4.4 Effective Bulk Modulus of a Saturated Pore, K_f^*

In this section, an expression is obtained for the effective bulk modulus of the saturated pore considered in section 4.3. The effective bulk modulus of the pore, K_f^*, is

$$K_f^* = \frac{\sigma_f(T)}{\varepsilon_v(T)} \tag{4.22}$$

in which $\sigma_f(T)$ is the hydrostatic stress in the pore fluid at time T and $\varepsilon_v(T)$ is the ratio of the total volume change due to the compressibility of the pore fluid ($\Delta V_c(T)$) and the flow of the pore fluid through the orifice ($\Delta V_o(T)$), divided by the initial volume of the pore (V_i). Thus,

$$K_f^* = \frac{\sigma_f(T)}{\frac{\Delta V_c(T)}{V_i} + \frac{\Delta V_o(T)}{V_i}} \tag{4.23}$$

To solve Eq. 4.23, we use the definition of the bulk modulus of the pore fluid, K_f.

$$K_f = \frac{\sigma_f(T)}{\Delta V_c(T)/V(T)} \tag{4.24}$$

$$\text{or} \quad \Delta V_c(T) = \frac{\sigma_f(T)V(T)}{K_f} \tag{4.25}$$

Also, integrating Eq. 4.8 between $0 \leq t \leq T$

$$\Delta V_o(T) = \frac{\pi d^4}{64\mu h} \int_o^T \sigma_f(t)dt \tag{4.26}$$

Substituting Eqs. 4.25 and 4.26 in Eq. 4.23 gives

$$K_f^* = \frac{\sigma_f(T)}{\frac{V(T)\sigma_f(T)}{V_i K_f} + \frac{\pi d^4}{64\mu h V_i} \int_o^T \sigma_f(t)dt} \tag{4.27}$$

Substituting Eq. 4.9 for V(T) and Eq. 4.16 for $\pi d^4/hV_i$ and simplifying gives

$$K_f^* = \frac{\sigma_f(T)}{\frac{\sigma_f(T)}{K_f} + (1 + \frac{\sigma_f(T)}{K_f})\frac{R_{cv}}{64\mu}\int_o^T \sigma_{ff}(t)dt} \tag{4.28}$$

4.5 Self-Consistent Procedure for Finding Composite Moduli, E^*, ν^*

As explained in sections 3.5 and 3.6, the following expressions are used to iteratively calculate the composite bulk and shear moduli, respectively.

$$K^*_{n+1} = \frac{\sum_{j=1}^{m} C_j K_j (P^{*j})_n}{\sum_{j=1}^{m} C_j (P^{*j})_n} \tag{4.29}$$

$$G^*_{n+1} = \frac{\sum_{j=1}^{m} C_j G_j (Q^{*j})_n}{\sum_{j=1}^{m} C_j (Q^{*j})_n} \tag{4.30}$$

in which, C_j, K_j, and G_j, $1 \leq j \leq m$, are the volume concentration, bulk modulus, and shear modulus of the j^{th} phase of the composite. P^{*j} and Q^{*j}, (Appendix D) are functions of shapes and moduli of the constituents. The subscripts n and n + 1 represent the values of the respective variables at the end of n^{th} and $(n + 1)^{th}$ iteration.

4.6 Procedure to Find Longitudinal and Transverse Strains, $\varepsilon_L^*, \varepsilon_T^*$

In this section, a self-consistent procedure is presented that finds the time-dependent longitudinal and transverse strains, ε_L^* and ε_T^*, for an equivalent porous solid. Before applying the procedure given below for calculating ε_L^* and ε_T^*, the procedure of section 3.8.1 is used to determine the constituent properties of the equivalent porous solid, e.g. the range of R_{cv}, a representative aspect ratio of the pores, and the moduli of the solid phase. These properties are determined so that the strain-rate sensitive analytical moduli match the average experimental values (Chapter 2). If the moduli of the specimen, E_i and ν_i, to be used for comparison are available, the moduli of the solid phase, E_s and ν_s, are modified so that the analytical moduli, E_i^* and ν_i^*, match those of the specimen. While calculating ε_L^* and ε_T^*, the time increments during the initial rise in stress, Δt_j, $j = 1,2,\ldots m-1$ are kept constant, while the time increments during the sustained loading, Δt_j, $m,m+1,\ldots n-1$, are increased geometrically. Thus, the time increments during the sustained loading are such that $\Delta t_j = F_2 t_j$, $j = m,m+1,\ldots n-1$, in which $F_2 << 1.0$ and Δt_m is the first time interval during the sustained loading.

4.6.1 Procedure

At time t_2 (Note, $\varepsilon_L^* = \varepsilon_T^* = 0$ at $t_1 = 0$), the initial estimates of the composite moduli, K_1^* and G_1^*, are made. Since the overall response of the composite is expected to be softer then the solid phase, K_1^* and G_1^* are set at fractions of the solid phase moduli, K_s and G_s, respectively. Values of hydrostatic stress, $\sigma_f(t_2)$, for all

pores are calculated using Eqs. 4.18-4.21. Using the values of $\sigma_f(t_2)$ and the values of R_{cv} selected, the values of the effective bulk modulus of the pores, K_f^*, are obtained (Eq. 4.28). Once K_f^* for all pores are obtained, they are used along with solid phase moduli, K_s and G_s, to estimate the composite moduli, K^* and G^*, iteratively (Eqs. 4.29 and 4.30). The iterative estimation of K^* and G^* is started using initial estimates K_1^* and G_1^*, and continued until two successive pairs of moduli are within reasonable tolerances. To ensure overall self-consistency, the iterative procedure is repeated after replacing K_1^* and G_1^* by the converged K^* and G^*, respectively, unless the former pair is within reasonable tolerances of the latter pair. The composite moduli, K^* and G^*, at time t_2, are used to calculate the longitudinal and transverse strains, ε_L^* and ε_T^*, using standard elasticity relations. The whole process of calculating the strains is repeated at the selected times, t_j, $j = 3,4,....n$.

During the iterative estimation of K^* and G^* using Eqs. 4.29 and 4.30, convergence is assumed when two successive pairs of K^* and G^* are within 1×10^{-6} K^* and $1 \times 10^{-6} G^*$, respectively. Also, for general self consistency, the values of K_1^* and G_1^* are replaced by the converged values of K^* and G^* unless the former pair is within $1 \times 10^{-3} K^*$ and $1 \times 10^{-3} G^*$, of the latter pair, respectively.

4.7 Numerical Examples and Discussion

In the following sections, the rate-sensitive model is used to compare the analytical response under sustained loading with the

response of cement paste with W/C = 0.5. The analytical strains, ε_L^* and ε_T^*, are obtained as functions of time by considering an equivalent porous solid, PS.5P. ε_L^* and ε_T^* are compared with short-term experimental values of ε_L and ε_T obtained by Terry and Darwin (83) and Attiogbe and Darwin (6). Long-term analytical creep behavior also is studied and compared with corresponding experimental results (65, 85). An example demonstrating the effect of changes in the parameters of the model (or the properties of the equivalent porous solid) on long-term creep predictions is presented. In the process of finding time-dependent strains, the corresponding time-dependent hydrostatic stress in the pore fluid, $\sigma_f(t)$, and the time dependent effective bulk moduli of the pores, K_f^*, are also obtained.

4.7.1 Constituent Properties

For the examples given here, the analytical results are obtained using the constituent properties, except the solid phase moduli, of an equivalent porous solid, PS.5P. For the example in section 4.7.7, the constituent properties of another equivalent porous solid, PS.5P', are also used for comparison. The properties of PS.5P, determined in section 3.8.2, are: the elastic modulus of the solid phase $E_s = 11.55 \times 10^6$ psi, the Poisson's ratio of the solid phase $\nu_s = 0.417$, bulk modulus of the pore fluid $K_f = 3.25 \times 10^5$, shear modulus of pore fluid $G_f = 0$, viscosity of pore fluid $\mu = 1.5 \times 10^{-7}$ psi-sec, pore aspect ratio $r = 0.0795$, total porosity = 40%, and 16 values of characteristic volume ratio, R_{cv}, geometrically equally

spaced in the range of 3.75×10^{-18} to 1.24×10^{-4}. For geometrically equal spacing, each successive R_{cv} value is a constant multiple of the previous value, with the first and the last R_{cv} values set at the limits of the range. In section 3.8.2, the constituent properties of PS.5P were determined so that the analytical moduli, E_i^* and ν_i^*, were very close to the average experimental values for paste with W/C = 0.5 at strain rates between 3×10^{-1} microstrain/sec to 3×10^{5} microstrain/sec. For section 4.7.5 the solid phase moduli, E_s and ν_s, are modified so that the analytical moduli match those of the specimen used for comparison (6, 83).

Attiogbe and Darwin (6) calculated the elastic modulus of a specimen, E_i, as the secant modulus for the first two sets of stress-strain data, and found it to be 2.53×10^{6} psi for the specimens used here. For Terry and Darwin's (83) results, E_i for each specimen is calculated following the procedure used in this study (section 2.3.2). E_i varies between 2.47×10^{6} psi and 2.55×10^{6} psi. Poisson's ratio, ν_i, is not available for the specimens in these two studies (section 4.7.5). Hence, values obtained from the least square line through ν_i versus logarithm of strain rate data of this study (Table 2.10) are used. For each specimen, the strain rate used for reading ν_i from the least squares line is the average strain rate for the initial rise in stress.

For the long-term creep results compared in section 4.7.6, neither the stress-strain relations nor the rate of loading during the initial rise in stress are available. Hence the solid phase

moduli of PS.5P and an initial rise time (15 seconds), corresponding to tests of Attiogbe and Darwin (6) and Terry and Darwin (83), are used.

As suggested in sections 4.3 and 4.6, the total time during sustained loading is divided into gradually increasing intervals. In the following examples, a constant time interval of 1 sec is used during the initial rise in the stress, i.e. for the first 15 sec. After that, the time for sustained loading is divided in to n geometrically increasing intervals such that $\Delta t_j = 0.1 t_j$, $j = 15,16 \ldots n-1$.

4.7.2 Applied Stress History, $\sigma(t)$

Terry and Darwin (83) conducted sustained load tests on cement paste, mortar and concrete. Paste specimens with W/C = 0.5 subjected to stress-strength ratios of 0.2, 0.4, 0.6 and 0.8 are used here for comparison. The stress was increased to a predetermined level in 15 seconds and then held constant for 4 hours. Fig. 4.1a shows the applied stress-time histories for the four specimens used here.

Attiogbe and Darwin (6) used sustained loading to study the submicroscopic cracking behavior of cement paste specimens. Like Terry and Darwin (83), the applied stress was increased to a predetermined level in 15 sec and then held constant. For the three W/C = 0.5 paste specimens used here, stress-strength ratios of 0.675, 0.725 and 0.800 were used to strain the specimens to 0.004, 0.0059 and 0.0074, respectively. Sustained load was applied for 4 hours for the first

two specimens and for 3.5 hours for the last specimen. Fig. 4.1b shows the three applied stress-time histories.

4.7.3 Hydrostatic Stress in Pore Fluid, $\sigma_f(t)$

In this and the next section, the second of the Attiogbe and Darwin specimens is used for comparison. An elastic modulus of the solid phase $E_s = 12.51 \times 10^6$ psi, a Poisson's ratio of the solid phase $\nu_s = 0.4122$, and a sustained stress of 4884 psi are used. These values are the same as those that are used for the comparisons shown in Fig. 4.6. Fig. 4.2 shows the variation in $\sigma_f(t)$ with time for two R_{cv} values, 6.0×10^{-17} and 1.6×10^{-13}, and pore orientations of 0°, 45°, and 90°.

As shown in Fig. 4.2, the hydrostatic stress in a pore, $\sigma_f(t)$, is greatly influenced by its characteristic volume ratio, R_{cv}, as well as its orientation, ψ. For a higher characteristic volume ratio, R_{cv}, the pore pressure, $\sigma_f(t)$, is lower and drops to zero sooner than that for a lower R_{cv}. This is expected, since an increased R_{cv} represents a larger diameter or shorter length orifice relative to the size of the pore, allowing the pore fluid to flow more quickly. In fact, if the R_{cv} is large enough, the pore develops negligible pressure. If, on the other hand, the value of R_{cv} is small enough, the pore develops pressure comparable to that developed in a pore without an orifice and stays so for a long time. Ultimately, the pore pressure drops to zero, even for the pore with the smallest diameter orifice. When this happens, there is no further flow through the orifice and the pore volumes reach equilibrium

(under a given sustained stress), causing the overall strains to become constant. As shown in Fig. 4.2, the orientation of a pore, ψ, influences $\sigma_f(t)$ drastically. For an oblate shape ($r = 0.08715$), $\sigma_f(t)$ is the highest for $\psi = 0°$ and is the lowest for $\psi = 90°$. This is consistent with the discussion of the influence of ψ on $\sigma_f(t)$ in section 3.3.

4.7.4 Effective Bulk Modulus of a Pore, K_f^*

Fig. 4.3 shows the variation in the effective bulk modulus of a pore, K_f^*, with time for five values of characteristic volume ratio, R_{cv}, between 6.0×10^{-17} to 4.1×10^{-10}. As discussed in section 3.4, the orientation of a pore, ψ, has very little effect on the effective bulk modulus of a pore, K_f^*, unless the applied strain is very high, e.g. ≥ 0.01. Accordingly, a single curve is obtained for $\psi = 0°$, 45°, and 90° at each R_{cv} value. Three of the K_f^* versus logarithm of time curves exhibit kinks at 15 sec, i.e the at the end of the initial rise in stress. The kinks occur due to the rate sensitive nature of K_f^*. As shown in Fig. 3.5, K_f^* is highly sensitive to loading (strain) rate; the higher the loading rate, the greater the value of K_f^*. At 15 sec, the loading rate suddenly becomes zero causing abrupt reduction in K_f^* and a discontinuity (or kink) in the K_f^* versus time relation. As expected, the kinks appear simultaneously with the sharp drop in the hydrostatic stress in the pore fluid (Fig. 4.2).

As Fig. 4.3 shows, the effective bulk modulus is higher and is sustained longer the lower the characteristic volume ratio. At a given time, the effective bulk modulus of a pore, K_f^*, is higher the

lower the characteristic volume ratio, R_{cv}. If R_{cv} is small enough, K_f^* approaches K_f (the bulk modulus of the pore fluid). A further reduction in R_{cv} results in no further increase in K_f^*; however, K_f^* remains at K_f for a longer time. As expected, the time when K_f^* reaches zero coincides with the time that the hydrostatic stress in the pore fluid reaches zero. After this time, no further softening of the composite occurs and strain becomes constant.

4.7.5 Longitudinal and Transverse Strains, ε_L^* and ε_T^*

The longitudinal and transverse strains, ε_L^* and ε_T^*, are calculated using the procedure described in section 4.5. Fig. 4.4 compares the analytical longitudinal strains with Terry and Darwin's experimental data for cement paste with W/C = 0.5 loaded at stress-strength ratios of 0.2, 0.4, 0.6, 0.8. The figure shows that as stress-strength ratio is increased, the analytical ε_L^* versus time predictions deviate more and more from the experimental results. creep strains at the end of 4 hours are calculated by subtracting ε_L^* at the beginning of the sustained loading (15 sec) from ε_L^* at the end of the sustained loading (4 hours). For stress-strength ratios of 0.2, 0.4, 0.6 and 0.8, the ratios of the analytical to experimental creep strain are 1.18, 0.75, 0.39 and 0.16, respectively. The match for a stress-strength ratio of 0.2 is good, within 23 microstrain, a difference that is within experimental scatter. The greater deviations at higher stress-strength ratios, is expected since the model does not consider cracking, which plays an important role as the stress level is increased (6). Fig. 4.4 also shows that as the level

of sustained stress is increased, the deviation of the analytical strains from the experimental values during the initial rise in stress becomes more noticeable. The close match at a stress-strength ratio of 0.2 illustrates that the key aspects of creep for short duration at low stress can be explained by moisture movement. As stress increases, other nonlinear behaviors play increasingly important roles.

Figs. 4.5-4.7 compare the analytical response with the experimental results of Attiogbe and Darwin. Since the experimental results are not available as function of time, the comparisons are made only in terms of stress-strain relations. The results show that for stress-strength ratios of 0.675, 0.725 and 0.800, the ratios of analytical to experimental creep strain are 0.31, 0.18 and 0.13, respectively. These ratios are consistent with the comparisons illustrated in Fig. 4.4 and the observation that the analytical response deviates more and more from the experimental results with a rise in stress-strength ratio.

Fig. 4.7 also compares the analytical stress versus transverse strain relation to the experimental results. Both the analytical and the experimental transverse strains increase under sustained stress, but the former is much smaller than the latter. The smaller increase in the analytical transverse strain, ε_T^*, compared to the increase in the experimental value, ε_T, is not surprising since cracking is not considered in the model.

For the results shown in Fig. 4.7, the Poisson's ratio values drop under sustained load for both the analytical (from 0.253 to 0.210) and the experimental (from 0.278 to 0.160) results. The drop in the analytical Poisson's ratio, ν_i^*, can be explained by considering the role of the fluid filled pores, whose effective bulk moduli decrease with time (Fig. 4.3), in the transverse deformation of the porous solid. Due to the presence of the softer pores, compared to the stiff solid phase, part of the transverse deformation of the solid phase is accommodated within the porous solid (in the pores). This is more so as the effective bulk moduli, K_f^*, decrease with time and approach zero. Under sustained loading, as K_f^* for a larger and larger number of pores approach zero (Fig. 4.3), ν_i^* becomes a smaller and smaller fraction of ν_s. This explanation is consistent with a similar explanation by Attiogbe and Darwin (6), that the decrease in the Poisson's ratio under sustained loading suggests consolidation or deformation of solid phase into pores. A smaller drop in ν_i^* than that in ν_i is expected due to the presence of cracks in the real material (cement paste). For cement paste subjected to sustained loading, some of the cracks, depending on the level of sustained loading, are expected to stabilize and may play a similar role to that of the pores in accommodating part of the transverse deformation of the solid phase.

4.7.6 Long-Term Creep

In the last section (Figs. 4.4-4.7), the analytical longitudinal strain values were calculated for periods up to 4 hours. It is of interest to compare the analytical response with experimental results for longer time periods. As discussed in sections 4.7.3 and 4.7.4, the longitudinal strain in the model, ε_L^*, will ultimately cease to increase as pores with the smallest characteristic volume ratio, R_{cv}, attain zero hydrostatic pressure, $\sigma_f(t)$. In this section, the analytical strain calculations are carried out until that happens.

Fig. 4.8 shows the analytical longitudinal strain, ε_L^*, versus time relations for cement paste with W/C = 0.5 loaded at stress-strength ratios of 0.2 and 0.4. The constituent properties of PS.5P and the sustained stress levels corresponding to the lowest stress-strength ratio (1312 psi at stress-strength ratio = 0.2) comparison of Fig. 4.4 are used. As expected, ε_L^* ceases to change after a finite time, in this case 2.4×10^8 sec (7.6 years), for both stress levels. As discussed in sections 4.7.3 and 4.7.4, the time at which this occurs, the "terminal time", depends on the minimum value of R_{cv} for PS.5P. The sensitivity of the terminal time to the change the parameters of the rate-sensitive model (or the properties of the equivalent porous solid) is discussed in section 4.7.7. Analytical versus experimental long-term creep strains will now be compared.

Timsuk and Ghose (85) conducted creep tests of cement paste with W/C = 0.5 for 28 days, starting 28 days after casting. To monitor the strength gain and the shrinkage of the wax coated creep

specimens, comparison specimens were kept in the same environment as the test specimens. The applied stress was increased in discrete steps so that a stress-strength ratio of approximately 0.15 was maintained for the 28 days of sustained loading. Creep strains were obtained by arithmetically deducting shrinkage and elastic strains from total strains. As stated in section 4.7.1, the analytical results are obtained using the constituent properties of the equivalent porous solid PS.5P, and the initial rise time (of 15 sec) corresponding to tests of Attiogbe and Darwin (6) and Terry and Darwin (83). Since the extent of gain in strength during the sustained loading is not available, a 15% gain in strength (from 5630 to 6470 psi) is assumed (60) for the analytical calculations. The analytical creep strain is obtained by subtracting ε_L^* at the beginning of the sustained loading from ε_L^* at a given time. Fig. 4.9 compares the analytical creep strain versus time relation with the results of Timsuk and Ghose (85). The experimental data correspond to those of Fig. 3 of Timsuk and Ghose's study (85), and indicate a creep strain at the end of 28 days of sustained loading of 0.000600. The creep strain (at the end of 28 days) for another specimen of the same study (their Fig. 5) is 0.000545. The analytical creep strain of 0.000355 at the end of 28 days of loading is 65% of 0.000545.

Rainford and Timsuk (65), using the same water-cement ratio paste and similar test conditions as Timsuk and Ghose (85), and a stress-strength ratio of 0.2, found the creep strain to be 0.000650 at the end of 28 days of loading. A comparison of the results of

Timsuk and Ghose (85) with those of Rainford and Timsuk (65) suggests that, for the former study, the lower creep strain value of 0.000545 is more likely than the higher value of 0.000600. Fig. 4.10 makes an analytical versus experimental creep strain comparison using test results of Rainford and Timsuk (65). The magnitudes of the sustained stress levels used in the experiments (65) are not available. Hence, an initial (at 15 sec) sustained stress of 1312 psi (used by Terry and Darwin (83) is used for the analytical results. Like Fig. 4.9, a 15% increase in strength is also assumed. The analytical creep strain of 0.000548 equals 84% of Rainford and Timsuk's experimental value of 0.000650.

In section 4.7.5 it was observed that the short-term (4 hours) analytical strain versus time relations for a stress-strength ratio of 0.2 (Fig. 4.4) were very close to the experimental values. However, the long-term analytical predictions (Figs. 4.9-4.10) using stress-strength ratios of 0.15 and 0.20 remain smaller (by 16% to 35%) than experimental values. The deviations in the long-term are likely due to of shrinkage, continued hydration, and maturation creep (85).

As stated earlier, the experimental creep strains were obtained (65, 85) by arithmetically subtracting the shrinkage (of control specimens) and elastic strains form the total strains. This way of finding creep strains does not completely account for the effect of shrinkage on the total strain. Thus, if shrinkage of the specimens had been completely avoided the experimental creep strains, and the

deviations of the analytical creep strains from the experimental values, would have been smaller.

With continuing hydration, the pore structure and the quantity of pore fluid do not remain the same as they were at the initiation of load. The model, however, assumes constant pore structure and quantity of pore fluid, irrespective of the duration of loading. In the short run (e.g. 4 hours used in section 4.7.5), the changes are negligible and a good match between the analytical and the experimental creep strains is obtained (Fig. 4.4).

Maturation creep (85) is a consequence of progress in hydration while the material remains under stress. At any time during the sustained loading, unhydrated cement particles and the load bearing gel share the applied load. As explained by Timsuk and Ghose (85), cement gel formed during sustained loading remains stress-free for some time and only gradually begins to share the applied load with the rest of the material. The newly formed gel is located in spaces that were originally cracks, pores or voids and becomes load bearing only after sufficient growth and/or further deformation (creep) in the load bearing portion of the material. The formation of cement gel occurs at the expense of unhydrated cement. As the load bearing material is removed, load is transferred to other portions of the material with a subsequent increase in strain. The lower the extent of hydration prior to loading, the greater the potential for maturation creep. The model does not consider the process involved in

maturation creep, and, as expected, provides significantly lower creep strains in the long run.

Timsuk and Ghose have shown that maturation creep indeed adds to the long-term creep strain. To stop the hydration, or maturation, of the specimens, they lowered the specimens temperature to -11° C, causing negligible strength gain during the tests. The average creep strain at -11° C was only 0.000400 (compared to the strain of 0.000545 at 75° C). According to the study by Fontenay and Sellevold (29) most of the pore fluid in cement paste with W/C = 0.5 remains unfrozen as a supercooled liquid at -11° C. To obtain the analytical creep strain at -11° C, all of the pore fluid is assumed to be supercooled and the magnitude of the sustained stress is kept constant at 984 psi (i.e. 15% of the strength of 6560 psi for the specimen tested at -11° C (85)). In this case, the analytical creep strain at the end of 28 days of loading is 0.000303 which is 76% of the experimental value of 0.0004 (85). This value is closer to the experimental value (76%) than obtained at 75° C (65%).

The analytical versus experimental comparisons of this section show that for periods up to 28 days, most (65% to 84%) of the creep in cement paste at low stresses (15% to 20% of the strength) can be explained using the current model. Shrinkage, hydration and maturation creep seem to be the major reasons for differences between the analytical and the experimental creep strains at these stress levels.

4.7.7 Variability of the Terminal Time

In this section, the effect of change in the constituent properties of the equivalent porous solid on the terminal time is examined. As defined in section 4.7.6, terminal time is the time after which the analytical strain, ε_L^*, becomes constant. In section 3.8.2.1, the constituent properties of an equivalent porous solid (e.g. PS.5P) are determined based on the magnitudes and the rate sensitivity of the experimental moduli (e.g. for paste with W/C = 0.5). The rate sensitivity of the elastic modulus (or the Poisson's ratio) is the percentage change in its value with an order of magnitude change in the strain rate. In section 3.8.2.4, it was observed that the range of R_{cv} of an equivalent porous solid (e.g. PS.5P) is highly sensitive to small errors in measuring the rate-sensitive moduli. Since the terminal time depends on the minimum value of R_{cv} (Sections 4.7.3 and 4.7.4), a variation in the range of R_{cv} is expected to change the terminal time.

Analytical results are obtained using the constituent properties of two equivalent porous solids, PS.5P and PS.5P'. The properties of PS.5P are the same as given at the beginning of section 4.7.1. The properties of PS.5P', determined in section 3.8.2.4, are: r = 0.0752, E_s = 12.8 x 10^6 psi, ν_s = 0.443, 16 R_{cv} values in the range of 3.75 x 10^{-19} to 1.24 x 10^{-3}, porosity = 40%, and the properties of the pore fluid are the same as PS.5P. The range of R_{cv} for PS.5P' is 100 times wider than that for PS.5P. Accordingly, the minimum value of R_{cv} for PS.5P' of 3.75 x 10^{-19} is 10 times smaller than the minimum

value of R_{cv} for PS.5P of 3.75×10^{-18}. The other differences in the properties of the two porous solids are: the pore shape for PS.5P' is flatter ($r = 0.0752$) compared to that for PS.5P ($r = 0.0795$) and the elastic moduli of the solid phase of PS.5P' are higher ($E_s = 12.8 \times 10^6$ psi and $\nu_s = 0.443$) than those for PS.5P ($E_s = 11.55 \times 10^6$ psi and $\nu_s = 0.417$). As shown in section 3.8.2.4, while the rate sensitivity of the elastic moduli of these two porous solids is the same, the rate sensitivity of the Poisson's ratio of PS.5P' is 10% is lower than the that of PS.5P.

Fig. 4.11 compares the ε_L^* versus time relations for the two equivalent porous solids for a stress-strength ratio of 0.2 (1312 psi (83)). The longitudinal strain-time relations are virtually identical until the terminal time of PS.5P. With the lower minimum value of R_{cv}, higher moduli of the solid phase, E_s and ν_s, and lower value of the aspect ratio, r, (PS.5P'), the terminal time and creep increases from 2.4×10^8 sec (or 7.6 years for PS.5P) to 3.7×10^9 sec (or 117.6 years for PS.5P'), and the maximum strain increases from 0.001214 (for PS.5P) to 0.001477 (for PS.5P'). The greater maximum strain for PS.5P' than that for PS.5P is expected because of the flatter pores and stiffer matrix in the former than in the latter.

The comparisons of this section show the sensitivity of the long-term response of the model to its parameters, and the importance of accuracy in measuring and matching (Figs. 3.24-3.26) the rate-sensitive moduli.

CHAPTER 5

SUMMARY AND CONCLUSIONS

5.1 Summary

The purpose of this investigation is to study the strain-rate sensitive behavior of the cement paste, mortar constituents of concrete. The investigation consists of both experimental and analytical work. Strain-rate sensitivity of the materials is measured in terms of the initial elastic moduli and the stress and strain at failure. An analytical model is developed to study the physical processes responsible for the strain-rate sensitivity of the materials at stress levels where cracking does not dominate the response.

Saturated cement paste and mortar specimens with water-cement ratios of 0.3, 0.4 and 0.5 are used. To study the effect of sand-cement ratio on strain-rate sensitivity, two mix designs are used for mortar with water-cement ratio of either 0.4 or 0.5. Specimens are tested at ages ranging from 27 to 29 days.

Specimens are loaded in compression using a closed-loop servo-hydraulic testing machine. The average longitudinal strain is measured over the total height of the specimen using two LVDT's. The average transverse strain is measured at midheight of the specimen using two extensometers. Each specimen is loaded to 15,000 microstrain to obtain the descending as well as the ascending portions of the stress-strain curve. Seven strain rates in the range of

0.3 to 300,000 microstrain/sec are used. The strain-rate sensitive response is measured in terms of the initial elastic modulus, the Poisson's ratio, the maximum stress, and the strain at the maximum stress.

A strain-rate sensitive analytical model is developed to study and duplicate the strain-rate sensitive elastic moduli of the materials. The model considers a nearly saturated porous solid, such as cement paste, mortar or concrete, as a composite consisting of saturated spheroidal pores and solid spherical grains. Each saturated pore is assumed to be in communication with an unsaturated region. Expressions are formulated for the strain-rate sensitive effective bulk modulus of a saturated pore. A self-consistent procedure is developed to estimate the composite moduli of the porous solid. The rate sensitivity of the composite moduli is studied analytically as a function of pore shape, porosity, and the degree of communication of the pore fluid between the pores and unsaturated regions. The analytical rate sensitive response is compared to the response of cement paste specimens.

The equations and the procedures of the strain-rate sensitive model are modified to simulate creep of the materials under sustained loading. The model is calibrated using the strain-rate sensitive response of cement paste. The analytical creep strains are compared with short-term and long-term experimental data for cement paste.

5.2 Conclusions

The following conclusions can be made based on the findings of this study:

1. The stress-strain curves for cement paste and mortar remain nonlinear up to the highest strain rate, 300,000 microstrain/sec, used. The nonlinearity decreases with increase in strain rate.
2. The failure mode of the specimens is sensitive to strain rate. The higher the strain rate, the more violent the failure. At higher strain rates, the failure cracks were straighter, cleaner and larger in number than those at lower strain rates.
3. The initial elastic moduli and strength of cement paste and mortar increase significantly with each order of magnitude increase in strain rate. For both cement paste and mortar, an order of magnitude increase in strain rate results in about 7% and 15% increases in initial elastic moduli and strength, respectively.
4. The strain-rate sensitivity of the Poisson's ratio of the materials, i.e. the increase in its magnitude with each order of magnitude increase in strain rate, increases with an increase in strain up to at least 2500 microstrain for mortar and up to at least 5000 microstrain for cement paste. The increase in strain-rate sensitivity with an

increase in strain is higher for cement paste than for mortar.

5. The strain at the maximum stress varies nonmonotonically with an increase in strain rate. The strain at the maximum stress is greatest for the lowest strain rate used, 0.3 microstrain/sec. As the strain rate is increased, the strain at the maximum stress first decreases, for several orders of magnitude increase in strain rate, and then increases.

6. The introduction of sand increases the initial stiffness of cement paste. Within the ranges of sand-cement ratio used, the higher the sand-cement ratio, the higher the stiffness of the mortar.

7. The introduction of sand lowers the maximum stress as well as the strain corresponding to the maximum stress. For cement paste and two mortars with W/C = 0.3 and 0.4, cement paste has the highest strength, followed in turn by the mortar with the lower sand-cement ratio and the mortar with the higher sand-cement ratio. For W/C = 0.5, the strengths of the two mortars, except for mortar A at 30,000 microstrain/sec and mortar B at 3 microstrain/sec, are within 6% (higher or lower) of the strength of cement paste.

8. Within the range of water-cement ratios used in this study, there is a trend towards decreased strain capacity with an

increase in water-cement ratio for both cement paste and mortar.

9. The rate sensitive stress-strain behavior of the materials at failure (stress and corresponding strain) can be qualitatively explained by the growth and propagation of cracks in the materials.

10. A nearly saturated porous solid, such as cement paste, mortar, or concrete, can be modeled as a composite consisting of saturated spheroidal pores, connected via orifices to unsaturated regions, and solid spherical grains.

11. The geometry of the orifice relative to the pore, represented by a characteristic volume ratio, $R_{cv} = \pi d^4/hV_i$, determines the degree of communication between the pore and an unsaturated region. The smaller the value of R_{cv}, the lower the degree of communication.

12. The hydrostatic stress in the pore fluid is a function of R_{cv}, the viscosity of the pore fluid, the moduli of the surrounding media, the strain rate, pore orientation, and the shape of the pore.

13. The volume of flow of pore fluid through an orifice depends on the pore shape. For a given porosity and pore size, the flatter the pore shape, the greater the volume of flow. For the strain rates and pore shapes used in this study, the total volume of the flow through the orifices does not exceed 1% of the porosity.

14. For small strains (e.g. $\varepsilon = 0.001$), the effective bulk modulus of a saturated spheroidal pore which is in communication with an unsaturated region is not dependent on the orientation of the pore.

15. The effective bulk modulus of a saturated pore, K_f^*, depends on strain rate as well as on R_{cv}. The higher the strain rate and the smaller the R_{cv}, the greater the K_f^*. For all values of strain rate and R_{cv}, K_f^* stays between zero and the bulk modulus of the pore fluid.

16. For a given R_{cv}, K_f^* remains significantly sensitive to the shape of the pore, r, for a certain range of strain rates. Outside of this range, K_f^* becomes virtually insensitive to r. The greater the R_{cv}, the higher the values of strain rate for which K_f^* is significantly sensitive to r. In the range of strain rates for which K_f^* is significantly sensitive to r, the pores with $r = 1$ (spherical pores) have the lowest K_f^*. The values of K_f^* for $r > 1$ (prolate spheroidal pores) are slightly greater than that for $r = 1$. However, values of K_f^* for $r < 1$ (oblate spheroidal pore) can be considerably greater, i.e. 30%, than that for $r = 1$.

17. For a macroisotropic and macrohomogeneous (or statistically isotropic and homogeneous) porous solid, the analytical strain-rate sensitive response does not depend on the pore size.

18. For a given porosity, the analytical strain-rate sensitivity of the composite moduli of a porous solid greatly depend on the pore shape. The more nonspherical the pores, the greater the rate sensitivity. The strain-rate sensitivity of a porous solid with prolate spheroidal pores is slightly greater than that with spherical pores. However, the strain-rate sensitivity of a porous solid with oblate spheroidal pores can be drastically greater than that with spherical pores.
19. The analytical strain-rate sensitivity of a porous solid greatly depends on its porosity. The higher the porosity, the more rate sensitive are the analytical composite moduli. This happens because the strain rate sensitivity of the composite behavior originates from the rate sensitivity of the pores.
20. To model a linear moduli versus logarithm of strain rate relation, a wide range of R_{cv} values is needed. The wider the range of linearity of the experimental moduli versus logarithm of strain rate relation, the wider the range of R_{cv} values needed.
21. For a finite range of R_{cv} values, the analytical moduli remain sensitive to strain rate over a finite range of strain rate. With an increase (or decrease) in the strain rate outside of this range, the analytical moduli become insensitive to strain rate.

22. The analytical model closely duplicates the strain-rate sensitive moduli of cement paste with W/C = 0.3, 0.4 and 0.5.

23. A wide range of R_{cv} values and a flat oblate representative pore shape are needed to duplicate the strain-rate sensitive moduli of cement paste.

24. The need for the use of a flat oblate representative pore shape strongly suggests that the typical pore in hydrated cement paste is markedly different from the circular shape commonly assumed in conventional porosimetry and capillary condensation techniques.

25. The response of the analytical model is very sensitive to the values of its parameters, e.g. the pore shape and the range of R_{cv} values.

26. At low stresses, most of the nonlinearity of the stress-strain curves of the materials (obtained at various strain rates) can be attributed to the flow of pore fluid. With an increase in stress, the relative contribution of the flow of the pore fluid to nonlinear behavior decreases as cracking starts to dominate the response. For example, for cement paste with W/C = 0.5, at 40% and 60% of the strength and a strain rate of either 3 or 300,000 microstrain/sec, about 60% and 30% of the nonlinear strain, respectively, can be attributed to the movement of the pore fluid.

27. The equations and procedures of the strain-rate sensitive model can be modified to simulate creep under sustained loading. For low sustained stress levels (e.g. 20% of the strength), the analytical creep strains match well with the experimental values in the short-term, e.g. up to 4 hr. For higher stress levels, the analytical creep strains are lower than the experimental values. The higher the level of the sustained stress, the greater the deviation from the experimental behavior.

28. In the long-term, no adequate experimental data are available for comparing the analytical results. While the analytical model simulates basic creep behavior, the experimental data are available only on total creep strains (includes shrinkage of the specimens).

29. The long-term analytical creep strains are expected to be lower than the experimental basic creep strains due to continued hydration and maturation creep. While these phenomena occur in real materials, they are not considered in the model.

30. For a finite range of R_{cv} values, the analytical creep strains stop increasing at a finite time, the "terminal time". The terminal time is very sensitive to the minimum value of R_{cv}. The high sensitivity of the terminal time to

the minimum value of R_{cv} indicates the importance of accuracy in calibrating the rate sensitive model if it is to be used for predicting the long-term creep.

5.3 Recommendations for Future Study

1. To widen the applicability of the strain-rate sensitive model, a more general, e.g. ellipsoidal, pore shape should be used in place of the spheroidal shape used here.
2. The transport of the pore fluid in smaller orifices, of the order of several molecules (of the pore fluid), is not the same as the simple lamellar flow assumed in this study. The incorporation of a mechanism of transport of fluid at the molecular level would provide a more realistic model of pore fluid movement in smaller orifices.
3. The stress-strain response at stress levels where appreciable cracking is present can be modelled more realistically by incorporating cracks in the solid phase.
4. While the response of the strain-rate sensitive model critically depends on the representative pore shape(s), conventional porosimetry and capillary condensation techniques do not address this issue. In order to find the pore shape distribution, a rigorous technique using a high resolution scanning electron microscope (SEM) should be considered.

5. In this study, an isotropic distribution of pores has been assumed, which may not be true for porous solids in general. To use the model for a general distribution of pores, a self-consistent technique incorporating an anisotropic distribution of pores should be used.

6. Prior to this study, there was a general lack of data on the strain-rate sensitive behavior of Poisson's ratio of cement paste, mortar and concrete. More data on Poisson's ratio at various strain rates and strains, particularly high strains, will be useful to support and compliment the findings of this study.

7. The applicability of the strain-rate sensitive model has been demonstrated for cement paste. The same should be demonstrated for other cementitious materials, as well as other porous solids, such as rock.

REFERENCES

1. Abrams, D. A., "Effect of Rate of Application of Load on the Compressive Strength of Concrete," Proceedings American Society for Testing and Materials, Vol. 17, Part II, 1917, pp. 364-374.

2. Ahmad, Shuaib, H., and Shah, Surendra P., "Behavior of Hoop Confined Concrete under High Strain Rates," Journal of the American Concrete Institute, Proc. Vol. 82, No. 5, September-October 1985, pp. 634-647.

3. American Society for Testing and Materials, Annual Book of ASTM Standards, Cement; Lime; Gypsum, Vol. 04.01, C305-82 (Reapproved 1987), pp. 197-199.

4. Arfken, G., Mathematical Methods for Physicists, Academic Press, New York, 1970, pp. 103-108.

5. Atchley, Bill L., and Furr, Howard L., "Strength and Energy Absorption Capabilities of Plain Concrete under Dynamic and Static Loading," Journal of the American Concrete Institute, Vol. 64, No. 11, November 1967, pp. 745-756.

6. Attiogbe, Emmanuel K., and Darwin, David, "Submicroscopic Cracking of Cement Paste and Mortar in Compression," SM Report No. 16, The University of Kansas Center for Research Inc., November, 1985, 439 pp.

7. Attiogbe, Emmanuel K., and Darwin, David, "Submicrocracking in Cement Paste and Mortar," ACI Materials Journal, V. 84, No. 6, November-December 1987, pp. 491-500.

8. Attiogbe, Emmanuel K., and Darwin, David, "Strain Due to Submicrocracking in Cement Paste and Mortar," ACI Materials Journal, V. 85, No. 1, January-February 1988, pp. 3-11.

9. Bazant, Zdenek P., "Material Behavior under Various Types of Loading," Proceedings, Workshop on High Strength Concrete, Department of Materials Engineering, University of Illinois at Chicago Circle, Chicago, IL, December 2-4, 1979, pp. 79-92.

10. Bazant, Zdenek P., "Advances in Deformation and Failure Models for Concrete," IABSE Colloquium on Advanced Mechanics of Reinforced Concrete: Introductory Report, Delft, Netherlands, 1981, pp. 9-39.

11. Berryman, J. G., "Long Wavelength Propagation in Composite Elastic Media I. Spherical Inclusions," Journal of the

Acoustical Society of America, Vol. 68, No. 6, December 1980, pp. 1809-1819

12. Berryman, J. G., "Long Wavelength Propagation in composite Elastic Media II. Ellipsoidal Inclusions," Journal of the Acoustical Society of America, Vol. 68, No. 6, December 1980, pp. 1820-1831

13. Berryman, J. G., "Effective Medium Approximation for Elastic Constants of Porous Solids with Microscopic Heterogeneity," Journal of Applied Physics, Vol. 59, No. 4, February 15, 1986, pp. 1136-1140

14. Bicanic, N. and Zienkiewicz, O. C., "Constitutive Model for Concrete Under Dynamic Loading," Earthquake Engineering and Structural Dynamics, Vol. 11, No. 5, September-October 1983, pp. 689-710.

15. Bresler, B., and Bertero, V. V., "Influence of High Strain Rate and Cyclic Loading on Behavior of Unconfined and Confined Concrete in Compression," Proceedings, Second Canadian Conference on Earthquake Engineering, McMaster University, June 5-6, 1975, pp. 1-13.

16. Budiansky, B., "On the Elastic Moduli of Some Heterogeneous Materials," Journal of the Mechanics and Physics of Solids, Vol. 13, No. 4, August 1965, pp. 223-227

17. Budiansky, B., and O'Connell, R., "Elastic Moduli of a Cracked Solid," International Journal of Solids and Structures, Vol. 12, No. 2, February 1976, pp. 81-97

18. Carrasquillo, Ramon L., Nilson, Arthur H., and Slate, Floyed O., "Properties of High Strength Concrete Subject to Short-Term Loads," Journal of the American Concrete Institute, Vol. 78, No. 3, May-June 1981, pp. 171-178.

19. Cleary, M. P., "Elastic and Dynamic Response Regimes of Fluid-Impregnated Solids with Diverse Microstructures," International Journal of Solids and Structures, Vol. 14, No. 10, Oct. 1978, pp. 795-819

20. Cleary, M. P., Chen, I., and Lee, S., "Self-Consistent Techniques for Heterogeneous Media," Journal of the Engineering Mechanics Division, Proceedings of the American Society of Civil Engineers, Vol. 106, No. EM5, October 1980, pp. 861-887

21. Darwin, David, and Attiogbe, Emmanuel K., "Effects of Loading Rate on Cracking of Cement Paste," Materials Research Society Symposia Proceedings, Vol. 64, Cement-Based Composites: Strain

Rate Effects on Fracture, Eds. Sidney Mindess and Surendra P. Shah, December 4-5, 1985, Boston Massachusetts, pp. 167-180.

22. Dean, E. A., "Elastic Moduli of Porous Sintered Material as Modeled by a Variable Aspect Ratio Self-Consistent Oblate-Spheroidal-Inclusion Theory," Journal of the American Ceramic Society, Vol. 66, No. 12, December 1983, pp. 847-854

23. Dhir, R. K., and Sangha, C. M., "A Study of the Relationships between Time, Strength, Deformation and Fracture of Plain Concrete," Magazine of Concrete Research, Vol. 24, No. 28, December 1972, pp. 197-208.

24. Dhir, R. K., and Sangha, C. M., "Development and Propagation of Microcracks in Plain Concrete," Materiaux et Constructions: Materials and Structures, Vol. 7, No. 37, January-February 1974, pp. 17-24.

25. Dilger, W. H., Koch, R., and Kowalczyk, R., "Ductility of Plain and Confined Concrete under Different Strain Rates ," Journal of the American Concrete Institute, Proc. Vol. 81, No. 1, January-February 1984, pp. 73-81.

26. Edward, R. H., "Stress Concentrations Around Spheroidal Inclusions and Cavities," Journal of Applied Mechanics, Vol. 18, No. 1, March 1951, pp. 19-30.

27. Eshelby, J. D., "The Determination of the Elastic Field of an Ellipsoidal Inclusion and Related Problems," Proceedings of the Royal Society of London, Series A, Vol. 1241, No. 1226, August 1957, pp. 376-396

28. Evans, R. H., "Effect of Rate of Loading on the Mechanical Properties of Some Materials," Journal of the Institution of Civil Engineers, Vol. 18, 1942, pp. 296-305.

29. Fontenay, C. S., and Sellevold, E. J., "Ice Formation in Hardened Cement Paste - I. Mature Water-Saturated Pastes," Proceedings of the First International Conference on Durability of Building Materials and Components, ASTM, STP 691, August 21-23, Ottawa, Canada, pp. 425-438

30. Fox, E. N., "Some Exploratory Tests on the Strength of Concrete Beams under Pulse Loads," Proceedings, Conference on Nonmetallic Brittle Materials, Mining Research Establishment of the National Coal Board, London, April 1958, pp. 283-299.

31. Galloway, J. W., and Raithby, K. D., "Effects of Rate of Loading on Flexural Strength and Fatigue Performance of Concrete,"

Transport and Road Research Laboratory, TTRL Report LR 547, Crowthorne, Berkshire, 1973, 18 pp.

32. Gokoz, Ulker N., and Naaman, Antoine E., "Effect of Strain-Rate on the Pull-Out Behavior of Fibers in Mortar," International Journal of Cement Composites, Vol. 3, No. 3, August 1981, pp. 187-202.

33. Gopalratnam, V. S., and Shah, S. P., "Instrumental Impact Testing of Brittle Materials," Proceedings, Fifth Engineering Mechanics Division Specialty Conference, American Society of Civil Engineers, Vol. 1, August 1-3, 1984, pp. 635-639.

34. Green, Harry, "Impact Strength of Concrete," The Institution of Civil Engineers, Proceeding Vol. 28, July 1964, pp. 383-396.

35. Harris C. M., and Crede, C. E., Shock and Vibration Handbook, McGraw Hill Book Company, New York, 1976, pp. 32.28-32.32.

36. Hashin, Z., "Analysis of Composite Materials - A Survey," Journal of Applied Mechanics, Vol. 50, No. 3, September 1983, pp. 481-505

37. Hashin, Z., and Shtrikman, S., "A Variational Approach to the Theory of Elastic Behaviour of Multiphase Materials," Journal of the Mechanics and Physics of Solids, Vol. 11, No. 2, March-April 1963, pp. 127-140

38. Hatano, T., and Tsutsumi, H., "Dynamical Compressive Deformation and Failure of Concrete under Earthquake Load," Proceedings, the Second World Conference on Earthquake Engineering, Science Council of Japan, Vol. III, Tokyo and Kyoto, Japan, July 11-18, 1960.

39. Hensen, Robert J., "Long Duration Impulsive Loading of Simple Beams," Journal of Boston Society of Civil Engineers, Vol. 35, No. 3, July 1948, pp. 272-285.

40. Henyey, F. S., and Pomphrey, N. "Self-Consistent Elastic Moduli of a Cracked Solid," Geophysical Research Letters, Vol. 9, No. 8, August 1982, pp. 903-906

41. Hill, R., "The Elastic Behaviour of a Crystalline Aggregate," Proceeding of the Physical Society of London, Section A, Vol. 65, No. 3894, Part 5, May 1952, pp. 349-354

42. Hill, R., "Elastic Properties of Reinforced Solids: Some Theoretical Principles," Journal of the Mechanics and Physics of Solids, Vol. 11, No. 5, September 1963, pp. 357-372

43. Hill, R., "A Self-Consistent Mechanics of Composite Materials," Journal of the Mechanics and Physics of Solids, Vol. 13, No. 4, August 1965, pp. 213-222

44. Jawed, I., Childs, G., Ritter, A., Winzer, S., Johnson, T., and Barker, D. "High-Strain-Rate Behavior of Hydrated Cement Pastes," Cement and Concrete Research, Vol. 17., No. 3, May 1987, pp. 433-440.

45. Jones, Paul G., and Richart, F. E., "The Effect of Testing Speed on Strength and Elastic Properties Concrete," Proceedings, American Society for Testing and Materials, Vol. 36, Part II, 1936, pp. 380-391.

46. Kaplan, Seyit Ali, "Factors Affecting the Relationship between Rate of Loading and Measured Compressive Strength of Concrete," Magazine of Concrete Research, Vol. 32, No. 111, June 1980, pp. 79-88.

47. Kawamato, Toshikazu, and Saito, Toshiaki, "The Behavior of Rock-Like Materials in Some Controlled Strain States," Proceeding, Third Congress of the International Society for Rock Mechanics, Themes 1-2, Denver, Colorado, September 1-7, 1974, pp. 161-166.

48. Ko, K. C., and Hass, C. J., "The Effective Modulus of Rock as a Composite Material," International Journal of Rock Mechanics and Mining Sciences, Vol. 9, No. 4, pp. 531-541

49. Korringa, J., Brown, R. J. S., Thompson, D. D., and Runge, R. J., "Self-Consistent Imbedding and the Ellipsoidal Model for Porous Rocks," Journal of Geophysical Research, Vol. 84, No. B10, September 10, 1979, pp. 5591-5598

50. Kuster, G. T., and Toksoz, M. N., "Velocity and Attenuation of Seismic Waves in Two-Phase Media: Part I. Theoretical Formulations," Geophysics, Vol. 39, No. 5, October 1974, pp. 587-606

51. Kvirikadze, O. P., "Determination of the Ultimate Strength and Modulus of Deformation of Concrete at Different Rates of Loading," Proceedings, International Symposium on Testing Insitu Concrete Structures V, 1977, Budapest, pp. 109-117.

52. Mainstone, R. J., "Properties of Materials at High Rates of Straining or Loading," Materiaux et Constructions: Materials and Structures, Vol. 8, No. 44, March-April 1975, pp. 102-116.

53. Malvern, L. E., Tang, T., Jenkins, D. A., and Gong, J. C., "Dynamic Compressive Strength of Cementitious Materials," Materials Research Society Symposia Proceedings, Vol. 64,

Cement-Based Composites: Strain Rate Effects on Fracture, Ed. Sidney Mindess and Surendra P. Shah, December 4-5, 1985, Boston Massachusetts, pp. 119-138.

54. McHenry, Douglas, and Shideler, J. J. "Review of Data on Effect of Speed in Mechanical Testing of Concrete," Symposium on Speed of Testing, American Society for Testing and Materials, STP 185, 1956, pp. 72-82.

55. Mihashi, Hirozoh, and Izumi, Masandri, "A Stochastic Theory for Concrete Fracture," Cement and Concrete Research, Vol. 7, No. 4, July 1977, pp. 411-422.

56. Miller, M. N., "Bounds for Effective Bulk Modulus of Heterogeneous Materials," Journal of Mathematical Physics, Vol. 10, No. 11, November 1969, pp. 2005-2012

57. Millstein, Leonid, and Sabnis, Gajanan M., "Concrete Strength under Impact Loading," RILEM-CEB-IABSE-IASS-Interassociation Symposium on Concrete Structures under Impact and Impulsive Loading, Introductory Report, Berlin (West), June 2-4, 1982, pp. 101-112.

58. Mlakar, Paul F., Vitaya-Udom, Ken P., and Cole, Robert A., "Dynamic Compressive Behavior of Concrete," Journal of the American Concrete Institute, Vol. 82, No. 4, July-August 1985, pp. 484-491.

59. Moore, O. L., "Report of Working Committee on Plastic Mortar Tests for Portland Cement," Proceedings, American Society for Testing and Materials, Vol. 34, Part I, 1934, pp. 332-355.

60. Neville, A. M., Properties of Concrete, Third Edition, Pitman Publishing Limited, London, 1981, pp. 66-67

61. Nielsen, Knud E. C., "Effect of Various Factors on the Flexural Strength of Concrete Test Beams," Magazine of Concrete Research, No. 15, March 1954, pp. 105-114.

62. Oshima, N., and Nomura, S. "A Method to Calculate Effective Modulus of Hybrid Composite Materials," Journal of Composite Materials, Vol. 19, No. 3, May 1985, pp. 287-293

63. Paul, B. "Prediction of Elastic Constants of Multiphase Materials," Transactions of the Metallurgical Society of AIME, Vol. 218, No. 1, February 1960, pp. 36-41

64. Price, Walter H., "Factors Influencing Concrete Strength," Journal of the American Concrete Institute, Proc. Vol. 51, No. 6, February 1951, pp. 417-432.

65. Rainford, E. C., and Timsuk, J., "Creep of Hardened Portland Cement Under Cyclic Temperature," Journal of the American Ceramic Society, Vol. 61, No. 9-10, September-October 1978, pp. 380-385

66. Rao, S. S., Mechanical Vibrations, Addison-Wesley Publishing Company, Reading, Massachusetts, 1986, pp. 24-27.

67. Reuss, A. "Berechung der Fliessgrenze von Mischkristallen auf Grund der Plstizitatsbedingung fur Einkristalle," Zeitschrift fuer Angewandte Mathematik und Mechanik, Vol. 9, 1929, pp. 49-58

68. Richart, F. E., and Jones, Paul G., "Concrete Takes Greater Load if Suddenly Applied," Concrete, Vol. 44, No. 1, January 1936, pp. 16.

69. Rusch, Hubert, "Researches Toward a General Flexural Theory for Structural Concrete," Journal of the American Concrete Institute, Vol. 57, No. 1, July 1960, pp. 1-28.

70. Sadowsky, M. A., and Sternberg, E., "Stress Concentration Around an Ellipsoidal Cavity in an Infinite Body Under Arbitrary Plane Stress Perpendicular to the Axis of Revolution of Cavity," Journal of Applied Mechanics, Vol. 55, No.3, September 1947, pp. A.191-A.201.

71. Shah, Surendra, P., and Winter, George, "Inelastic Behavior and Fracture of Concrete," Journal of the American Concrete Institute, Vol. 63, No. 9, September 1963, pp. 925-930.

72. Soroka, I., Portland Cement Paste and Concrete, Chemical Publishing Co. Inc., New York, 1980, 338 pp.

73. Sparks, P. R., and Menzies, J. B., "The Effect of Rate of Loading upon the Static and Fatigue Strength of Plain Concrete in Compression," Magazine of Concrete Research, Vol. 25, No. 88, June 1973, pp. 73-80.

74. Spooner, D. C., "Stress-Strain-Time Relationships for Concrete," Magazine of Concrete Research, Vol. 23, No. 75-76, June-September 1971, pp. 127-131.

75. Spooner, D. C., "The Stress-Strain Relationship for Hardened Cement Paste in Compression," Magazine of Concrete Research, Vol. 24, No. 79, June 1972, pp. 85-92.

76. Struck, W., and Voggenreiter, W., "Examples of Impact and Impulsive Loading in the Field of Civil Engineering," Materiaux et Constructions: Materials and Structures, Vol. 8, No. 44, September 1975, pp. 81-87.

77. Suaris, W., and Shah, Surendra, P., "Mechanical Properties of Materials Subjected to Impact," RILEM-CEB-IABSE-IASS-Interassociation Symposium on Concrete Structures under Impact and Impulsive Loading, Introductory Report, Berlin (West), June 2-4, 1982, pp. 33-62.

78. Suaris, Wimal, and Shah, Surendra, "Properties of Concrete Subjected to Impact," Journal of Structural Engineering, ASCE, Vol. 109, No. 7, July 1983, pp. 1727-1741.

79. Suaris, Wimal, and Shah, Surendra, "Rate Sensitive Damage Theory for Brittle Solids," Journal of Structural Engineering, ASCE, Vol. 110, No. 6, June 1984, pp. 985-997.

80. Suaris, Wimal, and Shah, Surendra, "Constitutive Model for Dynamic Loading of Concrete," Journal of Structural Engineering, ASCE, Vol. 111, No. 3, March 1985, pp. 563-576.

81. Takeda, Jin-Ichi, and Tachikawa, Hiroyuki, "Deformation and Fracture of Concrete Subjected to Dynamic Load," Proceedings, International Conference on Mechanical Behavior of Materials, Kyoto, Japan, 1971, pp. 267-277.

82. Tang, Tianxi, Malvern, Lawrence E., and Jenkins, David A., "Dynamic Compressive Testing of Concrete and Mortar," Proceedings, the Fifth Engineering Mechanics Division Specialty Conference, American Society of Civil Engineers, August 1-3, 1984, pp. 663-666.

83. Terry, R., and Darwin, D., Unpublished Experimental data 1980-1982

84. Thaulow, Sven, "Belastningshastighet ved Trykkprovning av Betong (Rate of Loading for Compressive Strength Tests)," Betong, Vol. 38, 1953, pp. 11-15.

85. Timsuk, J., and Ghose, R. S., "Maturing Creep of Portland Cement," Journal of the American Concrete Institute, Proceedings, Vol. 68, No. 12, December 1971, pp. 959-963

86. Trott, J. J., and Fox, E. N., "Comparison of the Behavior of Concrete Beams under Static and Dynamic Loading," Magazine of Concrete Research, Vol. 11, No. 31, March 1959, pp. 15-24.

87. Voigt, W., Lehrbuch der Kristallphysik, Teubner, Leipzig, 1928

88. Vos, E., and Reinhardt, H. W., "Influence of Loading Rate on Bond Behavior of Reinforcing Steel and Prestressing Strands," Materiaux et Constructions: Materials and Structures, Vol. 15, No. 85, January-February 1982, pp. 3-10.

89. Wang, C., Applied Elasticity, McGraw Hill Book Company, New York, 1953, pp. 7-9.

90. Watstein, D, "Effect of Straining Rate on the Compressive Strength and Elastic Properties of Concrete," Journal of the American Concrete Institute, Vol. 49, No. 8, April 1953, pp. 729-744.

91. Watt, J. P., Davis, G. F., and O'Connell, R. J., "The Elastic Properties of Composite Materials," Reviews in Geophysics and Space Physics, Vol. 14, No. 4, November 1976, pp. 541-563

92. Wittmann, F. H., "Mechanism and Mechanics of Fracture of Concrete," Proceedings, the 5th International Conference on Fracture, Cannes, France, March 29 to April 3, 1981, pp. 1467-1487.

93. Wright, P. J. F., and Garwood, F., "The Effect of the Method of Test on the Flexural Strength of Concrete," Magazine of Concrete Research, Vol. 11, October 1952, pp. 67-76.

94. Wu, Spencer T., "Some Notes on the Dynamic Properties on Unsaturated Concrete," Nuclear Engineering and Design, Vol. 53, No. 1, June 1979, pp. 97-103.

95. Wu, T. T., "The Effect of Inclusion Shape on the Elastic Moduli of a Two-Phase Material," International Journal of Solids and Structures, Vol. 2, No. 1, January 1966, pp. 1-8

96. Zech, B., and Wittmann, F. H., "Variability and Mean Value of Strength of Concrete as Function of Load," Journal of the American Concrete Institute, Vol. 77, No. 5, September-October, 1980, pp. 358-362.

97. Zielinski, A. J., "Model for Tensile Fracture of Concrete at High Rate of Loading," Cement and Concrete Research, Vol. 14, No. 2, March 1984, pp. 215-224.

98. Zielinski, A. J., and Reinhardt, H. W., "Stress-Strain Behavior of Concrete and Mortar at High Rates of Tensile Loading," Cement and Concrete Research, Vol. 12, No. 3, May 1982, pp. 309-319.

99. Zielinski, A. J., Reinhardt, H. W., and Kormeling, H. A., "Experiments on Concrete under Uniaxial Tensile Loading," Materiaux et Constructions: Materials and Structures, Vol. 14, No. 80, March-April 1981, pp. 103-112.

100. Zimmerman, R. W., "Elastic Moduli of a Solid with Spherical Pores: New Self Consistent Method," International Journal of

Rock Mechanics and Mining Sciences, Vol. 21, No. 6, December 1984, pp. 339-343

101. Zimmerman, R. W., "Compressibility of an Isolated Spheroidal Cavity in an Isotropic Elastic Medium," Journal of Applied Mechanics, Vol. 52, No. 3, September 1985, pp. 606-608.

102. Zimmerman, R. W., King, M. S., and Moteiro, P. J. M., "The Elastic Moduli of Mortar as a Porous Granular Material," Cement and Concrete Research, Vol. 16, No. 2, March 1986, pp. 239-245

TABLE 2.1

STRAIN RATE TEST DATA FOR CEMENT PASTE WITH W/C = 0.3

Specimen Number	Strain Rate (0-100%)	Strain Rate (5-20%)	Strain Rate (50-99%)	Maximum Stress	ε_p	ε_{pp}	E_i	ν_i
14-1/P-0.3/1	0.30	0.30	0.30	10987	6500	8991	3.082	0.142
15-1/P-0.3/1	0.30	0.30	0.30	12333	12215	13310	2.792	0.162
7-1/P-0.3/2	3.05	3.04	3.05	11741	6267	6644	3.355	0.234
7-2/P-0.3/2	3.03	2.95	3.03	12312	7096	7629	3.383	0.263
7-3/P-0.3/2	2.99	2.99	2.99	13077	6885	7751	3.551	0.217
8-1/P-0.3/2	3.02	3.02	3.04	13184	7905	8288	3.433	0.240
8-2/P-0.3/2	3.04	3.04	3.02	12152	6924	7391	3.513	0.252
8-3/P-0.3/2	3.04	3.04	3.07	12712	8170	8716	3.402	0.160
10-1/P-0.3/2	3.00	2.98	3.00	12437	7804	8209	3.394	0.181
10-2/P-0.3/2	3.00	3.00	3.00	12753	8687	9371	3.265	0.175
10-3/P-0.3/2	3.00	2.98	3.00	12608	8327	8775	3.319	0.223
14-1/P-0.3/2	3.01	3.00	3.01	11845	6434	6810	3.367	0.172
15-1/P-0.3/2	3.02	3.01	3.02	13048	7456	7754	3.371	--
14-1/P-0.3/3	30.3	30.1	30.3	13700	6792	7369	3.354	0.223
15-1/P-0.3/3	30.4	30.5	30.3	14422	7860	8529	3.457	0.256
14-1/P-0.3/4	304	300	310	15478	7261	7363	3.576	0.237
15-1/P-0.3/4	306	305	306	16130	6811	7337	3.772	0.258
7-1/P-0.3/5	--	3096	--	17640	5552	6910	3.843	0.195
7-2/P-0.3/5	3015	3194	3022	17482	6494	7176	3.834	0.204
7-3/P-0.3/5	3112	3254	3109	18731	7608	7917	3.760	0.306
8-1/P-0.3/5	3084	3187	3068	17745	7163	7685	3.784	0.306
8-2/P-0.3/5	3055	3217	3034	17988	7779	8325	3.781	0.306
8-3/P-0.3/5	3083	3181	3076	18185	7899	8283	3.890	0.271
10-1/P-0.3/5	3024	3181	4552	18359	7073	7329	3.890	0.266
10-2/P-0.3/5	3038	3094	3021	18487	7330	7660	3.853	0.279

TABLE 2.1, Cont'd.

Specimen Number	Strain Rate (0-100%)	Strain Rate (5-20%)	Strain Rate (50-99%)	Maximum Stress	ε_p	ε_{pp}	E_i	ν_i
10-3/P-0.3/5	3040	3207	3032	16445	6134	6762	3.747	0.309
14-3/P-0.3/5	3076	3184	3073	17710	7044	7425	3.671	0.266
15-1/P-0.3/5	3054	3197	3063	18571	7330	7637	3.756	0.266
14-1/P-0.3/6	31731	40384	31495	21648	8415	8801	3.976	0.271
15-1/P-0.3/5	31592	40057	30522	22330	8726	8977	3.994	--
7-1/P-0.3/7	287630	195120	360876	24786	8374	9384	4.334	0.267
7-2/P-0.3/7	259182	168433	360129	21833	6918	7668	4.211	0.325
7-3/P-0.3/7	278496	168433	431680	22693	8183	8520	4.259	0.284
8-1/P-0.3/7	290770	177009	428237	24282	8713	8991	4.301	0.217
8-2/P-0.3/7	285411	175481	429028	23563	8507	8887	4.190	0.272
8-3/P-0.3/7	283045	180910	408260	22062	7825	8509	4.149	0.325
10-1/P-0.3/7	265476	173529	358630	21770	7270	8158	4.090	0.282
10-2/P-0.3/7	272434	172944	391223	21593	7482	7919	4.141	0.298
10-3/P-0.3/7	262494	166916	375834	20699	6713	7446	4.253	0.233
14-2/P-0.3/7	294385	184290	449625	24027	9097	9619	4.139	0.188
15-3/P-0.3/7	280758	177572	432261	24336	8482	9442	4.194	0.205

-- Data not obtained

TABLE 2.2
STRAIN RATE TEST DATA FOR CEMENT PASTE WITH W/C = 0.4

Specimen Number	Strain Rate (0-100%)	Strain Rate (5-20%)	Strain Rate (50-99%)	Maximum Stress	ε_p	ε_{pp}	E_i	ν_i
12-1/P-0.4/1	0.30	0.30	0.30	7376	11194	11528	2.257	--
13-1/P-0.4/1	0.30	0.30	0.30	7536	10212	11296	2.255	--
12-1/P-0.4/2	3.06	3.07	3.06	7774	7779	9090	2.499	0.220
13-1/P-0.4/2	3.03	3.00	3.03	7736	6234	7704	2.488	0.221
12-1/P-0.4/3	30.5	31.0	30.05	8430	6440	7060	2.601	0.207
13-1/P-0.4/3	30.4	30.6	30.4	8573	6314	6706	2.699	0.256
12-1/P-0.4/4	305	303.6	305	9771	6852	7406	2.722	0.273
13-1/P-0.4/4	303	293.7	303	9317	6136	6751	2.782	0.235
12-1/P-0.4/5	3074	3270	3048	10791	6892	7427	2.740	0.267
13-1/P-0.4/5	3069	3270	3034	10322	6110	6770	2.763	0.202
12-1/P-0.4/6	32365	38604	30965	11974	6169	7231	2.878	0.281
13-1/P-0.4/6	32131	38831	30829	11937	7024	7387	2.845	0.224
12-1/P-0.4/7	278903	160519	388509	13239	6327	7231	3.135	0.266
13-1/P-0.4/7	285916	162248	407777	13572	6738	7070	3.134	0.261

-- Data not obtained

TABLE 2.3
STRAIN RATE TEST DATA FOR CEMENT PASTE WITH W/C = 0.5

Specimen Number	Strain Rate (0-100%)	Strain Rate (5-20%)	Strain Rate (50-99%)	Maximum Stress	ε_p	ε_{pp}	E_i	ν_i
9-1/P-0.5/1	0.30	0.30	0.30	4969	6392	8620	1.794	--
11-1/P-0.5/1	0.30	0.30	0.30	5127	7656	7994	1.725	0.218
2-1/P-0.5/2	2.99	3.00	2.99	5907	6879	8535	1.958	--
2-2/P-0.5/2	2.99	3.04	2.99	6233	6925	8982	2.041	--
2-3/P-0.5/2	2.97	2.98	2.97	6325	6841	8120	2.006	--
3-1/P-0.5/2	3.00	3.00	3.00	5693	6164	8784	2.160	--
3-2/P-0.5/2	3.00	2.99	3.00	5569	5042	6999	2.122	--
3-3/P-0.5/2	3.01	3.06	3.01	5456	5679	7091	2.049	--
6-1/P-0.5/2	3.00	2.97	3.00	6258	6352	8441	2.091	--
6-2/P-0.5/2	2.99	3.00	2.99	5964	6323	7968	2.102	--
6-3/P-0.5/2	3.00	3.00	3.00	6229	6950	8716	2.124	0.241
9-1/P-0.5/2	3.03	3.00	3.03	5435	5016	6399	1.846	0.228
11-1/P-0.5/2	3.03	3.05	3.03	5784	7248	8639	1.883	0.196
9-1/P-0.5/3	30.3	30.68	30.3	6513	5884	6491	1.902	0.231
11-1/P-0.5/3	30.4	30.28	30.4	6589	5830	7003	1.969	0.217
9-1/P-0.5/4	303	299.8	303	6866	5619	6142	2.124	0.277
11-1/P-0.5/4	307	297.7	307	6928	5096	6236	2.104	--
2-1/P-0.5/5	3027	3333	2997	8011	6039	6775	2.297	--
2-2/P-0.5/5	3026	3204	2976	7912	5982	6812	2.327	--
2-3/P-0.5/5	3040	3319	2998	8673	6859	7416	2.428	--
3-1/P-0.5/5	3052	3428	3006	7412	4743	6500	2.292	--
3-2/P-0.5/5	3050	3430	2992	7526	4966	5943	2.410	--
3-3/P-0.5/5	3048	3280	2996	7550	5067	5767	2.316	--
6-1/P-0.5/5	3044	3339	3012	7943	5462	5764	2.412	--
6-2/P-0.5/5	3039	3321	2995	8259	6133	7065	2.399	--
6-3/P-0.5/5	3033	3299	3011	8321	5765	6613	2.438	--
9-1/P-0.5/5	3070	3270	2990	7681	4704	5808	2.266	0.246

TABLE 2.3, Cont'd.

Specimen Number	Strain Rate (0-100%)	Strain Rate (5-20%)	Strain Rate (50-99%)	Maximum Stress	ε_p	ε_{pp}	E_i	ν_i
11-1/P-0.5/6	3097	3406	3006	7375	5526	6230	2.141	0.288
9-1/P-0.5/7	32849	37990	31392	8304	5459	6535	2.326	0.238
11-1/P-0.5/7	32516	38014	31351	7882	4936	5410	2.252	0.285
2-1/P-0.5/7	287762	166730	388873	10005	6419	8048	2.625	--
2-2/P-0.5/7	284285	169109	382513	10809	6426	7138	2.779	--
2-3/P-0.5/7	282516	162918	378903	10502	6093	6719	2.754	--
3-1/P-0.5/7	284994	163590	386514	9269	5393	6301	2.661	--
3-2/P-0.5/7	282633	155739	411411	8904	5145	5586	2.726	--
3-3/P-0.5/7	291745	161264	398272	9558	5684	6105	2.739	--
6-1/P-0.5/7	288418	168563	405208	10180	6259	7210	2.700	--
6-2/P-0.5/7	290794	168063	396061	10330	6021	7661	2.778	--
6-3/P-0.5/7	291186	160059	392553	10216	6286	7277	2.717	--
9-1/P-0.5/7	259086	148290	371060	8896	4704	6038	2.547	--
11-1/P-0.5/7	288521	158504	397014	9307	6321	6961	2.428	--

-- Data not obtained

TABLE 2.4
STRAIN RATE TEST DATA FOR MORTAR WITH W/C = 0.3

Specimen Number	Strain Rate (0-100%)	Strain Rate (5-20%)	Strain Rate (50-99%)	Maximum Stress	ε_p	ε_{pp}	E_i	ν_i
18-1/M-0.3/1	0.30	0.30	0.30	9986	4801	5572	4.228	--
20-1/M-0.3/1	0.30	0.29	0.30	9676	5001	5572	3.457	--
18-1/M-0.3/2	3.04	2.96	3.04	10819	4212	4741	4.597	--
20-1/M-0.3/2	3.04	3.01	3.06	10864	4102	4609	4.508	0.207
18-1/M-0.3/3	30.3	30.7	30.2	12108	4108	4439	4.965	--
20-1/M-0.3/3	30.3	30.2	30.3	12538	4220	4512	4.846	0.235
18-1/M-0.3/4	277	303	302	13182	4147	4396	5.137	0.215
20-1/M-0.3/4	304	309	302	13606	4220	4489	5.003	0.257
18-1/M-0.3/5	3080	3544	3056	14381	4411	4832	4.911	0.207
20-1/M-0.3/5	3099	3817	3080	14715	4041	4335	5.105	0.269
18-1/M-0.3/6	33069	31862	32042	15891	4471	4762	5.671	0.246
20-1/M-0.3/6	31241	27599	30852	15499	4282	4701	5.239	0.273
18-1/M-0.3/7	256772	131968	458920	17565	4669	5380	5.464	0.254
20-1/M-0.3/7	272291	151996	453588	18044	4603	5372	5.886	0.274

-- Data not obtained

TABLE 2.5
STRAIN RATE TEST DATA FOR MORTAR A WITH W/C = 0.4

Specimen Number	Strain Rate (0-100%)	Strain Rate (5-20%)	Strain Rate (50-99%)	Maximum Stress	ε_p	ε_{pp}	E_i	ν_i
21-1/MA-0.4/1	0.31	0.30	0.30	7318	4193	5346	3.798	--
22-1/MA-0.4/1	0.31	0.30	0.30	7395	4072	5274	3.998	--
21-1/MA-0.4/2	3.00	2.97	2.99	7874	3640	4411	4.301	--
22-1/MA-0.4/2	3.06	3.04	3.06	7755	3784	4666	4.21	--
21-1/MA-0.4/3	30.7	30.7	30.7	8875	3495	4086	4.518	0.230
22-1/MA-0.4/3	30.5	30.5	30.5	8681	3060	3557	4.95	--
21-1/MA-0.4/3	30.6	30.0	30.6	8879	3454	3891	4.746	--
22-1/MA-0.4/4	305	300	305	9772	3469	3864	5.057	0.239
21-1/MA-0.4/4	306	286	306	9404	3534	4017	4.899	0.273
22-1/MA-0.4/5	3122	3915	3051	10578	3296	3885	5.253	0.269
21-1/MA-0.4/5	2954	4026	3110	10218	3745	4204	4.623	--
22-1/MA-0.4/6	32813	26650	32326	11426	3588	4034	5.241	0.274
21-1/MA-0.4/6	31712	25620	31225	11130	3854	4426	4.959	0.272
22-1/MA-0.4/7	260791	123381	498269	12703	3422	3905	6.084	--
21-1/MA-0.4/7	270363	132542	562143	12513	3579	4508	5.673	0.270
22-1/MA-0.4/7	271971	123819	502855	12426	3858	4480	5.694	0.291

-- Data not obtained

TABLE 2.6
STRAIN RATE TEST DATA FOR MORTAR B WITH W/C = 0.4

Specimen Number	Strain Rate (0-100%)	Strain Rate (5-20%)	Strain Rate (50-99%)	Maximum Stress	ε_p	ε_{pp}	E_i	ν_i
23-1/MB-0.4/1	0.31	0.30	0.30	7566	4045	4958	3.888	--
23-1/MB-0.4/2	3.03	3.02	3.01	7974	3000	3721	5.018	0.201
23-2/MB-0.4/2	3.02	3.08	3.04	8106	3244	4017	4.511	0.255
23-3/MB-0.4/2	3.06	3.04	3.06	8287	3389	3957	4.626	--
24-1/MB-0.4/2	3.06	2.97	3.06	7806	3296	4093	4.405	--
24-2/MB-0.4/2	3.01	2.92	3.00	7939	3430	4174	4.529	--
23-1/MB-0.4/3	30.5	29.8	30.5	8703	3210	3736	4.923	0.228
24-1/MB-0.4/3	30.6	30.6	30.3	8818	3191	3606	4.778	0.271
23-1/MB-0.4/4	305	300	304	9812	3389	3864	5.063	0.270
24-1/MB-0.4/4	303	293	302	9637	3145	3595	5.326	--
23-1/MB-0.4/5	3133	3915	3063	10456	3033	3519	5.459	0.283
24-1/MB-0.4/5	3089	3915	3031	10560	3251	3666	5.441	0.272
23-1/MB-0.4/6	31371	29238	30142	11440	3298	3737	5.883	--
24-1/MB-0.4/6	31848	24563	32788	11581	3482	4007	5.395	0.273
24-2/MB-0.4/6	33815	33095	32146	11524	3415	3973	5.788	--
23-1/MB-0.4/7	267985	123256	527860	12934	3713	4487	5.930	--
24-1/MB-0.4/7	260414	124233	496908	12507	3422	3980	5.978	--

-- Data not obtained

TABLE 2.7
STRAIN RATE TEST DATA FOR MORTAR A WITH W/C = 0.5

Specimen Number	Strain Rate (0-100%)	Strain Rate (5-20%)	Strain Rate (50-99%)	Maximum Stress	ε_p	ε_{pp}	E_i	ν_i
16-1/MA-0.5/1	0.31	0.31	0.31	5472	3024	4693	3.725	--
17-1/MA-0.5/1	0.31	0.29	0.31	5329	3410	4940	3.467	--
19-1/MA-0.5/1	0.31	0.31	0.31	5337	4075	5693	3.277	--
16-1/MA-0.5/2	3.03	2.90	3.02	5657	2743	3713	4.001	0.194
17-1/MA-0.5/2	3.06	2.99	3.07	5719	2973	3966	3.768	0.186
19-1/MA-0.5/2	3.05	2.97	3.05	5852	3151	4111	3.847	--
1-1/MA-0.5/2	3.01	2.99	3.01	5006	2725	3623	4.155	--
1-2/MA-0.5/2	2.98	2.85	2.98	5019	2399	3277	4.029	--
1-3/MA-0.5/2	3.00	2.95	3.00	5394	2654	3502	4.124	--
5-1/MA-0.5/2	3.00	3.14	3.00	5810	2925	4025	4.063	--
5-2/MA-0.5/2	3.00	3.08	3.00	5778	2919	4025	3.825	--
5-3/MA-0.5/2	3.00	3.04	3.00	5725	2916	3964	3.903	--
4-1/MA-0.5/2	3.00	3.01	3.00	5729	2715	3690	4.028	--
4-2/MA-0.5/2	3.00	2.84	3.00	5579	2934	3838	4.356	--
4-3/MA-0.5/2	3.00	2.96	3.00	5714	2875	3763	4.188	--
19-1/MA-0.5/3	30.3	29.8	30.4	6278	2823	3305	4.022	--
17-1/MA-0.5/3	30.5	30.3	303.6	6373	2841	3367	4.274	0.179
16-1/MA-0.5/3	30.5	30.1	30.5	6570	3060	3943	4.146	0.241
16-1/MA-0.5/4	307	292	303	6991	2955	3517	4.499	0.249
17-1/MA-0.5/4	307	294	305	7143	2888	3425	4.552	0.186
19-1/MA-0.5/4	308	294	306	7135	3000	3709	4.633	--
16-1/MA-0.5/5	3105	4242	3017	7437	2994	3655	4.293	0.223
16-2/MA-0.5/5	3125	4242	3044	7624	3013	3538	4.622	--
17-1/MA-0.5/5	3140	4373	3054	7647	2795	3430	4.471	0.231
19-1/MA-0.5/5	3126	4242	3045	7886	3166	3669	4.662	--
5-1/MA-0.5/5	3087	3642	3028	7472	2840	3374	4.880	--
5-2/MA-0.5/5	3059	3678	3001	7537	2973	3484	4.533	--

TABLE 2.7, Cont'd.

Specimen Number	Strain Rate (0-100%)	Strain Rate (5-20%)	Strain Rate (50-99%)	Maximum Stress	ε_p	ε_{pp}	E_i	ν_i
5-3/MA-0.5/5	3079	4427	3006	7529	3054	3652	4.565	--
4-1/MA-0.5/5	3086	4178	3005	7309	2878	3322	4.611	--
4-2/MA-0.5/5	3070	4414	3026	7361	3045	3506	4.482	--
4-3/MA-0.5/5	3079	4404	3004	7560	2931	3510	4.804	--
1-1/MA-0.5/5	3056	4406	3001	7007	2442	3015	4.476	--
1-2/MA-0.5/5	3054	4288	2976	6842	2755	3469	4.613	--
16-2/MA-0.5/6	34611	28288	34352	9027	3059	3599	5.171	0.294
17-1/MA-0.5/6	34407	27733	33659	8997	3034	3616	5.156	0.241
19-1/MA-0.5/6	34918	26439	34201	8448	3311	3851	4.823	--
16-2/MA-0.5/7	210039	96038	402184	10956	2981	3539	5.921	--
17-1/MA-0.5/7	221155	94908	439024	9298	2961	3710	5.381	--
19-1/MA-0.5/7	265349	113595	520369	10046	3093	3969	5.642	--
5-1/MA-0.5/7	222538	107761	447276	9451	3027	3671	5.229	--
5-2/MA-0.5/7	217052	93276	442502	9218	2889	3599	5.536	--
5-3/MA-0.5/7	216740	93156	451043	9499	2875	3633	5.415	--
4-1/MA-0.5/7	213997	93568	435711	9307	2769	3442	5.455	--
4-2/MA-0.5/7	211198	95341	430441	9266	2800	3316	5.386	--
4-3/MA-0.5/7	215491	92565	441618	9163	2771	3500	5.310	--
1-1/MA-0.5/7	228904	96381	439352	9067	2674	3388	5.329	--
1-2/MA-0.5/7	211174	93415	417711	8912	2703	3358	5.479	--
1-3/MA-0.5/7	203097	97502	393794	8514	2525	3171	5.330	--

-- Data not obtained

TABLE 2.8
STRAIN RATE TEST DATA FOR MORTAR B WITH W/C = 0.5

Specimen Number	Strain Rate (0-100%)	Strain Rate (5-20%)	Strain Rate (50-99%)	Maximum Stress	ε_p	ε_{pp}	E_i	ν_i
25-1/MB-0.5/1	0.30	0.31	0.30	5761	4284	6178	2.838	--
26-1/MB-0.5/1	0.30	0.30	0.30	5663	4284	6183	3.203	--
25-1/MB-0.5/2	3.04	2.98	3.04	6187	3659	4555	3.435	0.176
25-2/MB-0.5/2	3.03	2.94	3.04	6285	4134	5085	3.312	0.185
25-3/MB-0.5/2	3.03	2.92	3.03	5947	3566	4540	3.573	--
26-1/MB-0.5/2	3.05	2.97	3.04	6361	3653	4851	3.602	0.215
26-2/MB-0.5/2	3.02	3.00	3.02	6238	3711	4792	3.579	0.220
25-1/MB-0.5/3	30.3	29.8	30.4	6573	3653	4241	3.658	--
26-1/MB-0.5/3	30.3	29.8	30.2	6680	3599	4264	3.721	0.224
25-1/MB-0.5/4	305	302	303	7285	3752	4161	3.802	0.180
26-1/MB-0.5/4	304	293	302	7309	3522	4077	4.045	0.282
25-1/MB-0.5/5	3083	3539	3062	7727	3640	4251	3.849	0.224
26-1/MB-0.5/5	3074	3621	3014	8088	3719	4342	4.055	0.239
25-1/MB-0.5/6	31556	34800	29944	8137	3869	4708	3.914	0.274
26-1/MB-0.5/6	33718	33635	32019	8409	3931	4542	3.515	0.228
25-1/MB-0.5/7	285361	129288	535849	9711	3666	4321	4.710	0.261
26-1/MB-0.5/7	302289	145617	529640	10370	3732	4460	5.071	0.272

-- Data not obtained

TABLE 2.9
SUMMARY OF STRAIN-RATE TESTS

Strain Rate (0-100%) με/sec Average (Std Dev)	Strain Rate (5-20%) με/sec Average (Std Dev)	Strain Rate (50-99%) με/sec Average (Std Dev)	No. of Samples (No. of Samples for ν_i)	Maximum Stress psi Average (Std Dev)	ε_p με Average (Std Dev)	ε_{pp} με Average (Std Dev)	E_i psi x 10^6 Average (Std Dev)	ν_i Average (Std Dev)
				CEMENT PASTE, W/C = 0.3				
0.30 (0)	0.30 (0)	0.30 (0)	2 (2)	11675 (675)	9358 (2858)	11151 (2160)	2.94 (0.25)	-- --
3.02 (0.02)	3.01 (0.032)	3.02 (0.02)	11 (10)	12534 (464)	7450 (752)	7940 (796)	3.396 (0.077)	0.212 (0.035)
30.4 (0.05)	30.3 (0.2)	30.3 (0)	2 (2)	14061 (326)	7326 (755)	7949 (820)	3.406 (0.073)	0.240 (0.016)
305 (1.00)	303 (3)	308 (2)	2 (2)	15804 (326)	7036 (225)	7350 (18)	3.649 (0.10)	0.247 (0.011)
3052 (32.4)	3181 (48.6)	3186 (432)	11 (11)	17940 (617)	7037 (716)	7556 (505)	3.792 (0.064)	0.270 (0.038)
31662 (70)	40221 (163)	31009 (486)	2 (2)	21989 (342)	8571 (220)	8889 (124)	3.985 (0.013)	0.271 (0)
278156 (11239)	176421 (7820)	402344 (32540)	11 (11)	22876 (1313)	7960 (776)	8595 (740)	4.206 (0.075)	0.262 (0.045)

-- Data not obtained

TABLE 2.9, continued
SUMMARY OF STRAIN-RATE TESTS

Strain Rate (0-100%) με/sec Average (Std Dev)	Strain Rate (5-20%) με/sec Average (Std Dev)	Strain Rate (50-99%) με/sec Average (Std Dev)	No. of Samples (No. of Samples for ν_i)	Maximum Stress psi Average (Std Dev)	ε_p με Average (Std Dev)	ε_{pp} με Average (Std Dev)	E_i psi$\times 10^6$ Average (Std Dev)	ν_i Average (Std Dev)
				CEMENT PASTE, W/C = 0.4				
0.30 (0)	0.30 (0)	0.30 (0)	2 (2)	7456 (80)	10703 (491)	11412 (116)	2.256 (0.001)	0.218 (0.024)
3.05 (0.02)	3.04 (0.05)	3.05 (0.02)	2 (4)	7755 (19)	7007 (772)	8047 (1043)	2.494 (0.005)	0.227 (0.019)
30.5 (0.05)	30.8 (0.2)	30.5 (0.05)	2 (4)	8502 (71)	6377 (63)	6883 (177)	2.65 (0.049)	0.245 (0.025)
304 (1)	298.6 (4.9)	304 (1.4)	2 (4)	9544 (227)	6494 (358)	7079 (327)	2.777 (0.005)	0.256 (0.033)
3072 (2)	3270 (0)	3041 (7)	2 (4)	10557 (235)	6501 (391)	7099 (328)	2.752 (0.016)	0.247 (0.029)
32248 (117)	38718 (113)	30897 (68)	2 (4)	11956 (19)	6597 (427)	7309 (78)	2.862 0.016)	0.269 (0.028)
282410 (3515)	161384 (864)	398143 (9634)	2 (4)	13406 (106)	6533 (205)	7151 (81)	3.135 (0.001)	0.273 (0.019)

TABLE 2.9, continued
SUMMARY OF STRAIN-RATE TESTS

Strain Rate (0-100%) με/sec Average (Std Dev)	Strain Rate (5-20%) με/sec Average (Std Dev)	Strain Rate (50-99%) με/sec Average (Std Dev)	No. of Samples (No. of Samples for ν_i)	Maximum Stress psi Average (Std Dev)	ε_p με Average (Std Dev)	ε_{pp} με Average (Std Dev)	E_i psi x 10^6 Average (Std Dev)	ν_i Average (Std Dev)
				CEMENT PASTE, W/C = 0.5				
0.30 (0)	0.31 (0)	0.30 (0)	2 (3)	5048 (79)	7024 (632)	8307 (313)	1.760 (0.034)	0.218 (0.0)
3.0 (0.02)	3.01 (0.029)	3.0 (0.02)	11 (3)	5896 (318)	6311 (737)	8061 (817)	2.035 (0.097)	0.234 (0.007)
30.4 (0.05)	30.5 (0.20)	30.4 (0.05)	2 (2)	6551 (38)	5857 (27)	6747 (256)	1.935 (0.032)	0.214 (0.017)
305 (2)	298.8 (1)	305 (2)	2 (1)	6897 (31)	5358 (262)	6189 (41)	2.114 (0.010)	0.247 (0.030)
3048 (20)	3330 (66.7)	3007 (21.9)	11 (2)	7878 (398)	5568 (638)	6427 (541)	2.339 (0.086)	0.267 (0.021)
32863 (167)	38002 (12)	31160 (191)	2 (2)	8093 (211)	5198 (261)	6119 (416)	2.289 (0.037)	0.261 (0.024)
284722 (8700)	162043 (6064)	391875 (10801)	11 (0)	9816 (629)	5886 (552)	6822 (715)	2.678 (0.103)	0.281 (0.012)

TABLE 2.9, continued
SUMMARY OF STRAIN-RATE TESTS

Strain Rate (0-100%) με/sec Average (Std Dev)	Strain Rate (5-20%) με/sec Average (Std Dev)	Strain Rate (50-99%) με/sec Average (Std Dev)	No. of Samples (No. of Samples for ν_i)	Maximum Stress psi Average (Std Dev)	ε_p με Average (Std Dev)	ε_{pp} με Average (Std Dev)	E_i psi$\times 10^6$ Average (Std Dev)	ν_i Average (Std Dev)
				MORTAR, W/C = 0.3, S/C = 0.97				
0.30 (0)	0.30 (0.005)	0.30 (0)	2 (0)	9831 (155)	4901 (100)	5572 (0)	3.843 (0.386)	-- --
3.04 (0)	2.99 (0.03)	3.05 (0.01)	2 (1)	10841 (23)	4157 (55)	4675 (66)	4.553 (0.045)	0.207 (0.0)
30.3 (0)	30.5 (0.025)	30.3 (0.5)	2 (2)	12323 (215)	4164 (56)	4475 (37)	4.906 (0.059)	0.235 (0.0)
291 (13)	306 (3)	302 (0)	2 (2)	13394 (212)	4183 (37)	4442 (47)	5.070 (0.067)	0.236 (0.021)
3090 (10)	3681 (136)	3068 (12)	2 (2)	14548 (167)	4226 (185)	4584 (248)	5.008 (0.097)	0.238 (0.031)
32155 (914)	29730 (2132)	31447 (595)	2 (2)	15695 (196)	4377 (94)	4732 (30)	5.955 (0.716)	0.260 (0.014)
264352 (7939)	141982 (10014)	465254 (2666)	2 (2)	17804 (240)	4636 (33)	5376 (4)	5.675 (0.211)	0.274 (0.020)

-- Data not obtained

TABLE 2.9, continued
SUMMARY OF STRAIN-RATE TESTS

Strain Rate (0-100%) με/sec Average (Std Dev)	Strain Rate (5-20%) με/sec Average (Std Dev)	Strain Rate (50-99%) με/sec Average (Std Dev)	No. of Samples (No. of Samples for ν_i)	Maximum Stress psi Average (Std Dev)	$\varepsilon_{\mu\varepsilon}^{p}$ Average (Std Dev)	$\varepsilon_{\mu\varepsilon}^{pp}$ Average (Std Dev)	E_i psi$\times 10^6$ Average (Std Dev)	ν_i Average (Std Dev)
MORTAR-A, W/C = 0.4, S/C = 1.59								
0.31 (0)	0.30 (0)	0.30 (0)	2 (0)	7356 (39)	4132 (61)	5310 (36)	3.898 (0.10)	-- --
3.03 (0.03)	3.01 (0.38)	3.03 (0.04)	2 (0)	7814 (60)	3712 (72)	4538 (128)	4.256 (0.046)	-- --
30.6 (0.5)	30.4 (0.38)	30.6 (0.01)	2 (1)	8812 (92)	3336 (196)	3845 (219)	4.738 (0.176)	0.205 (0.0)
306 (.5)	293 (7)	306 (0.1)	2 (2)	9588 (184)	3502 (32)	3940 (77)	4.978 (0.079)	0.256 (0.017)
3038 (84)	3970 (56)	3080 (30)	2 (1)	10398 (180)	3520 (225)	4044 (160)	4.938 (0.315)	0.269 (0.001)
32262 (551)	26135 (515)	31776 (551)	2 (2)	11278 (148)	3721 (133)	4230 (196)	5.100 (0.141)	0.273 (0.001)
267708 (4935)	126581 (4219)	521089 (29090)	3 (2)	12547 (116)	3620 (180)	4298 (278)	5.817 (0.189)	0.281 (0.011)

-- Data not obtained

TABLE 2.9, continued
SUMMARY OF STRAIN-RATE TESTS

Strain Rate (0-100%) με/sec Average (Std Dev)	Strain Rate (5-20%) με/sec Average (Std Dev)	Strain Rate (50-99%) με/sec Average (Std Dev)	No. of Samples (No. of Samples for ν_i)	Maximum Stress psi Average (Std Dev)	ε_p με Average (Std Dev)	ε_{pp} με Average (Std Dev)	E_i psi$\times 10^6$ Average (Std Dev)	ν_i Average (Std Dev)
			MORTAR-B, W/C = 0.4, S/C = 1.97					
0.31	0.30	0.30	1 (0)	7566	4045	4958	3.888	--
3.04 (0.02)	3.01 (0.05)	3.03 (0.027)	5 (2)	8002 (178)	3272 (151)	3992 (154)	4.618 (0.212)	0.228 (0.027)
30.6 (0.05)	30.2 (0.4)	30.4 (0.1)	2 (2)	8760 (57)	3200 (10)	3671 (65)	4.851 (0.073)	0.249 (0.022)
304 (1)	297 (3.5)	303 (1)	2 (1)	9724 (87)	3267 (122)	3730 (134)	5.195 (0.132)	0.270 (0.0)
3111 (22)	3915 (0)	3047 (16)	2 (2)	10508 (52)	3142 (109)	3592 (104)	5.450 (0.009)	0.278 (0.006)
32345 (1057)	28965 (3489)	31692 (1127)	3 (1)	11515 (58)	3398 (76)	3906 (147)	5.689 (0.211)	0.273 (0.0)
264199 (3785)	123744 (489)	512384 (15476)	2 (0)	12720 (213)	3568 (146)	4234 (359)	5.954 (0.024)	--

-- Data not obtained

TABLE 2.9, continued
SUMMARY OF STRAIN-RATE TESTS

Strain Rate (0-100%) με/sec Average (Std Dev)	Strain Rate (5-20%) με/sec Average (Std Dev)	Strain Rate (50-99%) με/sec Average (Std Dev)	No. of Samples (No. of Samples for ν_i)	Maximum Stress psi Average (Std Dev)	ε_p με Average (Std Dev)	ε_{pp} με Average (Std Dev)	E_i psi$\times 10^6$ Average (Std Dev)	ν_i Average (Std Dev)
			MORTAR-A, W/C = 0.5, S/C = 2.28					
0.31	0.30	0.31	3 (0)	5379 (65)	3503 (434)	4909 (165)	3.490 (0.184)	--
3.01 (0.02)	2.98 (0.09)	3.01 (0.03)	12 (2)	5582 (279)	2827 (185)	3791 (236)	4.024 (0.163)	0.190 (0.004)
30.4 (0.08)	30.1 (0.24)	30.5 (0.08)	3 (2)	6407 (122)	2908 (108)	3538 (287)	4.147 (0.103)	0.210 (0.031)
307 (0.81)	293 (1)	305 (1.63)	3 (2)	7090 (70)	2948 (46)	3550 (118)	4.561 (0.055)	0.218 (0.031)
3089 (28)	4211 (259)	3017 (22)	12 (2)	7434 (270)	2907 (180)	3469 (171)	4.584 (0.149)	0.227 0.004
34645 (210)	27487 (775)	34071 (297)	3 (2)	8824 (266)	3135 (125)	3689 (115)	5.050 (0.161)	0.248 (0.0)
219728 (15162)	97292 (6318)	438418 (29980)	12 (0)	9391 (585)	2839 (156)	3525 (203)	5.451 (0.177)	--

-- Data not obtained

TABLE 2.9, continued
SUMMARY OF STRAIN-RATE TESTS

Strain Rate (0-100%) με/sec Average (Std Dev)	Strain Rate (5-20%) με/sec Average (Std Dev)	Strain Rate (50-99%) με/sec Average (Std Dev)	No. of Samples (No. of Samples for ν_i)	Maximum Stress psi Average (Std Dev)	ε_p με Average (Std Dev)	ε_{pp} με Average (Std Dev)	E_i psi$\times 10^6$ Average (Std Dev)	ν_i Average (Std Dev)
			MORTAR-B, W/C = 0.5, S/C = 1.29					
0.30 (0)	0.31 (0.1)	0.30 (0)	2 (0)	5712 (49)	4284 (0)	6180 (3)	3.020 (0.258)	--
3.03 (0.01)	2.96 (0.03)	3.03 (0.01)	5 (4)	6240 (140)	3745 (200)	4765 (203)	3.500 (0.111)	0.199 (0.019)
30.3 (0)	29.8 (0)	30.3 (0.1)	2 (1)	6626 (54)	3626 (27)	4252 (12)	3.690 (0.031)	0.224 (0.0)
304 (0.5)	298 (5)	302 (0.5)	2 (2)	7297 (12)	3637 (115)	4119 (42)	3.923 (0.121)	0.231 (0.051)
3078 (5)	3580 (41)	3038 (24)	2 (2)	7908 (80)	3680 (39)	4296 (46)	3.952 (0.1103	0.232 (0.008)
32637 (1081)	34218 (582)	30982 (1037)	2 (2)	8273 (136)	3900 (31)	4625 (83)	3.714 (0.200)	0.251 (0.023)
293825 (8464)	137452 (8165)	532744 (3105)	2 (2)	10040 (330)	3699 (33)	4390 (70)	4.891 (0.181)	0.267 (0.006)

-- Data not obtained

TABLE 2.10
AVERAGE POISSON'S RATIO AT VARIOUS STRAIN LEVELS
AND STRAIN RATES FOR CEMENT PASTE WITH W/C = 0.3

Strain Level με	0.3 με/sec	3 με/sec	30 με/sec	300 με/sec	3,000 με/sec	30,000 με/sec	300,000 με/sec
1000	0.141	0.210	0.230	0.259	0.286	0.253	0.262
2000	0.147	0.221	0.230	0.273	0.291	0.253	0.277
3000	0.157	0.238	0.230	0.282	0.297	0.253	0.294
4000	0.164	0.255	0.239	0.300	0.308	0.253	0.316
5000	0.163	0.270	0.253	0.317	0.326	0.260	0.327
6000	0.162	0.287	0.265	0.343	0.349	0.273	0.350

TABLE 2.11
AVERAGE POISSON'S RATIO AT VARIOUS STRAIN LEVELS
AND STRAIN RATES FOR CEMENT PASTE WITH W/C = 0.4

Strain Level με	0.3 με/sec	3 με/sec	30 με/sec	300 με/sec	3,000 με/sec	30,000 με/sec	300,000 με/sec
1000	0.187	0.232	0.255	0.271	0.278	0.282	0.303
2000	0.187	0.240	0.262	0.278	0.287	0.290	0.313
3000	0.182	0.249	0.273	0.283	0.297	0.304	0.327
4000	0.178	0.254	0.288	0.296	0.317	0.318	0.343
5000	0.176	0.265	0.294	0.324	0.345	0.334	0.365
6000	0.180	0.280	0.360	0.381	0.382	0.358	0.384

TABLE 2.12
AVERAGE POISSON'S RATIO AT VARIOUS STRAIN LEVELS
AND STRAIN RATES FOR CEMENT PASTE WITH W/C = 0.5

Strain Level με	0.3 με/sec	3 με/sec	30 με/sec	300 με/sec	3,000 με/sec	30,000 με/sec	300,000 με/sec
1000	0.191	0.214	0.207	0.236	0.263	0.274	0.294
2000	0.188	0.202	0.207	0.236	0.283	0.293	0.316
3000	0.192	0.195	0.208	0.245	0.304	0.317	0.335
4000	0.197	0.203	0.217	0.268	0.320	0.339	0.367
5000	0.205	0.214	0.231	0.278	0.344	0.361	0.393

TABLE 2.13
AVERAGE POISSON'S RATIO AT VARIOUS STRAIN LEVELS
AND STRAIN RATES FOR MORTAR WITH W/C = 0.3

Strain Level με	3 με/sec	30 με/sec	300 με/sec	3,000 με/sec	30,000 με/sec	300,000 με/sec
500	0.196	0.230	0.253	0.230	0.258	0.270
1000	0.190	0.242	0.253	0.230	0.265	0.277
1500	0.200	0.264	0.261	0.238	0.277	0.300
2000	0.213	0.282	0.282	0.253	0.288	0.311
2500	0.226	0.300	0.304	0.277	0.304	0.323
3000	0.246	0.322	0.342	0.300	0.334	0.342
3500	0.263	0.359	0.392	0.320	0.365	0.356
4000	0.300	0.406	0.455	0.366	0.409	0.363

TABLE 2.14
AVERAGE POISSON'S RATIO AT VARIOUS STRAIN LEVELS
AND STRAIN RATES FOR MORTAR A WITH W/C = 0.4

Strain Level με	3 με/sec	30 με/sec	300 με/sec	3,000 με/sec	30,000 με/sec	300,000 με/sec
500	0.196	0.230	0.253	0.230	0.258	0.270
1000	0.190	0.242	0.253	0.230	0.265	0.277
1500	0.200	0.264	0.261	0.238	0.277	0.300
2000	0.213	0.282	0.282	0.253	0.288	0.311
2500	0.226	0.300	0.304	0.277	0.304	0.323
3000	0.246	0.322	0.342	0.300	0.334	0.342
3500	0.263	0.359	0.392	0.320	0.365	0.356
4000	0.300	0.406	0.455	0.366	0.409	0.363

TABLE 2.15
AVERAGE POISSON'S RATIO AT VARIOUS STRAIN LEVELS
AND STRAIN RATES FOR MORTAR B WITH W/C = 0.4

Strain Level με	3 με/sec	30 με/sec	300 με/sec	3,000 με/sec	30,000 με/sec
500	0.230	0.230	0.253	0.243	0.265
1000	0.242	0.230	0.276	0.241	0.271
1500	0.253	0.264	0.242	0.277	0.277
2000	0.282	0.279	0.323	0.317	0.294
2500	0.327	0.313	0.359	0.382	0.341
3000	0.401	0.365	0.426	0.492	0.422

TABLE 2.16
AVERAGE POISSON'S RATIO AT VARIOUS STRAIN LEVELS
AND STRAIN RATES FOR MORTAR A WITH W/C = 0.5

Strain Level με	3 με/sec	30 με/sec	300 με/sec	3,000 με/sec	30,000 με/sec
500	0.180	0.207	0.219	0.242	0.253
1000	0.190	0.225	0.230	0.265	0.276
1500	0.222	0.257	0.253	0.300	0.303
2000	0.271	0.282	0.253	0.340	0.351
2500	0.336	0.346	0.364	0.396	0.419

TABLE 2.17
AVERAGE POISSON'S RATIO AT VARIOUS STRAIN LEVELS
AND STRAIN RATES FOR MORTAR B WITH W/C = 0.5

Strain Level με	3 με/sec	30 με/sec	300 με/sec	3,000 με/sec	30,000 με/sec
500	0.219	0.230	0.242	0.253	0.253
1000	0.219	0.230	0.253	0.264	0.253
1500	0.232	0.245	0.288	0.276	0.261
2000	0.259	0.274	0.317	0.311	0.288
2500	0.293	0.299	0.341	0.327	0.313

TABLE 2.18
INITIAL POISSON'S RATIO FOR SPECIMENS TESTED EXCLUSIVELY FOR THE STRAIN-RATE SENSITIVITY OF THE POISSON'S RATIO

CEMENT PASTE WITH W/C = 0.4

Specimen Number	Strain Rate (0-100%)	Strain Rate (5-20%)	Strain Rate (5-99%)	ν_i
29-1/P-0.4/1	0.31	0.31	0.31	0.241
28-1/P-0.4/1	0.30	0.30	0.30	0.194
29-1/P-0.4/2	3.0	3.0	3.0	0.209
28-1/P-0.4/2	3.1	3.1	3.1	0.227
29-1/P-0.4/3	30.6	30.7	30.7	0.276
28-1/P-0.4/3	30.6	30.4	30.5	0.241
29-1/P-0.4/4	305	305	306	0.300
28-1/P-0.4/4	306	308	307	0.214
28-1/P-0.4/5	3023	3230	3000	0.278
29-1/P-0.4/5	3165	3221	3093	0.242
29-1/P-0.4/6	31646	34984	30395	0.298
28-1/P-0.4/6	32022	35438	31115	0.275
29-1/P-0.4/7	252527	104595	411818	0.260
28-1/P-0.4/7	349473	108261	407700	0.307
CEMENT PASTE WITH W/C = 0.5				
27-1/P-0.5/1	0.30	0.30	0.30	0.262
27-1/P-0.5/7	0.31	0.31	0.31	0.242

TABLE 3.1

Normalized K_f^* Versus Strain Rate at Various Strains

Strain Rate με/sec	Strain = 0.001		Strain = 0.002		Strain = 0.005		Strain = 0.010	
	Norm. K_f^* at $\psi = 45°$	Norm. K_f^* at $\psi = 90°$	Norm. K_f^* at $\psi = 45°$	Norm. K_f^* at $\psi = 90°$	Norm. K_f^* at $\psi = 45°$	Norm. K_f^* at $\psi = 90°$	Norm. K_f^* at $\psi = 45°$	Norm. K_f^* at $\psi = 90°$
1	1.0008	1.0016	1.0007	1.0015	1.0007	1.0015	1.0007	1.0015
4	1.0025	1.0050	1.0032	1.0065	1.0030	1.0061	1.0029	1.0059
10	1.0025	1.0049	1.0052	1.0105	1.0079	1.0160	1.0076	1.0155
40	1.0011	1.0023	1.0036	1.0072	1.0126	1.0257	1.0235	1.0485
100	1.0005	1.0011	1.0019	1.0038	1.0089	1.0181	1.0235	1.0485
400	1.0001	1.0003	1.0006	1.0011	1.0032	1.0064	1.0111	1.0226
1000	1.0001	1.0001	1.0002	1.0005	1.0014	1.0028	1.0052	1.0105
4000	1.0000	1.0000	1.0001	1.0001	1.0004	1.0007	1.0014	1.0028

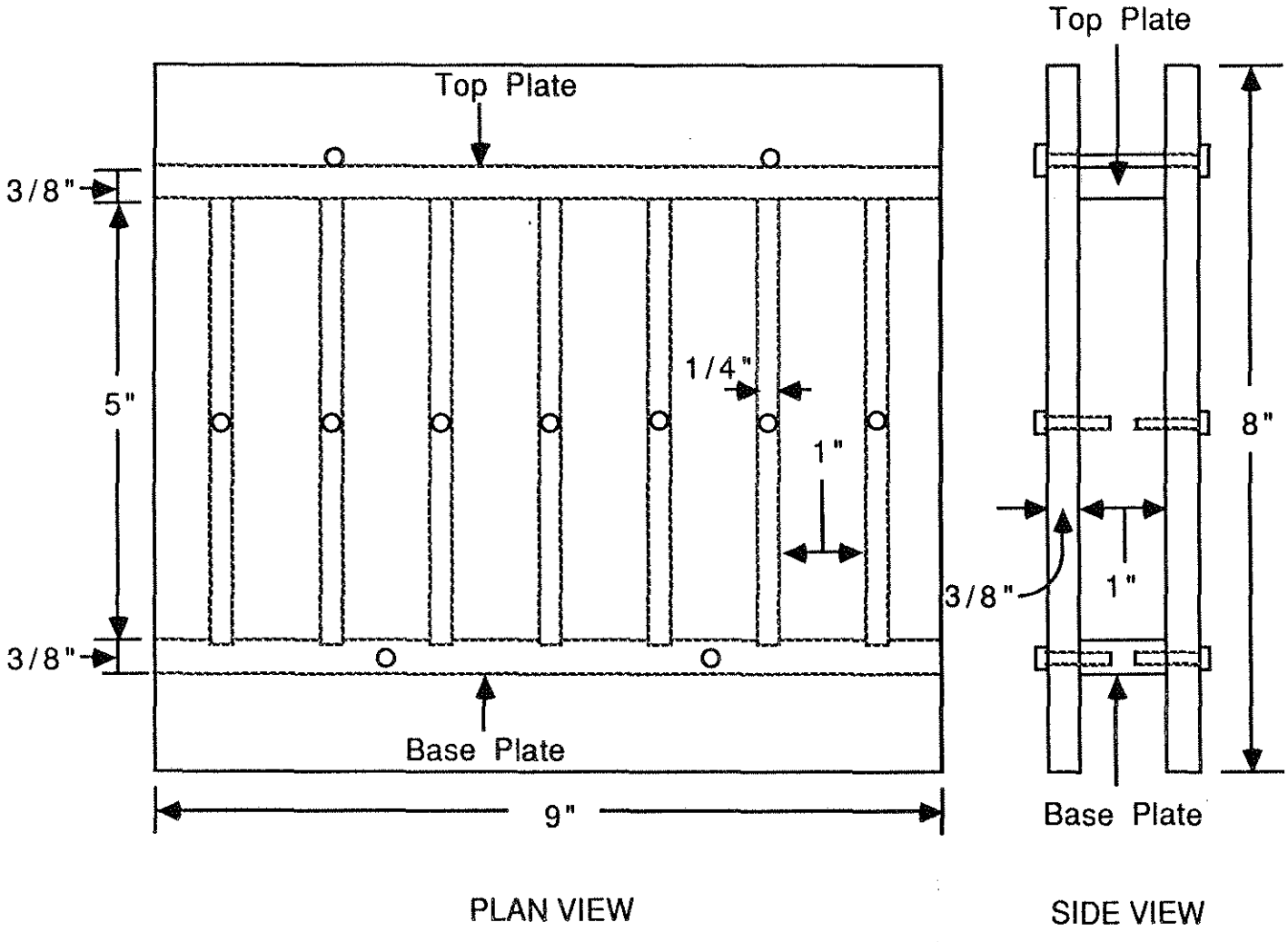

Fig. 2.1 Steel Mold

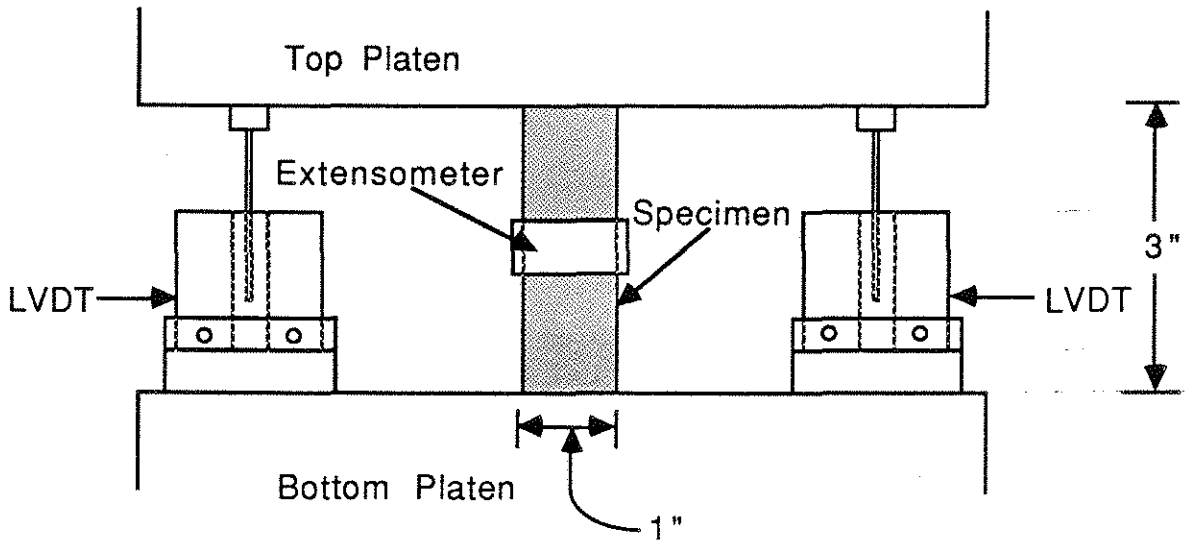

Fig. 2.2 Schematic of the Test Set Up

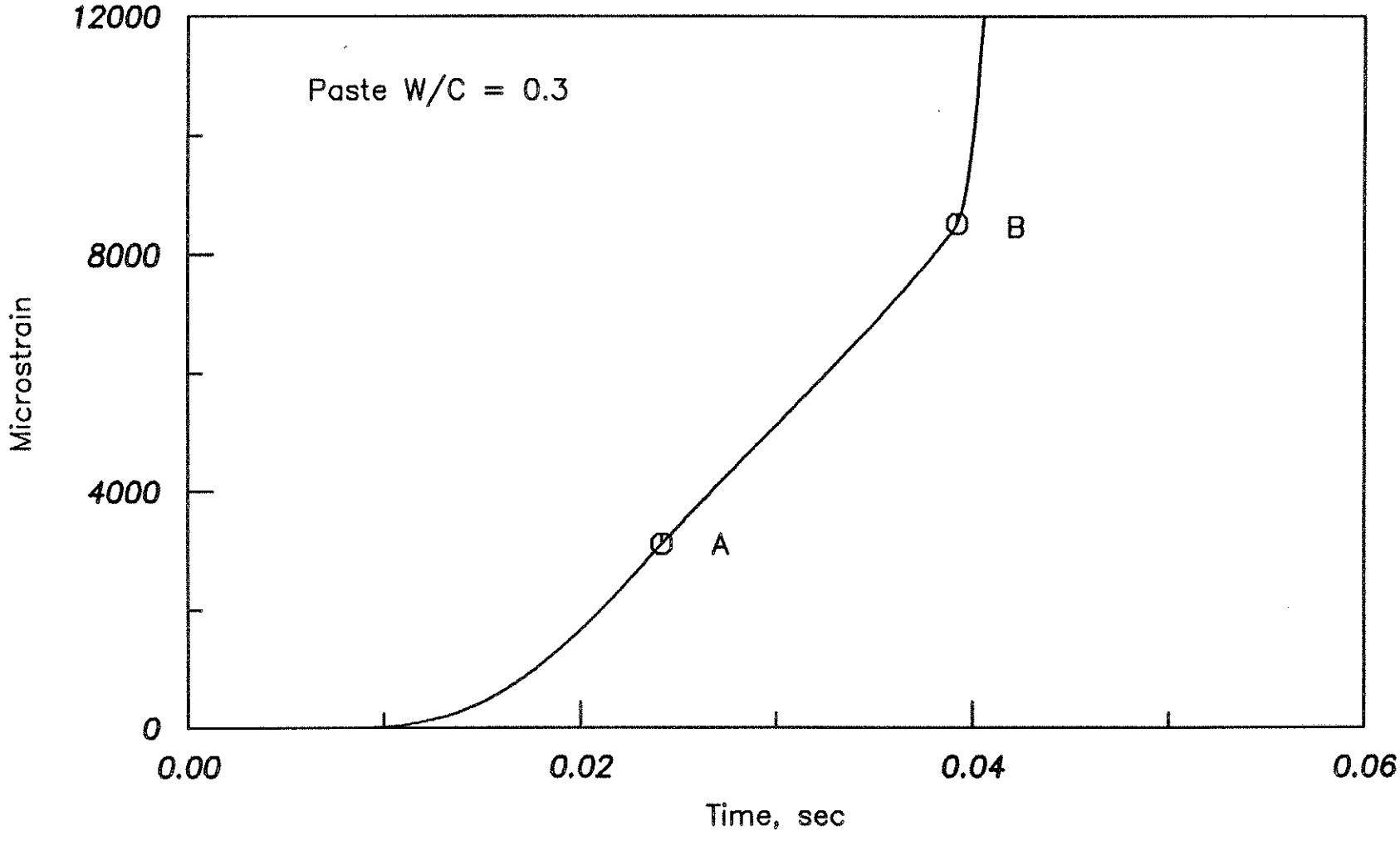

Fig. 2.3 Strain versus Time Relation for Cement Paste Tested at 300,000 Microstrain/sec. Point A Corresponds to 50% of the Strength and Point B Corresponds to 99% of the Strength After the Peak.

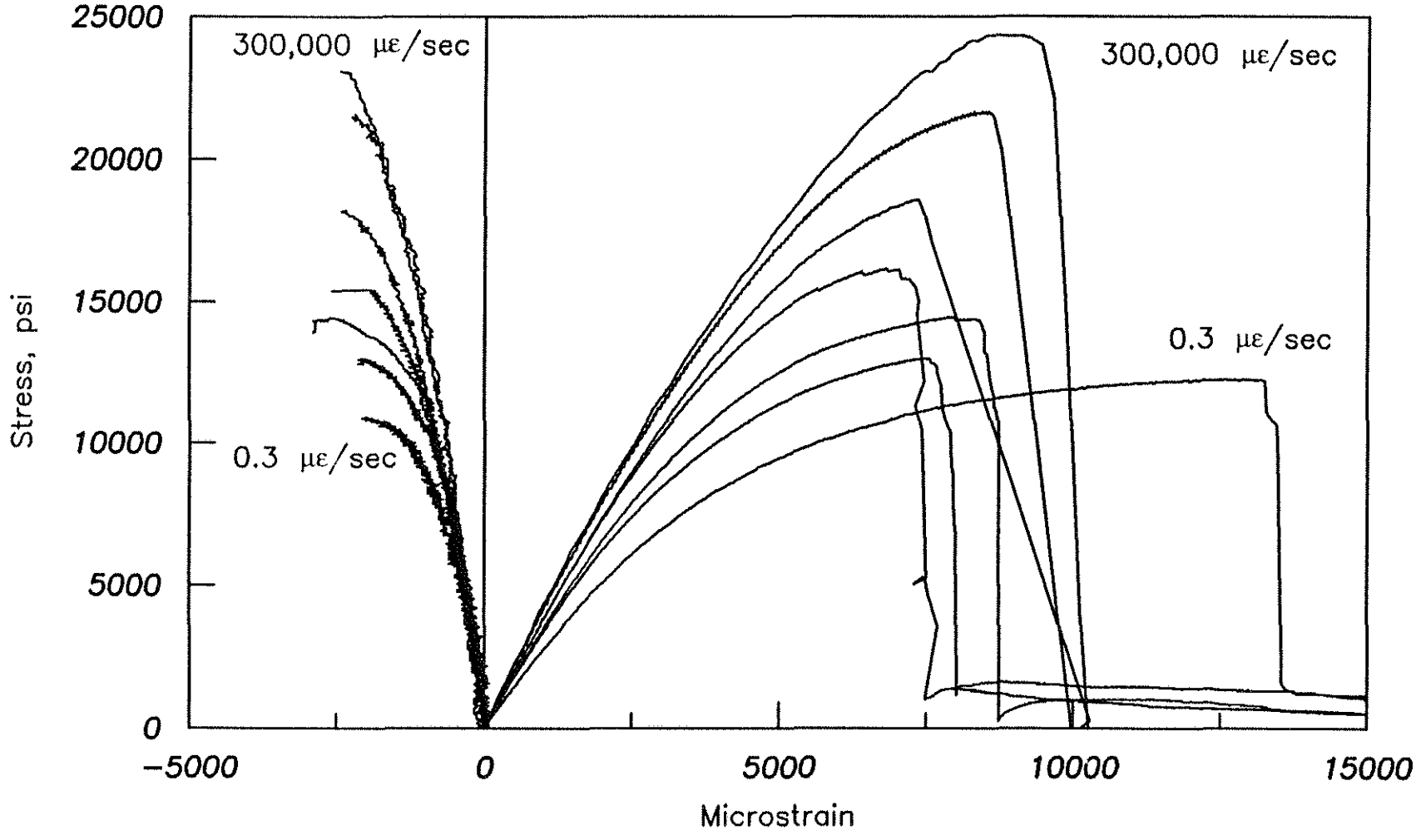

Fig. 2.4 Stress versus Longitudinal and Transverse Strains for Cement Paste with W/C = 0.3, Tested at Strain Rates from 0.3 to 300,000 Microstrain/sec

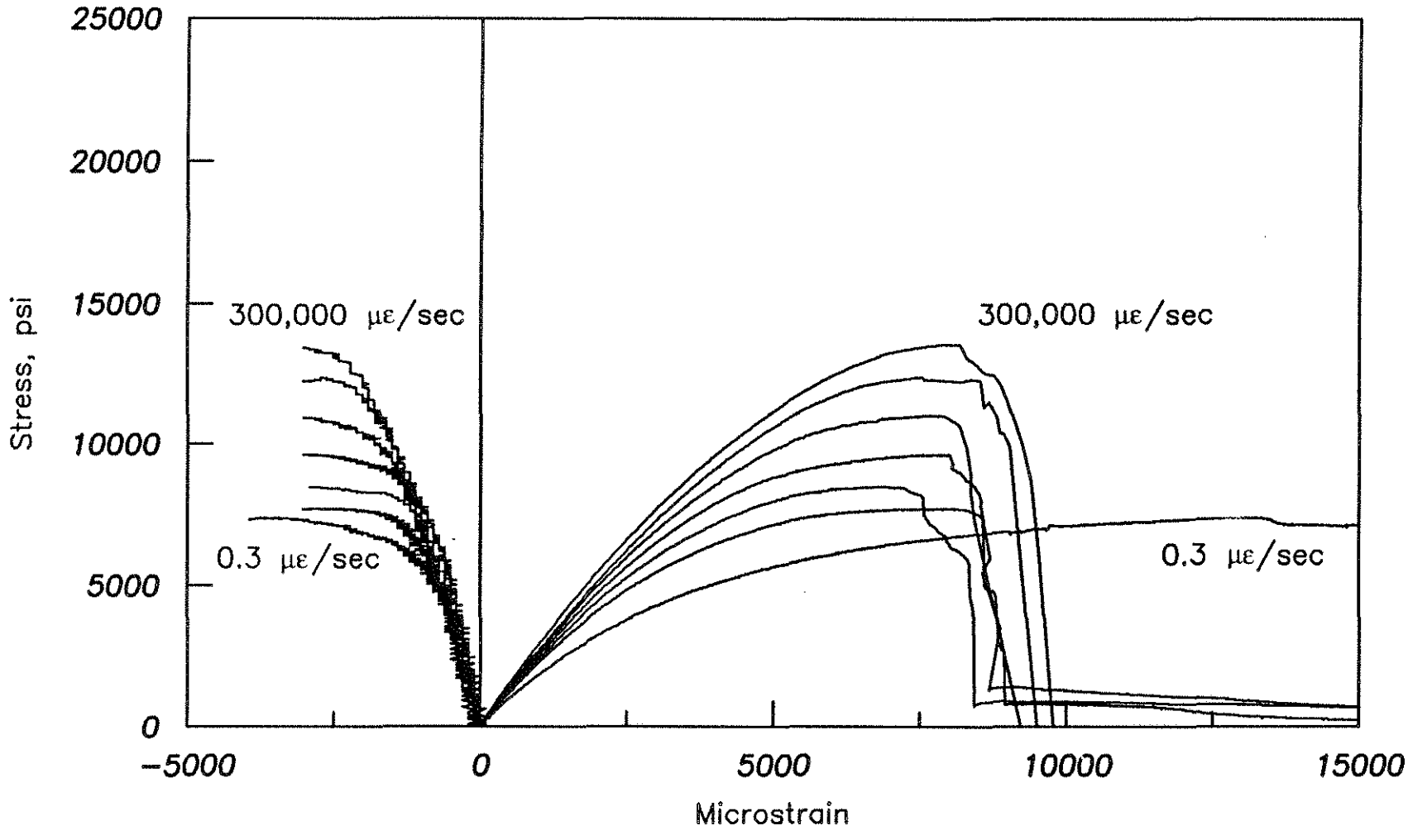

Fig. 2.5 Stress versus Longitudinal and Transverse Strains for Cement Paste with W/C = 0.4, Tested at Strain Rates from 0.3 to 300,000 Microstrain/sec

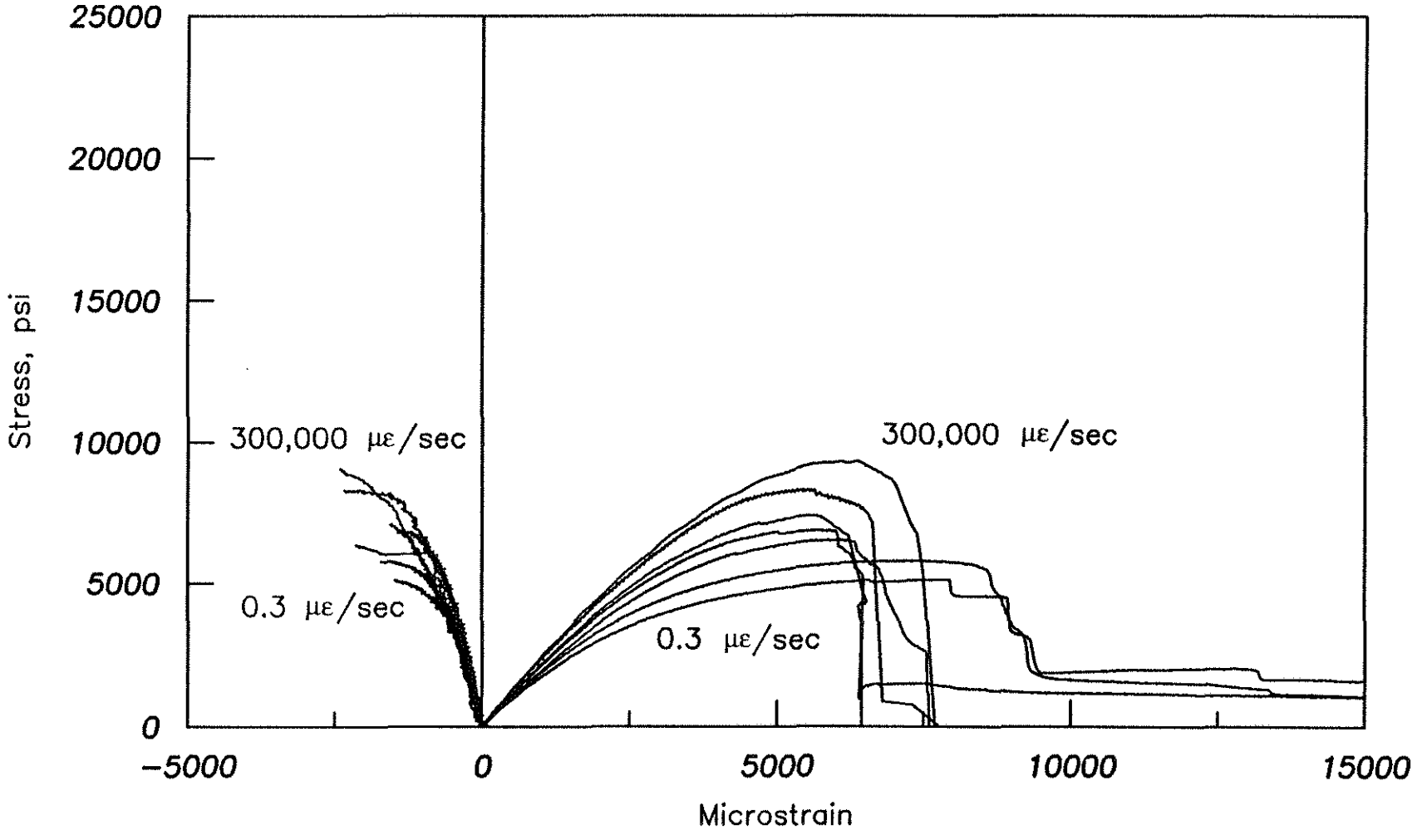

Fig. 2.6 Stress versus Longitudinal and Transverse Strains for Cement Paste with W/C = 0.5, Tested at Strain Rates from 0.3 to 300,000 Microstrain/sec

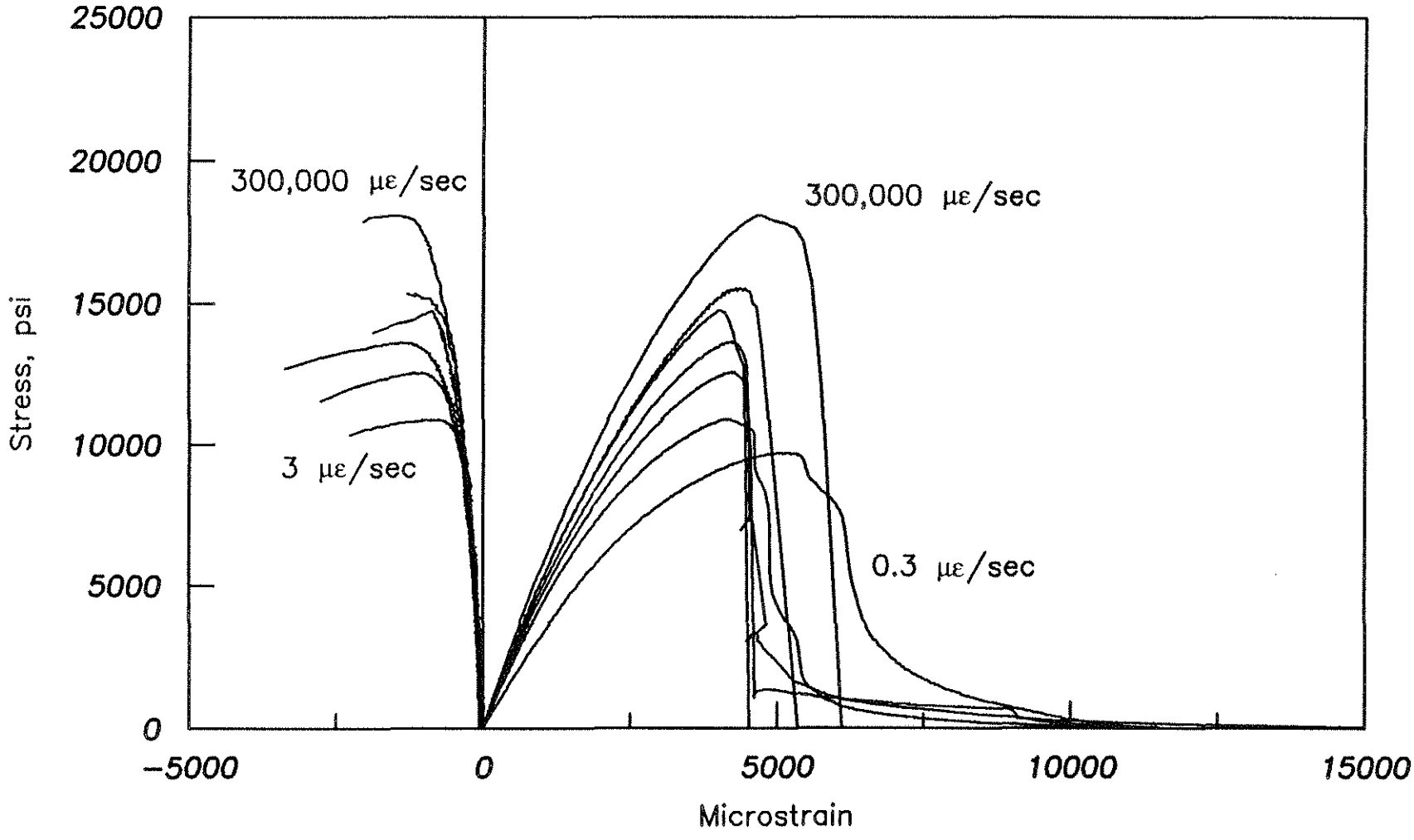

Fig. 2.7 Stress versus Longitudinal and Transverse Strains for Mortar with W/C = 0.3, Tested at Strain Rates from 0.3 to 300,000 Microstrain/sec

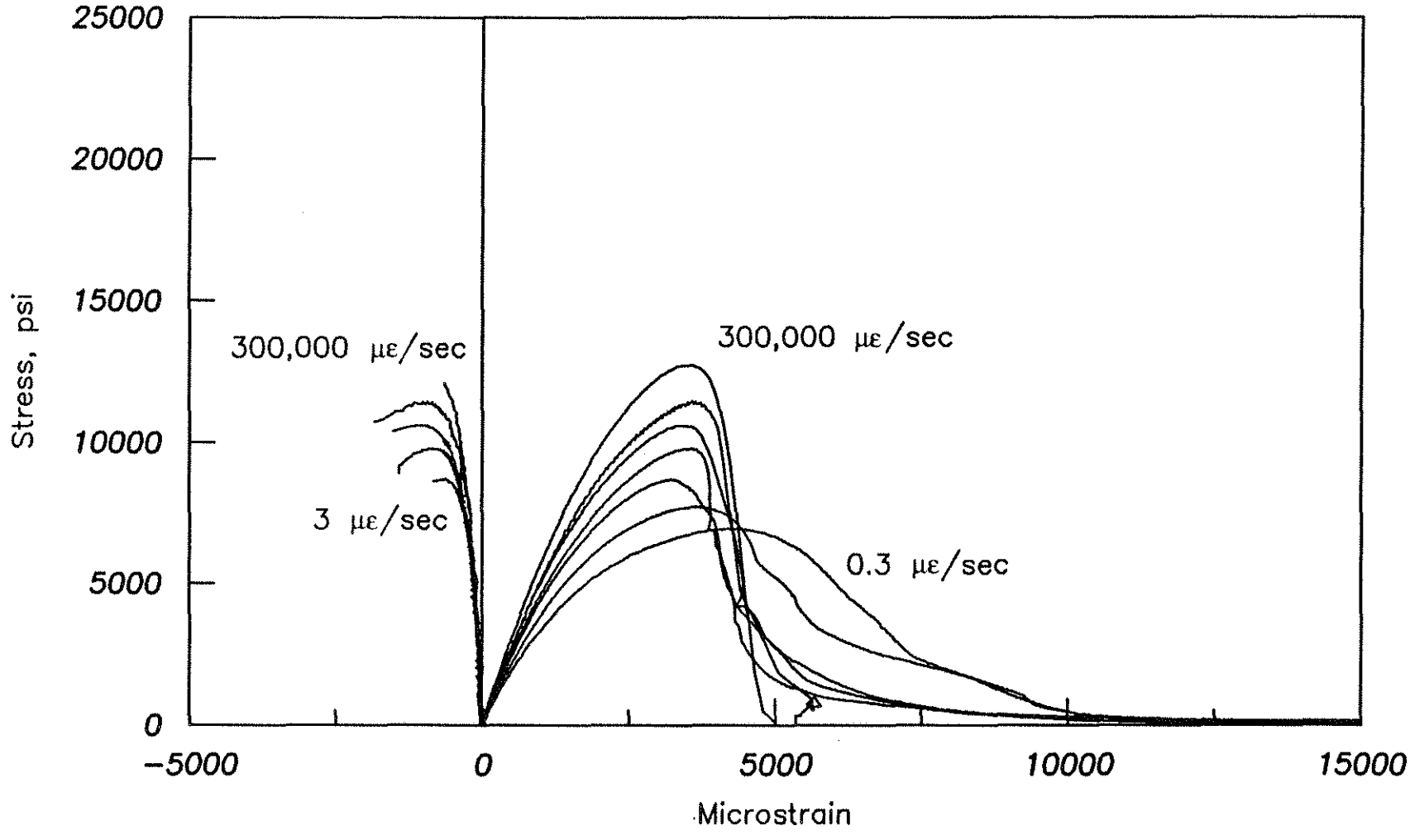

Fig. 2.8 Stress versus Longitudinal and Transverse Strains for Mortar A with W/C = 0.4, Tested at Strain Rates from 0.3 to 300,000 Microstrain/sec

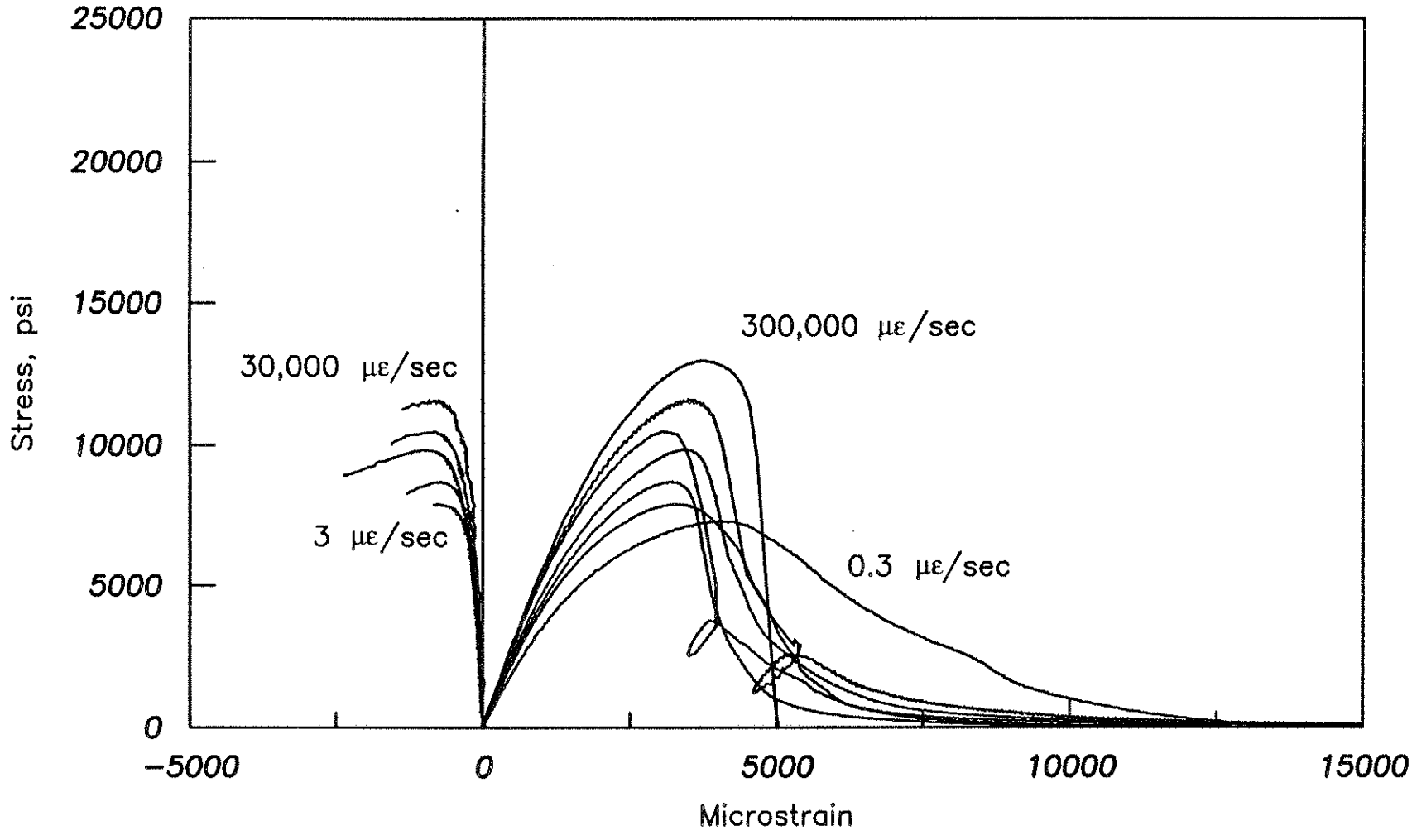

Fig. 2.9 Stress versus Longitudinal and Transverse Strains for Mortar B with W/C = 0.4, Tested at Strain Rates from 0.3 to 300,000 Microstrain/sec

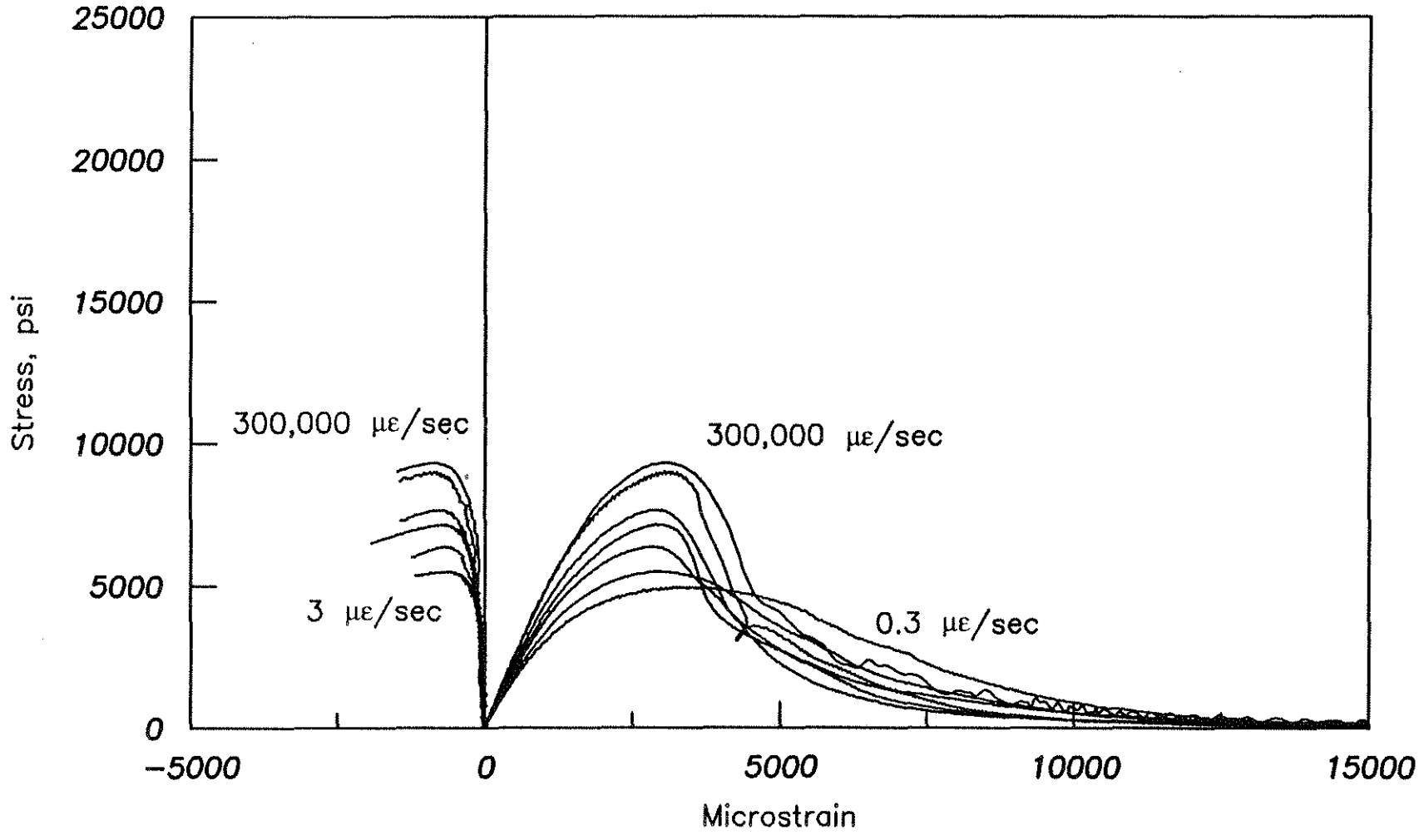

Fig. 2.10 Stress versus Longitudinal and Transverse Strains for Mortar A with W/C = 0.5, Tested at Strain Rates from 0.3 to 300,000 Microstrain/sec

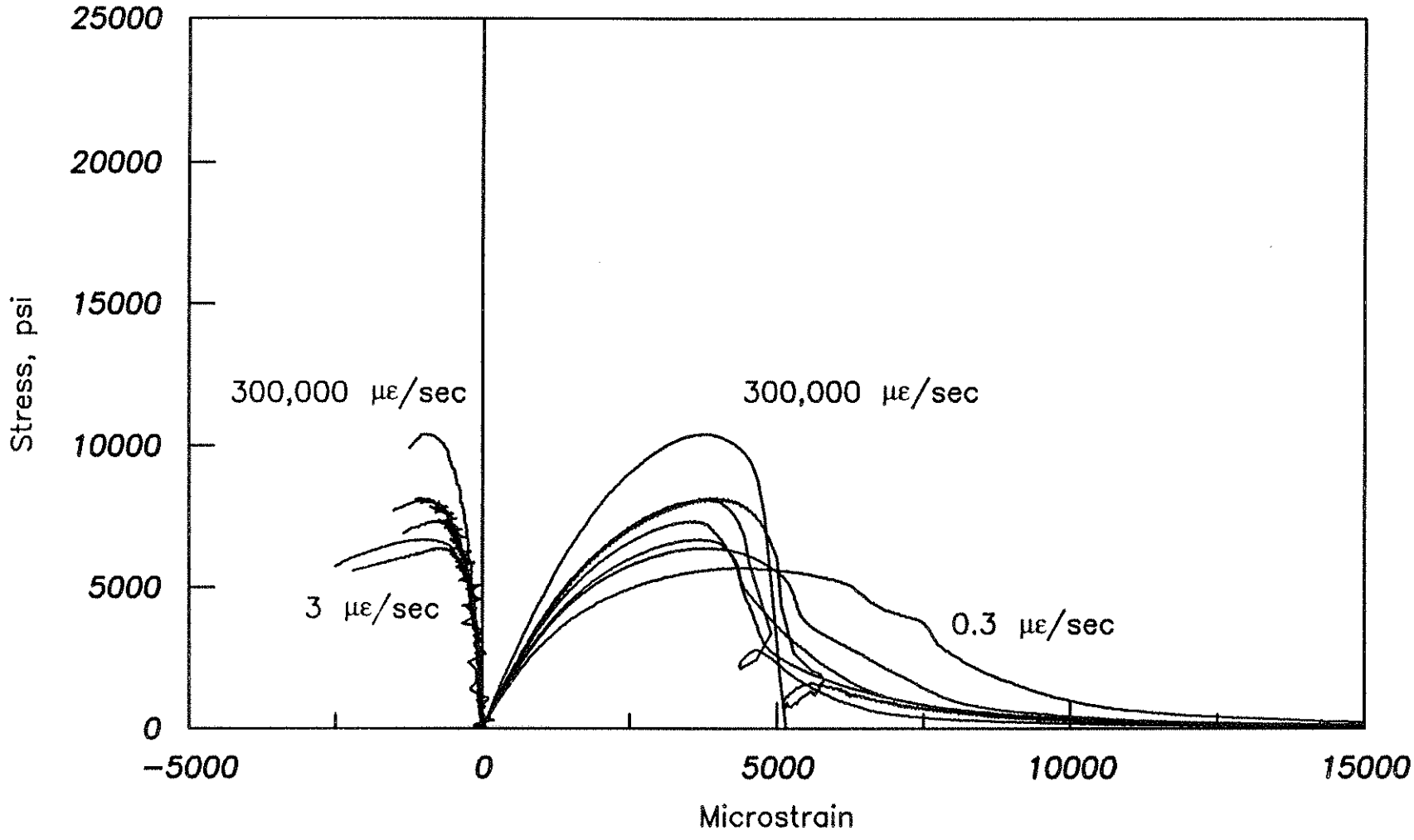

Fig. 2.11 Stress versus Longitudinal and Transverse Strains for Mortar B with W/C = 0.5, Tested at Strain Rates from 0.3 to 300,000 Microstrain/sec

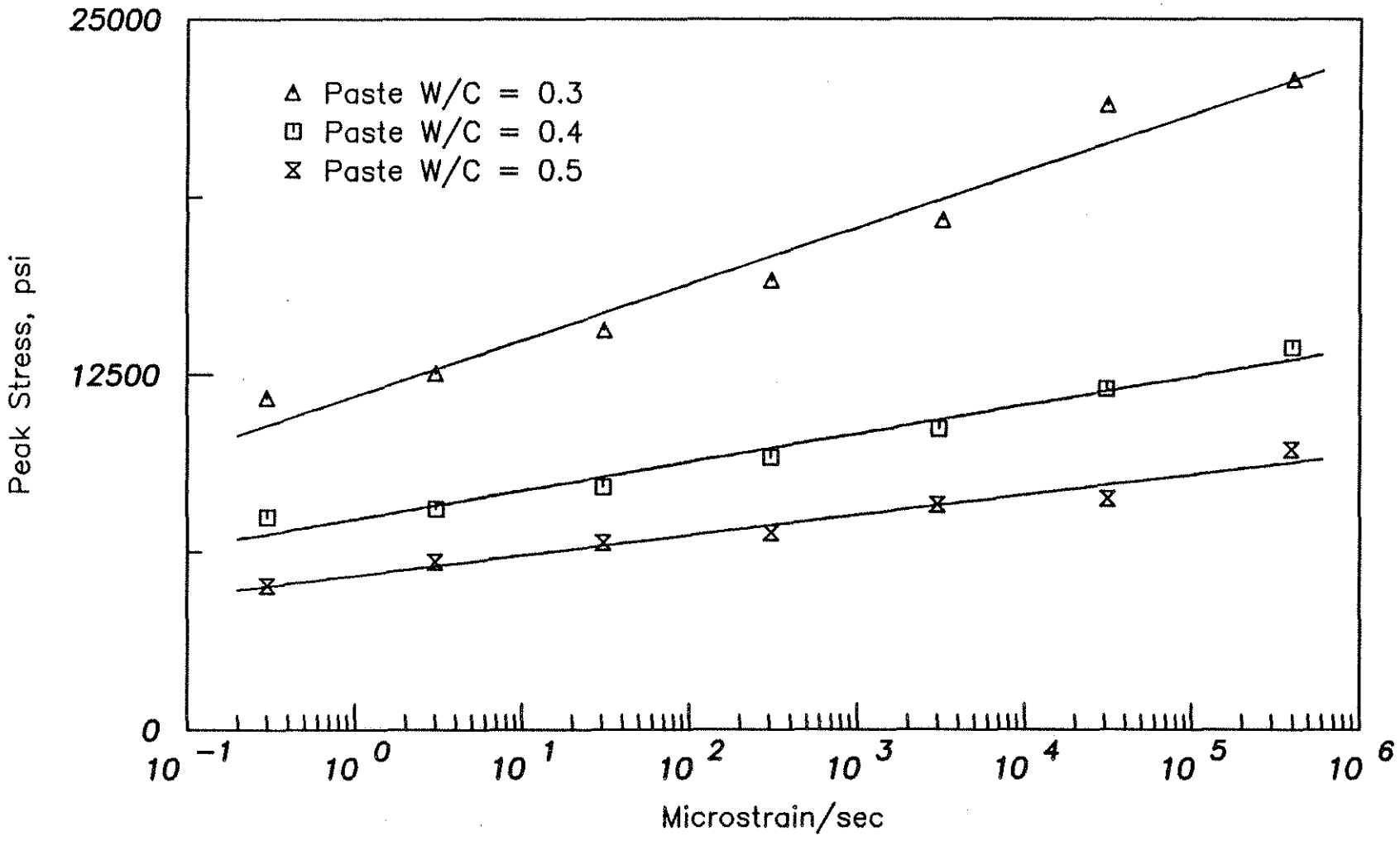

Fig. 2.12 Peak Stress versus Strain Rate ($\dot{\varepsilon}_{50\text{-}99}$) for Cement Paste with W/C = 0.3, 0.4, and 0.5

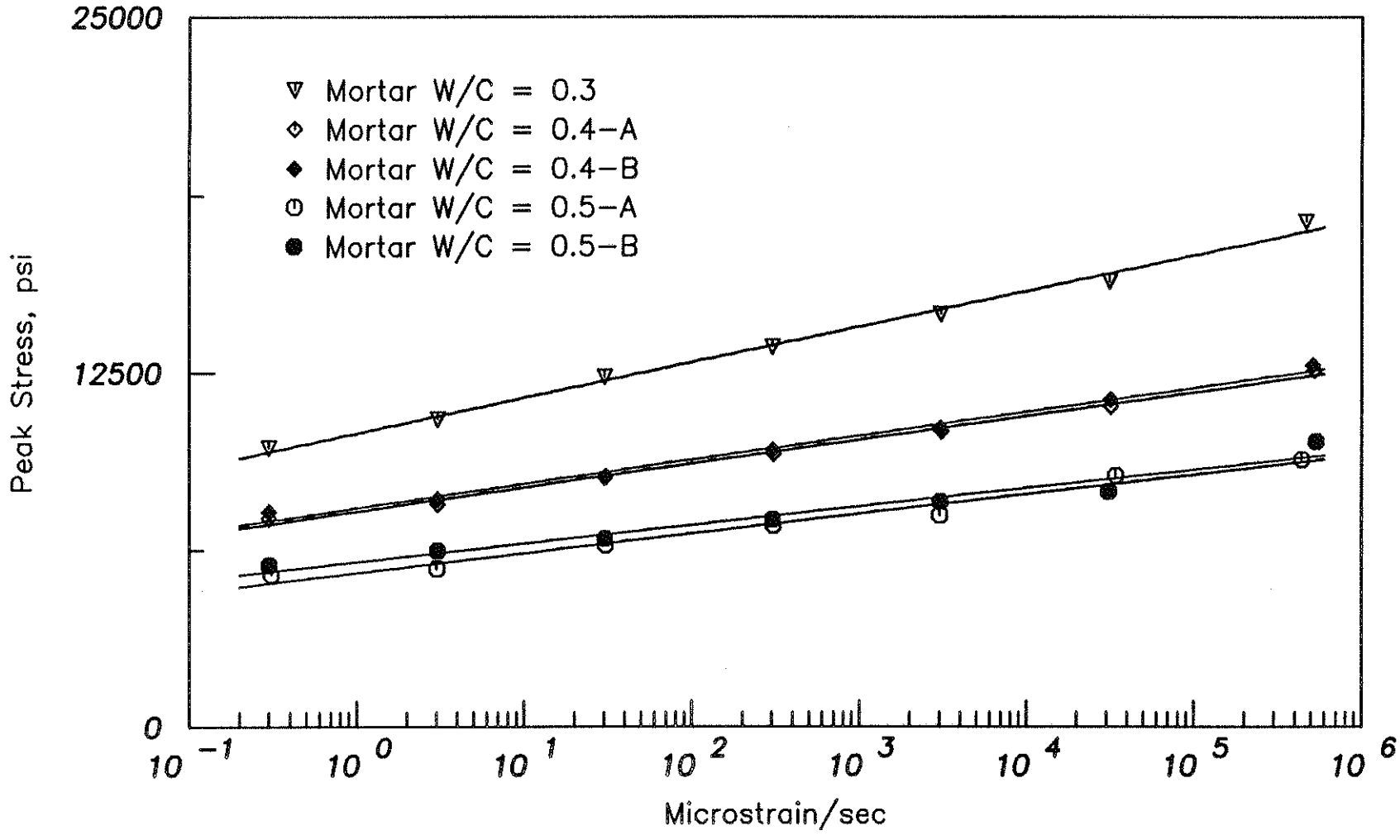

Fig. 2.13 Peak Stress versus Strain Rate ($\dot{\varepsilon}_{50-99}$) for Mortar with W/C = 0.3, 0.4, and 0.5

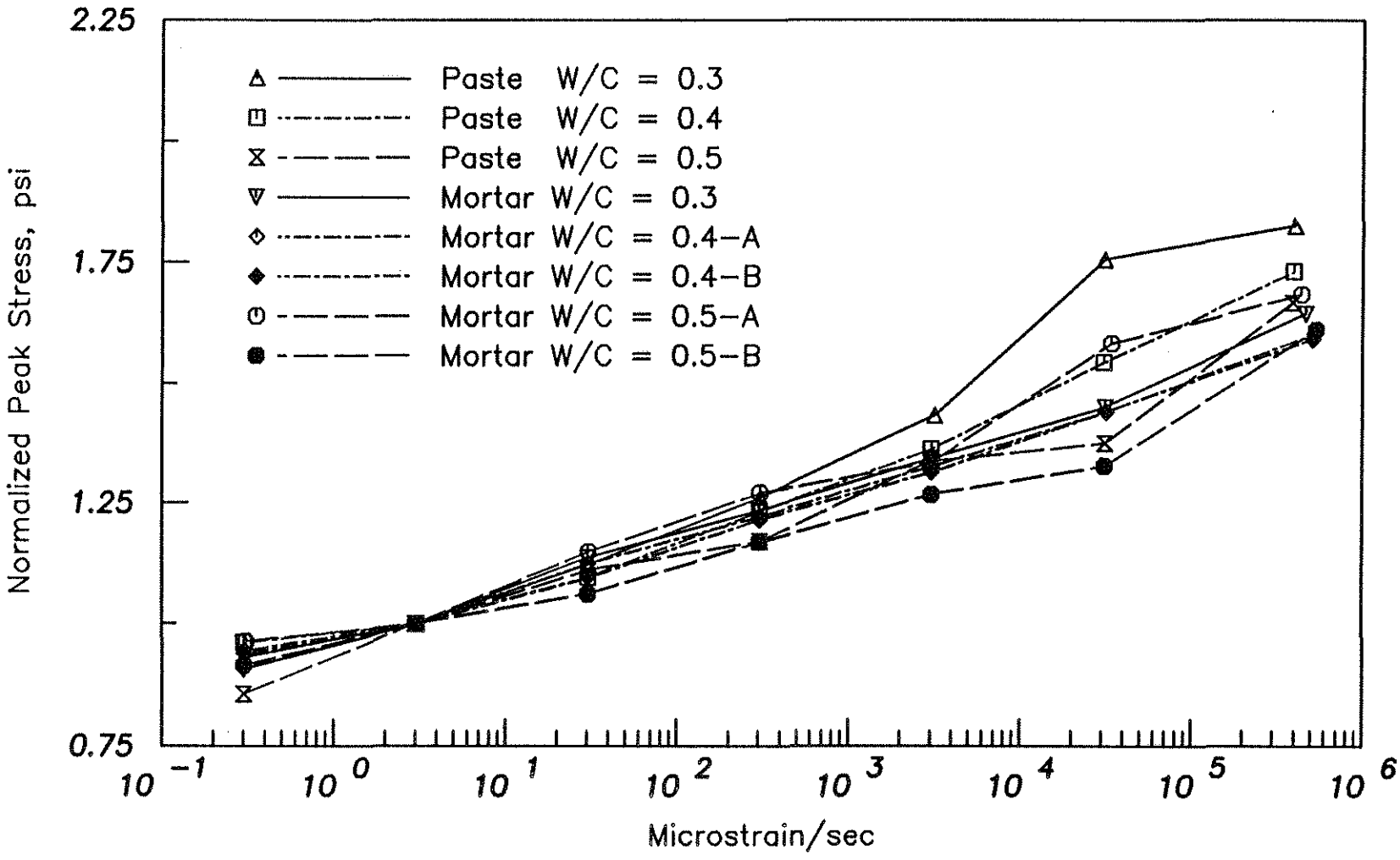

Fig. 2.14 Normalized Peak Stress versus Strain Rate ($\dot{\varepsilon}_{50-99}$) for Cement Paste and Mortar with W/C = 0.3, 0.4, and 0.5

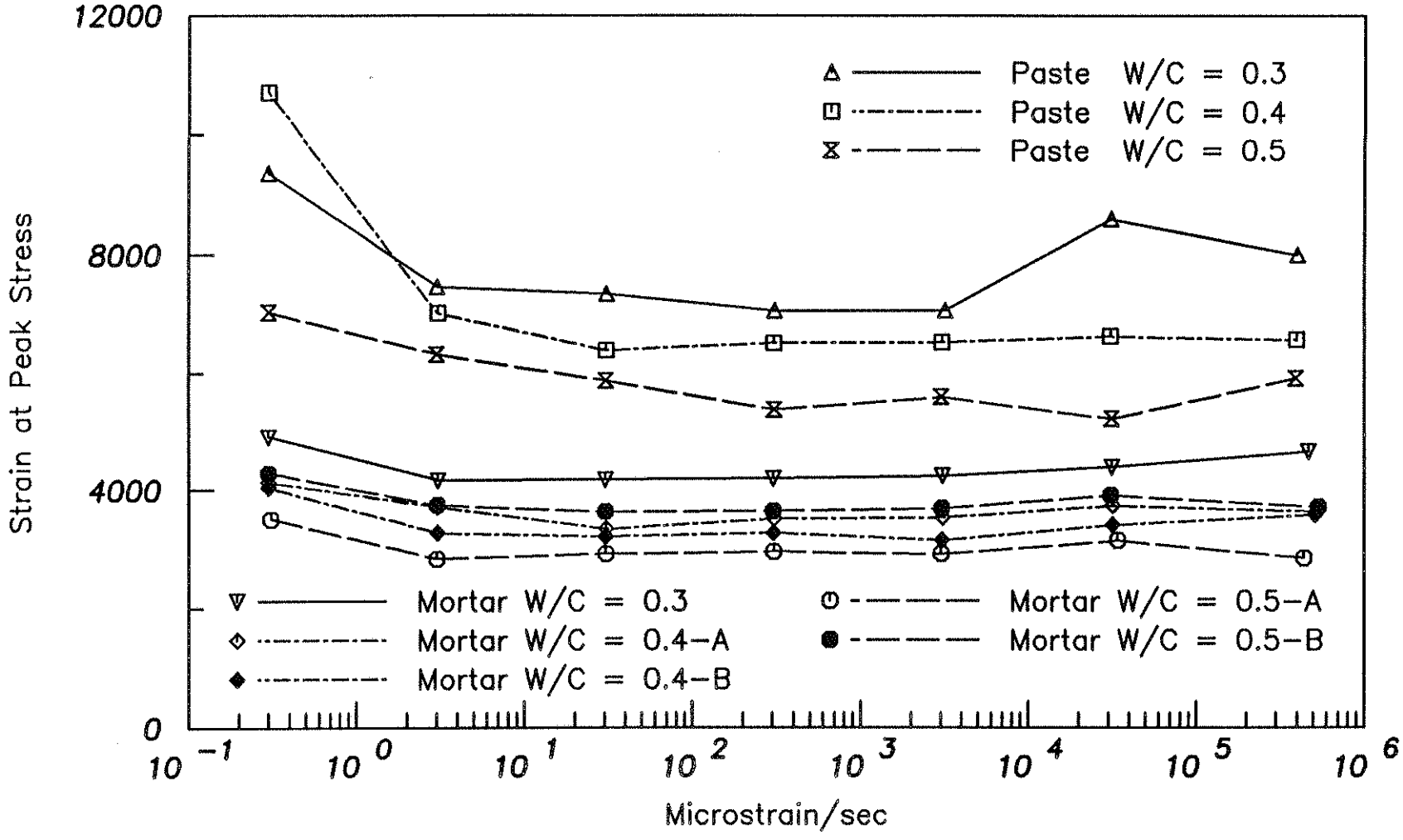

Fig. 2.15 Strain at the Peak Stress versus Strain Rate ($\dot{\varepsilon}_{50-99}$) for Cement Paste and Mortar with W/C = 0.3, 0.4, and 0.5

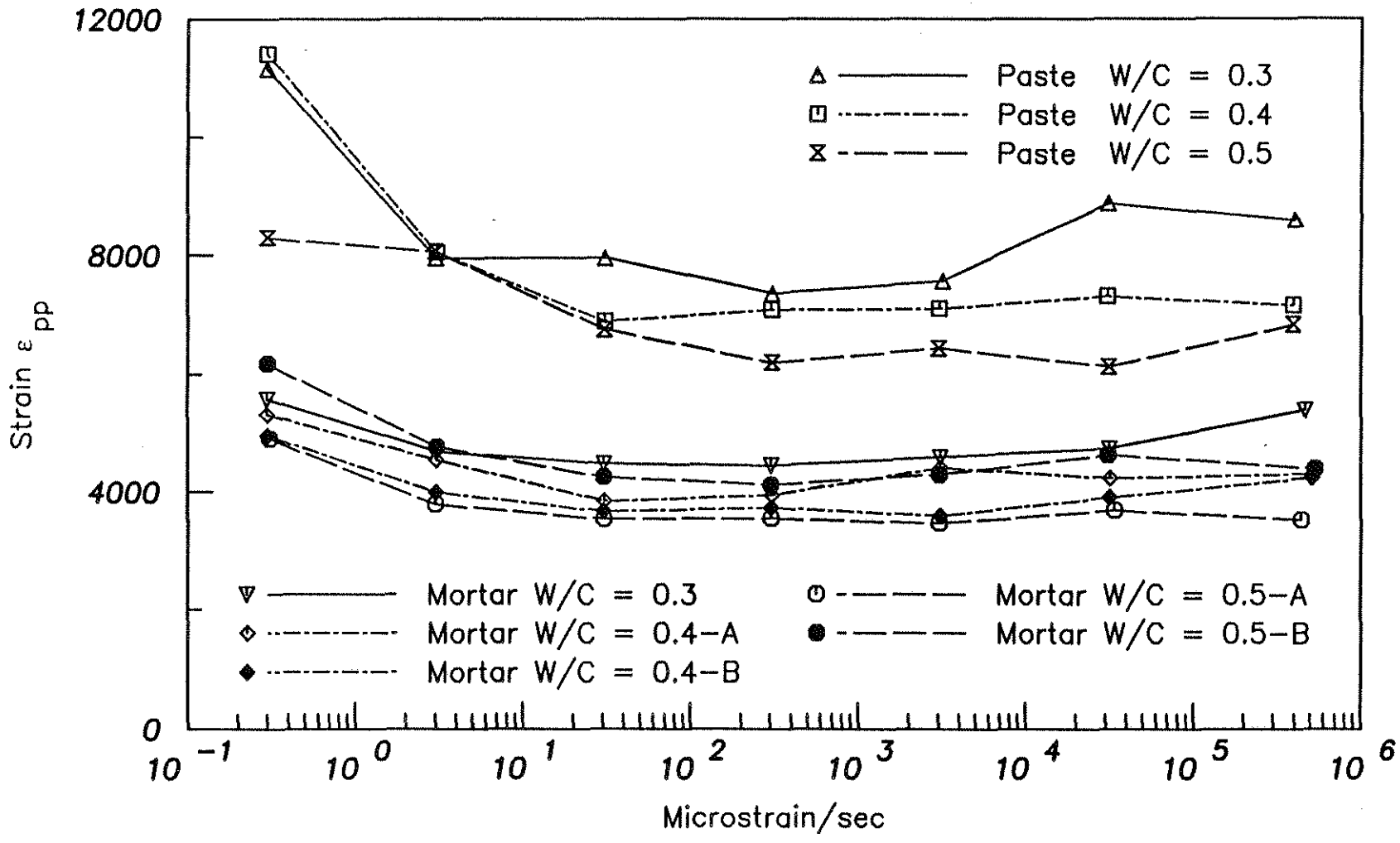

Fig. 2.16 Post Peak Strain at 90 Percent of the Peak Stress, ε_{pp}, versus Strain Rate ($\dot{\varepsilon}_{50-99}$) for Cement Paste and Mortar with W/C = 0.3, 0.4, and 0.5

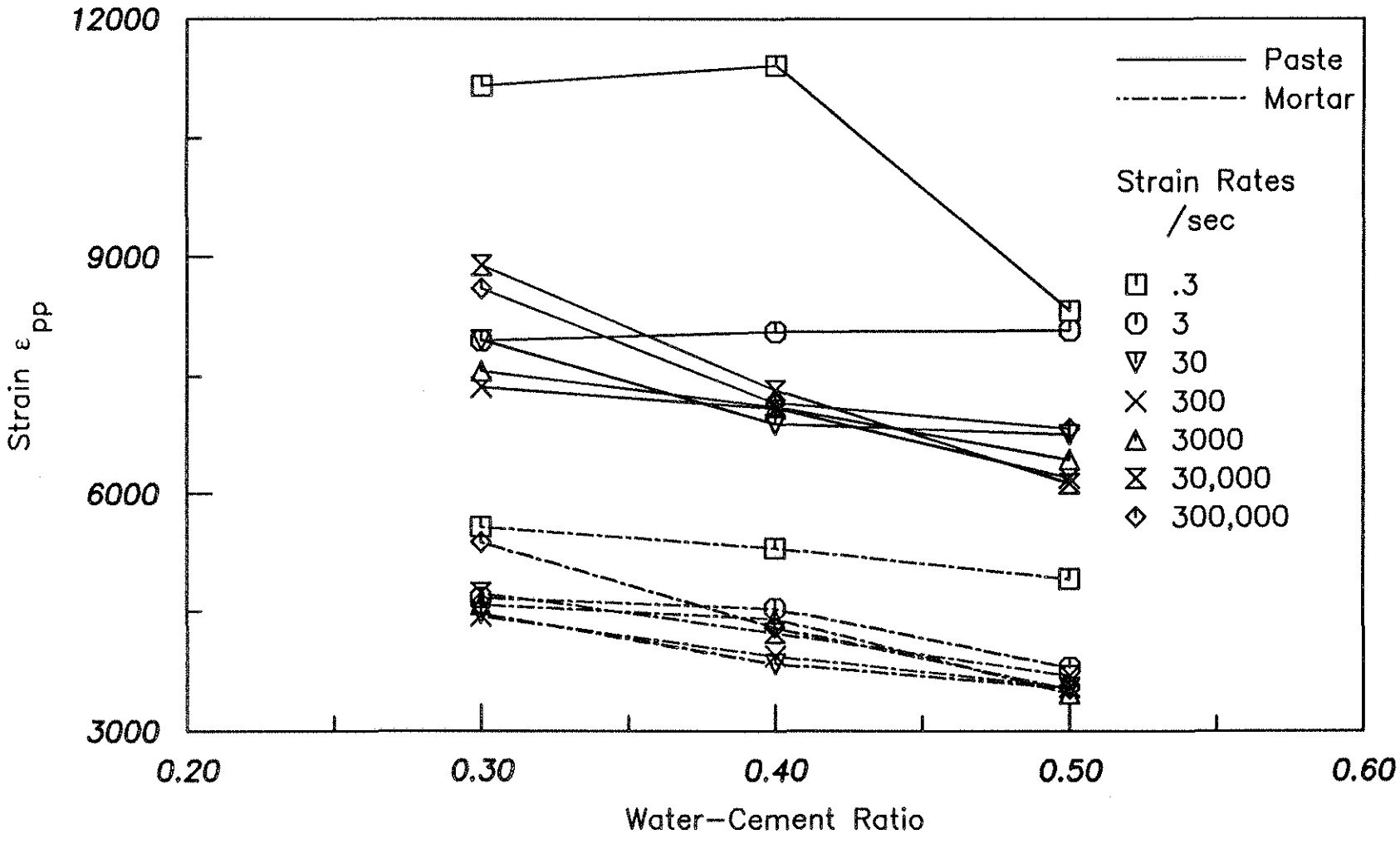

Fig. 2.17 Post Peak Strain at 90 Percent of the Peak Stress, ε_{pp}, versus Water-Cement Ratio for Cement Paste and Mortar at Different Strain Rates ($\dot{\varepsilon}_{50-99}$)

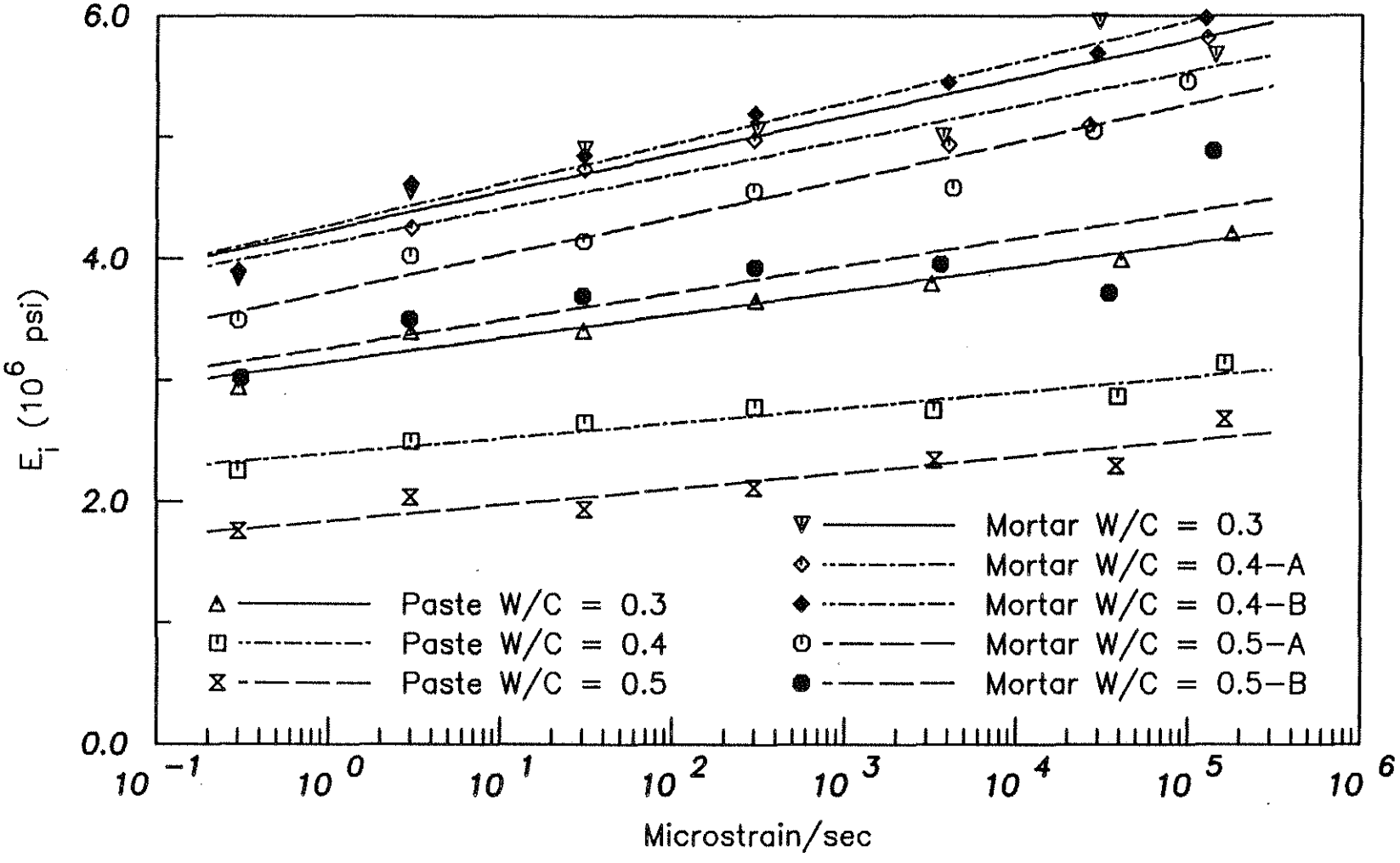

Fig. 2.18 Initial Modulus of Elasticity versus Strain Rate ($\dot{\varepsilon}_{5-20}$) for Cement Paste and Mortar with W/C = 0.3, 0.4, and 0.5

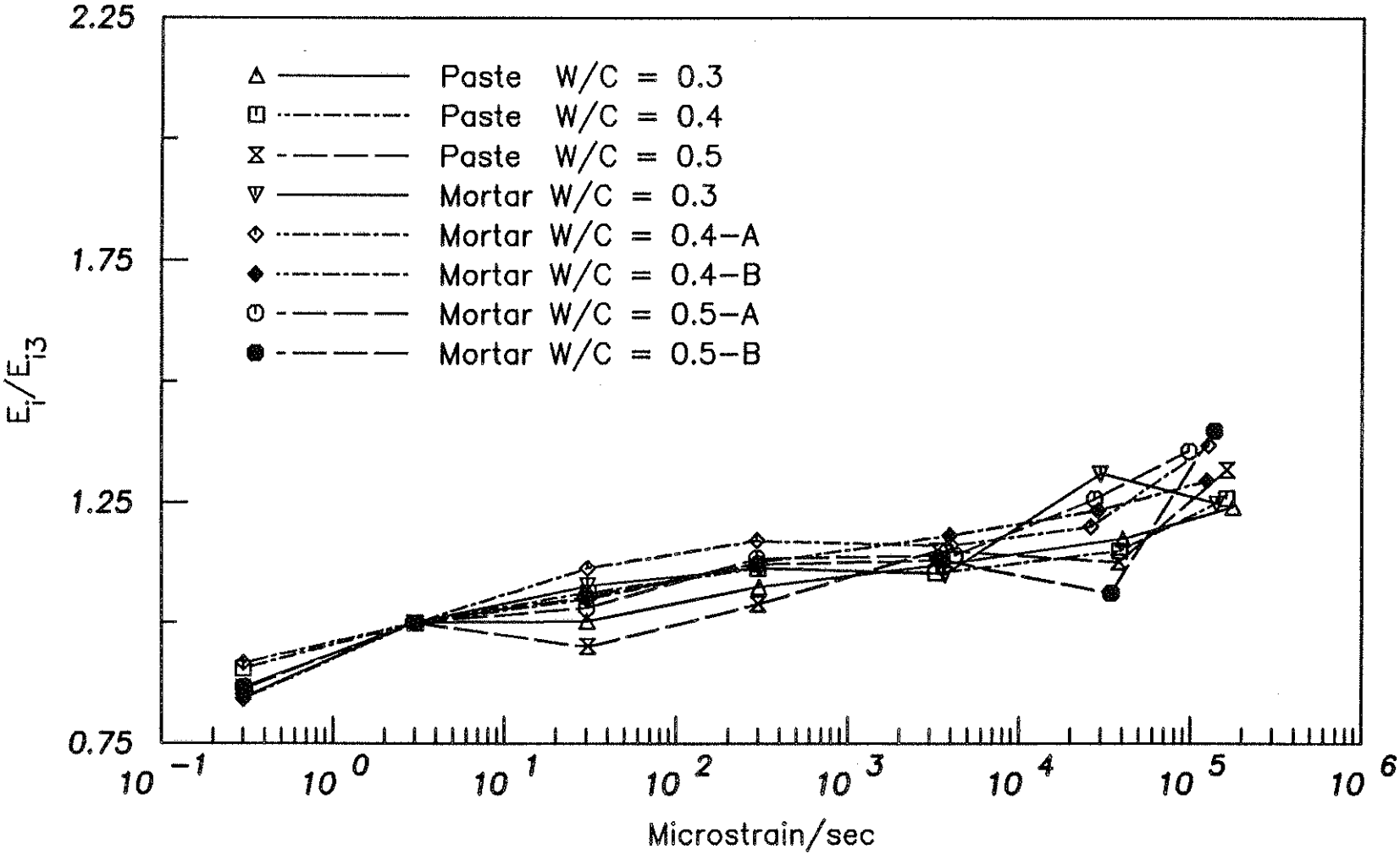

Fig. 2.19 Normalized Initial Modulus of Elasticity versus Strain Rate ($\dot{\varepsilon}_{5-20}$) for Cement Paste and Mortar with W/C = 0.3, 0.4, and 0.5

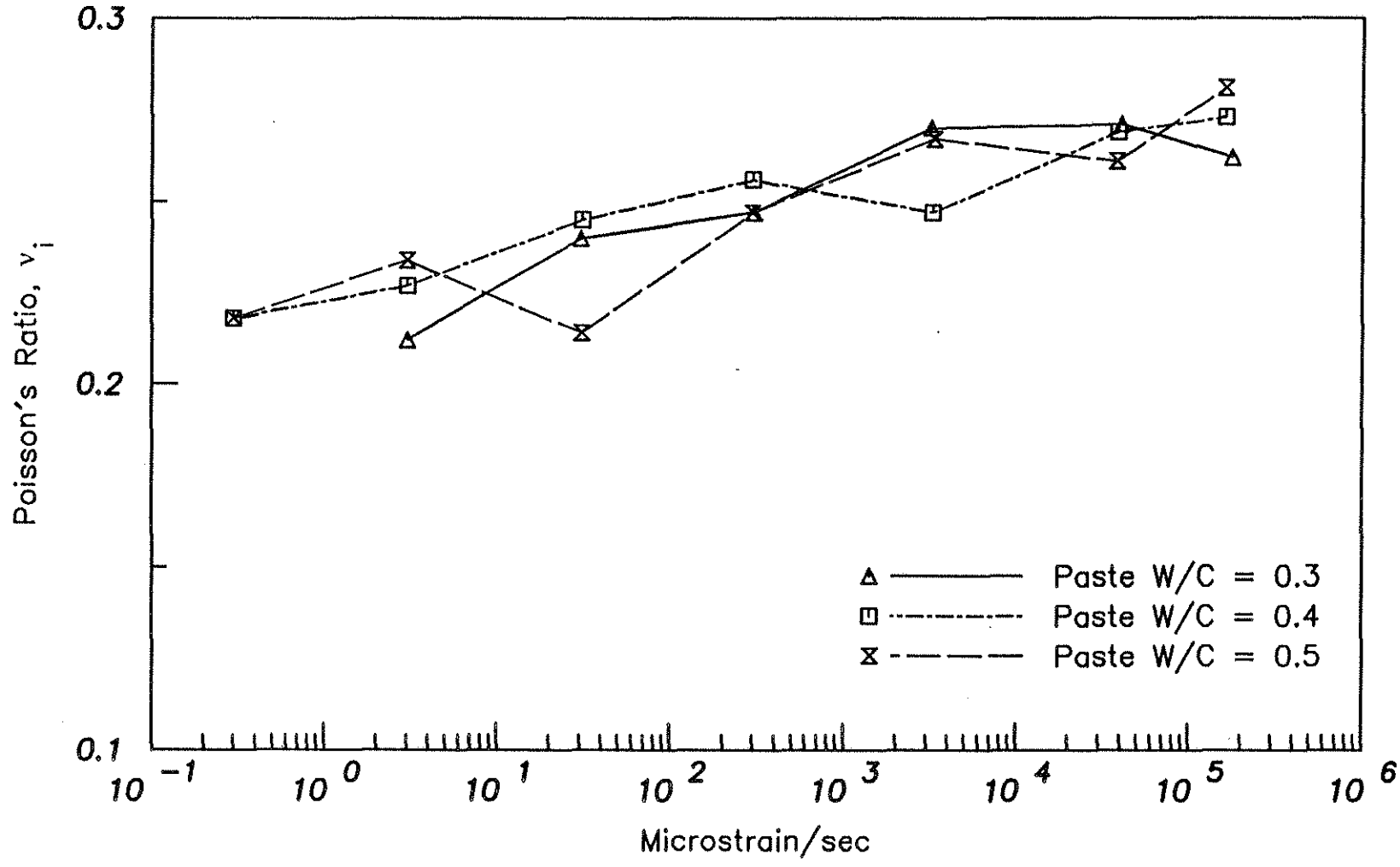

Fig. 2.20 Initial Poisson's Ratio versus Strain Rate ($\dot{\varepsilon}_{5-20}$) for Cement Paste with W/C = 0.3, 0.4, and 0.5

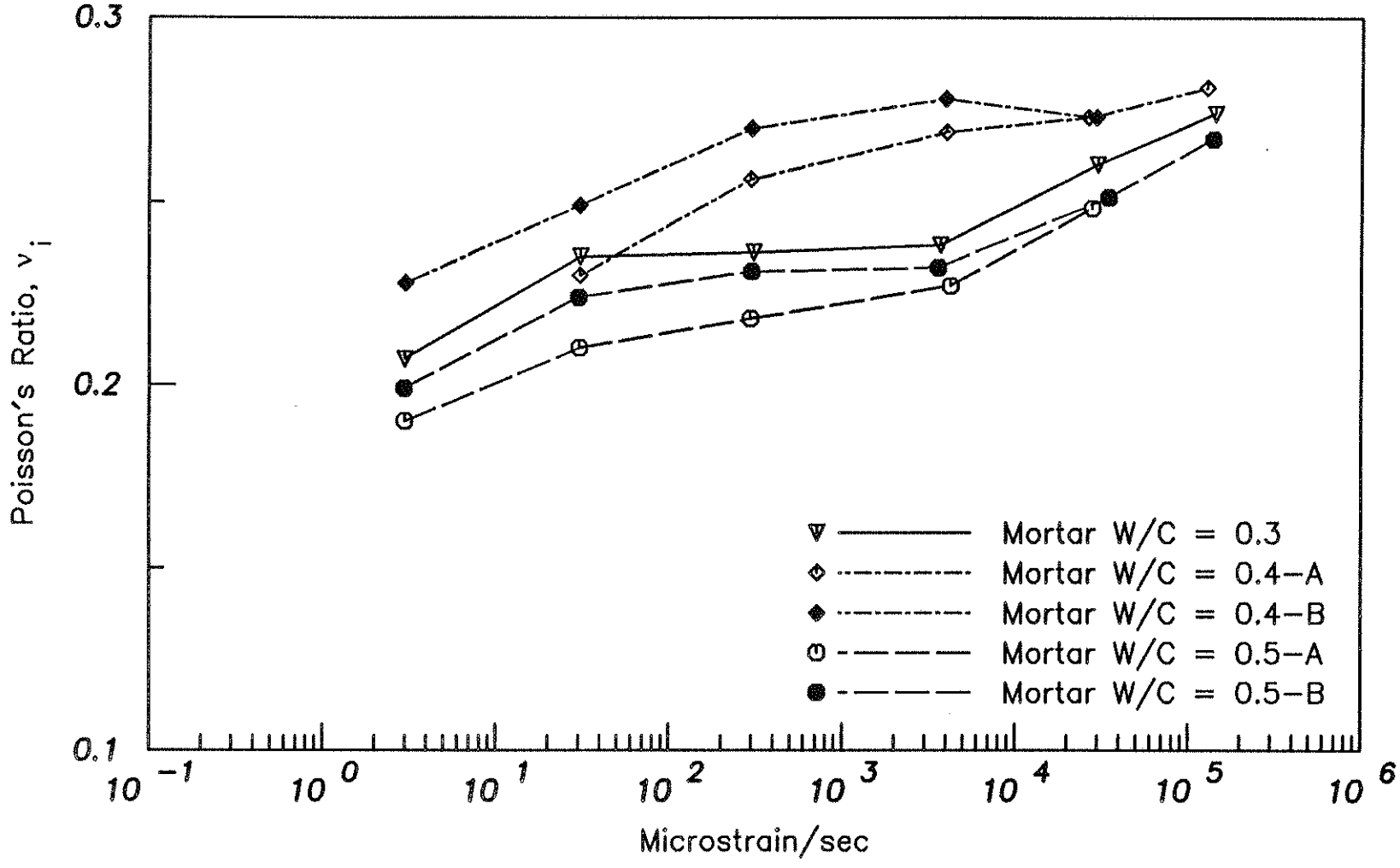

Fig. 2.21 Initial Poisson's Ratio versus Strain Rate ($\dot{\varepsilon}_{5\text{-}20}$) for Mortar with W/C = 0.3, 0.4, and 0.5

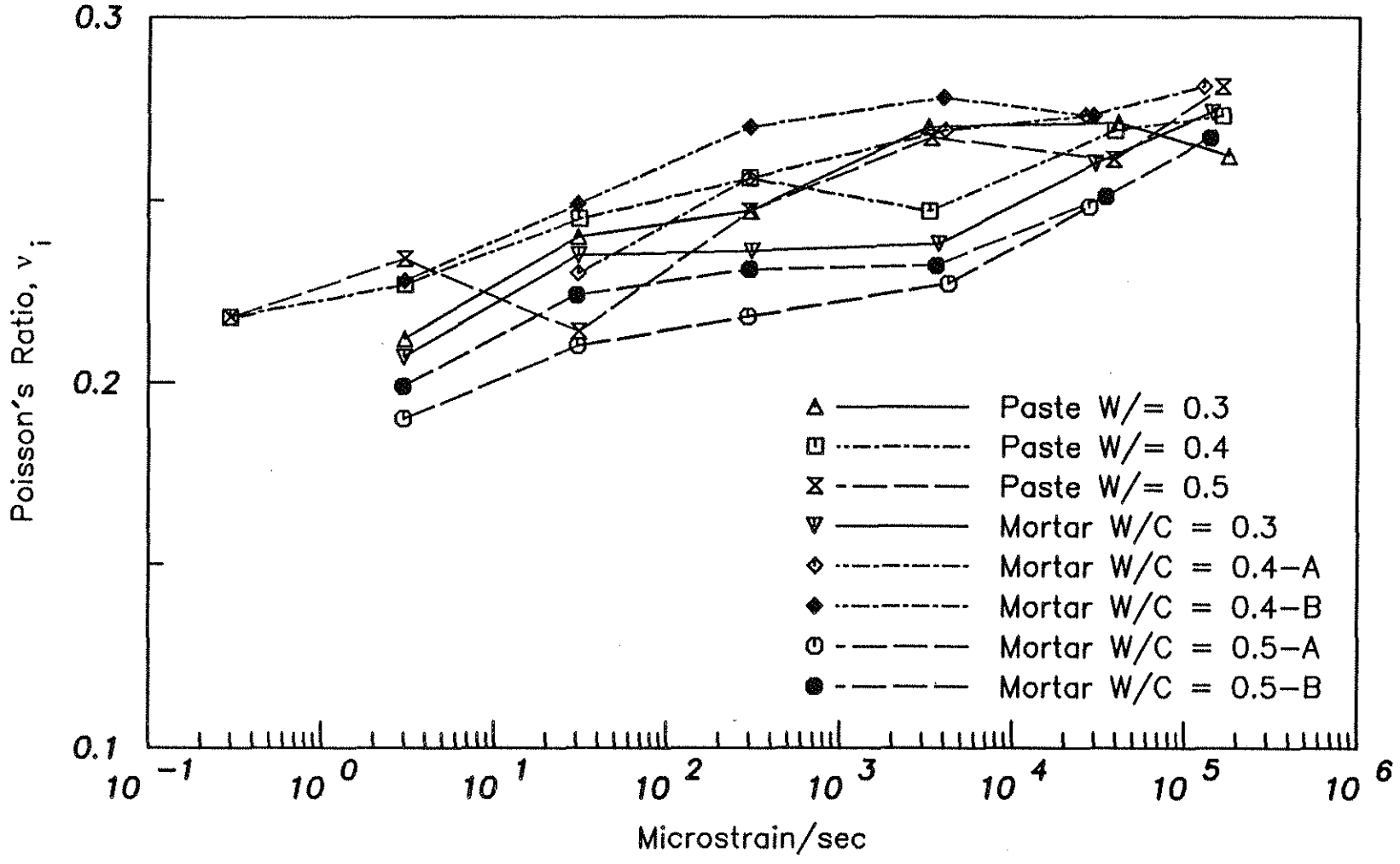

Fig. 2.22 Initial Poisson's Ratio versus Strain Rate ($\dot{\varepsilon}_{5-20}$) for Cement Paste and Mortar with W/C = 0.3, 0.4, and 0.5

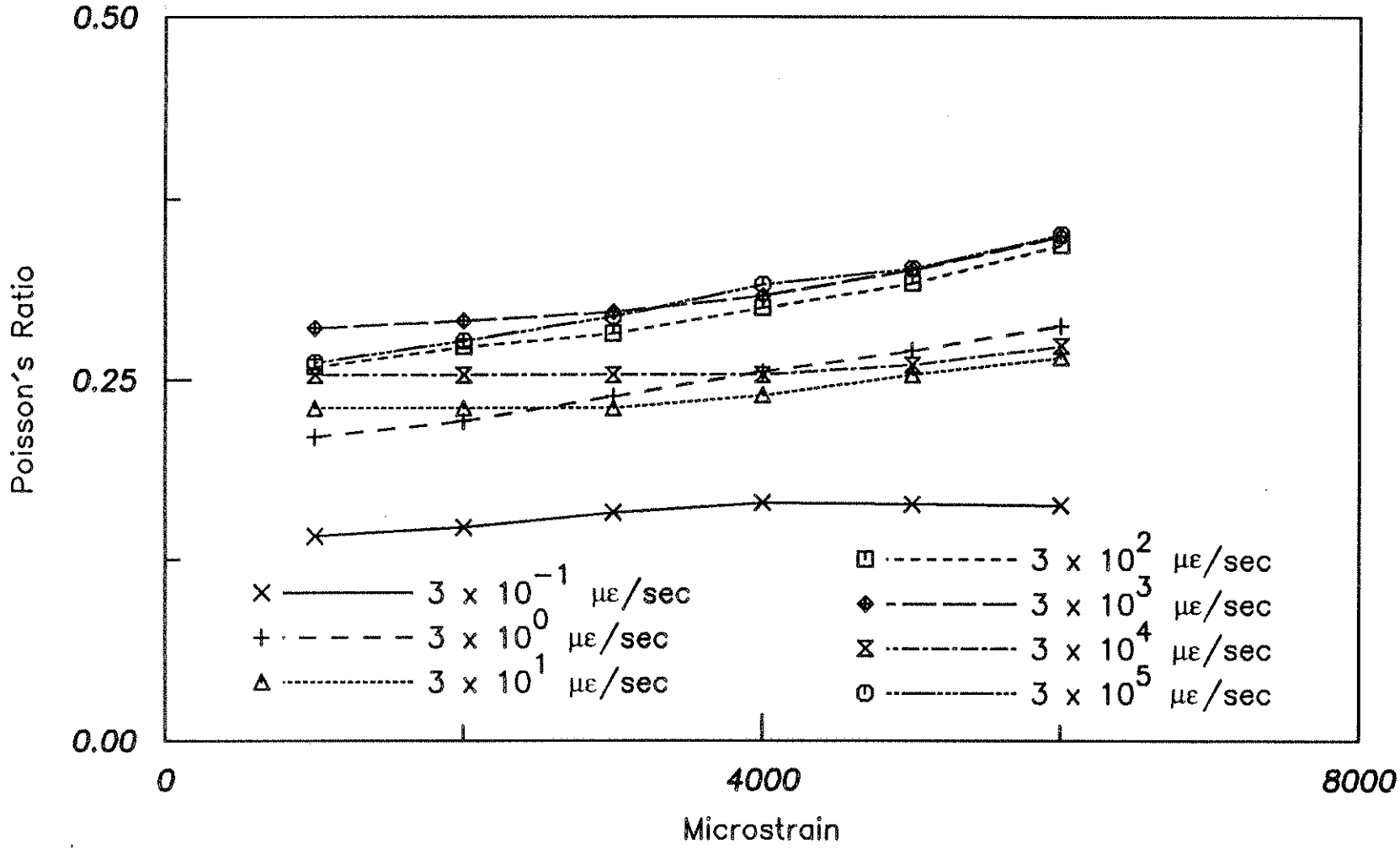

Fig. 2.23 Poisson's Ratio versus Strain at Different Strain Rates for Cement Paste with W/C = 0.3

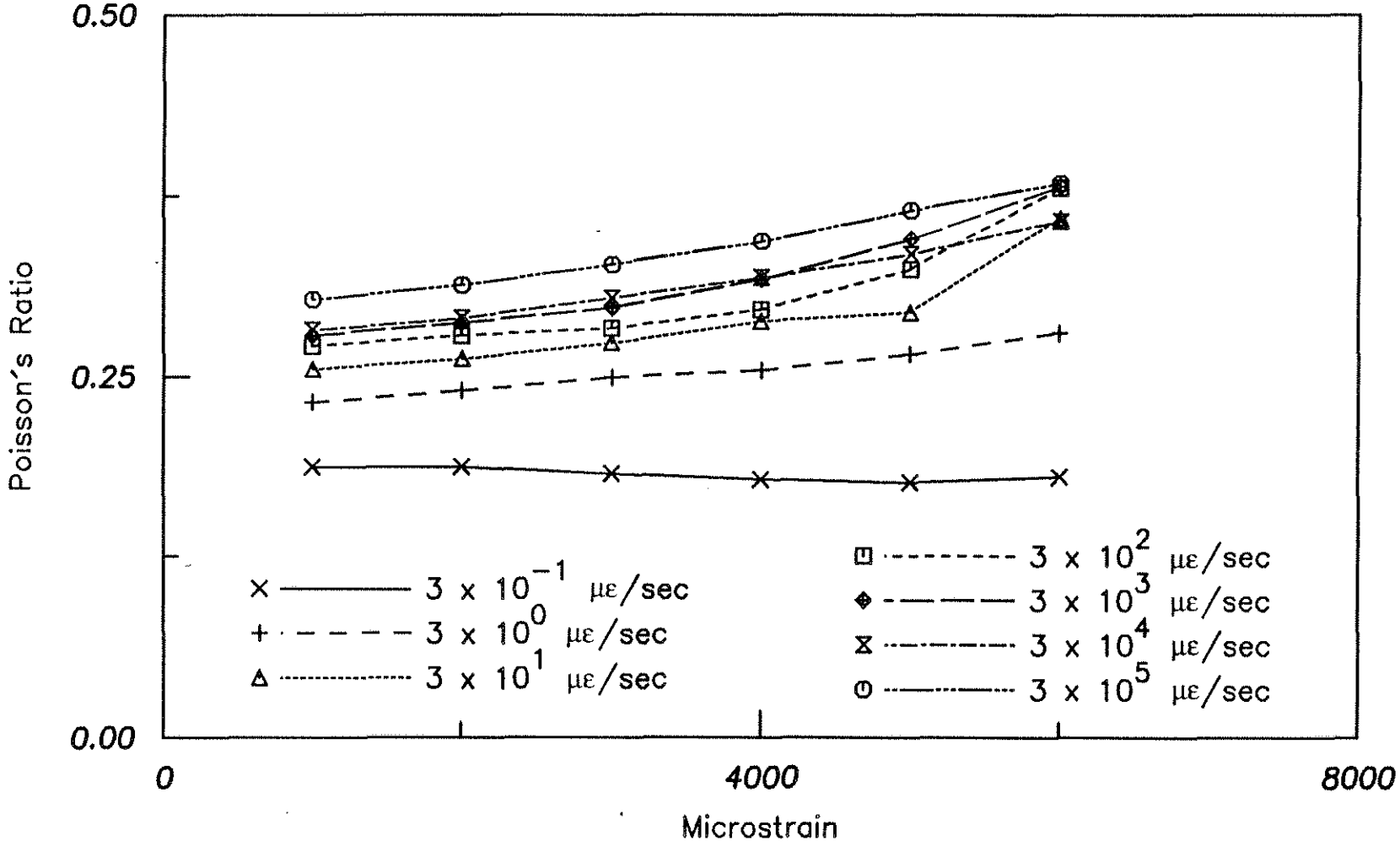

Fig. 2.24 Poisson's Ratio versus Strain at Different Strain Rates for Cement Paste with W/C = 0.4

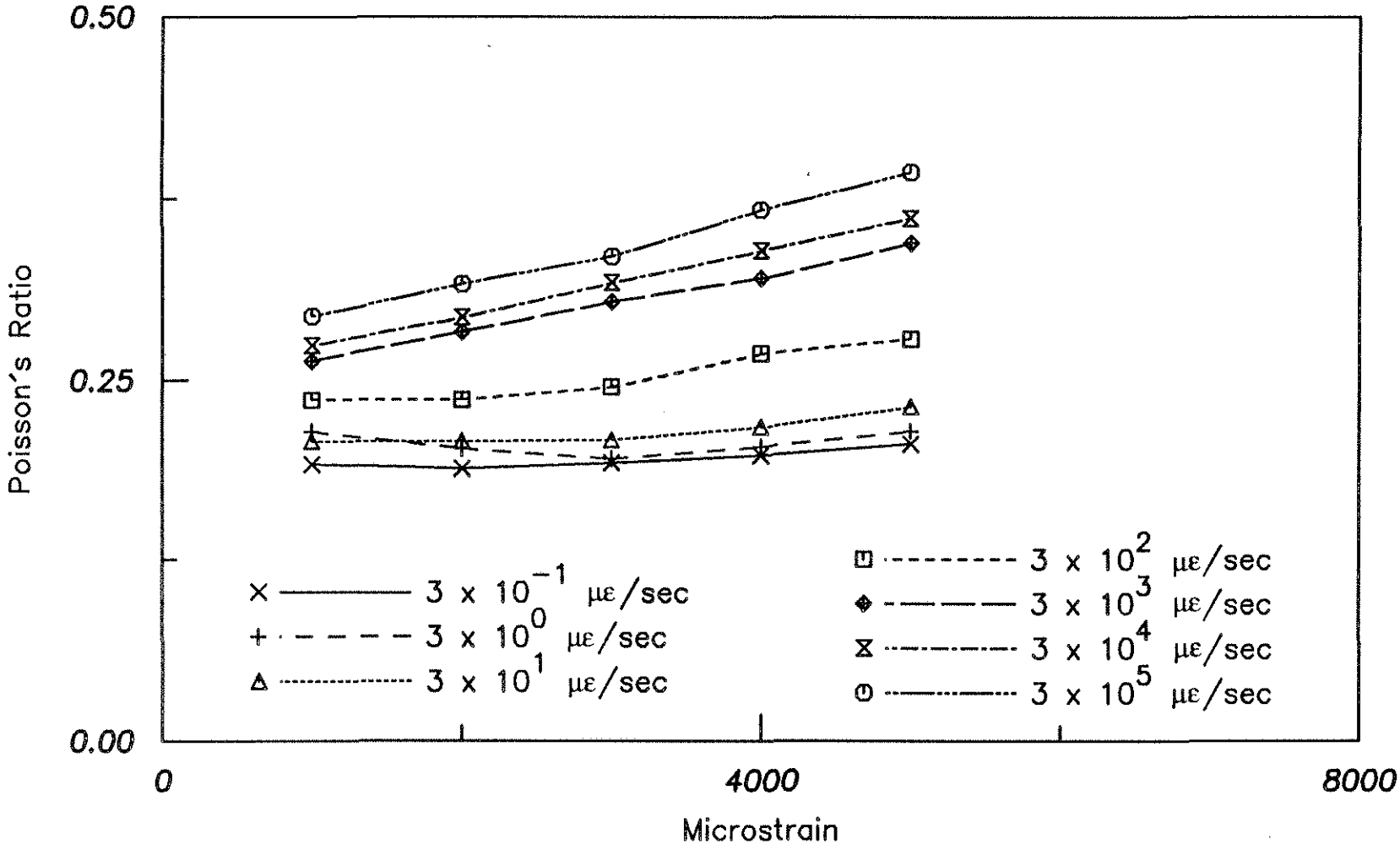

Fig. 4.25 Poisson's Ratio versus Strain at Different Strain Rates for Cement Paste with W/C = 0.5

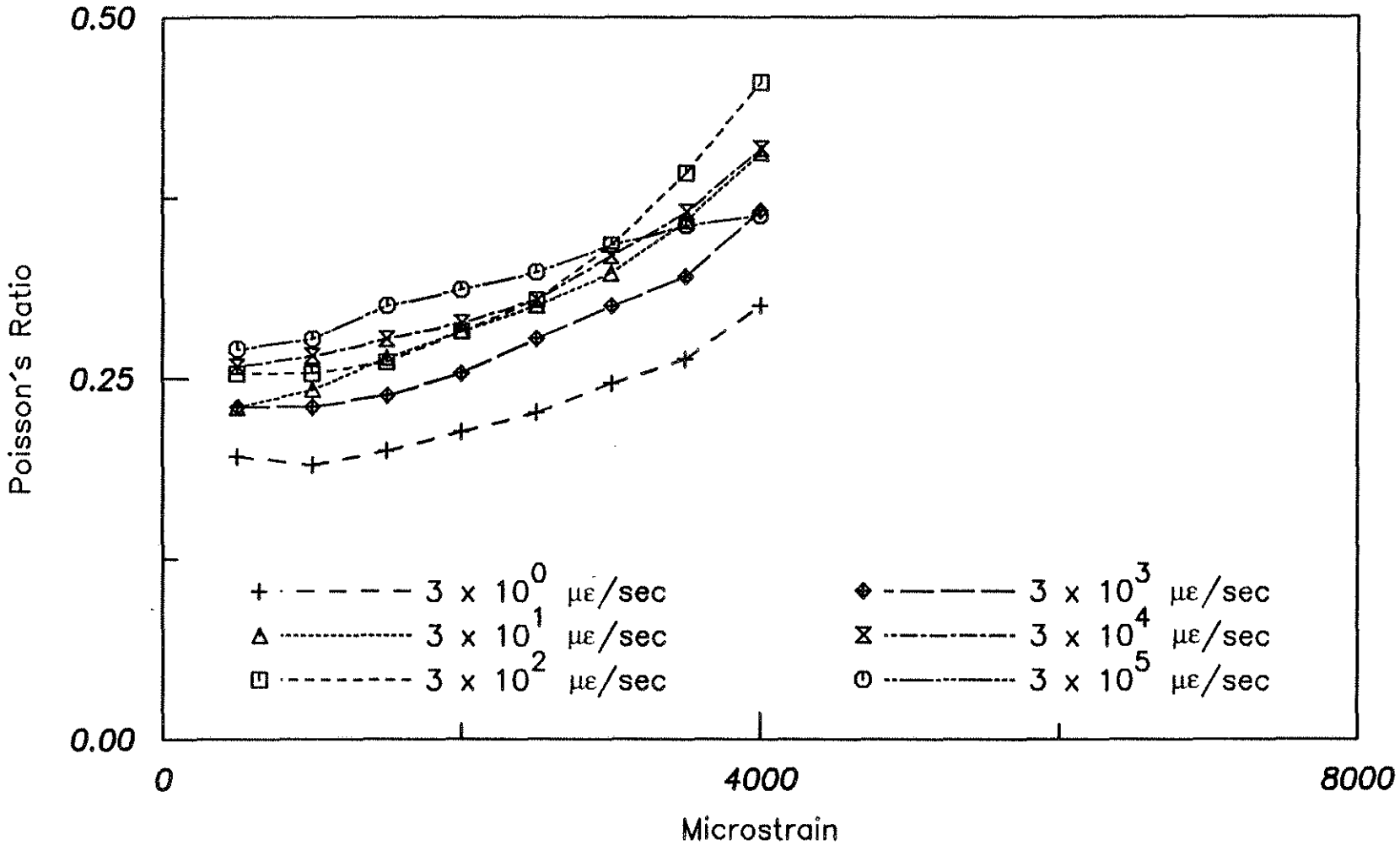

Fig. 2.26 Poisson's Ratio versus Strain at Different Strain Rates for Mortar with W/C = 0.3

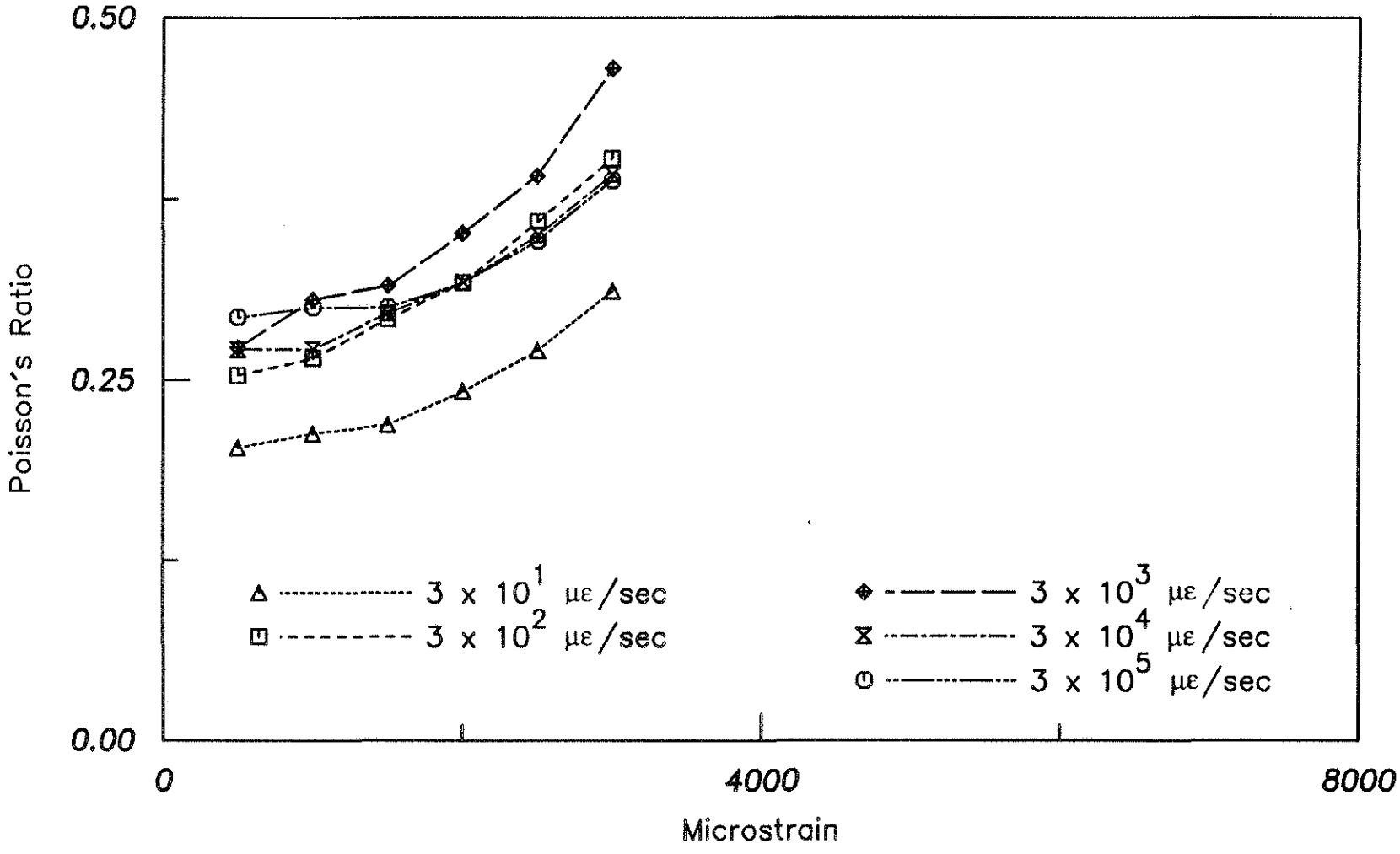

Fig. 2.27 Poisson's Ratio versus Strain at Different Strain Rates for Mortar A with W/C = 0.4

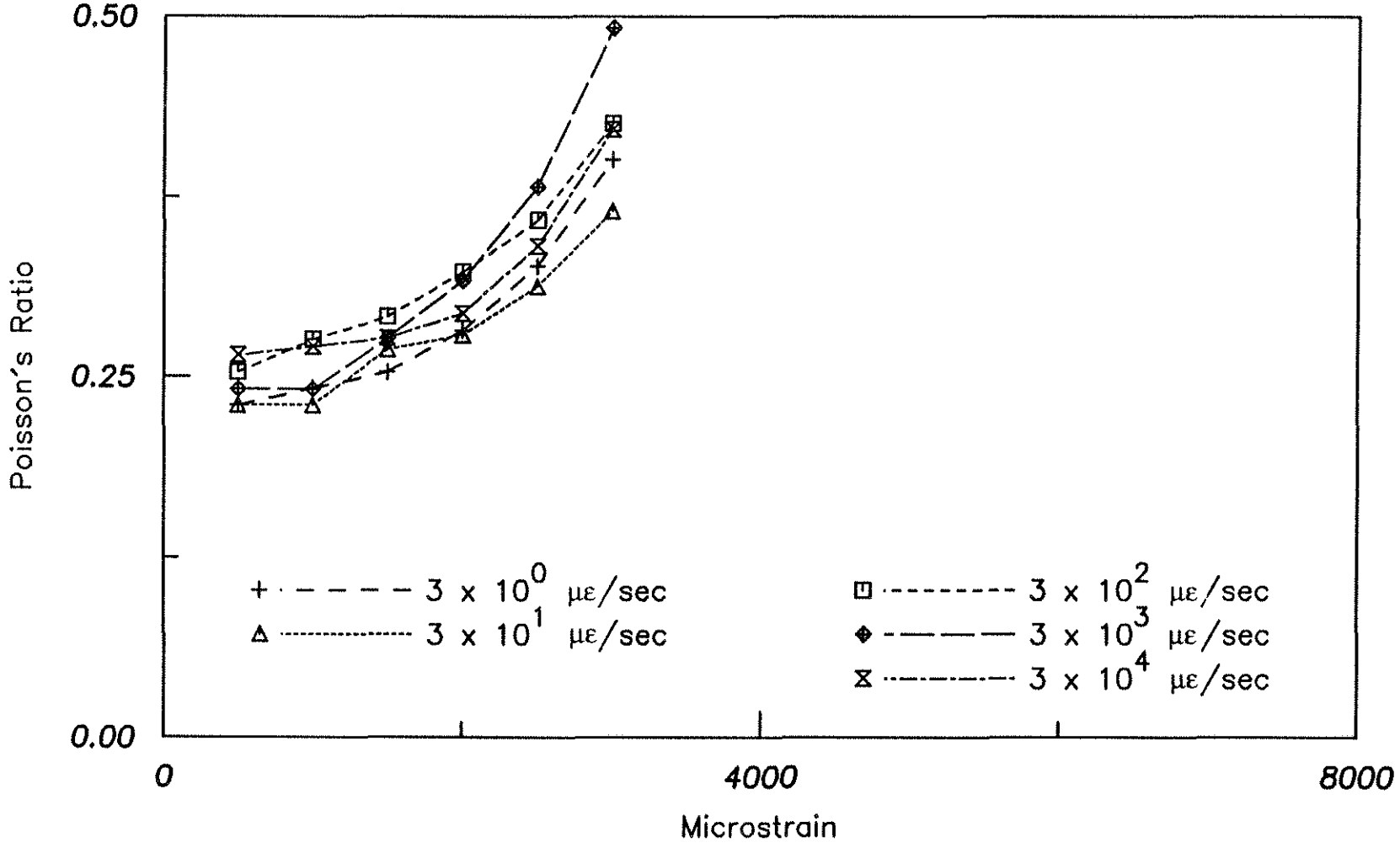

Fig. 2.28 Poisson's Ratio versus Strain at Different Strain Rates for Mortar B with W/C = 0.4

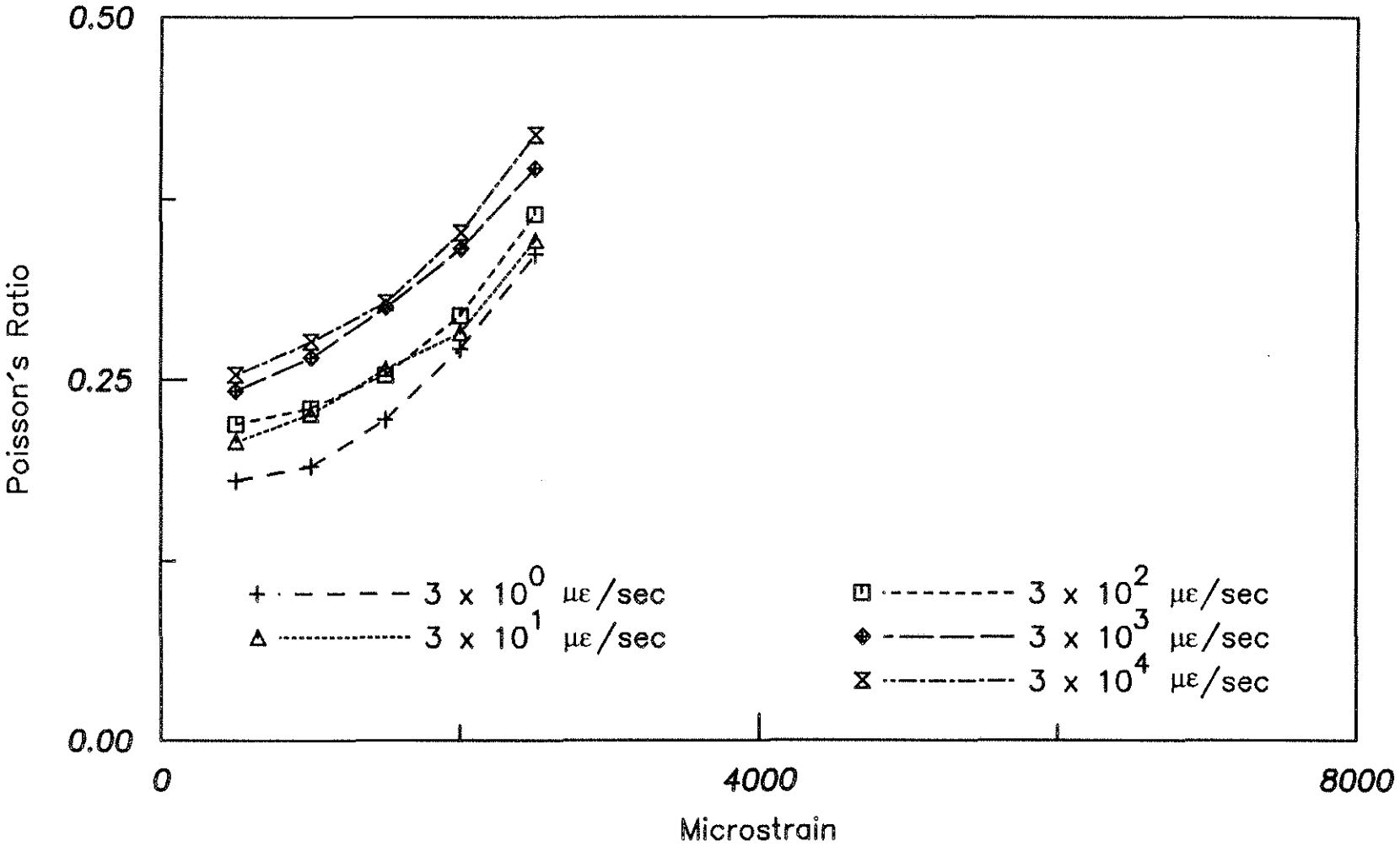

Fig. 2.29 Poisson's Ratio versus Strain at Different Strain Rates for Mortar A with W/C = 0.5

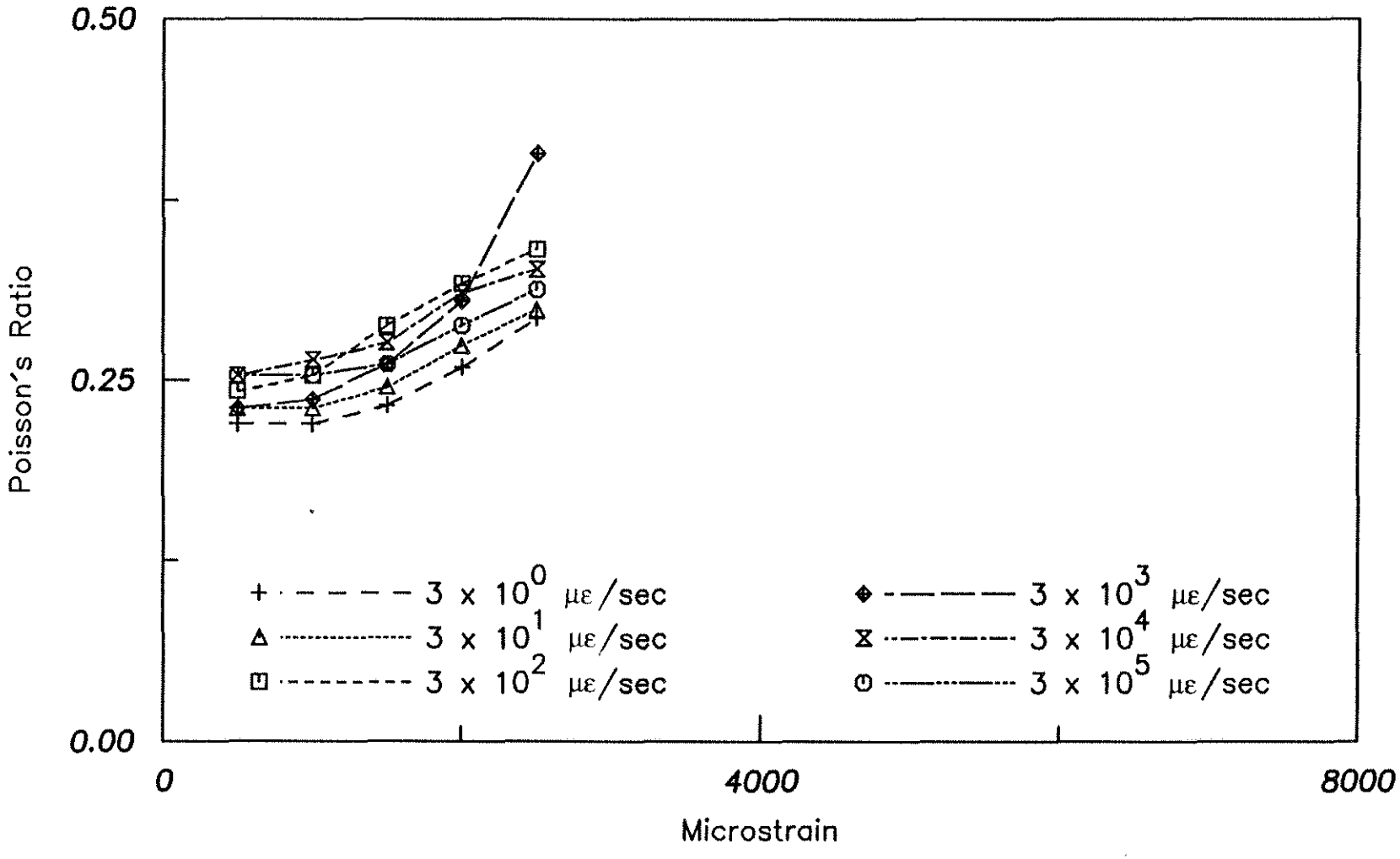

Fig. 2.30 Poisson's Ratio versus Strain at Different Strain Rates for Mortar B with W/C = 0.5

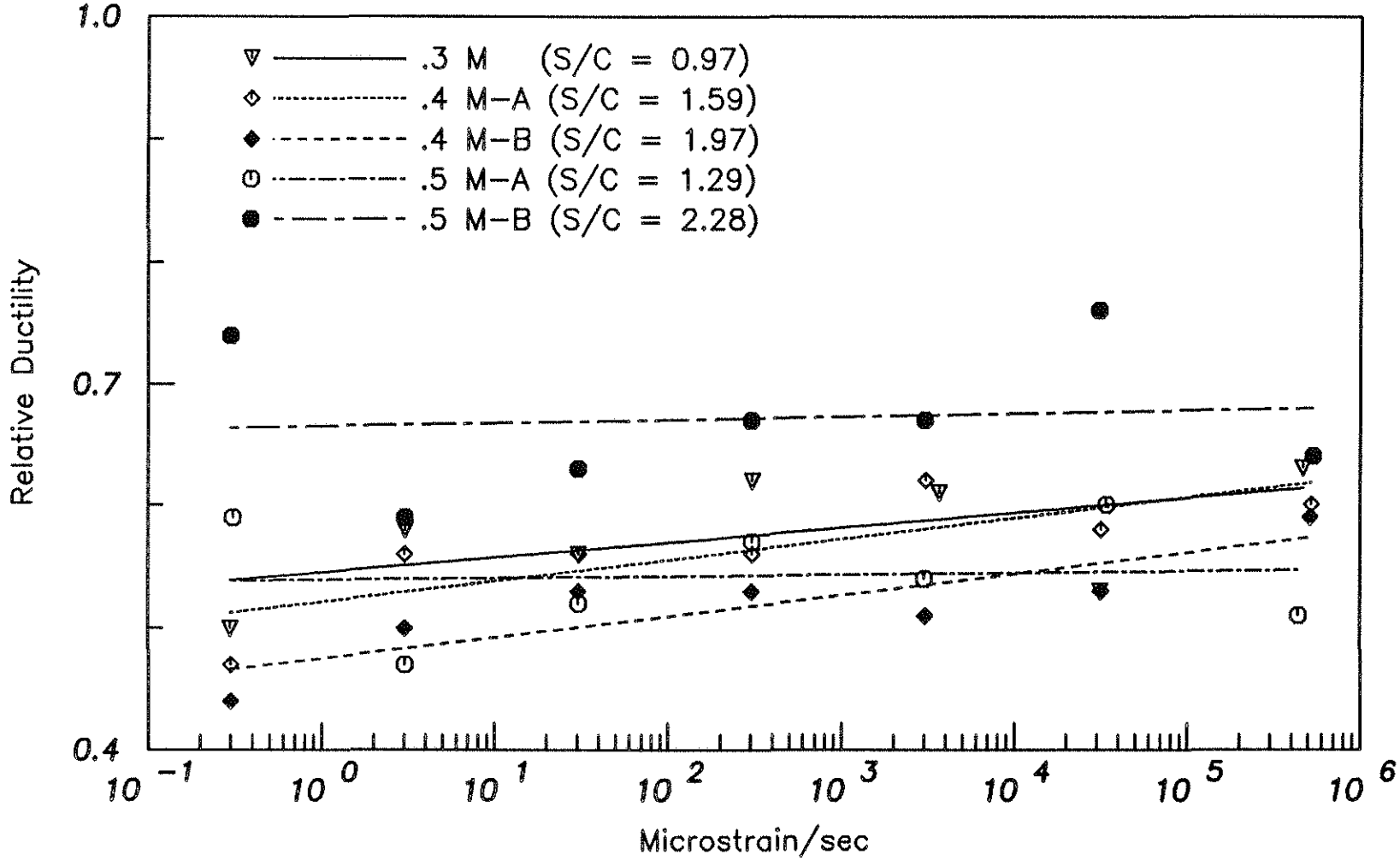

Fig. 2.31 Relative Ductility, the Ratio of ε_{pp} for Mortar and ε_{pp} of the Same Water-Cement Ratio Paste, versus Strain Rate ($\dot{\varepsilon}_{50-99}$) for Mortars with W/C = 0.3, 0.4, and 0.5

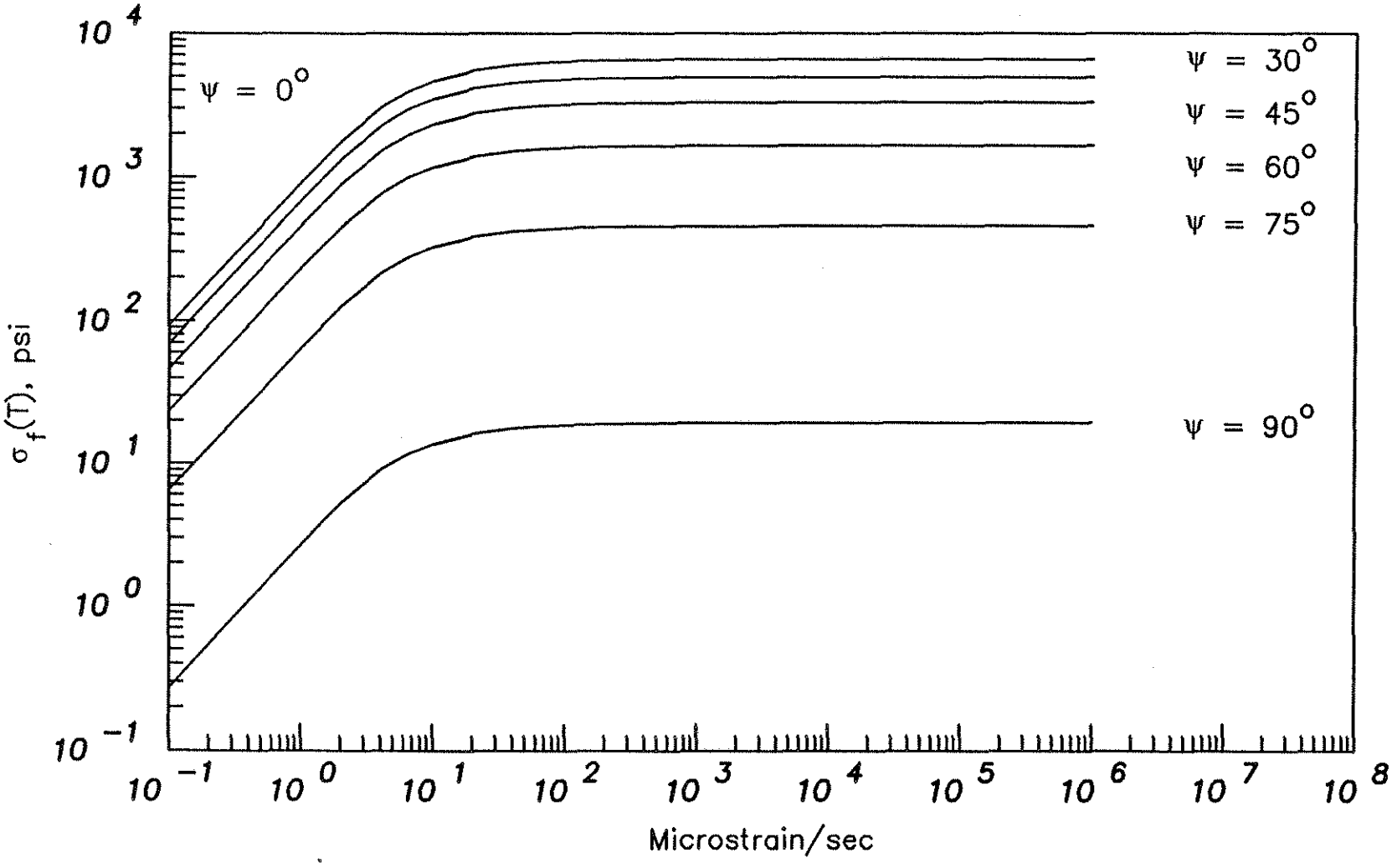

Fig. 3.1 Hydrostatic Stress in Pore Fluid, $\sigma_f(T)$, for an Oblate Spheroidal Pore with Aspect Ratio r = 0.02 at Various Orientations, ψ

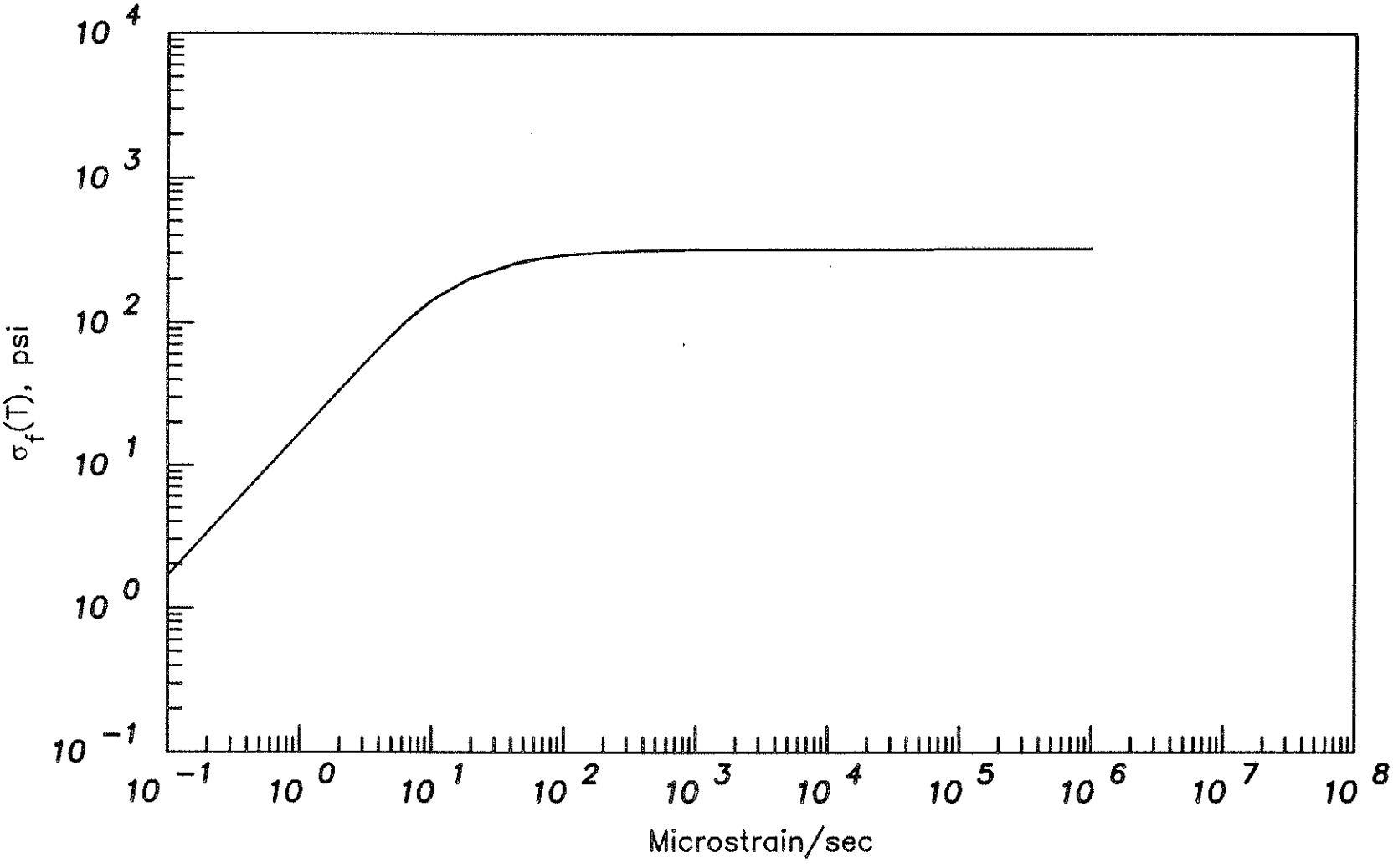

Fig. 3.2 Hydrostatic Stress in Pore Fluid, $\sigma_f(T)$, for a Spherical Pore

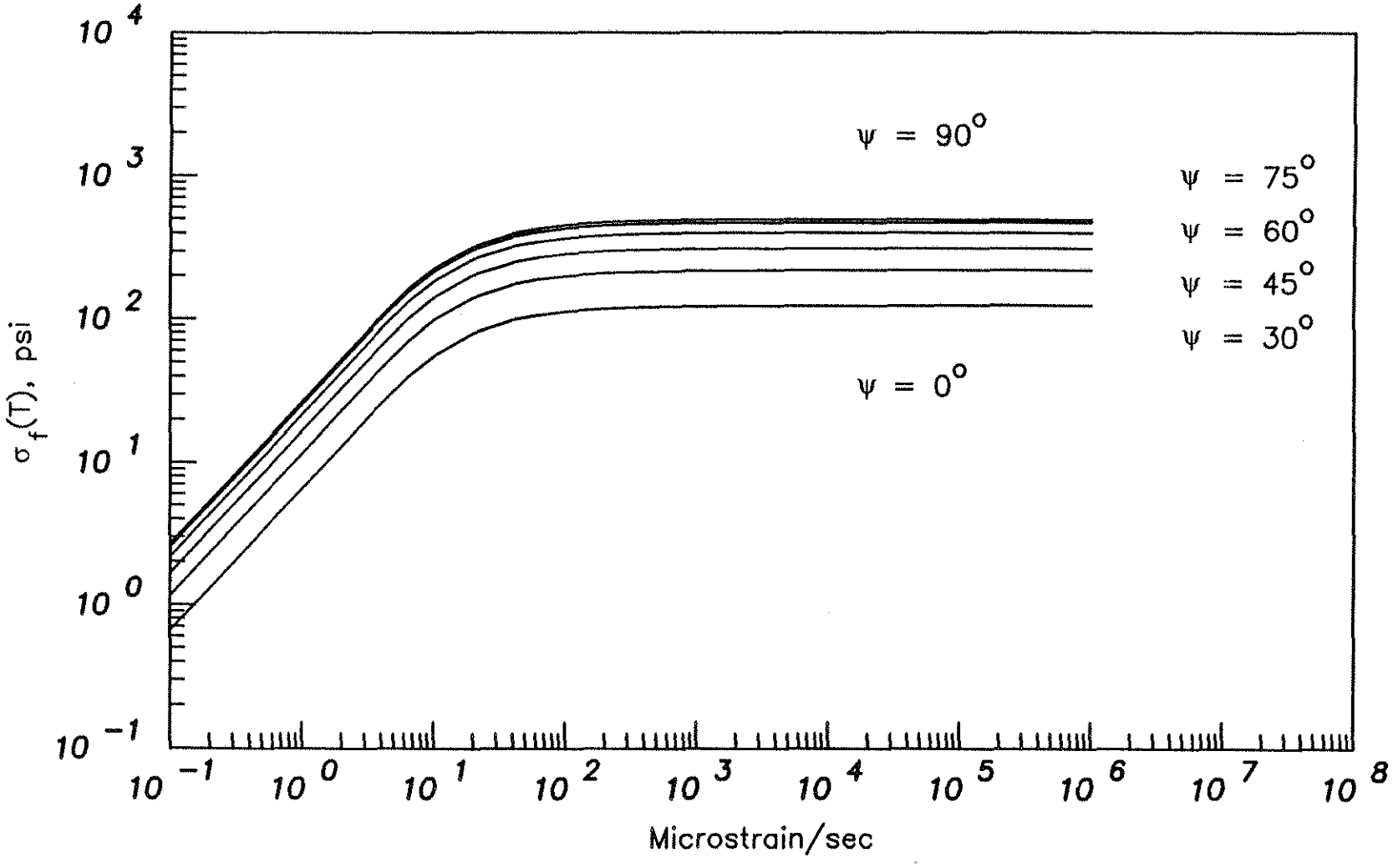

Fig. 3.3 Hydrostatic Stress in Pore Fluid, $\sigma_f(T)$, for an Prolate Spheroidal Pore with Aspect Ratio r = 10.0 at Various Orientations, ψ

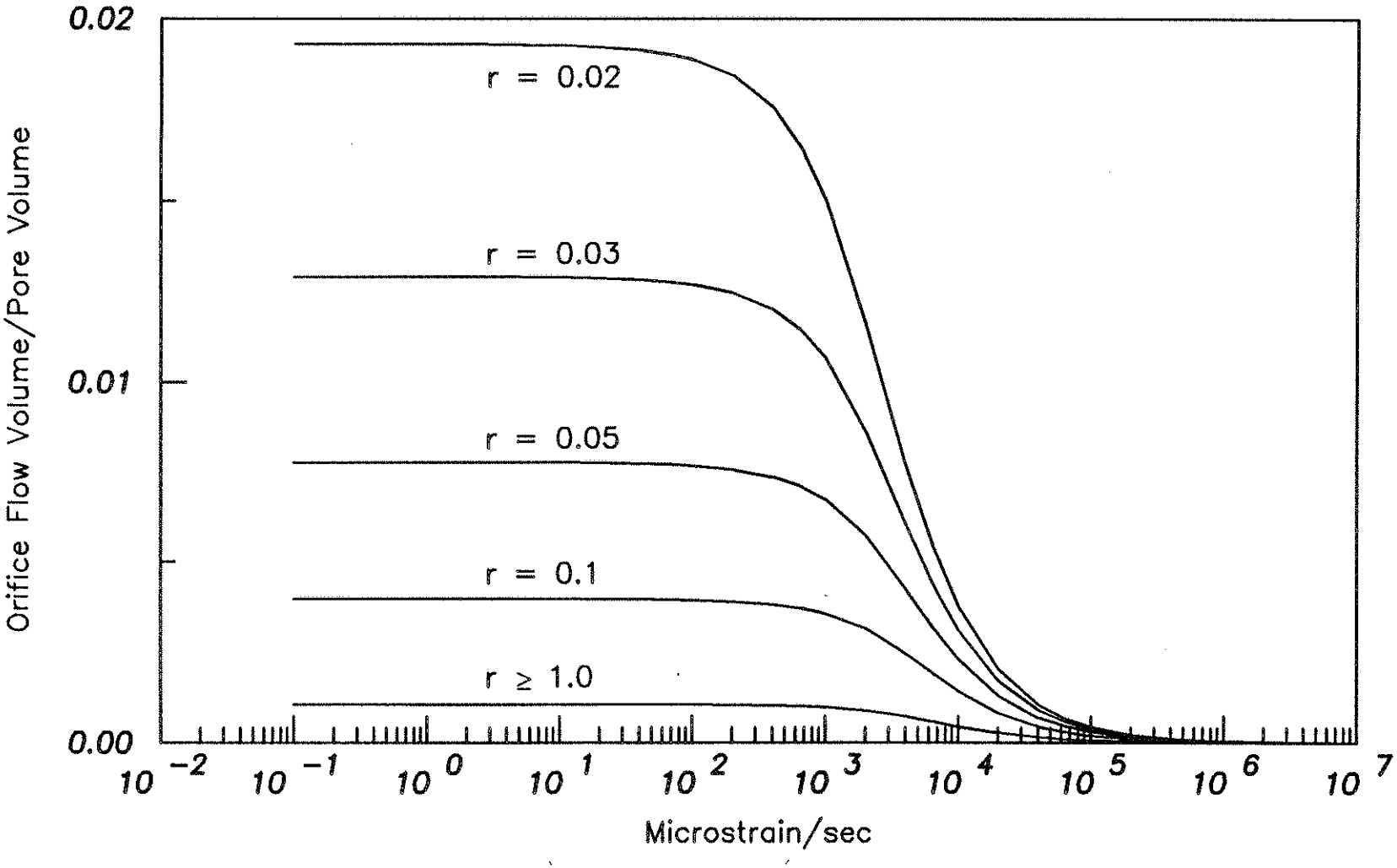

Fig. 4.4 Cumulative Orifice Flow Volume at All Orientations versus Strain Rate For Pores with Various Aspect Ratio, r

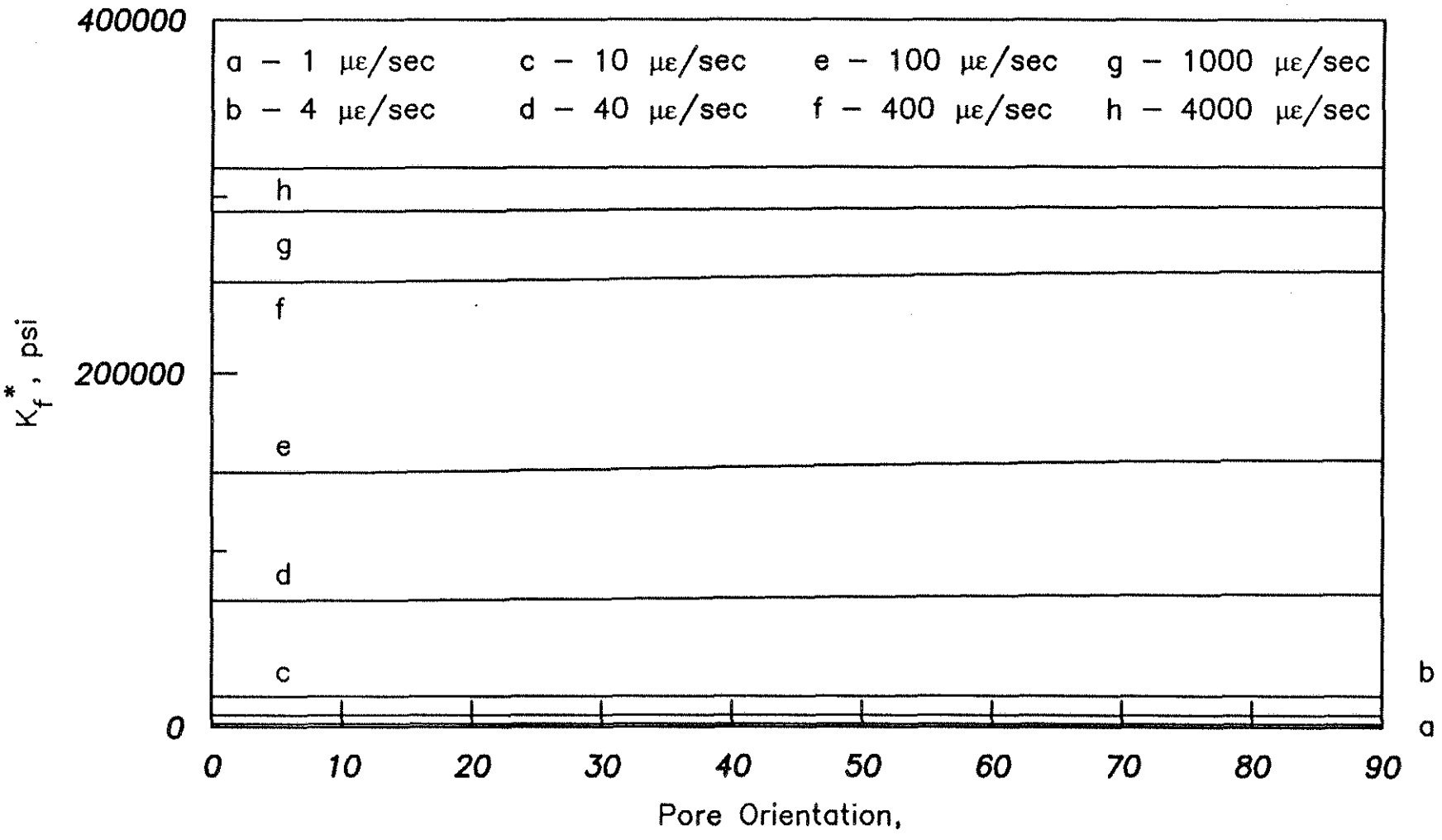

Fig. 3.5 Effective Bulk Modulus of a Pore, K_f^*, versus Pore Orientation, ψ, for Strain Rates in the Range 1 to 4000 με/sec

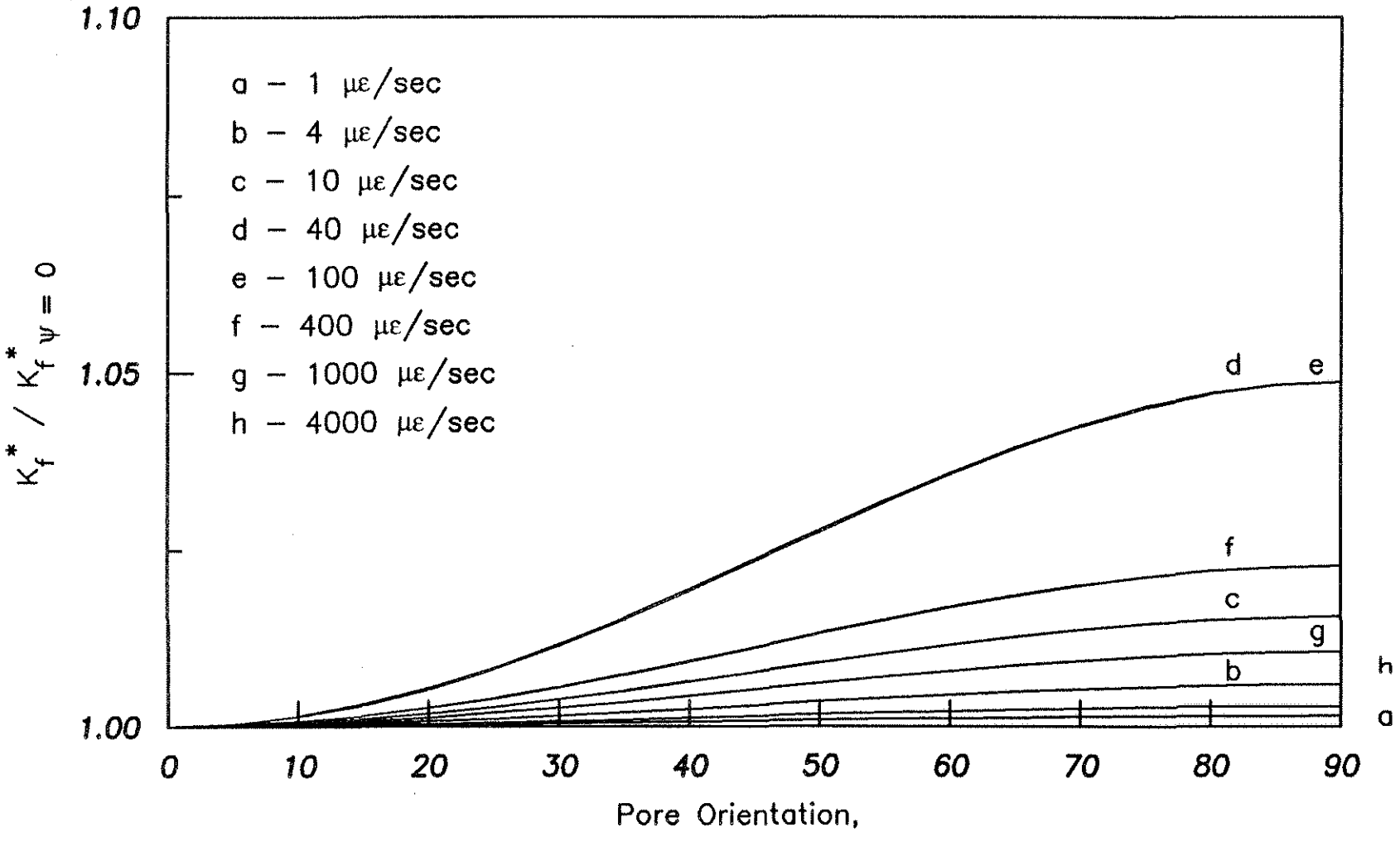

Fig. 3.6 Normalized Effective Bulk Modulus of a Pore, $K_f^*/K_{f\psi=0}^*$, versus Pore Orientation, ψ, for Strain Rates in the Range 1 to 4000 με/sec

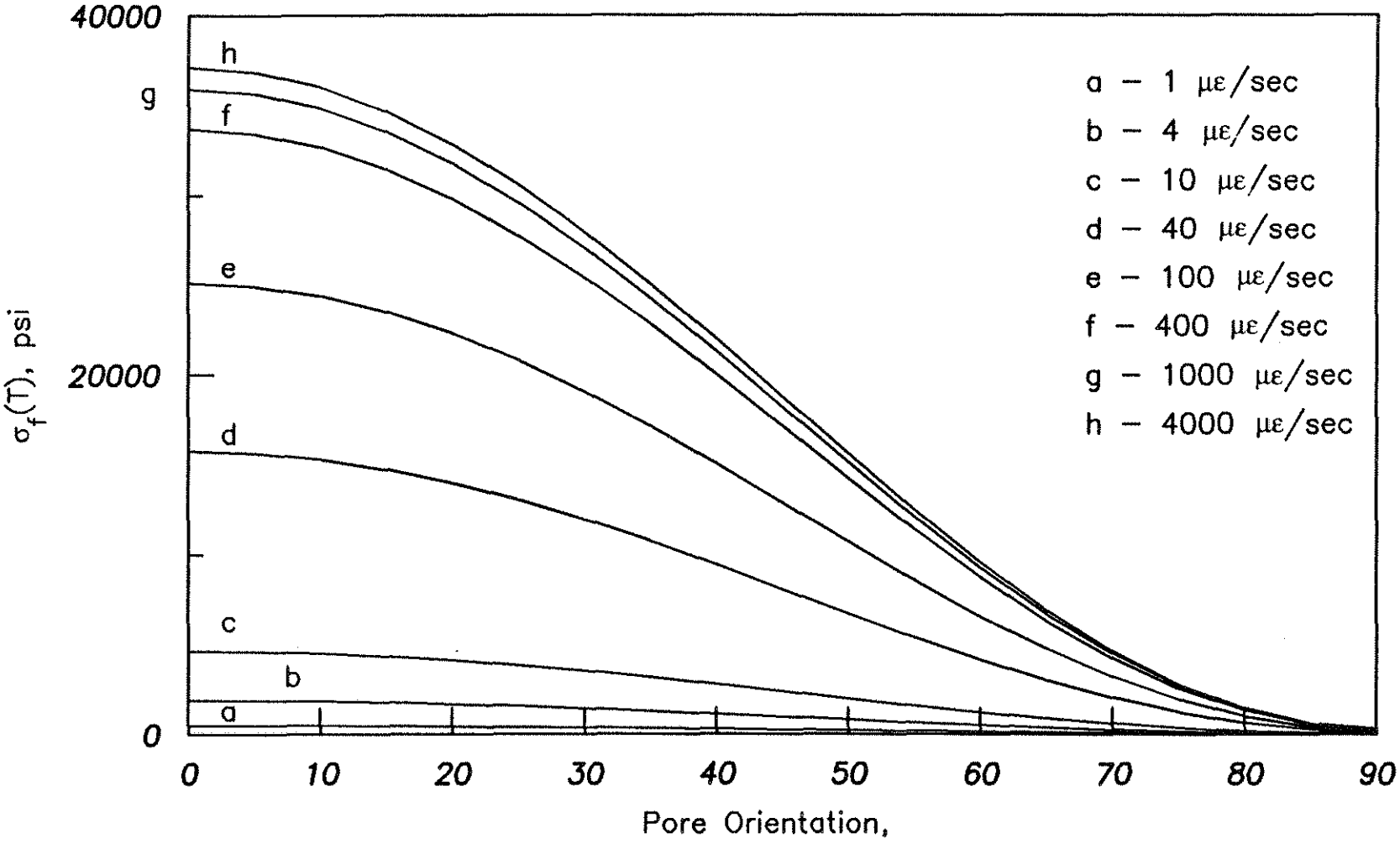

Fig. 3.7 Hydrostatic Stress in the Pore Fluid, $\sigma_f(T)$, versus Pore Orientation, ψ, for Strain Rates in the Range 1 to 4000 με/sec

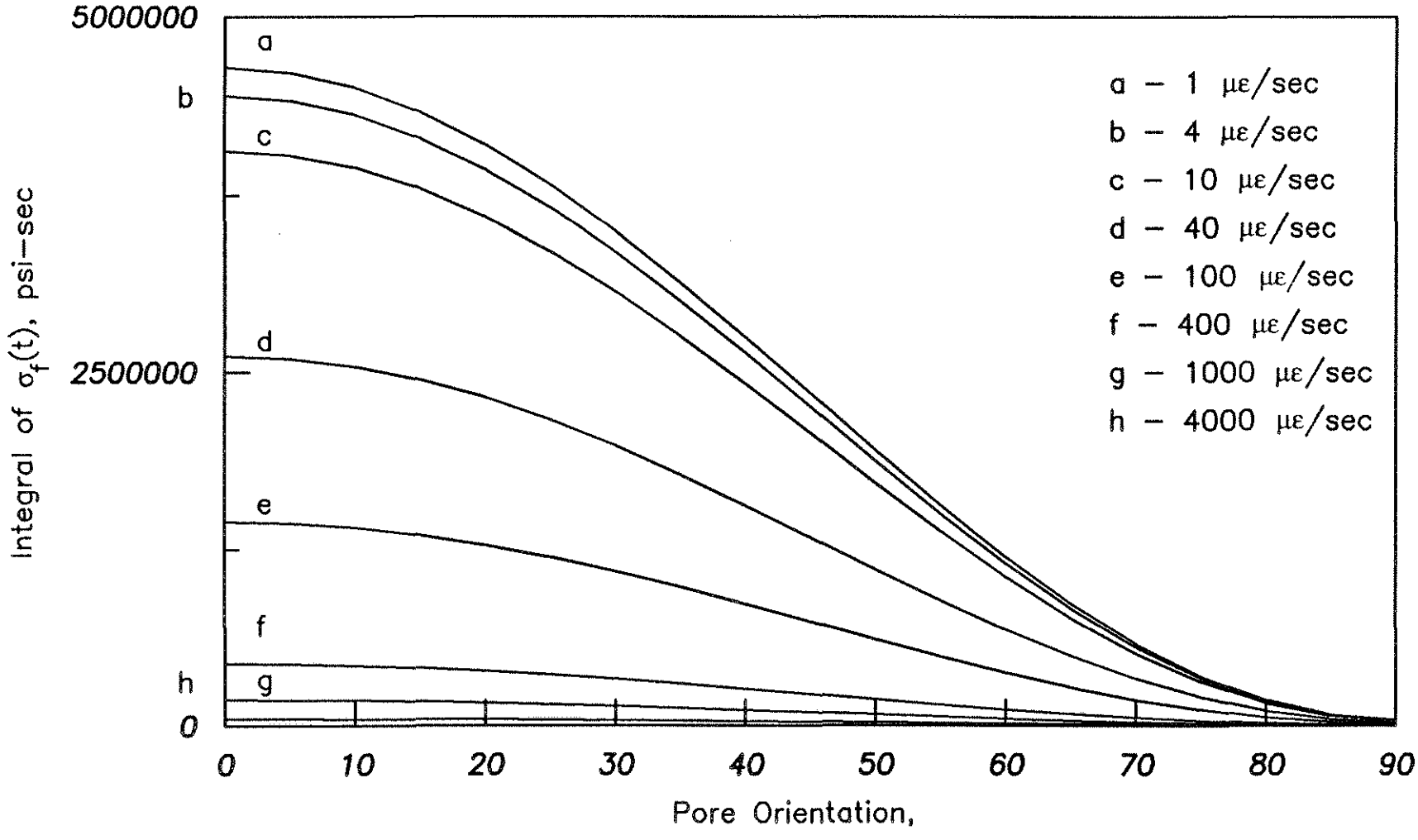

Fig. 3.8 Integral of Hydrostatic Stress in the Pore Fluid, $\sigma_f(t)$, with Respect to Time versus Pore Orientation, ψ, for Strain Rates in the Range 1 to 4000 με/sec

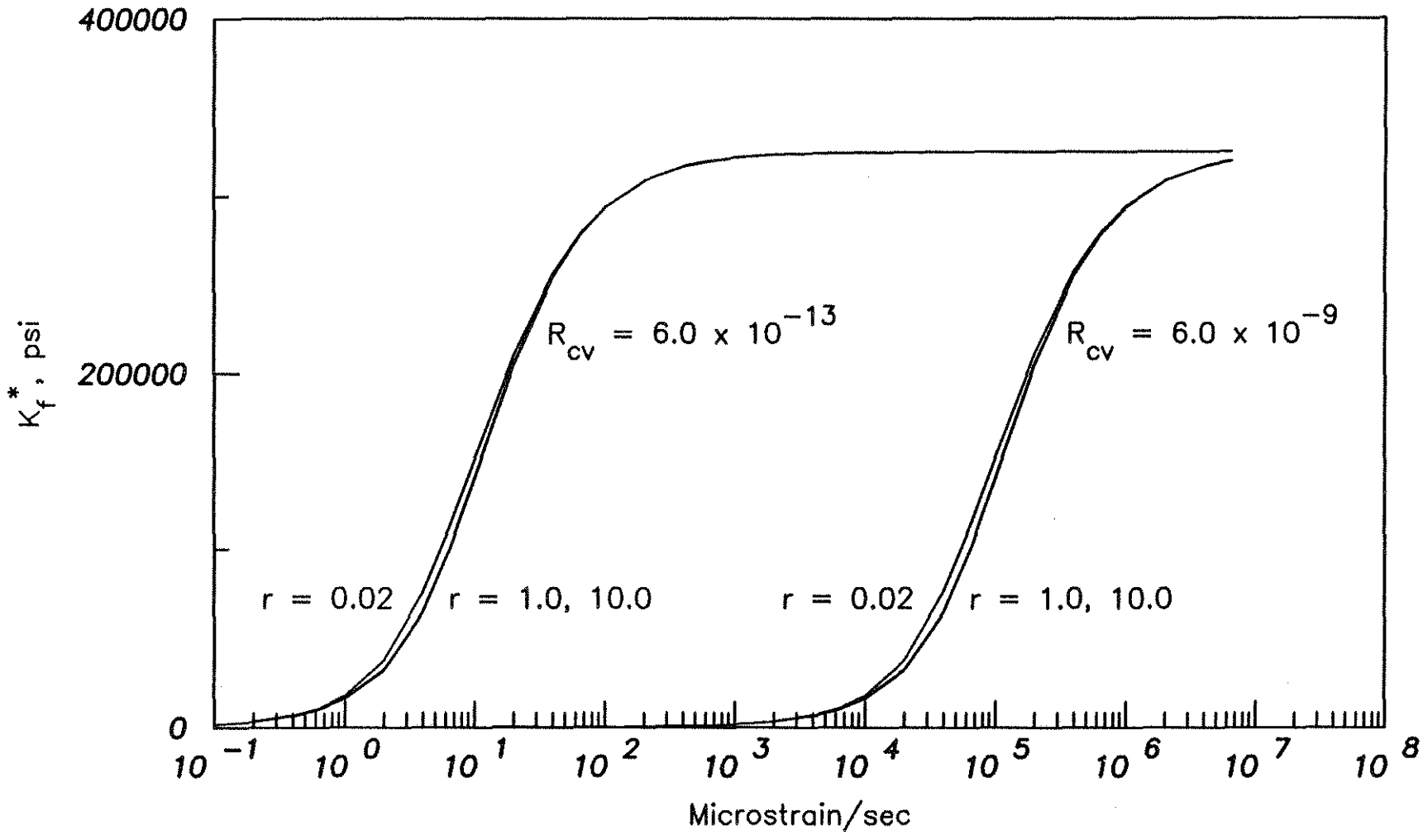

Fig. 3.9 Effective Bulk Modulus of a Pore, K_f^*, versus Strain Rate for Two Values of R_{cv} and Three Aspect Ratio, r

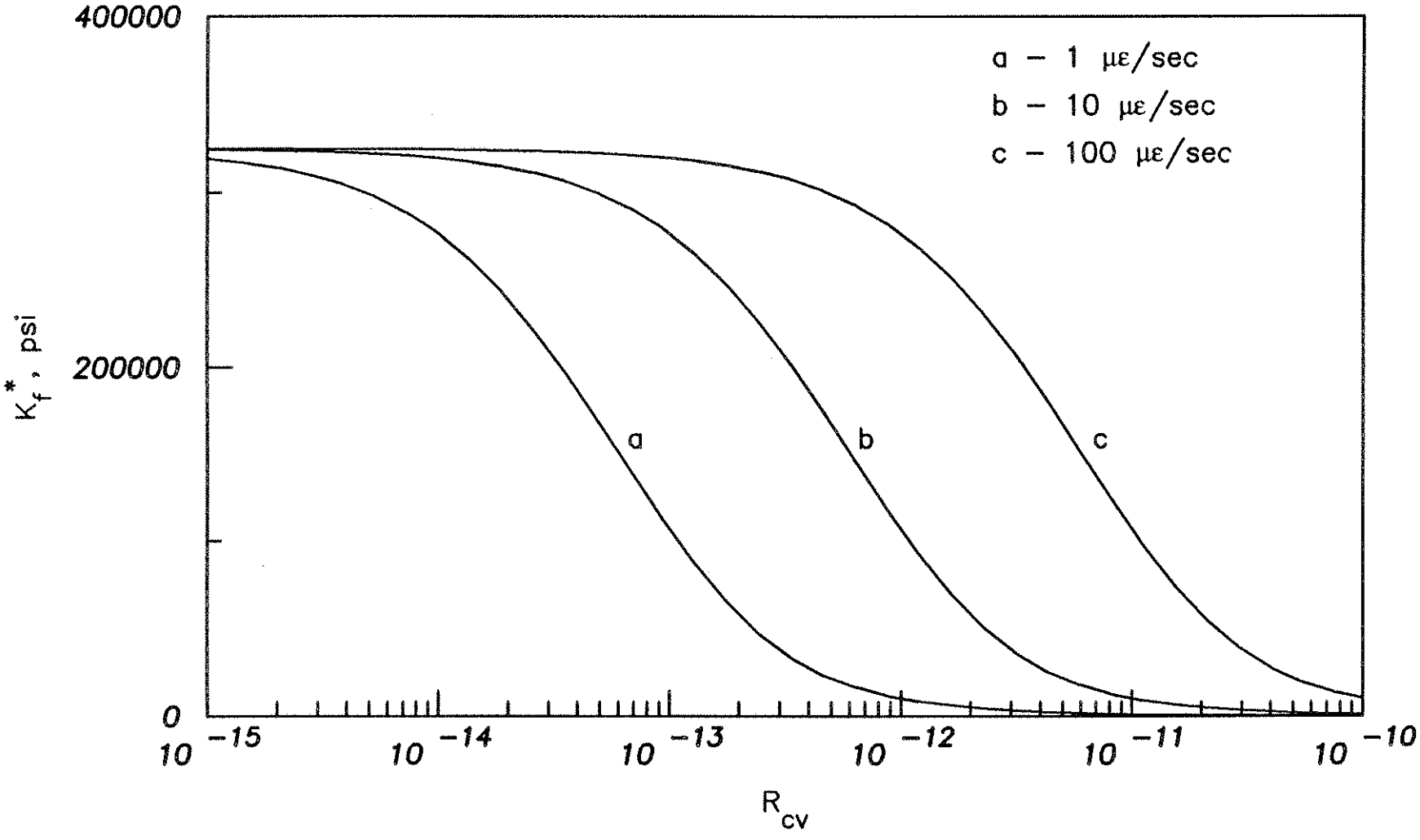

Fig. 3.10 Effective Bulk Modulus of a Pore, K_f^*, versus R_{cv} with Aspect Ratio r = 0.02 at Three Strain Rates

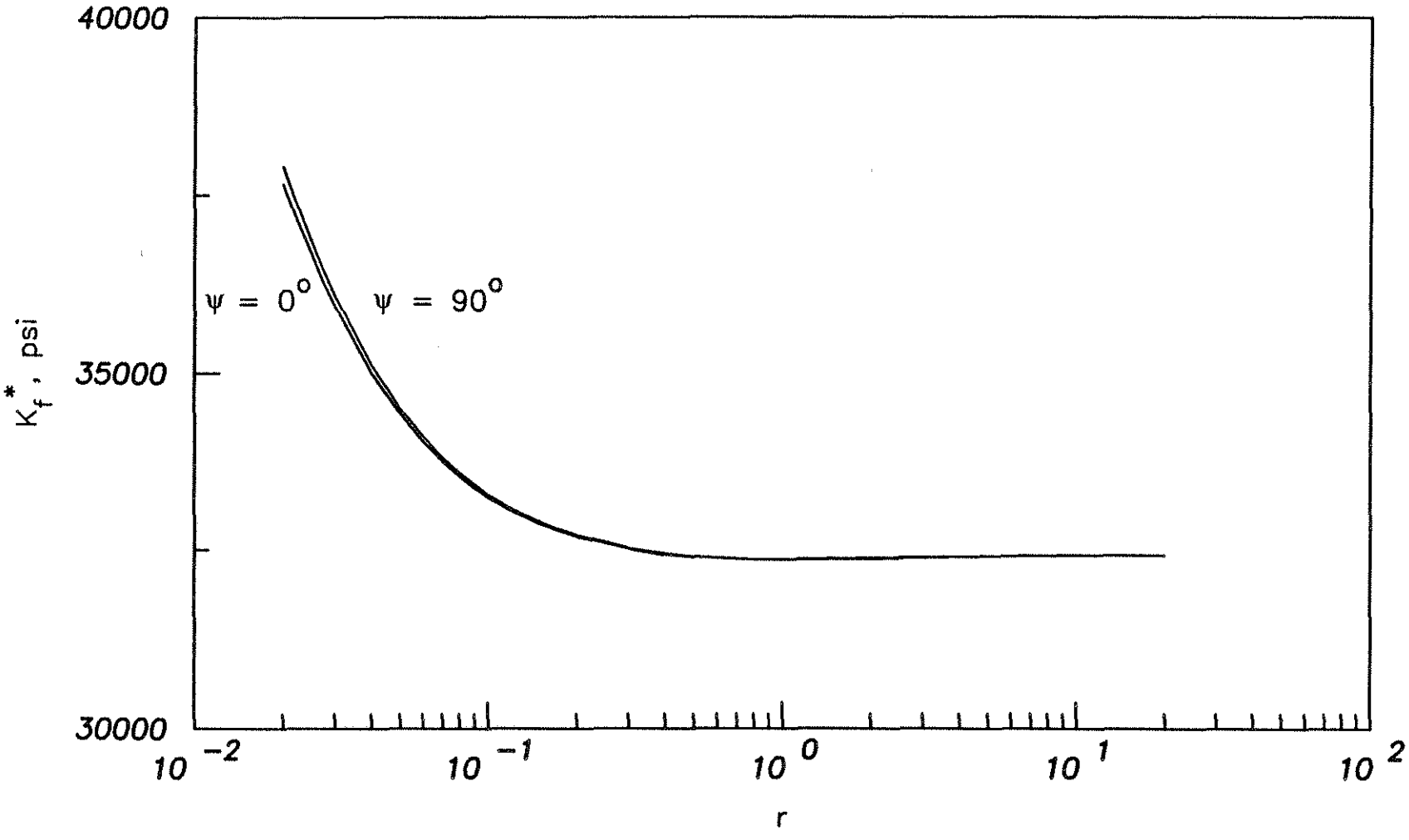

Fig. 3.11 Effective Bulk Modulus of a Pore, K_f^*, versus Pore Aspect Ratio, r, at Strain Rate = 2 με/sec for Two Pore Orientations, ψ = 0° and 90°

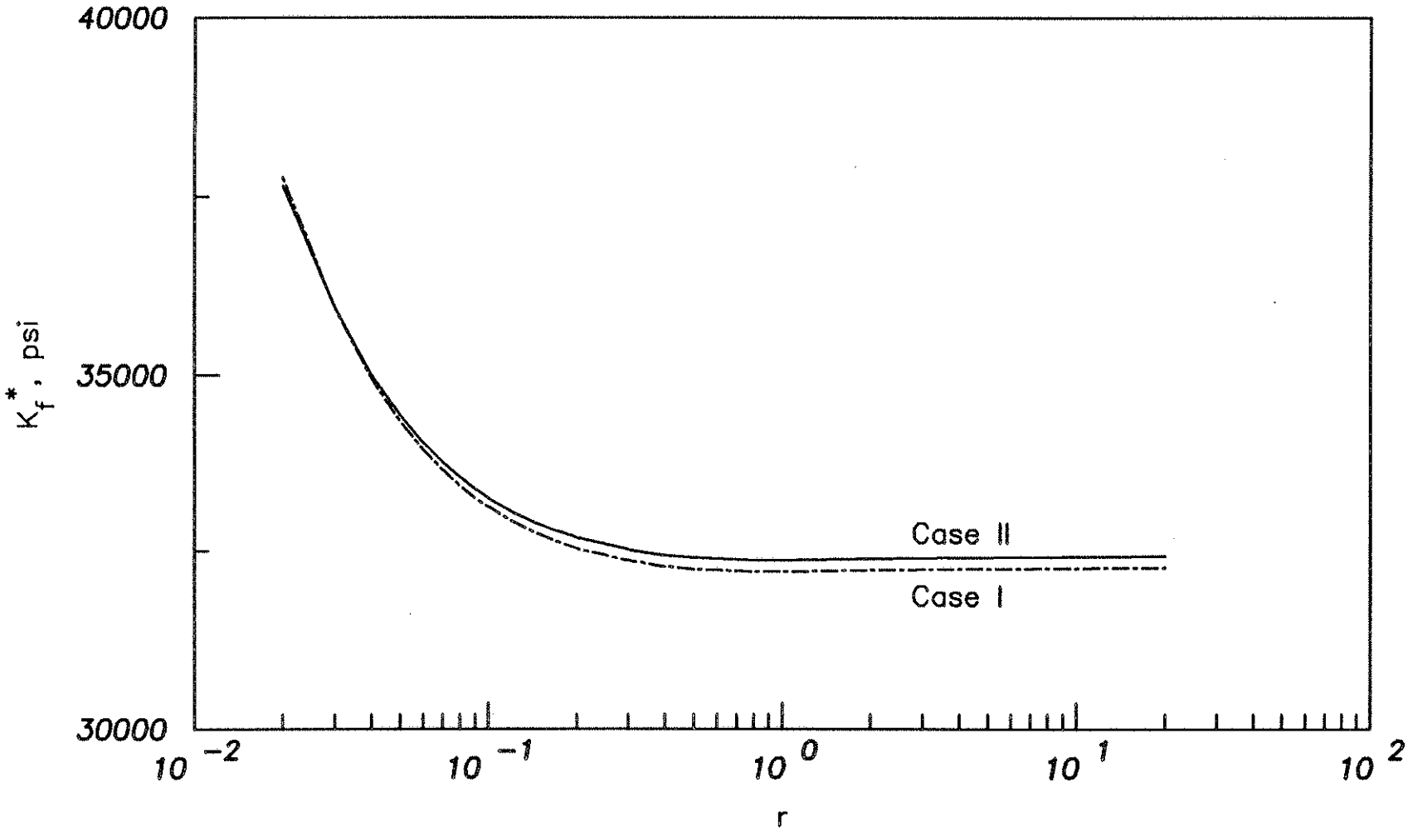

Fig. 3.12 Effective Bulk Modulus of a Pore, K_f^*, versus Pore Aspect Ratio, r, at Pore Orientation $\psi = 0°$ for Case I and Case II

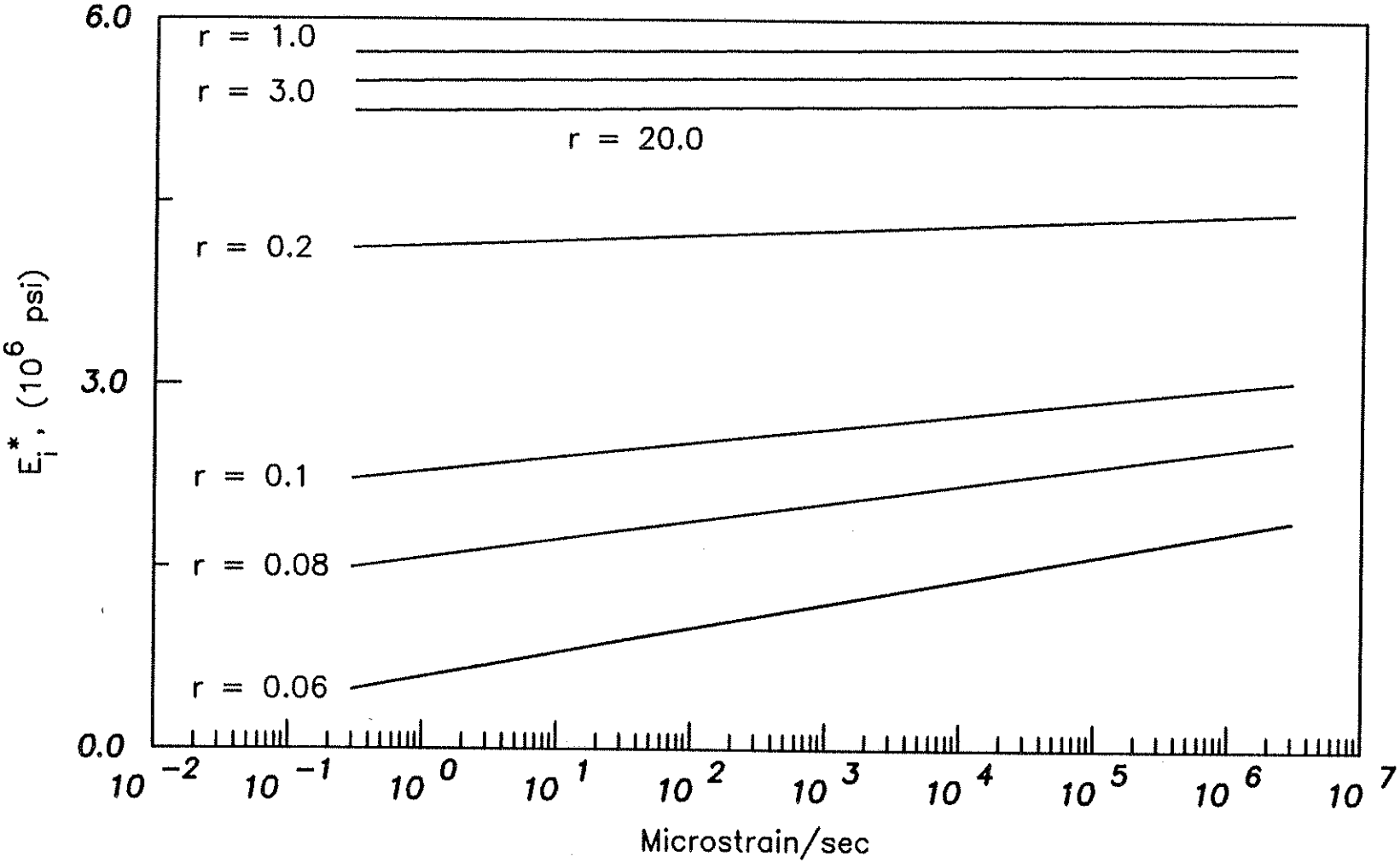

Fig. 3.13 Analytical Elastic Modulus, E_i^*, versus Strain Rate for Various Aspect Ratios in the Range r = 0.06 to 20.0

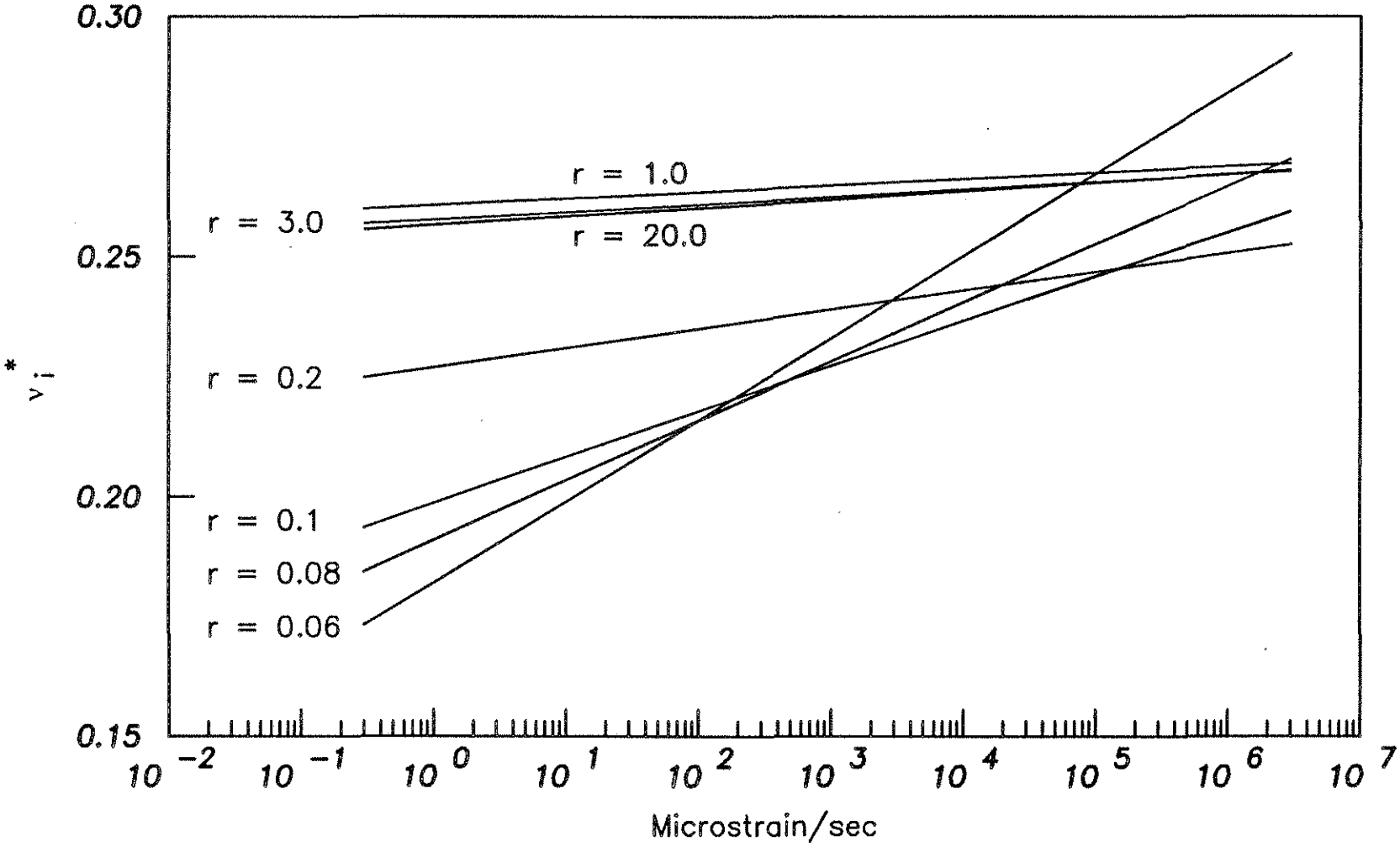

Fig. 3.14 Analytical Poisson's Ratio, ν_i^*, versus Strain Rate for Various Aspect Ratios in the Range r = 0.06 to 20.0

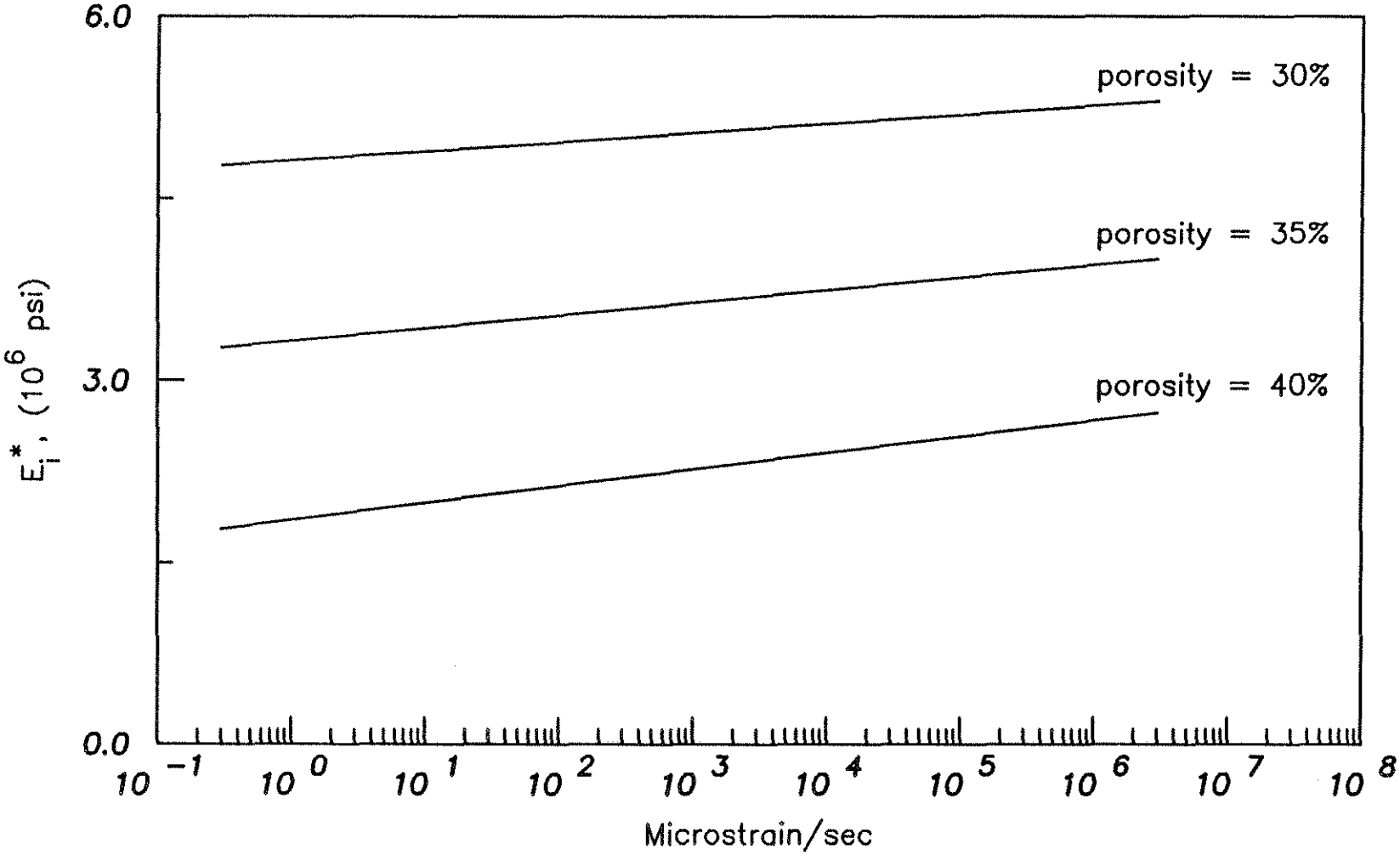

Fig. 3.15 Analytical Elastic Modulus, E_i^*, versus Strain Rate for Porosity = 30%, 35%, and 40%

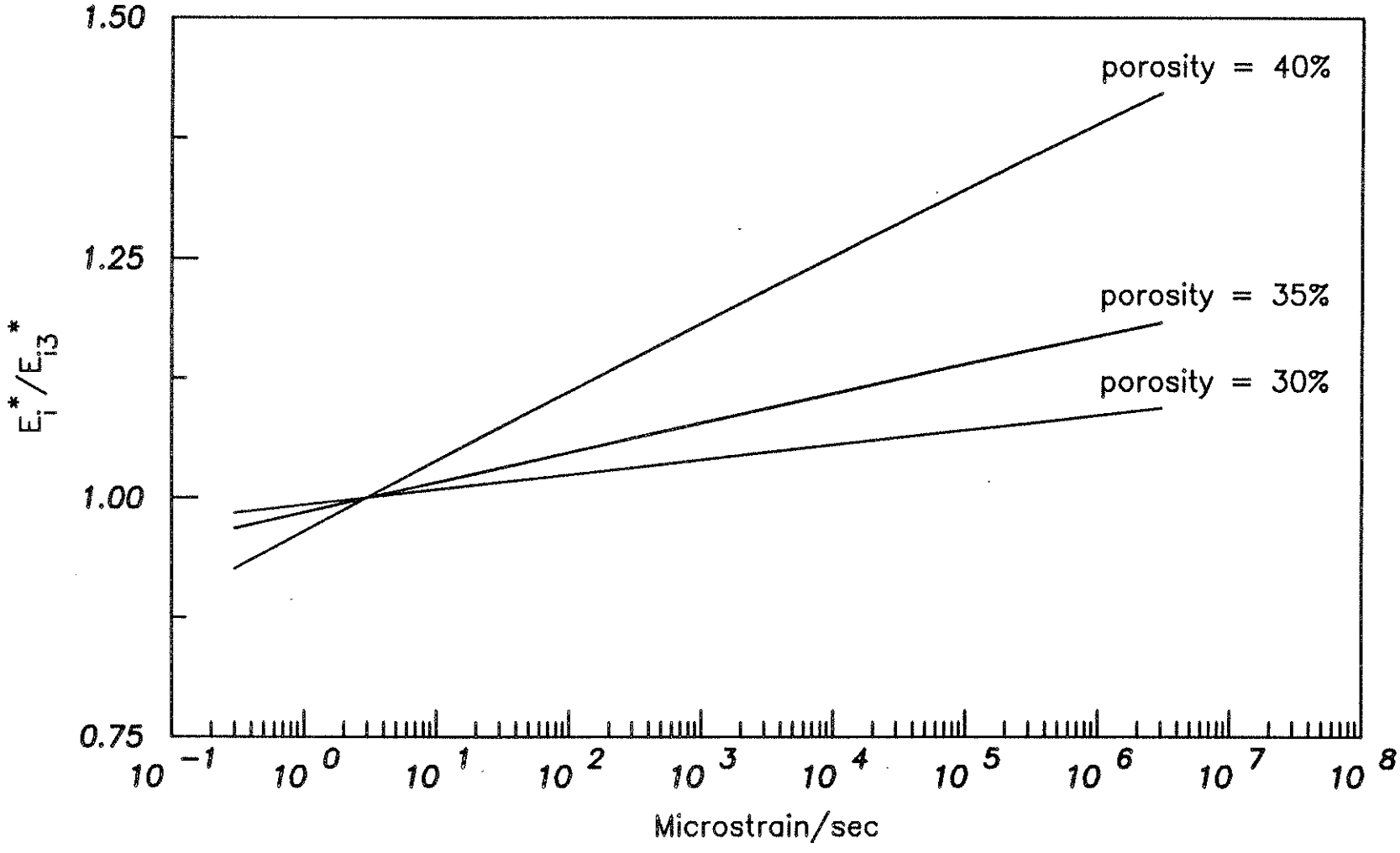

Fig. 3.16 Normalized Analytical Elastic Modulus, E_i^*/E_{i3}^* (E_{i3}^* = Elastic Modulus at 3 με/sec), versus Strain Rate for Porosity = 30%, 35%, and 40%

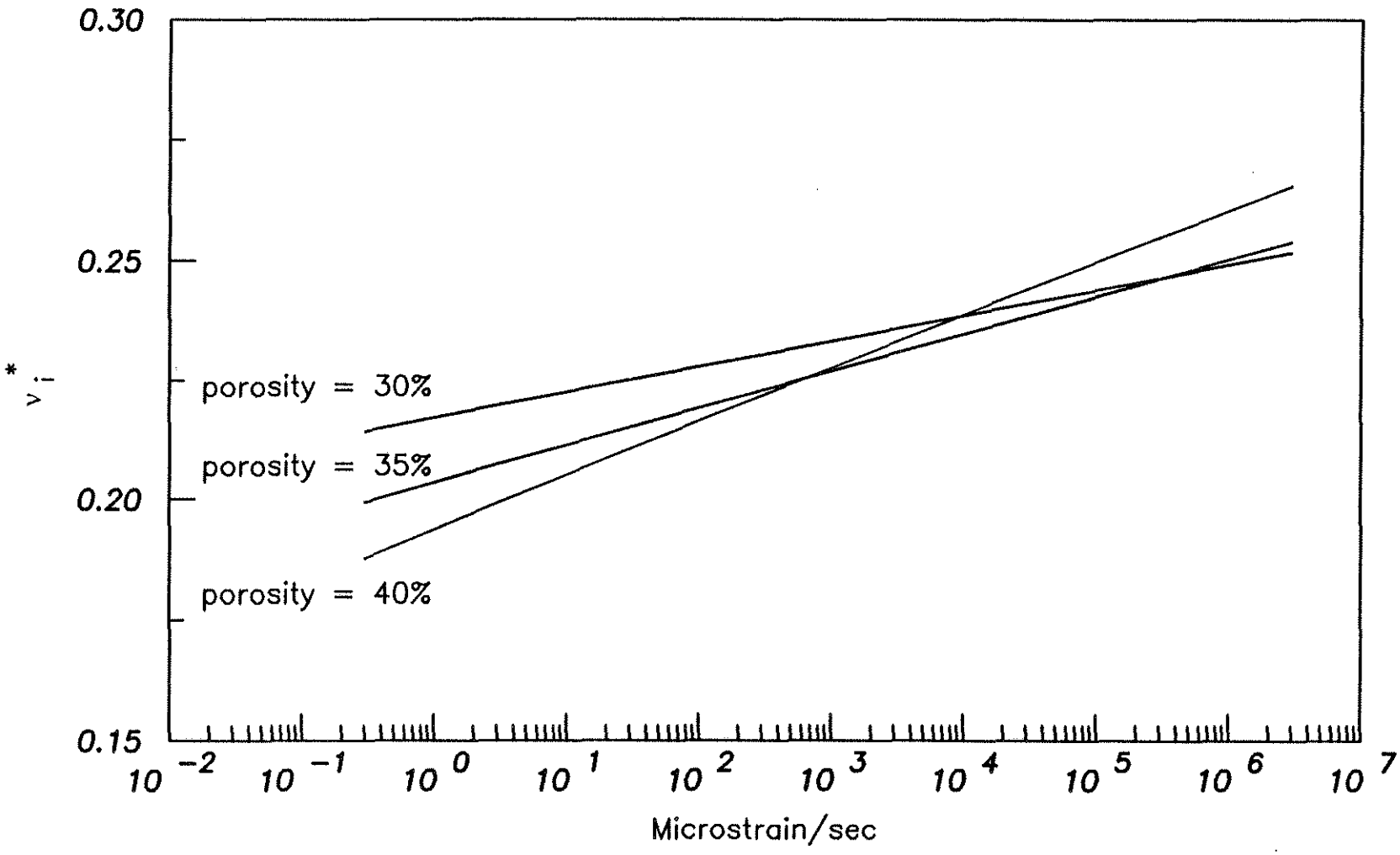

Fig. 3.17 Analytical Poisson's Ratio, ν_i^*, versus Strain Rate for Porosity = 30%, 35%, and 40%

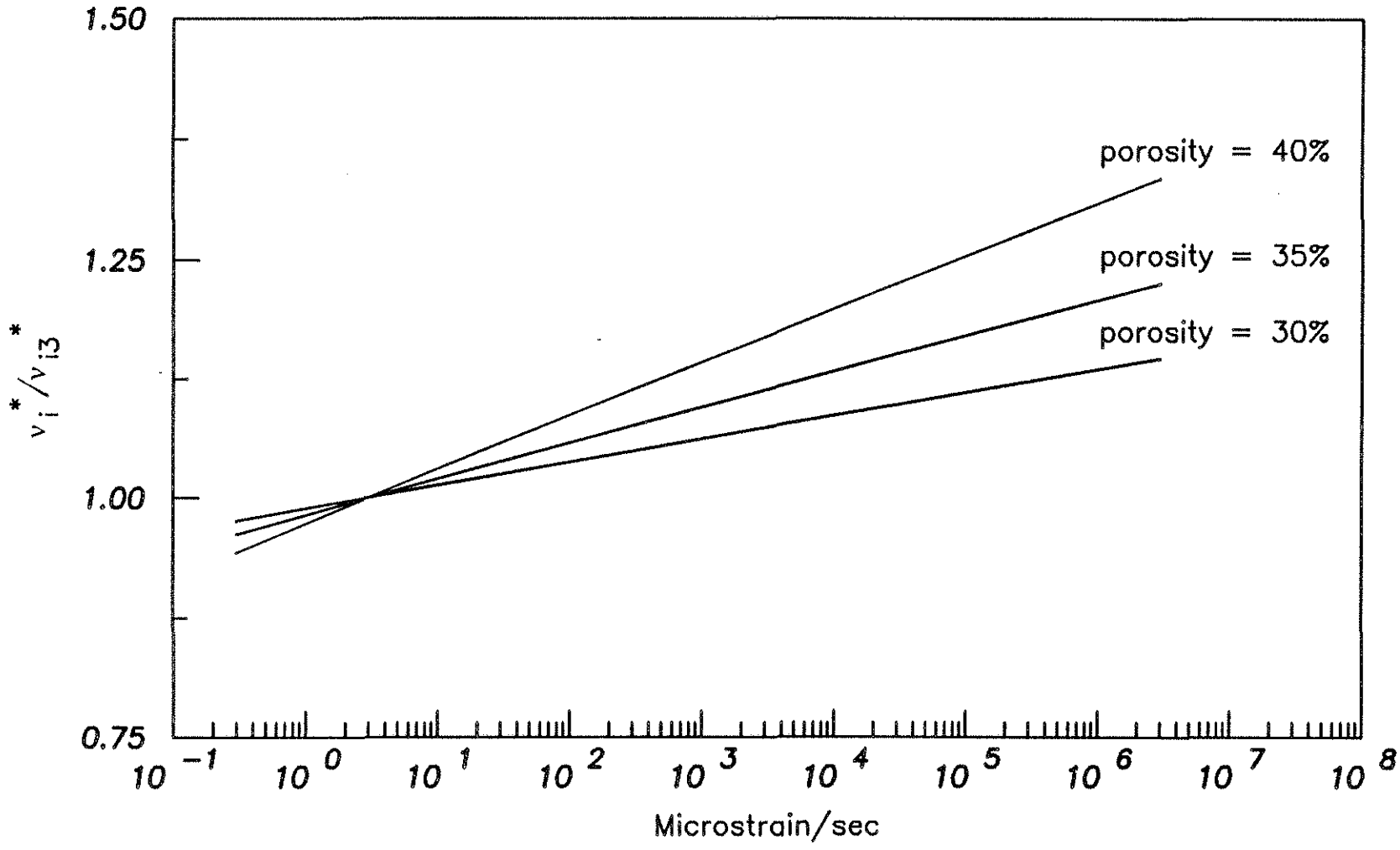

Fig. 3.18 Normalized Analytical Poisson's Ratio, ν_i^*/ν_{i3}^* (ν_{i3}^* = Poisson's Ratio at 3 με/sec), versus Strain Rate for Porosity = 30%, 35%, and 40%

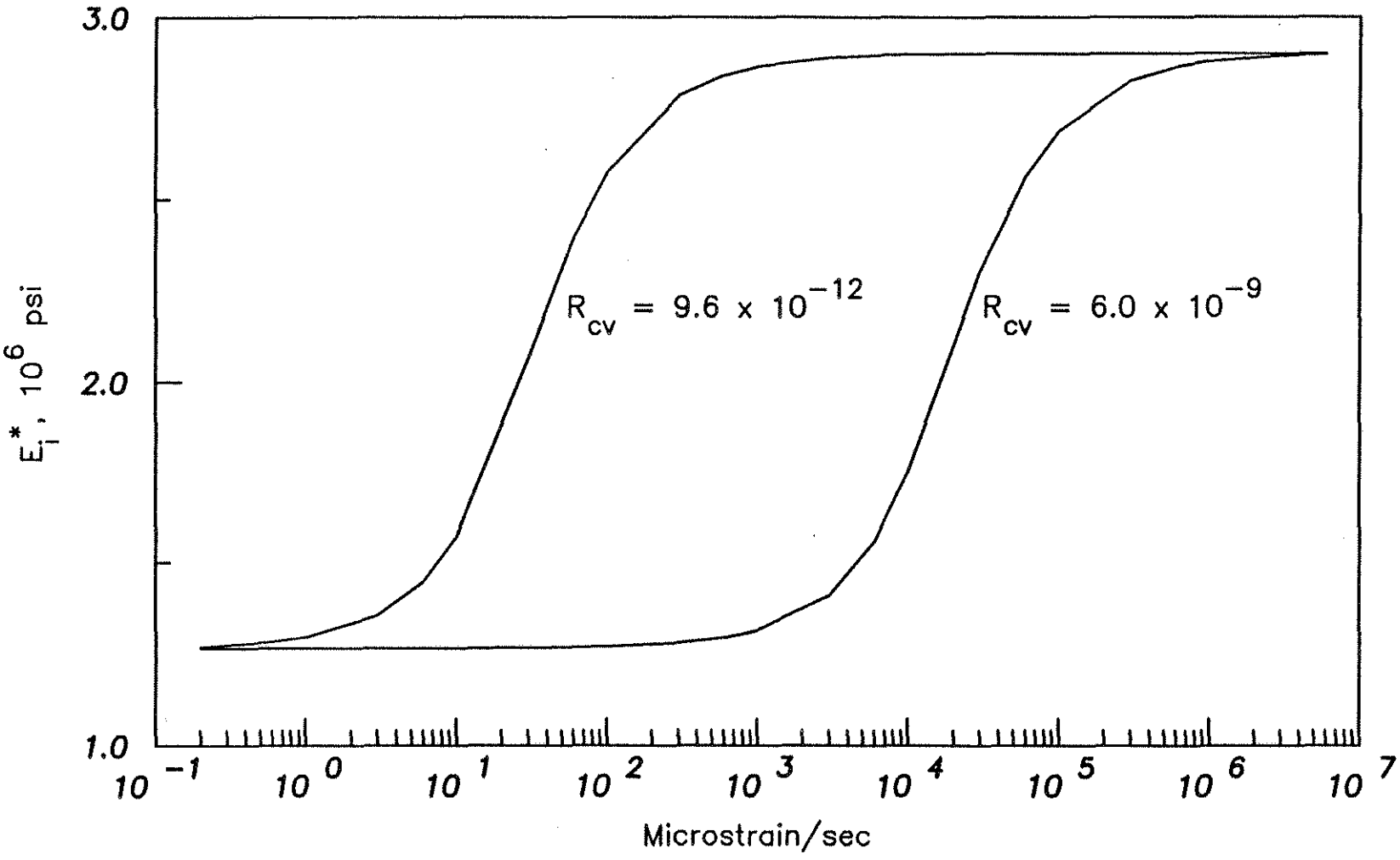

Fig. 3.19 Analytical Elastic Modulus, E_i^*, versus Strain Rate for Porous Solids Having a Single R_{cv} = 9.6 x 10^{-12} or 6.0 x 10^{-9}

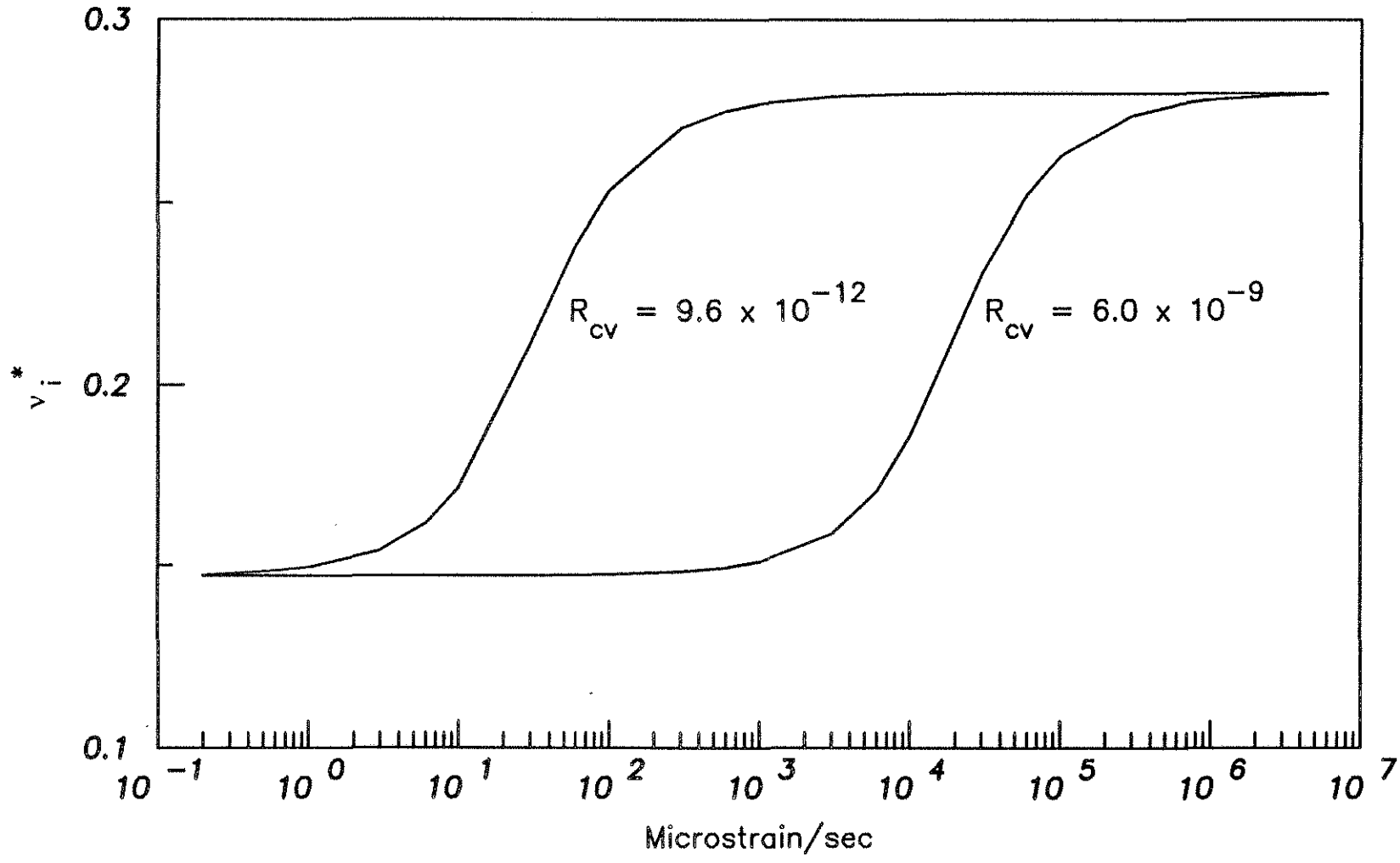

Fig. 3.20 Analytical Poisson's Ratio, ν_i^*, versus Strain Rate for Porous Solids Having a Single $R_{cv} = 9.6 \times 10^{-12}$ or 6.0×10^{-9}

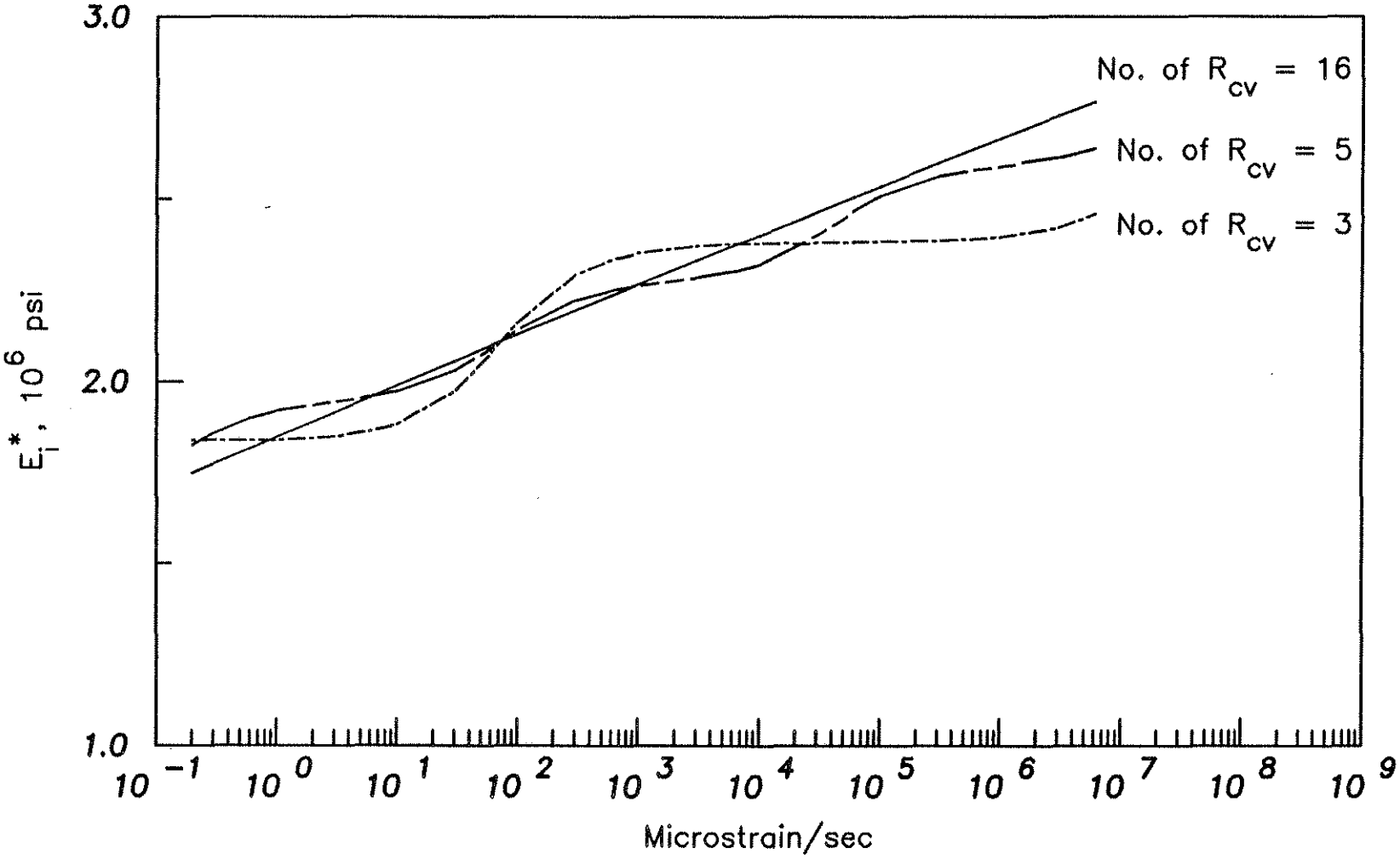

Fig. 3.21 Analytical Elastic Modulus, E_i^*, versus Strain Rate for Porous Solids Having Multiple R_{cv}

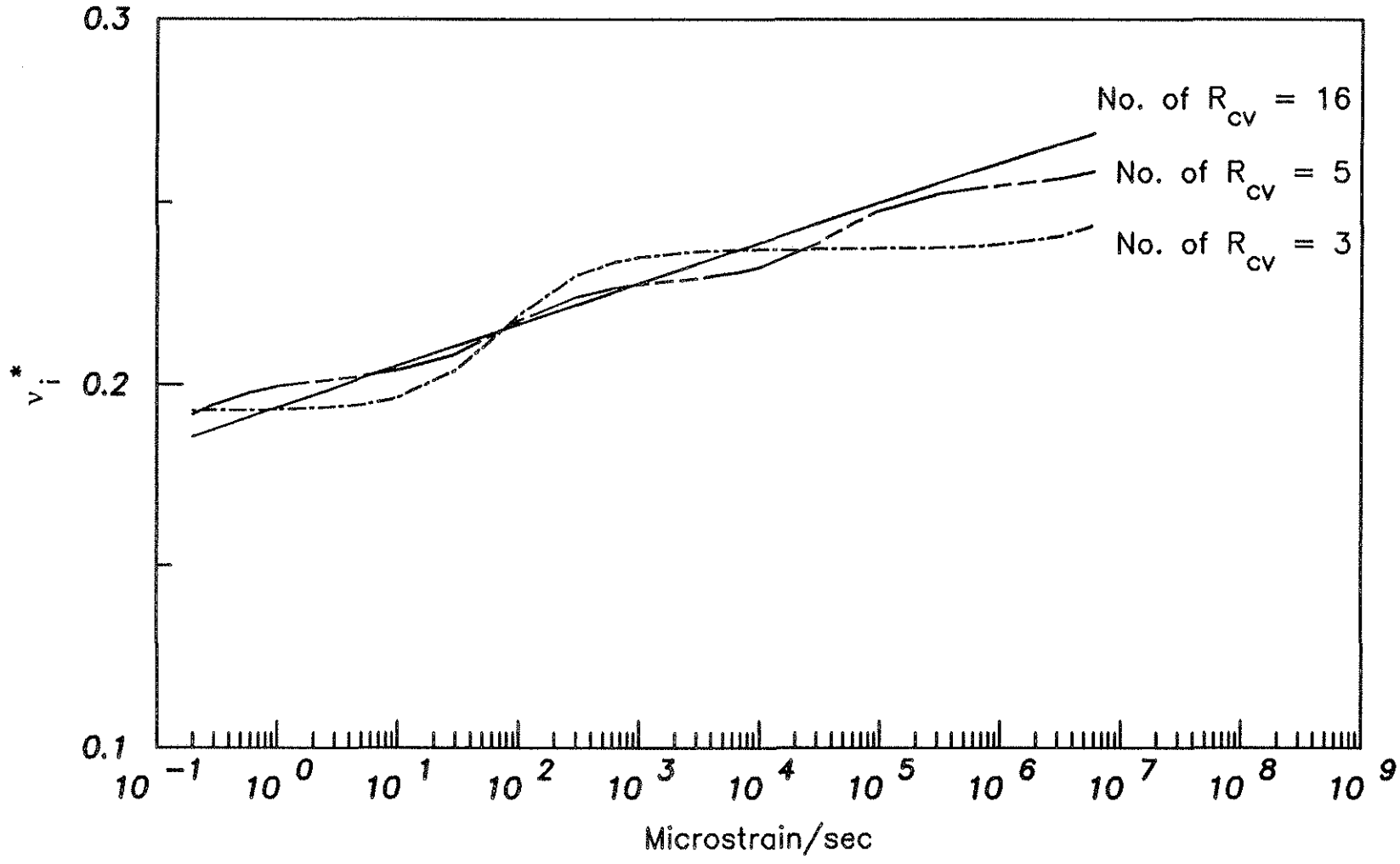

Fig. 3.22 Analytical Poisson's Ratio, ν_i^*, versus Strain Rate for Porous Solids Having a Multiple R_{cv}

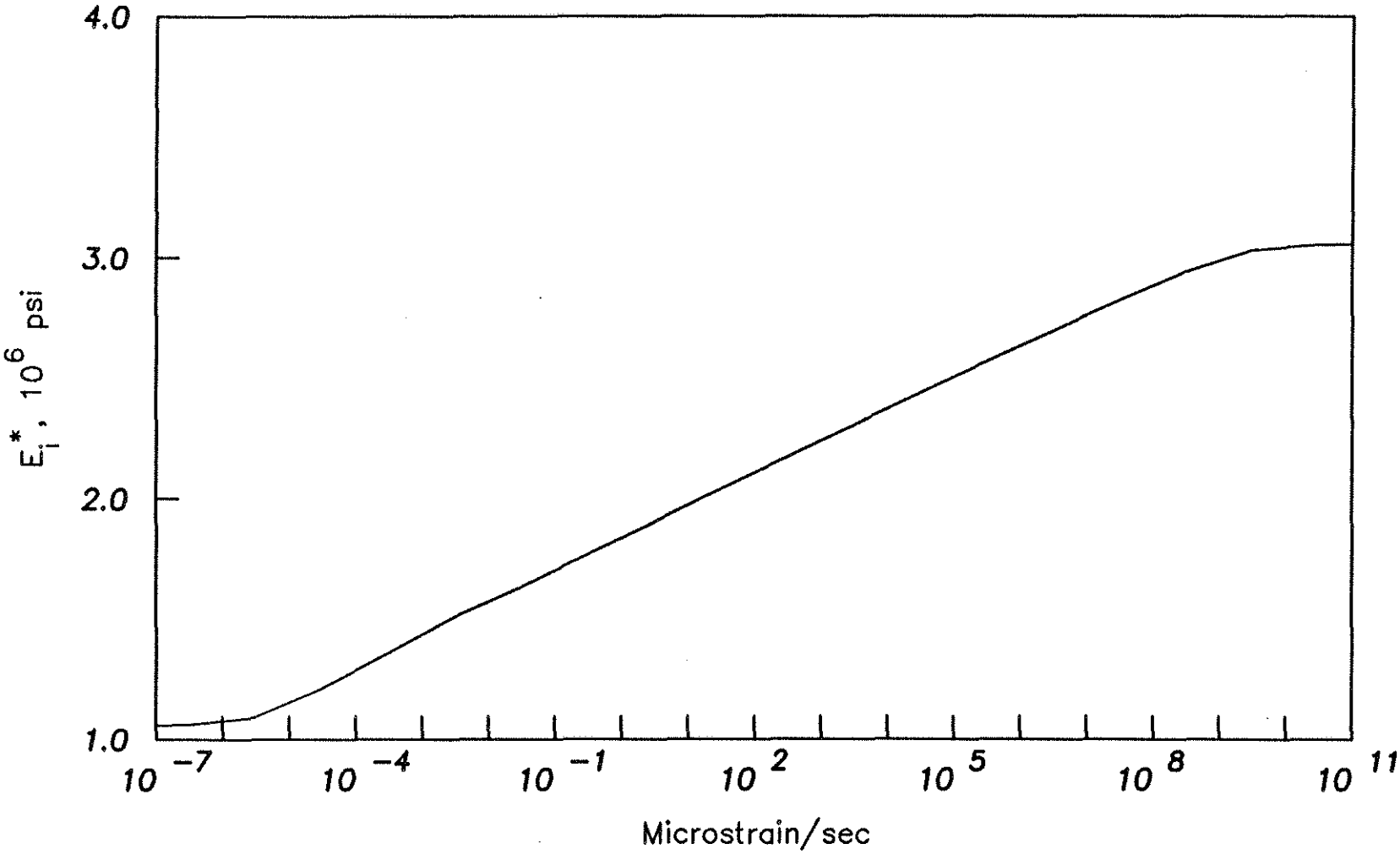

Fig. 3.23a Analytical Composite Elastic Modulus, E_i^*, versus Strain Rate for PS.5P

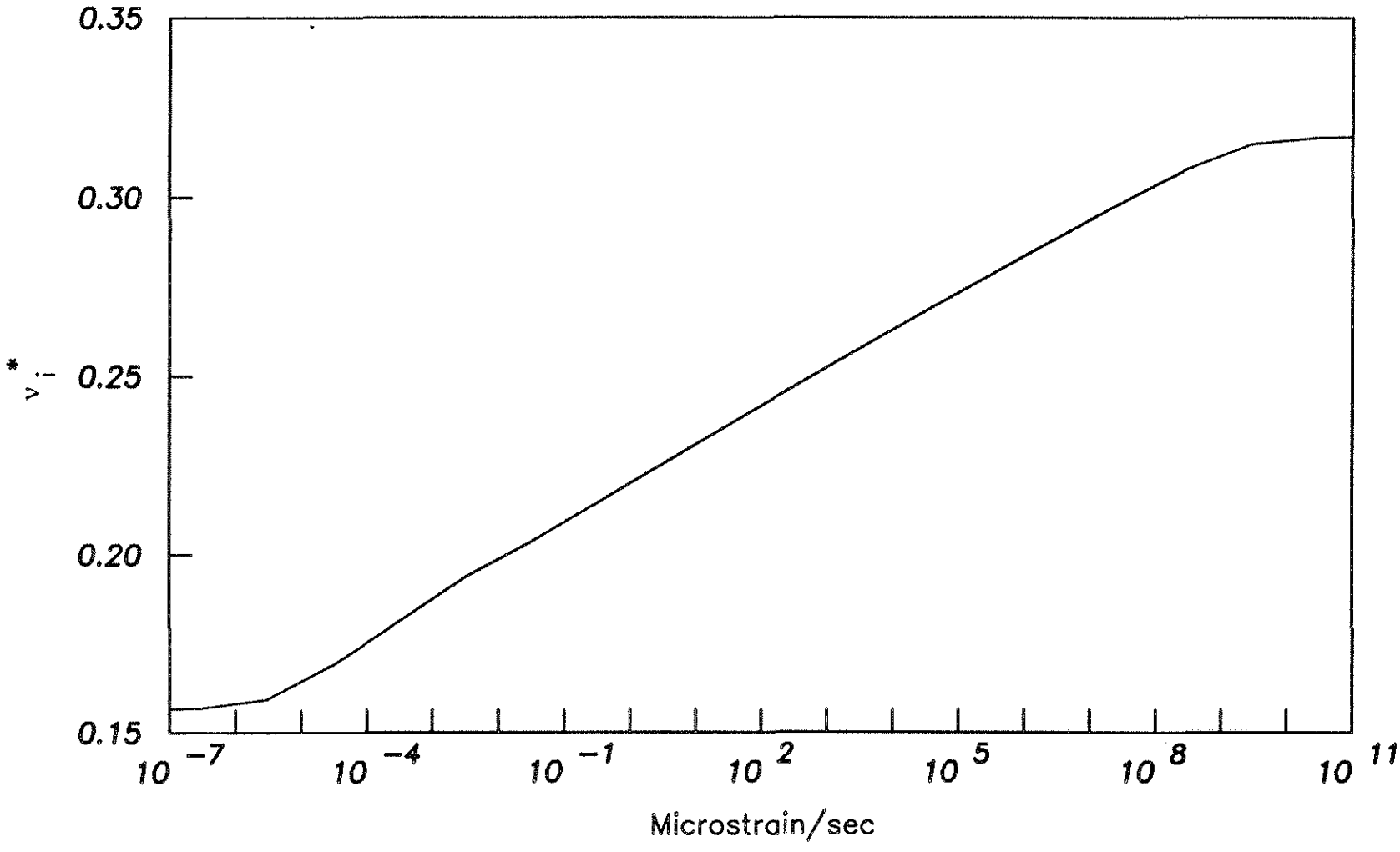

Fig. 3.23b Analytical Composite Poisson's Ratio, ν_i^*, versus Strain Rate for PS.5P

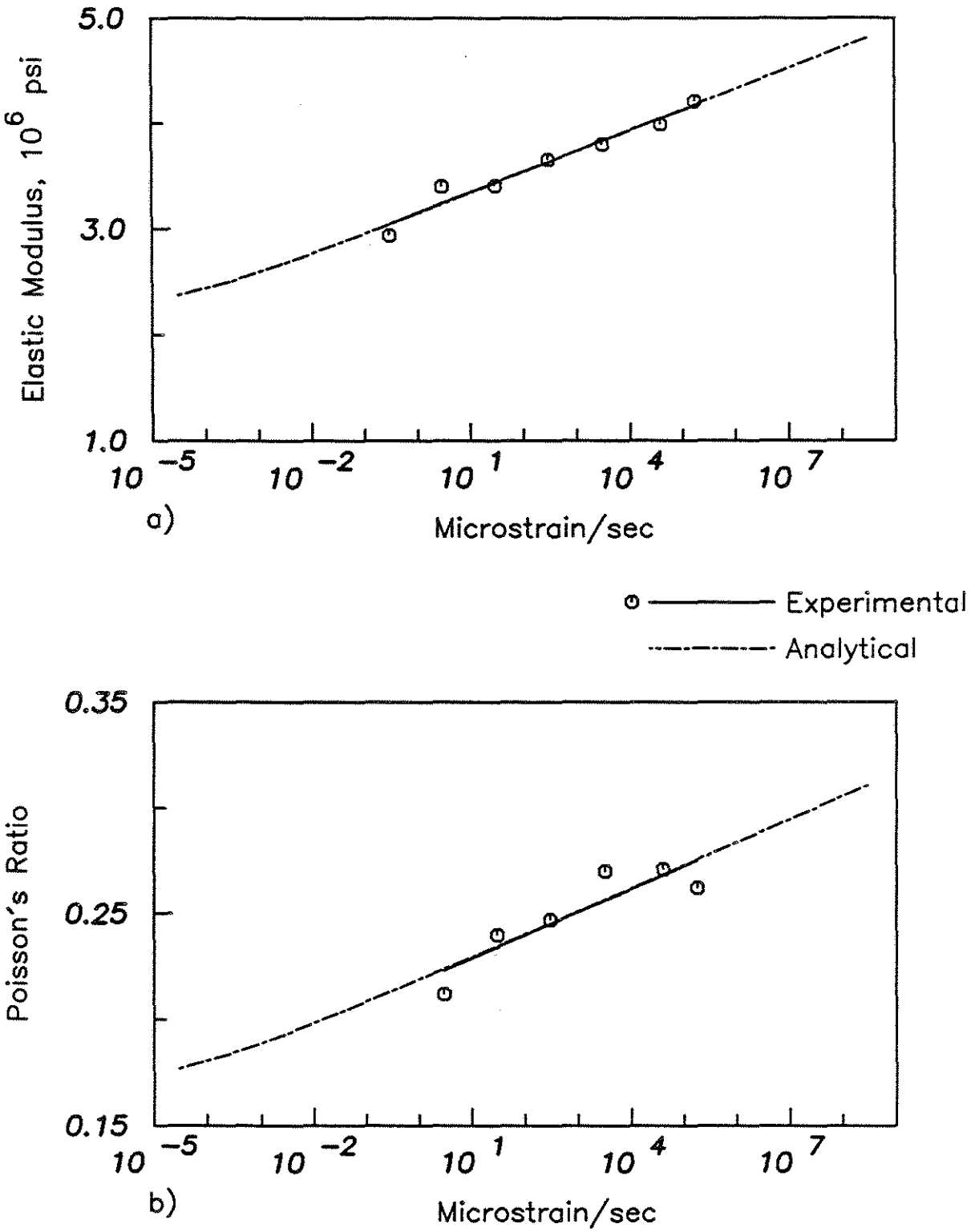

Fig. 3.24 Analytical and Experimental Moduli versus Strain Rate for Cement Paste with W/C = 0.3

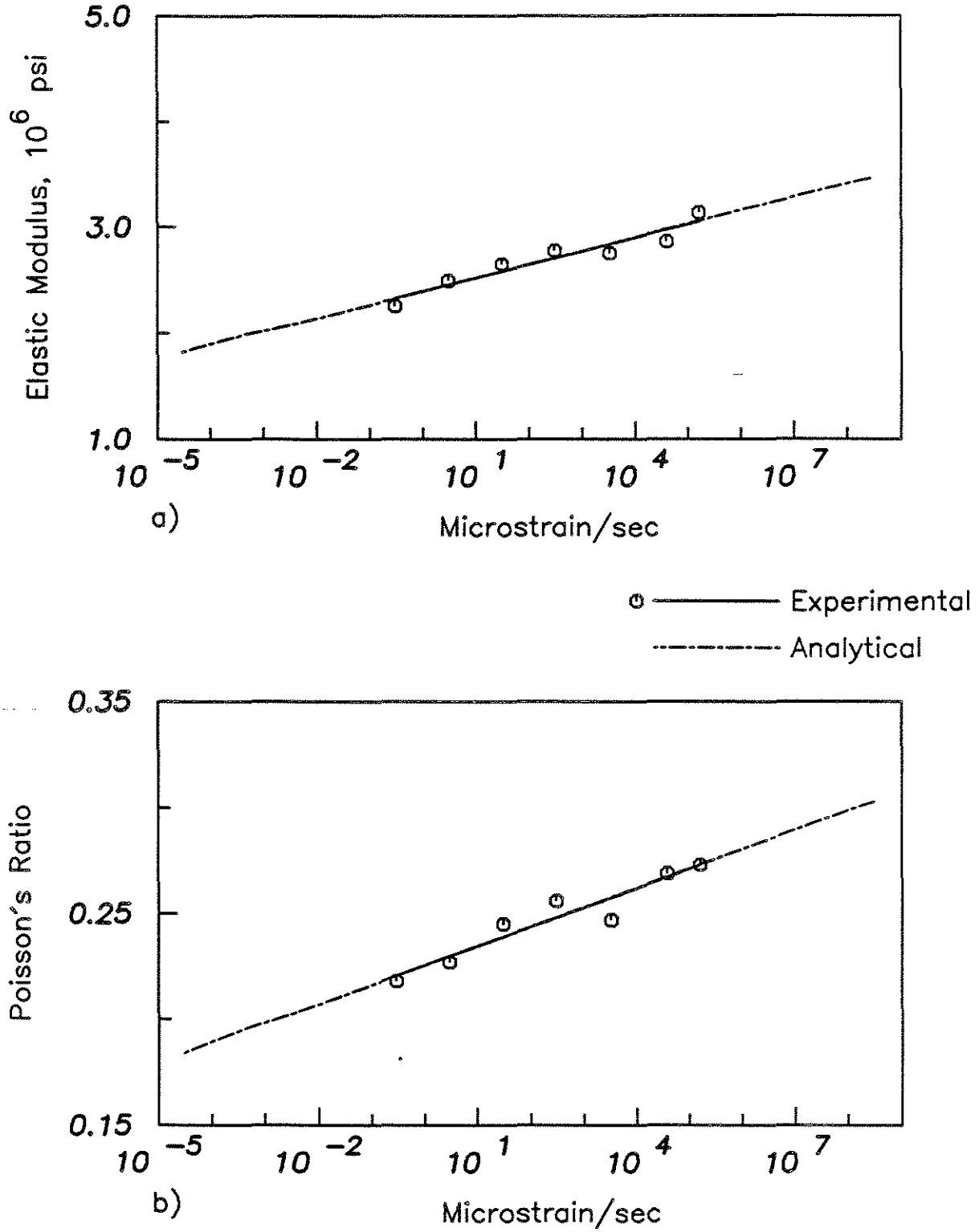

Fig. 3.25 Analytical and Experimental Moduli versus Strain Rate for Cement Paste with W/C = 0.4

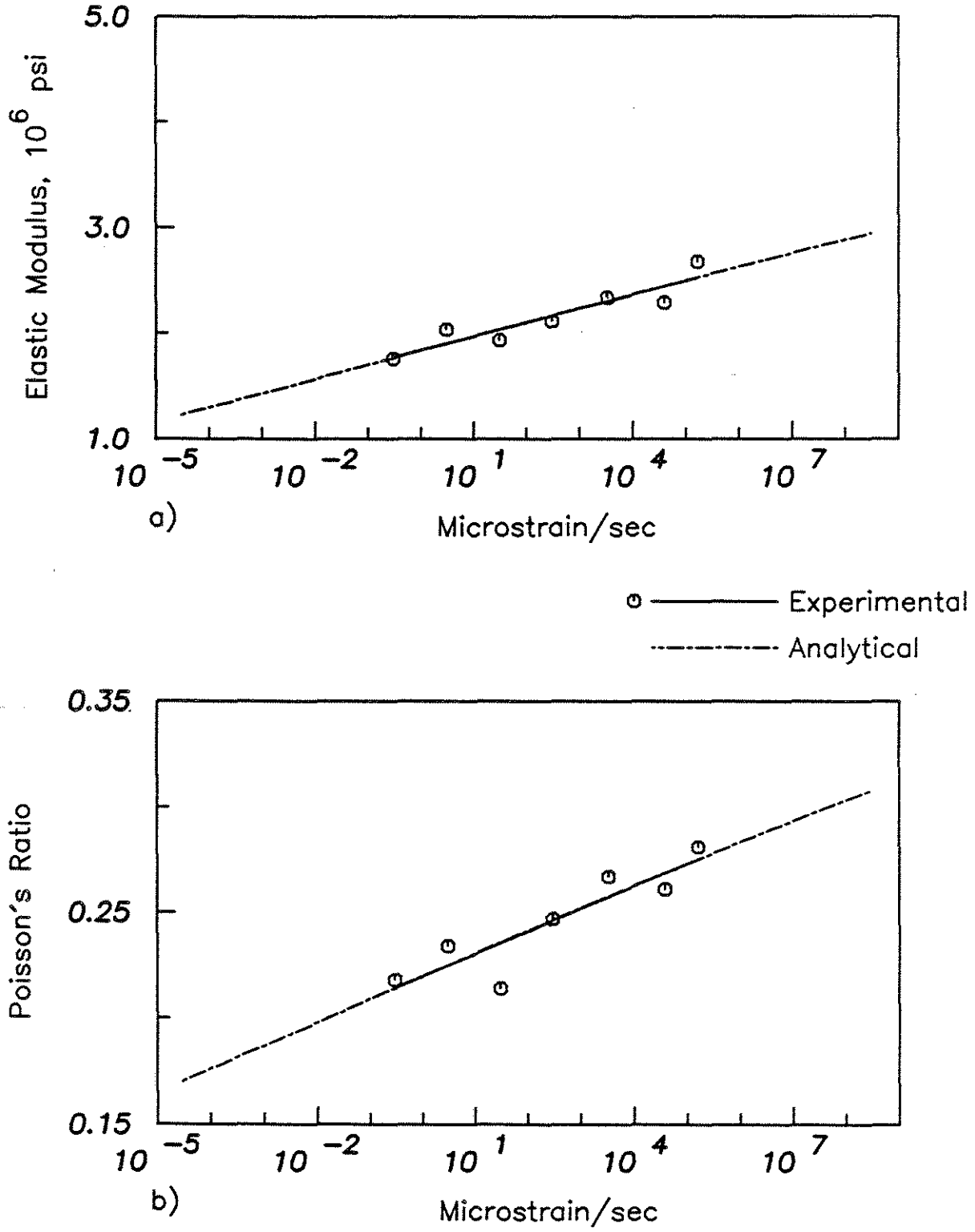

Fig. 3.26 Analytical and Experimental Moduli versus Strain Rate for Cement Paste with W/C = 0.5

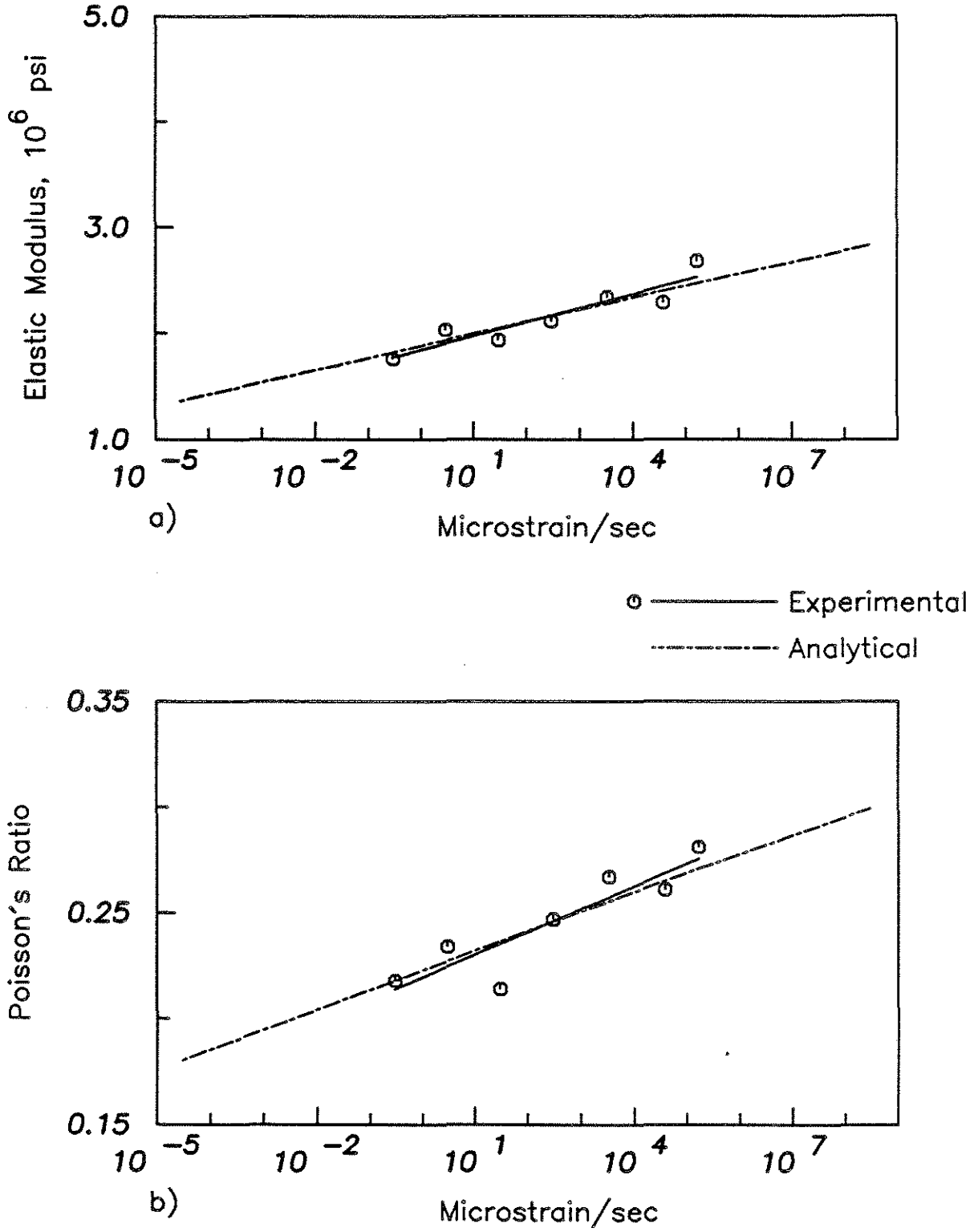

Fig. 3.27 Comparison of the Rate Sensitive Analytical and Experimental Moduli Using Properties of PS.5P with a 100 Times Wider Range of R_{cv}

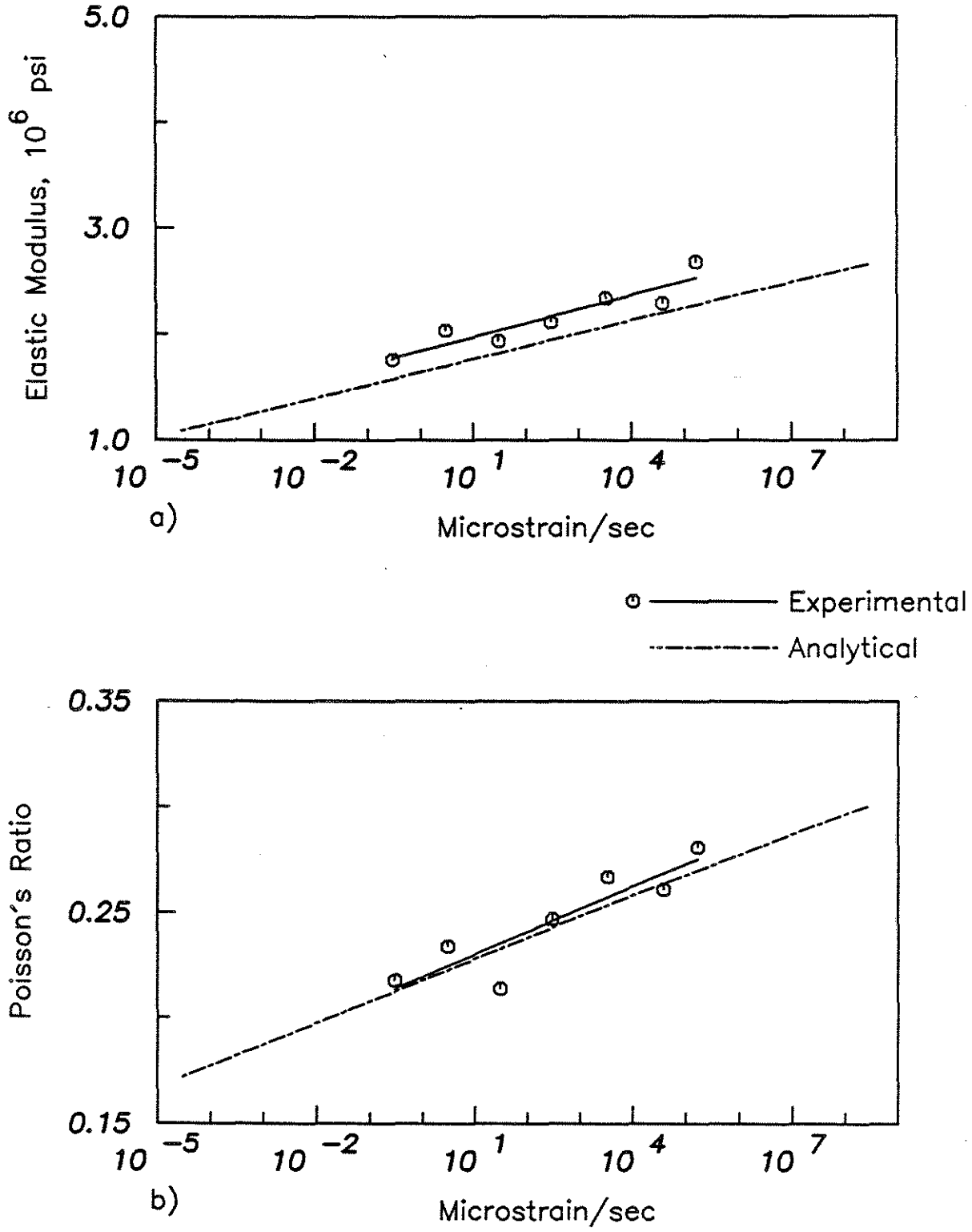

Fig. 3.28 Comparison of the Rate Sensitive Analytical and Experimental Moduli Using Properties of PS.5P with a 100 Times Wider Range of R_{cv} and r = 0.0752

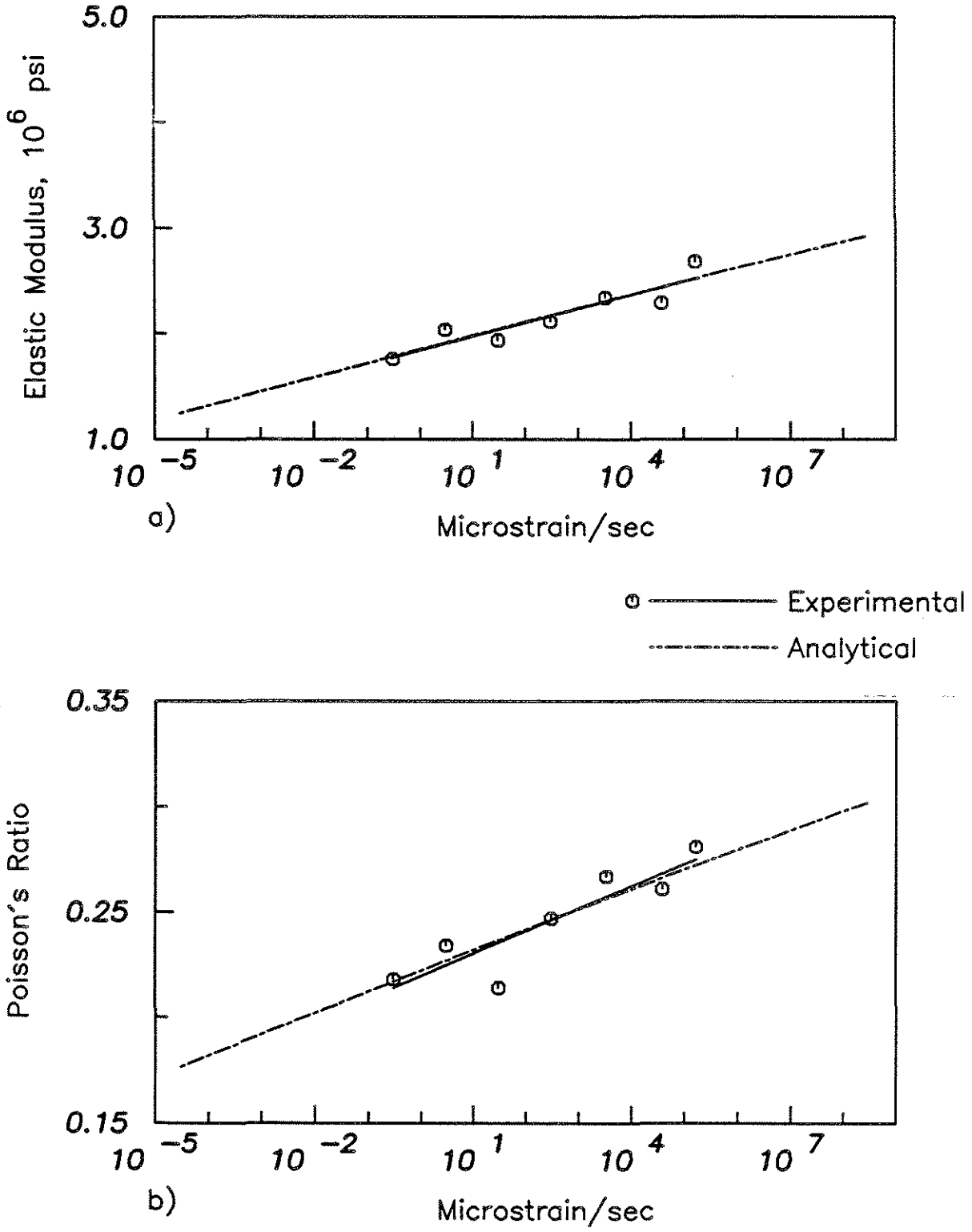

Fig. 3.29 Comparison of the Rate Sensitive Analytical and Experimental Moduli Using Properties of PS.5P'

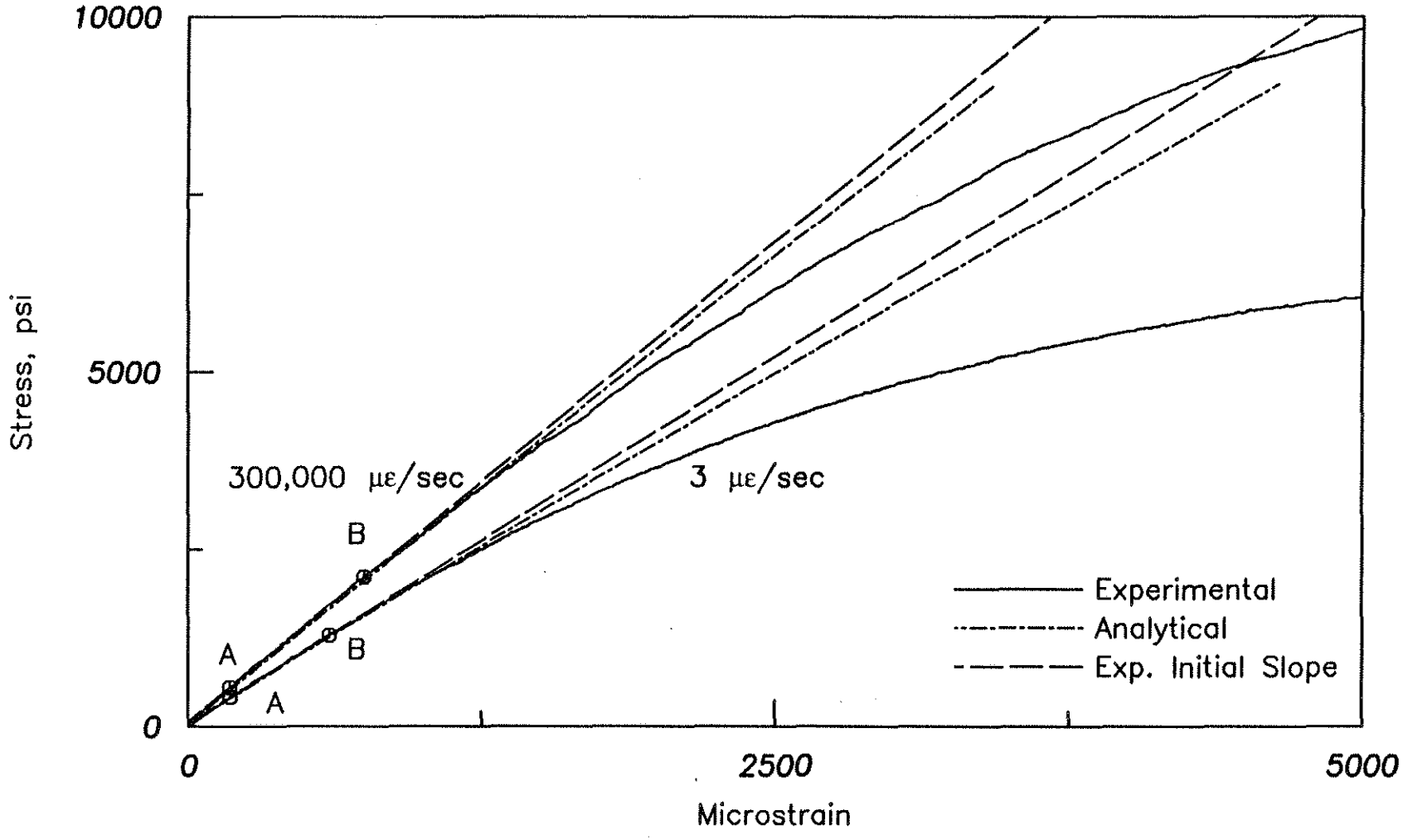

Fig. 3.30 Comparison of Analytical and Experimental Stress-Strain Behaviors for Cement Paste with W/C = 0.5

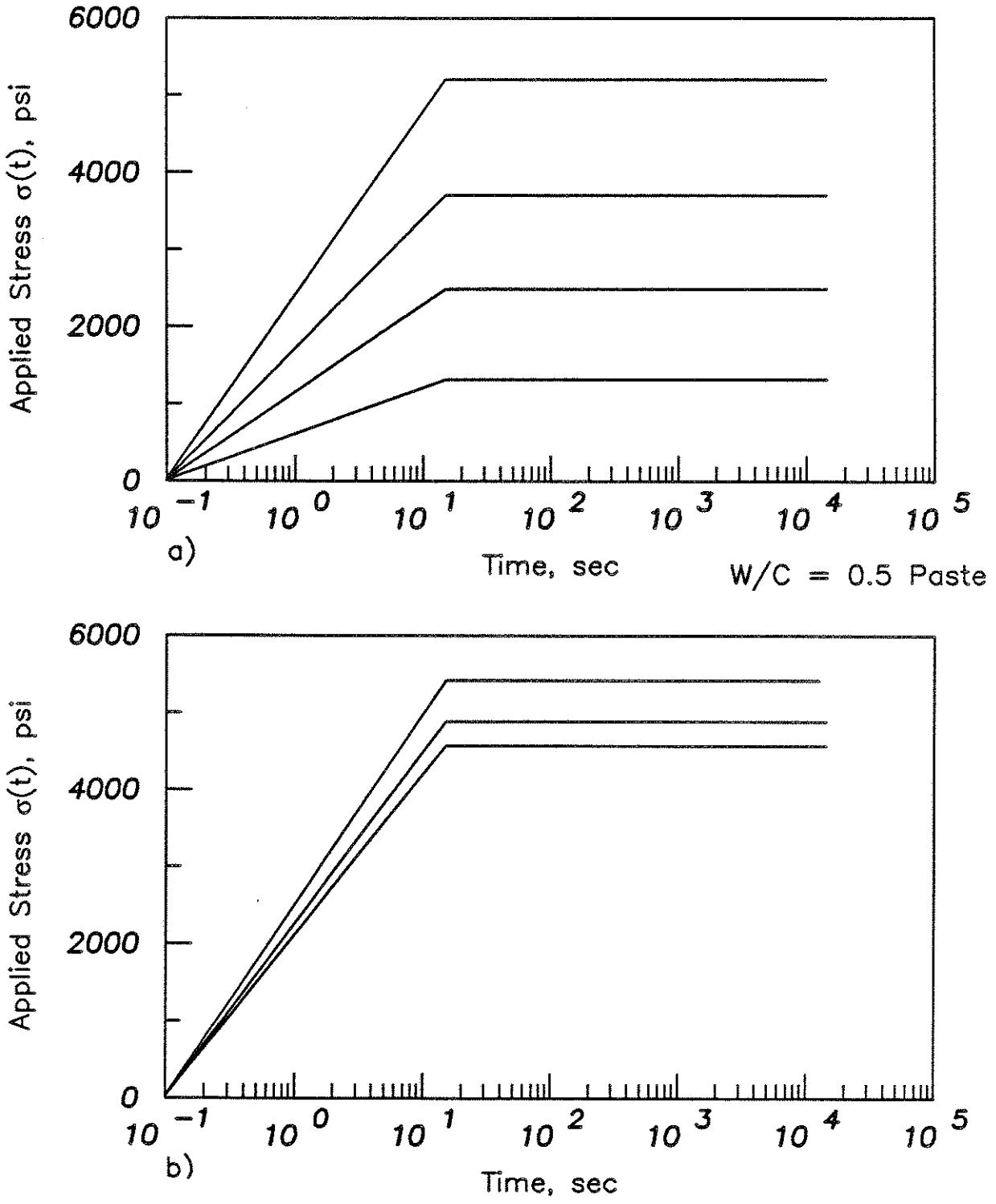

Fig. 4.1 Stress Histories of a) Terry and Darwin's, and b) Attiogbe and Darwin's Specimens

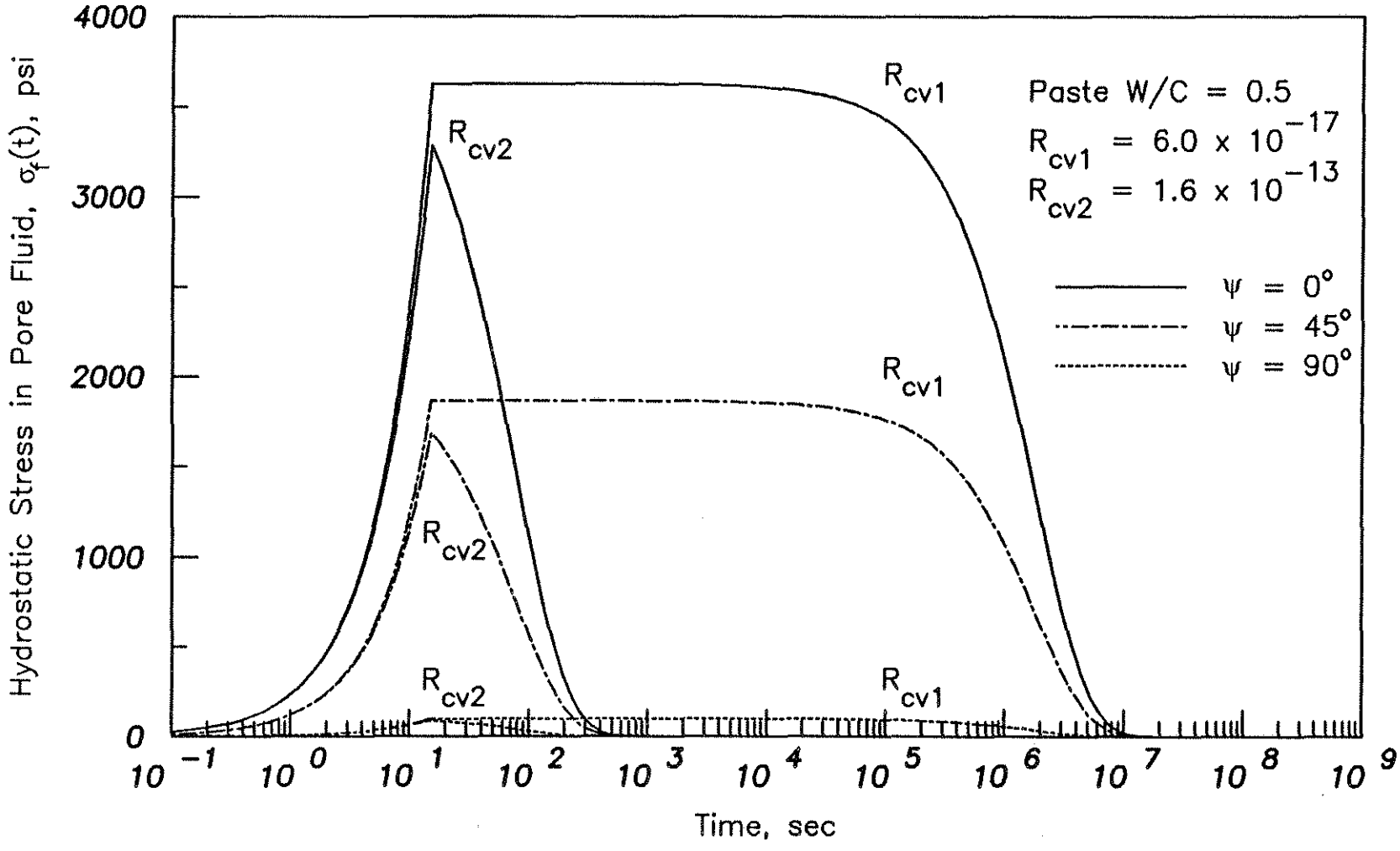

Fig. 4.2 Hydrostatic Stress in the Pore Fluid, $\sigma_f(t)$, versus Time for Paste with a W/C = 0.5 and Applied Stress = 4884 psi

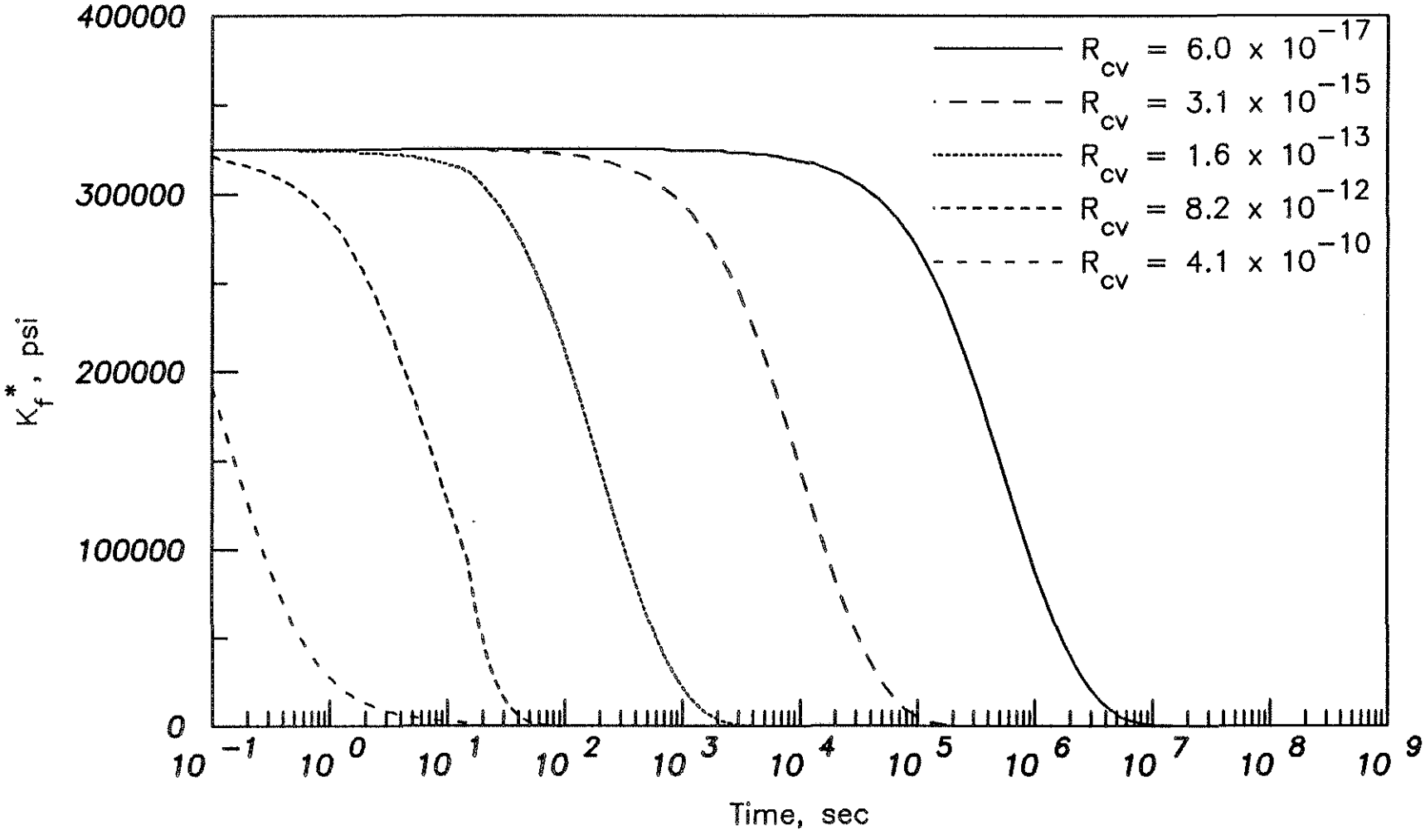

Fig. 4.3 Effective Bulk Modulus of a Pore, K_f^*, versus Time for Paste with a W/C = 0.5 and Applied Stress = 4884 psi

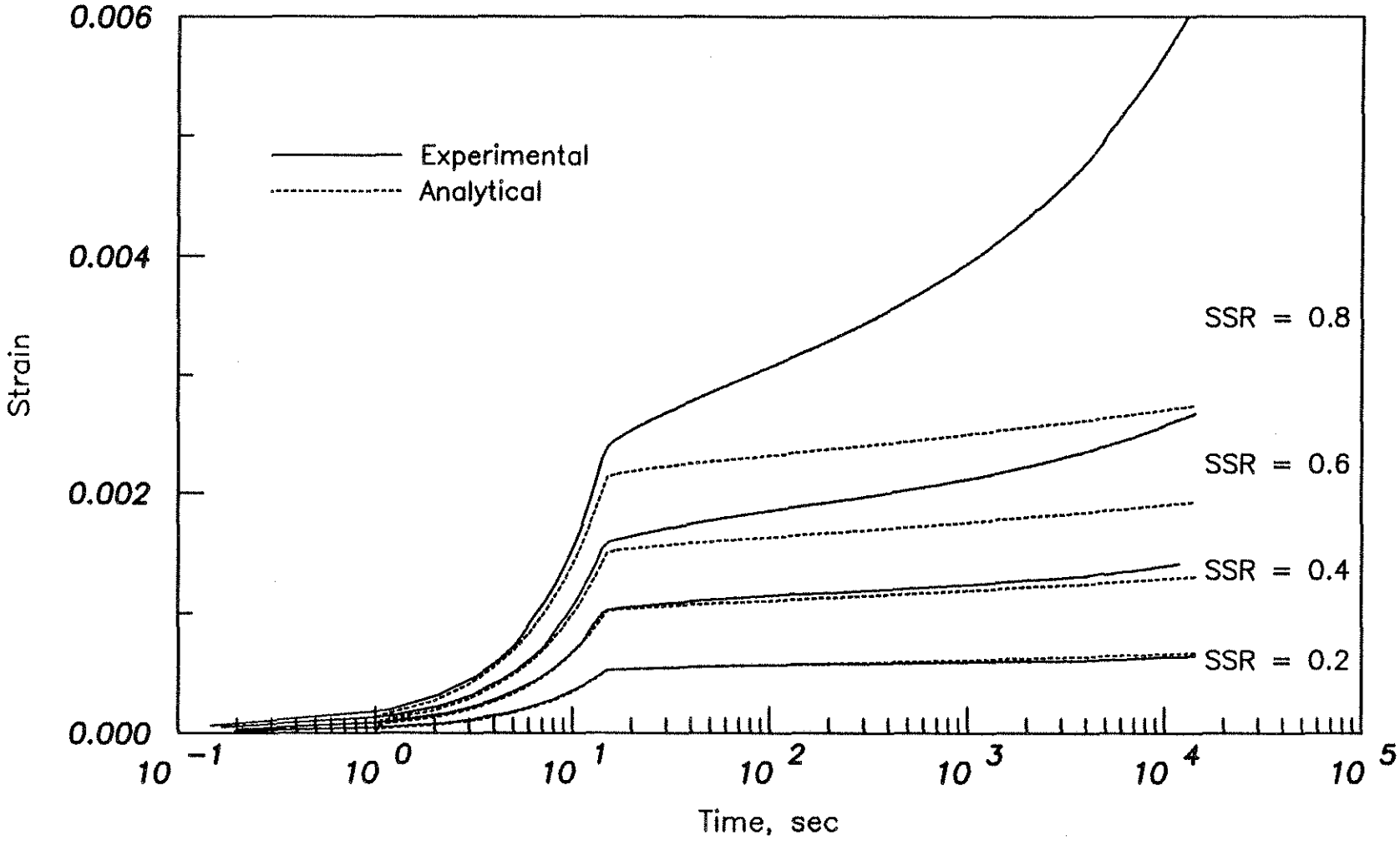

Fig. 4.4 Experimental and Analytical Strain versus Time Curves for Stress-Strength Ratios (SSR) of 0.2, 0.4, 0.6 and 0.8 of Paste with W/C = 0.5

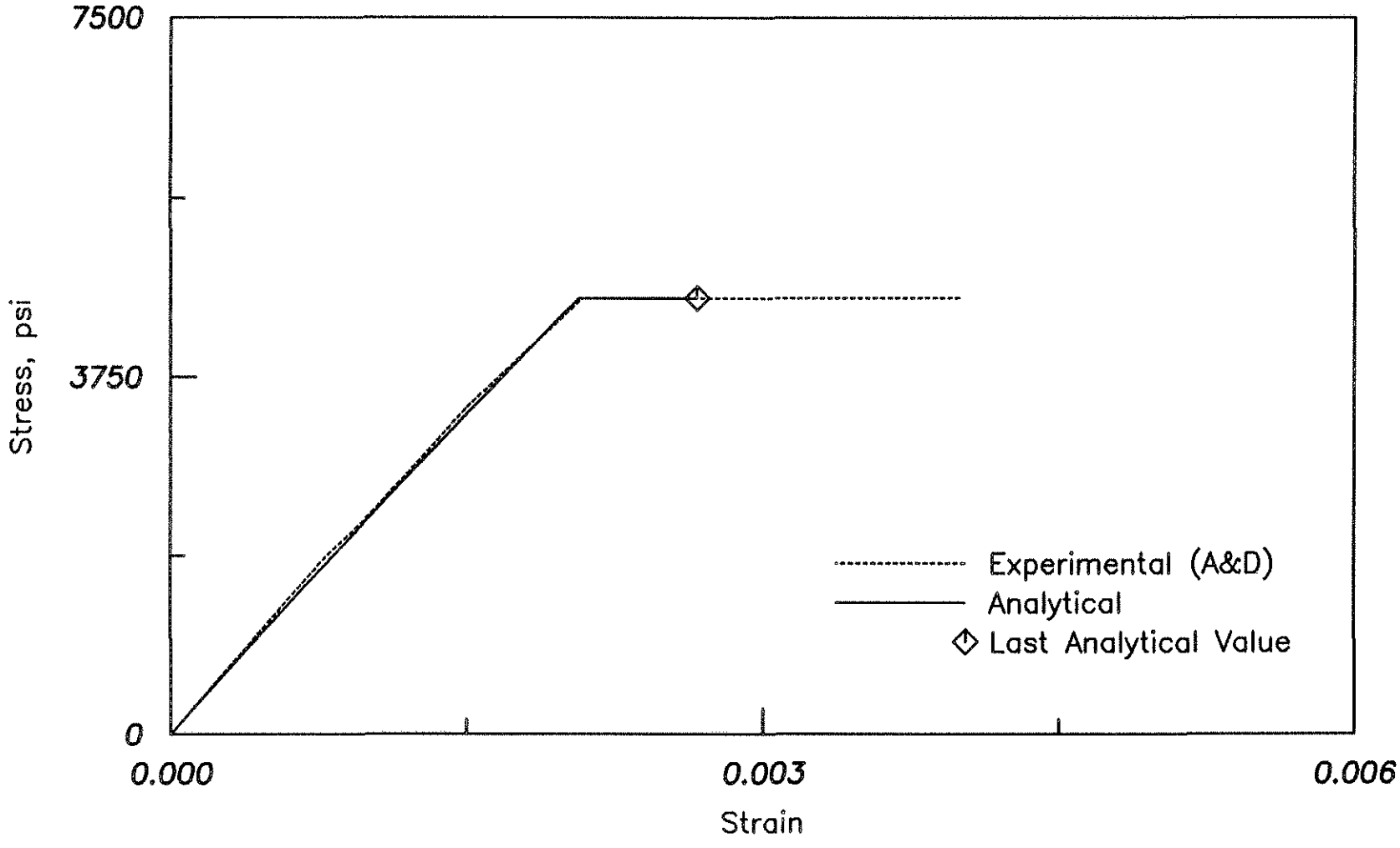

Fig. 4.5 Experimental (Attiogbe and Darwin) and Analytical Stress-Strain Curves for Stress-Strength Ratio of 0.675 for Paste with W/C = 0.5

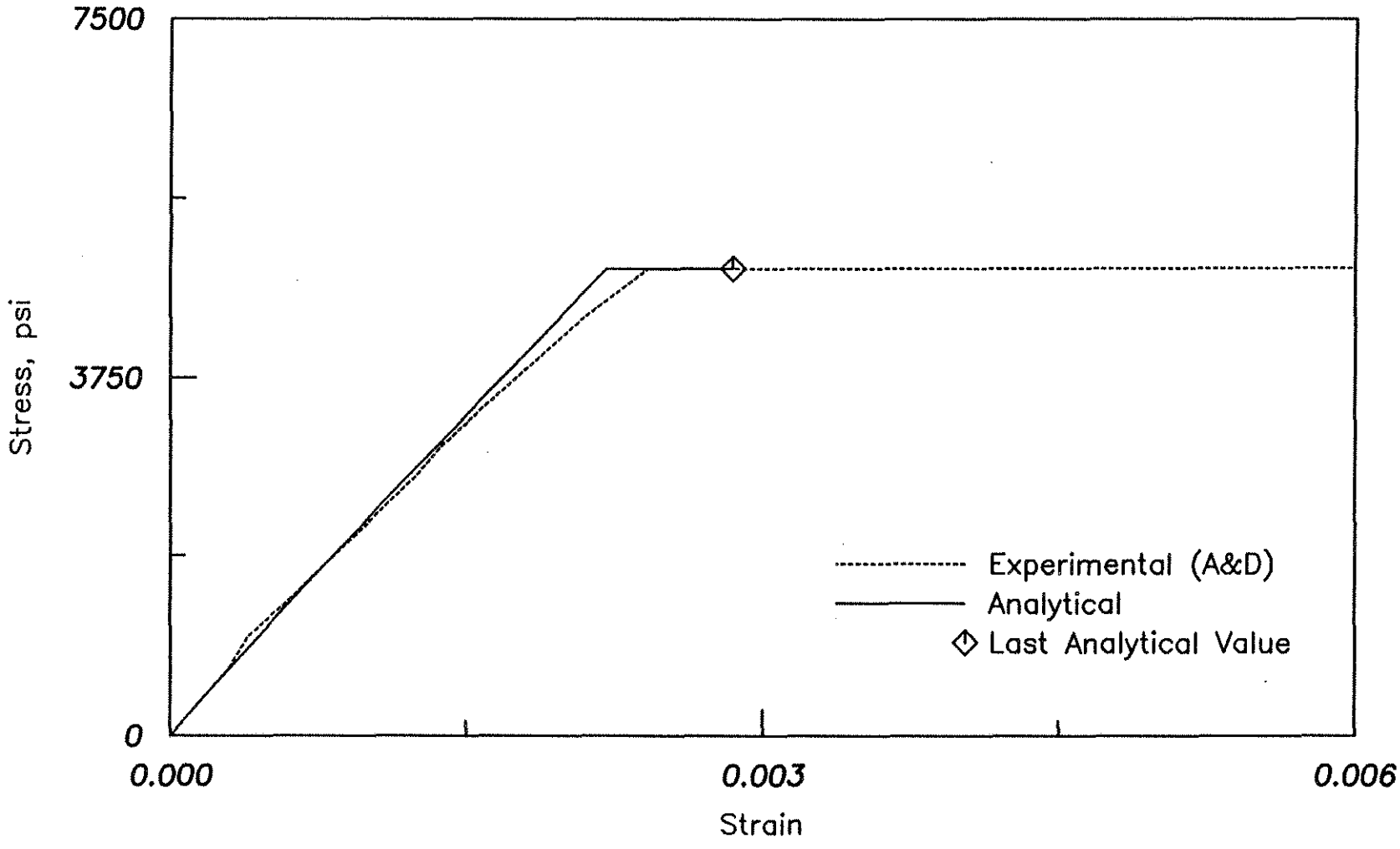

Fig. 4.6 Experimental (Attiogbe and Darwin) and Analytical Stress-Strain Curves for Stress-Strength Ratio of 0.725 for Paste with W/C = 0.5

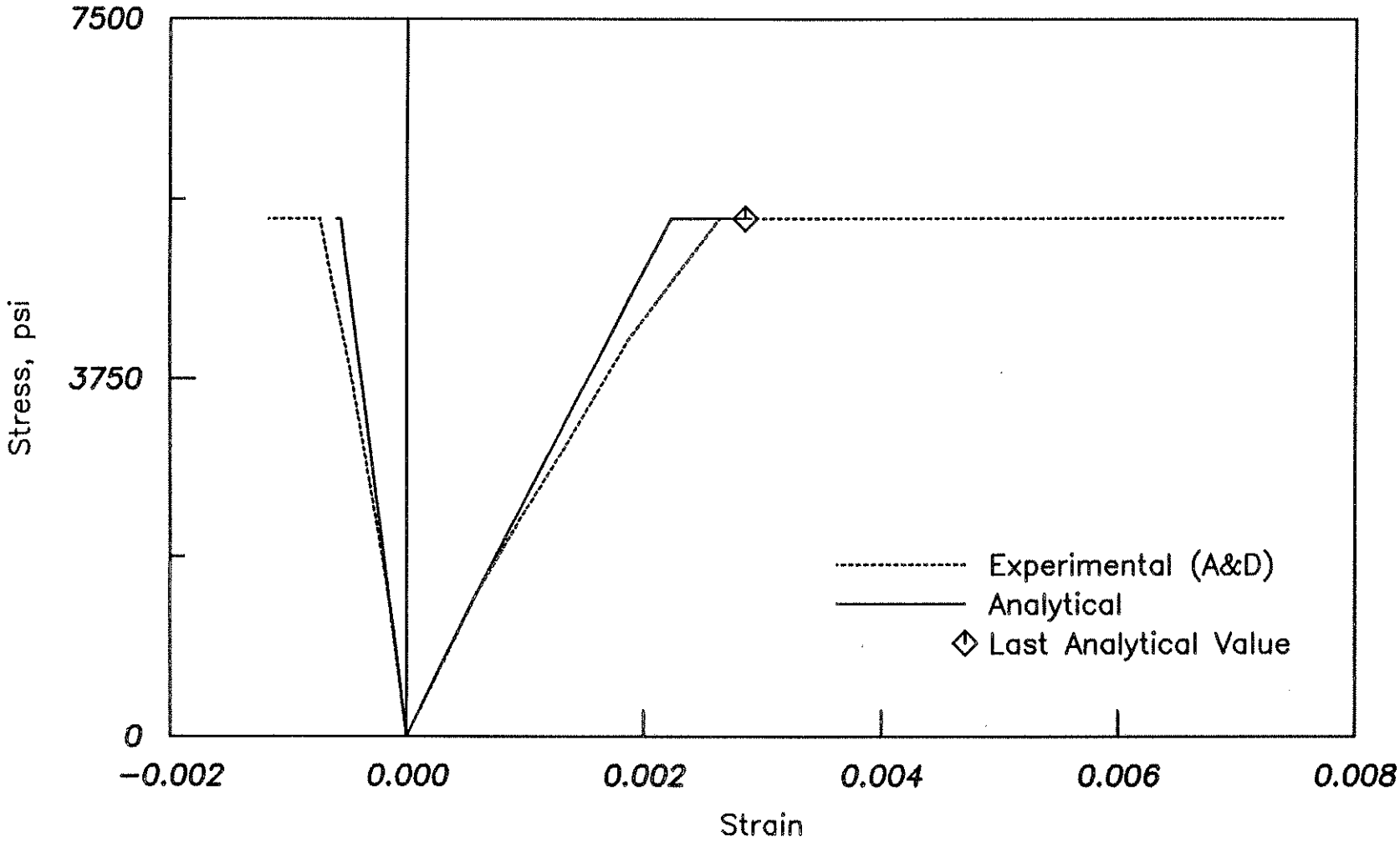

Fig. 4.7 Experimental (Attiogbe and Darwin) and Analytical Stress-Strain Curves for Stress-Strength Ratio of 0.800 for Paste with W/C = 0.5

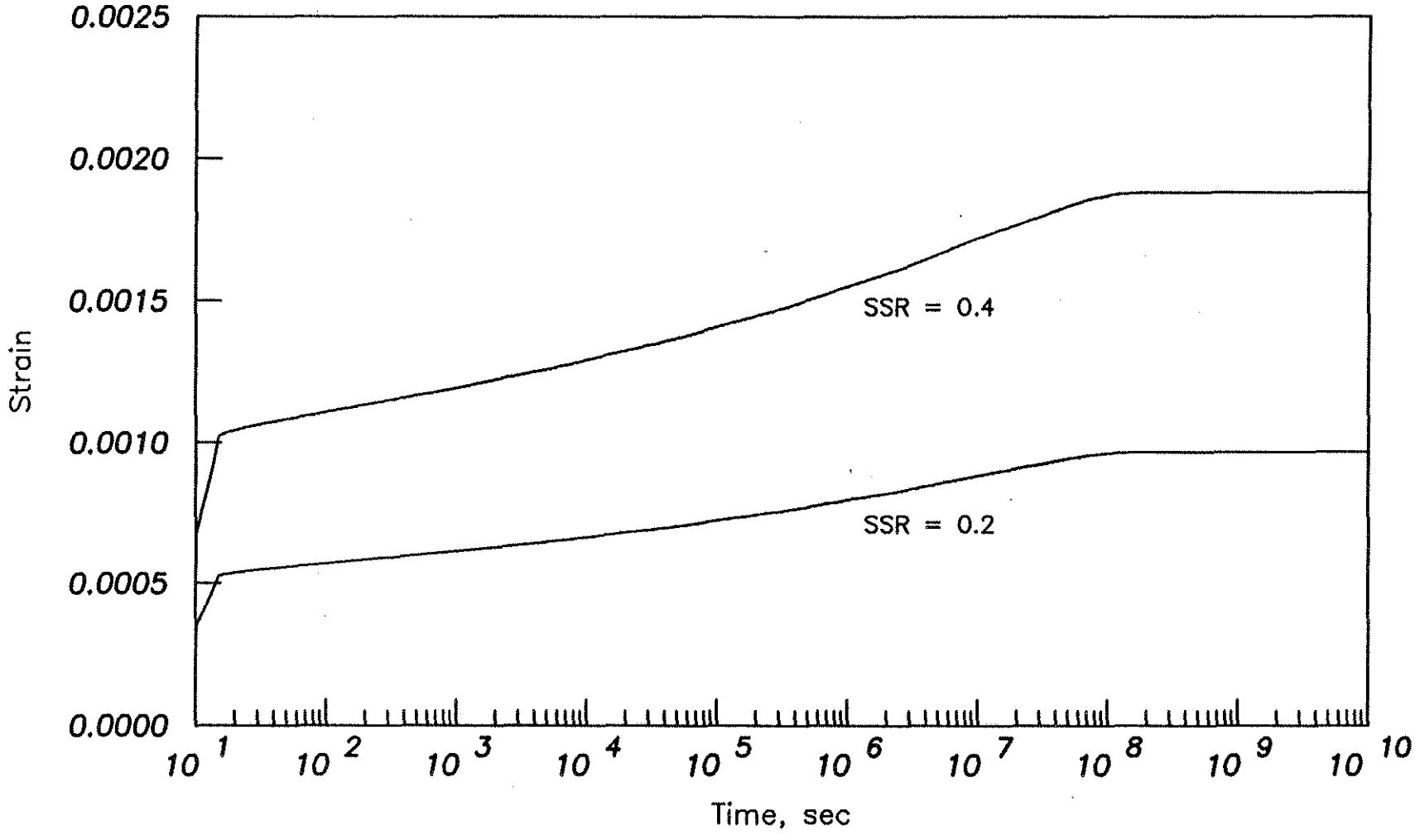

Fig. 4.8 Analytical Longitudinal Strain Versus Time Curves for Stress-Strength Ratios (SSR) of 0.2 and 0.4 for Paste with W/C = 0.5

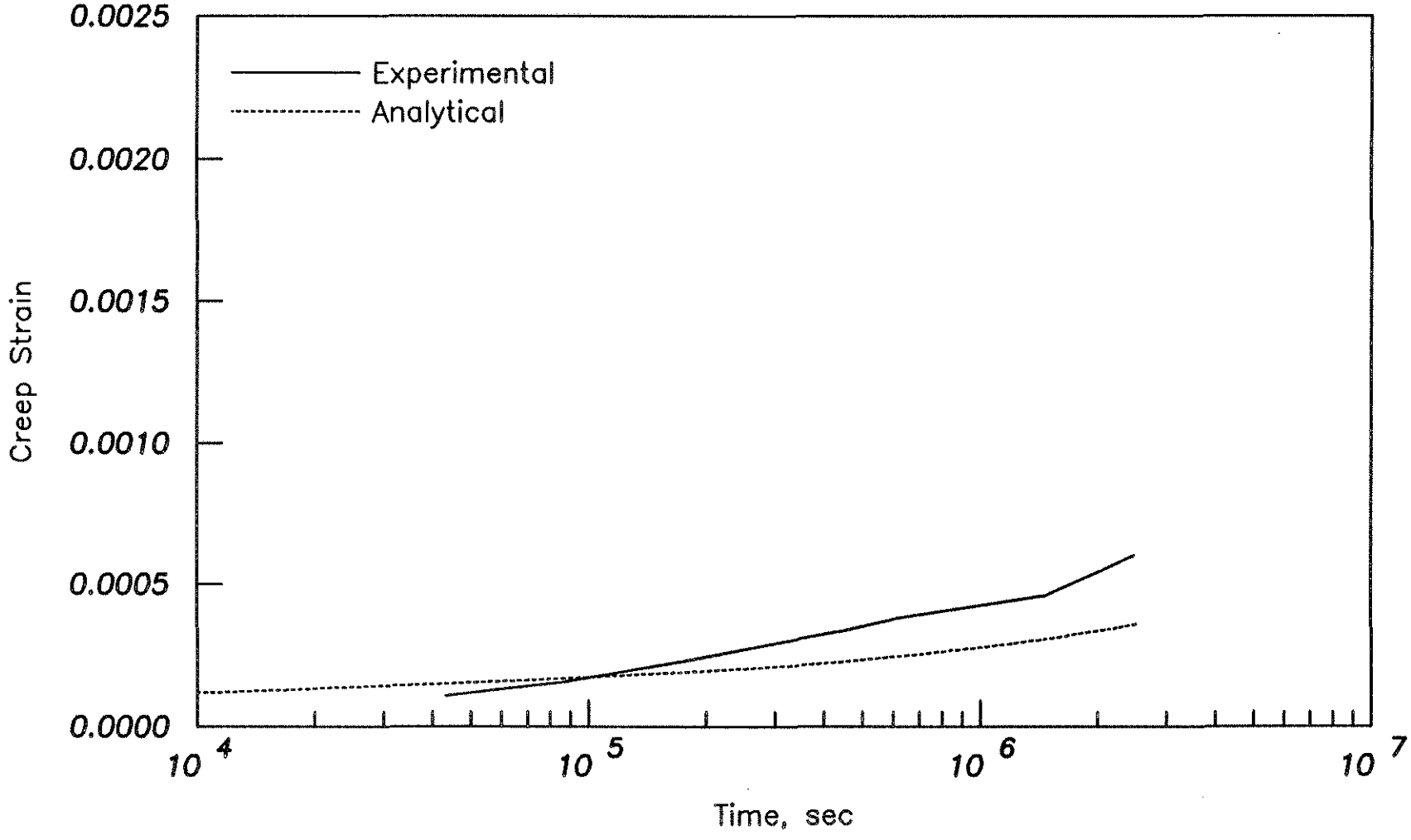

Fig. 4.9 Experimental (Timsuk and Ghose) and Analytical Creep Curves for Stress-Strength Ratio of 0.15 for Paste with W/C = 0.5

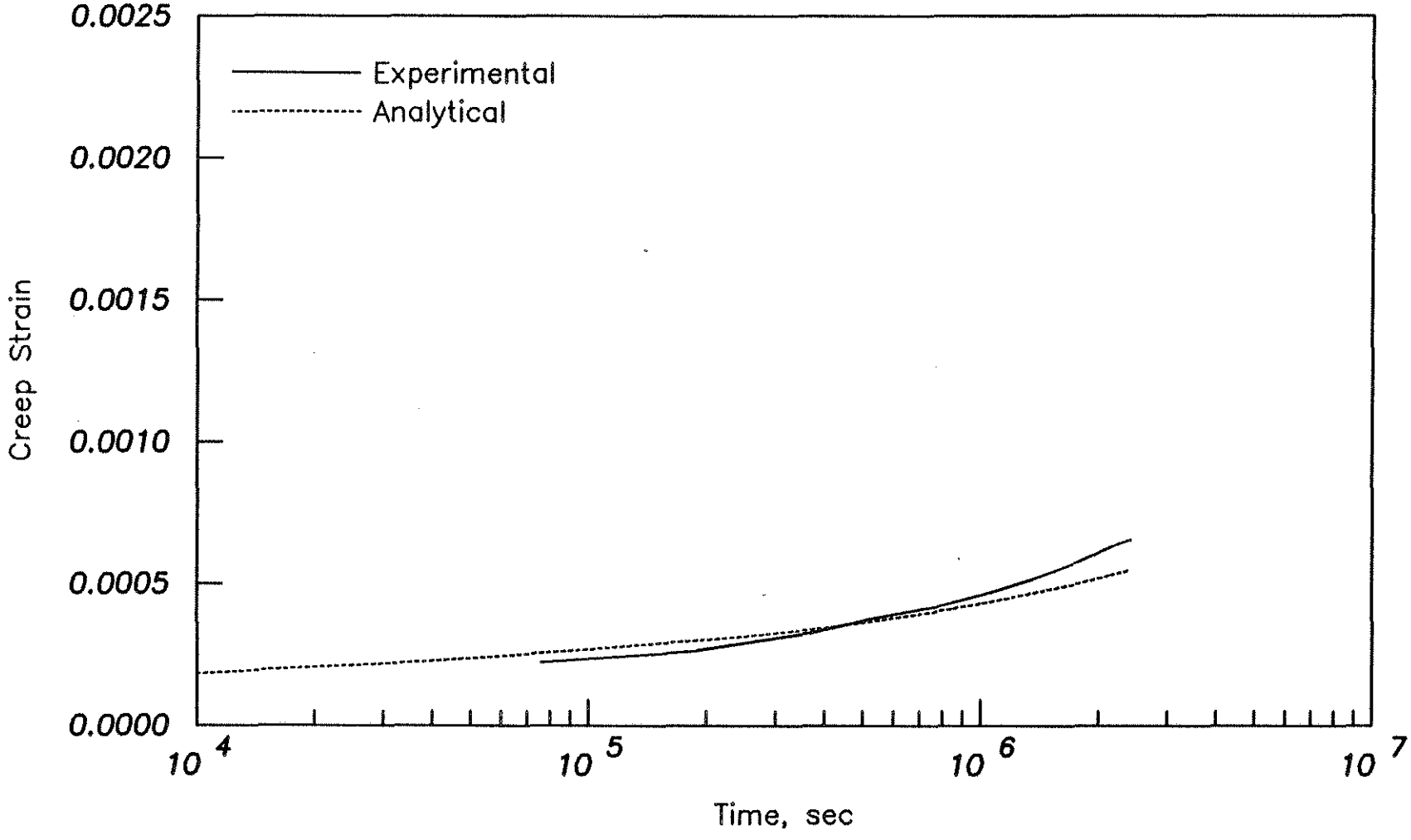

Fig. 4.10 Experimental (Rainford and Timsuk) and Analytical Creep Curves for Stress-Strength Ratio of 0.2 for Paste with W/C = 0.5

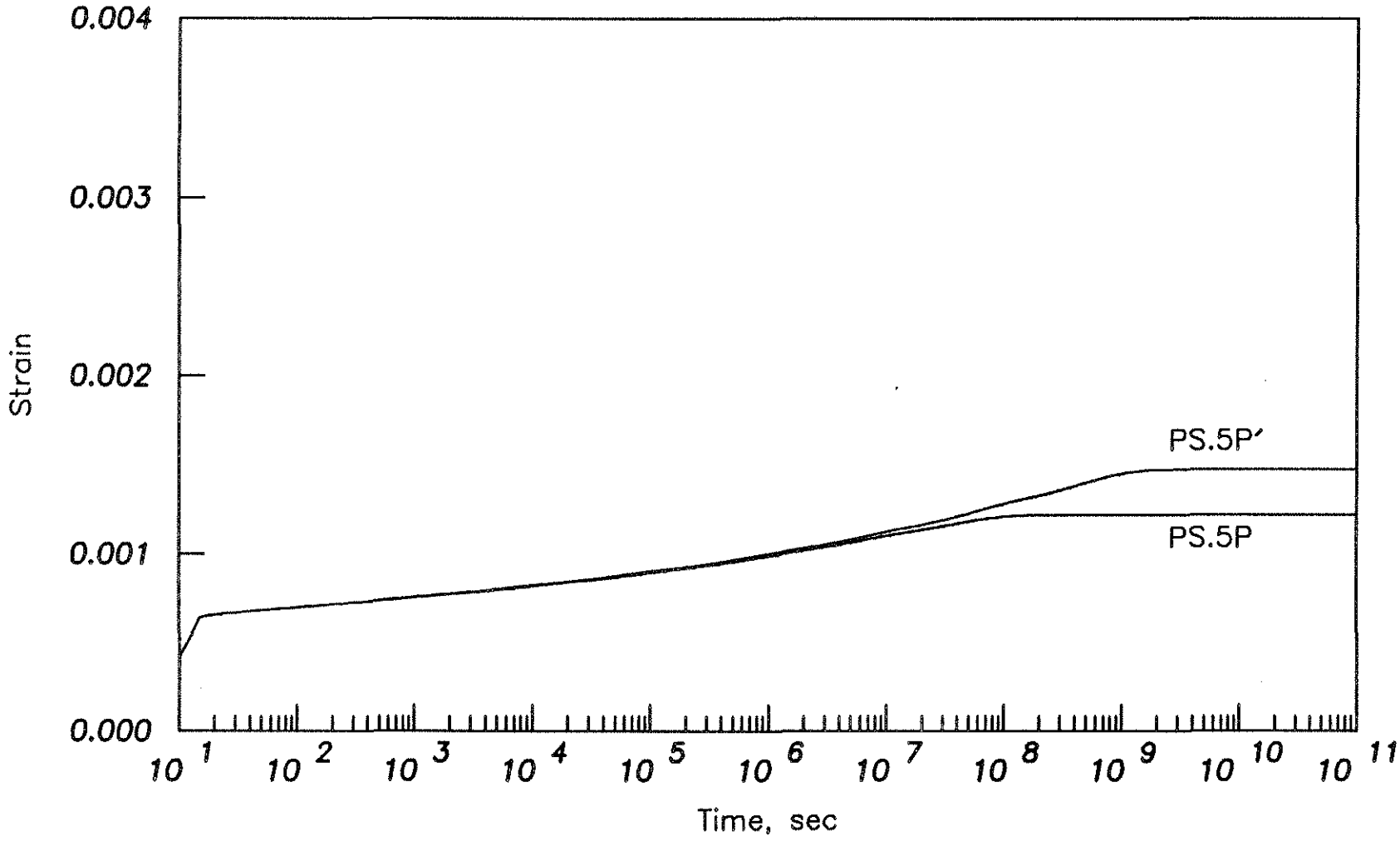

Fig. 4.11 Analytical Longitudinal Strain versus Time Curves at Stress-Strength Ratio of 0.2 for Equivalent Porous Solids PS.5P and PS.5P'

APPENDIX A
CHANGE IN PORE VOLUME PER UNIT AVERAGE STRAIN, v^*

A.1 Introduction

Consider an isolated spheroidal pore in a homogeneous isotropic elastic medium. The spheroidal pore is empty and is extremely small compared to the dimensions of the surrounding medium. Thus, the presence of the pore does not affect the overall behavior of the medium significantly. If a uniform strain ε_z' is applied along the global z-axis of the medium, the pore deforms, and there is a corresponding change in the volume of the pore, v_p. For a linear and elastic medium, v_p is proportional to the applied strain (or applied stress), and is a function of the moduli of the medium and the geometry of the pore. In this Appendix expressions are derived for the change in the volume of the pore per unit average strain along the global z-axis of the medium, v^*, or

$$v^* = \frac{v_p}{\varepsilon_z'} \tag{A.1}$$

in which v_p is the total change in the volume of the pore for applied strain of ε_z'. v_p can be found from the corresponding displacements on the surface of the pore. The displacement components are given in the spheroidal coordinate system (4, 26, 70). A brief introduction to spheroidal coordinate systems will be given next. After the

introduction, expressions for the displacements (26) will be presented, and finally the expressions for v^* will be derived. In each of the following sections, expressions for both prolate and oblate spheroids are provided.

A.2 Spheroidal Coordinate System

In the spheroidal coordinate system (4, 26, 70), the spheroidal pores of a given shape are represented by a single prototype spheroid with polar and equatorial semi-axes of a and b, respectively. a and b are functions of only the pore shape, r (Eq. A.5 or Eq. A.7 below). In general, the size of the prototype spheroid cannot be equal to the size of the pore. Hence, the change in the volume of a pore, v_p, is obtained by multiplying the change in volume of the prototype, v'_p, by the ratio of the initial volume of the pore, V_i, to the initial volume of the prototype, V'_i. In the following sections, the expressions, except as noted, are for the prototype spheroid. The size of the polar and the equatorial semi-axes of the pore, a_p and b_p, are used only to calculate the original volume of the pore. For the balance of the discussion, the term 'spheroid' is used for the prototype spheroid.

The cartesian coordinates x, y, and z are related to the spheroidal coordinates α, β, and γ through the following equations (70).

$$x = \sinh\alpha \sin\beta \cos\gamma \qquad (A.2a)$$

$$y = \sinh\alpha \sin\beta \sin\gamma \tag{A.2b}$$

$$z = \cosh\alpha \cos\beta \tag{A.2c}$$

Eq. A.2 can also be rearranged in the following form

$$\frac{x^2}{\sinh^2\alpha} + \frac{y^2}{\sinh^2\alpha} + \frac{z^2}{\cosh^2\alpha} = 1 \tag{A.3a}$$

$$-\frac{x^2}{\sin^2\beta} - \frac{y^2}{\sin^2\beta} + \frac{z^2}{\cos^2\beta} = 1 \tag{A.3b}$$

$$\frac{y}{x} = \tan\gamma \tag{A.3c}$$

in which $0 \leq \alpha \leq \infty$, $0 \leq \beta \leq \pi$ and $0 \leq \gamma < 2\pi$. The surfaces α = constant, β = constant, and γ = constant form a triply orthogonal family of prolate spheroids, hyperboloids of two sheets, and plane surfaces, respectively (Fig. A.1a). $\alpha = \alpha_o$ represents the surface of the spheroid. Points inside and outside of the this surface are represented by other values of α. For a point on the surface $\alpha = \alpha_o$, β represents the angle measured from the positive polar-axis (or z-axis) to the normal to the spheroidal surface at the point selected (Fig. A.1). All points with the same value of β lie on a circle centered on the polar axis of the spheroid. As a point is moved from the positive pole to the equator β changes from 0 to $\pi/2$. γ is the angle measured from the positive x-axis to the plane passing through the poles and a point on the surface of the spheroid.

Prolate Spheroid: For the points on the surface of a prolate spheroid, the following trigonometric conditions are required (Fig. A.1a).

$$a = \cosh\alpha_o = q_o \tag{A.4a}$$

$$b = \sinh\alpha_o = \bar{q}_o \tag{A.4b}$$

in which a and b are the polar and equatorial semiaxes of the spheroid (prototype), respectively. Eq. A.4 implies that

$$a^2 - b^2 = 1 \tag{A.5a}$$

$$a^2 = \frac{r^2}{r^2 - 1} = q_o^2 \tag{A.5a}$$

$$b^2 = \frac{1}{r^2 - 1} = \bar{q}_o^2 \tag{A.5c}$$

in which $r = a/b$ is the aspect ratio of the spheroid (and also of the pore).

Oblate Spheroid: For the points on the surface of an oblate spheroid, the following trigonometric conditions are required (Fig. A.1b).

$$a = \sinh\alpha_o = \bar{q}_o \tag{A.6a}$$

$$b = \cosh\alpha_o = q_o \tag{A.6b}$$

in which a and b are the polar and equatorial semiaxes of the spheroid, respectively. Eq. A.6 implies that

$$b^2 - a^2 = 1 \tag{A.7a}$$

$$a^2 = \frac{r^2}{1 - r^2} = \bar{q}_o^2 \tag{A.7b}$$

$$b^2 = \frac{1}{1 - r^2} = q_o^2 \tag{A.7c}$$

in which $r = a/b$ is the aspect ratio of the spheroid (and also of the pore). Thus, for the pores of given shape, r, a unique size for the prototype spheroid is determined by either Eq. A.5 or Eq. A.7.

A.3 Intermediate Variables

This section defines the intermediate variables used to express the displacements and the volume change in a concise manner (26, 70).

Prolate Spheroid:

$$p = \cos\beta \tag{A.8}$$

From Eq. A.2c for $\alpha = \alpha_o$, i.e. on the surface of the spheroid,

$$\cos\beta = \frac{z}{\cosh\alpha_o} \tag{A.9}$$

$$\text{or} \quad \cos\beta = \frac{z}{a} \tag{A.10}$$

Substituting Eq. A.10 into Eq. A.8,

$$p = \frac{z}{a} \tag{A.11}$$

$$\bar{p} = \sin\beta \tag{A.12a}$$

or $$\bar{p} = \sqrt{1 - \cos^2\beta} \tag{A.12b}$$

or $$\bar{p} = \sqrt{1 - z^2/a^2} \tag{A.12c}$$

$$h = \frac{1}{\sqrt{q_o^2 - p^2}} \tag{A.13}$$

Substituting Eq. A.11 for p and Eq. A.4a for q_o into Eq. A.13,

$$h = \frac{a}{\sqrt{a^4 - z^2}} \tag{A.14}$$

$$Q_o = 1 + \frac{q_o}{2} \ln \frac{q_o - 1}{q_o + 1} \tag{A.15}$$

$$D = (1 + \nu)\left[(4\nu - 2)Q_o^2 + \frac{Q_o}{\bar{q}_o^2}(4\nu - 4 - 3\bar{q}_o^2) - \frac{1}{\bar{q}_o^2}\right] + \frac{Q_o}{\bar{q}_o^2}\left[(8 - 4\nu)(1 - \nu) + 9(1 - \nu)\bar{q}_o^2\right] + \frac{2(1 - \nu)(1 - 2\nu)}{\bar{q}_o^4} + \frac{3 - 3\nu}{\bar{q}_o^2} \tag{A.16}$$

$$H = \left(\frac{G'}{G} - 1\right) \tag{A.17}$$

in which G' and G are the shear moduli of the material contained in the pore and the medium, respectively. Substituting G' = 0 (empty pores) in Eq. A.17 gives:

$$H = -1 \tag{A.18}$$

Oblate Spheroid: For an oblate spheroidal pore, the expressions for p, $\bar{p}$ and H are the same as a prolate spheroid (Eq. A.11 and A.12c, and Eq. A.18). The expressions for h, Q_o and D for an oblate spheroidal pore are obtained from those for a prolate spheroid (Eqs. A.13, A.15 and A.16) by replacing q_o and $\bar{q}_o$ with the imaginary quantities $i\bar{q}_o$ and iq_o, respectively (70). Thus,

$$h = \frac{1}{i\sqrt{\bar{q}_o^2 + p^2}} \tag{A.19a}$$

Substituting Eq. A.11 for p and Eq. A.6a for $\bar{q}_o$ into Eq. A.19a,

$$h = \frac{a}{i\sqrt{a^4 + z^2}} \tag{A.19b}$$

$$Q_o = 1 + \bar{q}_o \cot^{-1}(\bar{q}_o) \tag{A.20}$$

$$D = (1 + \nu)\left[(4\nu - 2)Q_o^2 - \frac{Q_o}{q_o^2}(4\nu - 4 + 3q_o^2) + \frac{1}{q_o^2}\right]$$

$$+ \frac{Q_o}{q_o^2}\left[(8 - 4\nu)(1 - \nu) - 9(1 - \nu)q_o^2\right] +$$

$$\frac{2(1 - \nu)(1 - 2\nu)}{q_o^4} + \frac{3 - 3\nu}{q_o^2} \tag{A.21}$$

A.4 Displacements on the Surface of a Spheroid, $u_{\alpha j}$

While the applied stress considered here is along the global z-axis of the medium, the displacements on the surface of the spheroid are given in the local coordinate system of the spheroid (26, 70).

Hence, a coordinate transformation of stresses (89) from global (medium) to local (spheroid) axes is necessary. Let the global axes be denoted by x', y', and z' and the local axes be denoted by x, y, and z (Fig. A.2). Due to the symmetry of the spheroid and the global stress is applied uniaxially, all orientations of the spheroid (or of the pore) can be represented by angle ψ between z' and z (also between y' and y), while x' and x coincide. The direction cosines between the two coordinate systems are given in Table A.1. Using $\sigma'_z = 1$ and applying the coordinate transformation of stresses, three nonzero stress components are obtained in the local coordinate system:

$$\sigma_y = \sin^2\psi \tag{A.22a}$$

$$\sigma_z = \cos^2\psi \tag{A.22b}$$

$$\tau_{yz} = \sin\psi\cos\psi \tag{A.22c}$$

Edwards (26) has derived expressions for displacement components for any point in a medium containing an extremely small spheroid. He considered the following five load cases using the local coordinate system.

$$\text{Load Case 1: } \sigma_x = \sigma_y = 1 \tag{A.23a}$$

$$\text{Load Case 2: } \sigma_x = -\sigma_y = 1 \tag{A.23b}$$

$$\text{Load Case 3: } \sigma_z = 1 \tag{A.23c}$$

$$\text{Load Case 4: } \tau_{zx} = 1 \tag{A.23d}$$

Load Case 5: $\tau_{yz} = 1$ (A.23e)

In each load case, stress components other than those shown in the specific equation are zero.

In general, the expression for the change in the volume of a spheroid surrounded by a medium with an average stress $\sigma_z' = 1$ (or the equivalent stress components given by Eq. A.22) can be found using a combination of displacements for load case 1, 2, 3 and 5. However, in load case 2 the change in the volume of the spheroid is zero due to the symmetry of spheroids and the isotropic nature of the surrounding medium. Thus, load case 2 does not need to be considered to derive the expression for the change in the volume of the spheroid. For example, to find the change in volume under stresses $\sigma_x = 0$ and $\sigma_y = 1$ (equivalent to one-half the volume change of load case 1 minus load case 2), it is sufficient to integrate the net displacements for load case 1 over the surface of the spheroid and divide the result by 2. For load case 5, the volume change is also zero. However, since this fact is not obvious, the displacement expressions for load case 5 are developed to demonstrate this point.

In section A.5, while deriving the expression for the change in the volume of a spheroid due the stress components given by Eq. A.22 (i.e. for $\sigma_z' = 1$), displacement expressions for load cases 2 and 5 are ignored, and only those for load cases 1 and 3 are considered. Note: Edwards (26) has provided expressions for all components of displacement for any point in the medium. However, as shown in

section A.5, the volume change calculations require only the expressions for normal displacement components on the surface of the spheroid.

A.4.1 Load Case 1 ($\sigma_x = \sigma_y = 1$)

For load case 1, the normal displacement at any point on the surface of the spheroid is expressed as:

$$u_{\alpha_1} = u_{\alpha_{01}} + a_{13}u_{\alpha_{13}} + a_{23}u_{\alpha_{23}} + a_{33}u_{\alpha_{33}} \tag{A.24}$$

in which $u_{\alpha ij}$, $i \neq 0$, are the normal displacement fields around the spheroid, $u_{\alpha_{01}}$ is the uniform normal displacement field in the absence of the spheroidal cavity (prototype). a_{ij} are coefficients of superposition and are functions of spheroidal geometry and elastic moduli of the medium. Using Edwards' (26) expressions for $u_{\alpha 01}$, $u_{\alpha ij}$ and a_{ij}, $i = 1,2,3$ and $j = 1$,

$$u_{\alpha 1} = K_3 h + K_4 h p^2 \tag{A.25}$$

in which, K_3 and K_4 are constants which depend on shape of the spheroid and the moduli of the medium. Expressions for K_3 and K_4 for both a prolate and an oblate spheroidal pore are presented next. The expressions for an oblate spheroidal pore for this and the other load cases are obtained from those for the prolate spheroidal pores (Eqs. A.26-A.28) by replacing q_o and $\bar{q}_o$ with the imaginary quantities $i\bar{q}_o$ and iq_o, respectively (70).

Prolate Spheroid: For a prolate spheroid, the following expressions for K_3 and K_4 are obtained.

$$K_3 = \frac{q_o \bar{q}_o (1 - \nu)}{2G(1 + \nu)} + \frac{a_{11}}{2G\bar{q}_o} - \frac{a_{31}\bar{q}_o}{4G}(3Q_o + \frac{1}{\bar{q}_o^2}) \tag{A.26}$$

$$K_4 = - \frac{q_o \bar{q}_o}{2G} + \frac{a_{21}\bar{q}_o}{2G}\{(4\nu - 2)Q_o + \frac{1}{\bar{q}_o^2}\} + \frac{3a_{31}\bar{q}_o}{4G}(3Q_o + \frac{1}{\bar{q}_o^2}) \tag{A.27}$$

a_{11}, a_{21} and a_{31}, for $H = -1$ and $\nu' = \nu$ (empty pores), are given by

$$a_{11} = - a_{21} q_o^2 - a_{31} \tag{A.28a}$$

$$a_{21} = - \frac{q_o}{D} (2 - 4\nu)(Q_o + \frac{1}{\bar{q}_o^2}) \tag{A.28b}$$

$$a_{31} = \frac{4q_o}{3D} (1 - 2\nu)\{1 + \frac{\nu}{\bar{q}_o^2} - (1 - \nu)Q_o\} \tag{A.28c}$$

Oblate Spheroid: For an oblate spheroid, the following expressions for K_3 and K_4 are obtained.

$$K_3 = - \frac{q_o \bar{q}_o (1 - \nu)}{2G(1 + \nu)} - \frac{ia_{11}}{2Gq_o} - \frac{ia_{31} q_o}{4G}(3Q_o - \frac{1}{q_o^2}) \tag{A.29}$$

$$K_4 = \frac{q_o \bar{q}_o}{2G} + \frac{ia_{21}q_o}{2G}\{(4\nu - 2)Q_o - \frac{1}{q_o^2}\} + \frac{i3a_{31}q_o}{4G}(3Q_o - \frac{1}{q_o^2}) \quad (A.30)$$

a_{11}, a_{21} and a_{31}, for $H = -1$ and $\nu' = \nu$ (empty pores), are given by

$$a_{11} = a_{21}\bar{q}_o^2 - a_{31} \quad (A.31a)$$

$$a_{21} = -\frac{i\bar{q}_o}{D}(2 - 4\nu)(Q_o - \frac{1}{q_o^2}) \quad (A.31b)$$

$$a_{31} = \frac{i4\bar{q}_o}{3D}(1 - 2\nu)\{1 - \frac{\nu}{q_o^2} - (1 - \nu)Q_o\} \quad (A.31c)$$

A.4.2 Load Case 3 ($\sigma_z = 1$)

In this case, the normal displacement component at any point on the surface of the spheroid is expressed as:

$$u\alpha_3 = u_{\alpha_{03}} + a_{13}u_{\alpha_{13}} + a_{23}u_{\alpha_{23}} \quad (A.32)$$

Using Edwards' (26) expressions for displacement,

$$u_{\alpha_3} = K_1 h + K_2 h p^2 \quad (A.33)$$

Like load case 1, K_1 and K_2 are functions of pore shape and moduli of the medium.

Prolate Spheroid: For a prolate spheroid, the expressions for K_1 and K_2 are

$$K_1 = \frac{-q_o \bar{q}_o \nu}{2G(1+\nu)} + \frac{a_{13}}{2G\bar{q}_o} - \frac{a_{33}\bar{q}_o}{4G}\left(3Q_o + \frac{1}{\bar{q}_o^2}\right) \tag{A.34a}$$

$$K_2 = \frac{q_o \bar{q}_o}{2G} + \frac{a_{23}\bar{q}_o}{2G}\left[(4\nu - 2)Q_o + \frac{1}{\bar{q}_o^2}\right] + \frac{3a_{33}\bar{q}_o}{4G}\left(3Q_o + \frac{1}{\bar{q}_o^2}\right) \tag{A.34b}$$

in which, a_{13}, a_{23} and a_{33} for $\nu = \nu'$ and $H = -1$ are given by

$$a_{13} = -a_{23}q_o^2 - a_{33} \tag{A.35a}$$

$$a_{23} = -\frac{q_o}{D}(1 - 2\nu)\left(Q_o - \frac{1}{\bar{q}_o^2}\right) \tag{A.35b}$$

$$a_{33} = \frac{2}{3}\frac{q_o}{D}(1 - 2\nu)\left(2\nu Q_o - 2 - \frac{1}{\bar{q}_o^2}\right) \tag{A.35c}$$

Oblate Spheroid: For an oblate spheroid, the expressions for K_1 and K_2 are

$$K_1 = \frac{q_o \bar{q}_o \nu}{2G(1+\nu)} - \frac{ia_{13}}{2Gq_o} - \frac{ia_{33}q_o}{4G}\left(3Q_o - \frac{1}{q_o^2}\right) \tag{A.36a}$$

$$K_2 = -\frac{q_o\bar{q}_o}{2G} + \frac{ia_{23}q_o}{2G}\{(4\nu - 2)Q_o - \frac{1}{q_o^2}\} + \frac{i3a_{33}q_o}{4G}(3Q_o - \frac{1}{q_o^2}) \qquad (A.36b)$$

in which, a_{13}, a_{23} and a_{33} for $\nu = \nu'$ and $H = -1$ are given by

$$a_{13} = a_{23}\bar{q}_o^2 - a_{33} \qquad (A.37a)$$

$$a_{23} = \frac{i\bar{q}_o}{D}(2\nu - 1)(Q_o + \frac{1}{q_o^2}) \qquad (A.37b)$$

$$a_{33} = \frac{i2\bar{q}_o}{3D}(1 - 2\nu)(2\nu Q_o - 2 + \frac{1}{q_o^2}) \qquad (A.37c)$$

A.4.3 Load Case 5 ($\tau_{yz} = 1$)

For spheroids, load case 4 and load case 5 give the same magnitudes of displacements due to symmetry. Hence, Edwards (26) provided the expressions for for displacement for load case 4 only. Using Edwards (26) expressions for displacement for load case 4, the displacement for load case 5 at any point on the surface of the spheroid can be expressed as

$$u_{\alpha_4} = u_{\alpha_{04}} + a_{14}u_{\alpha_{14}} + a_{24}u_{\alpha_{24}} + a_{34}u_{\alpha_{34}} + a_{44}u_{\alpha_{44}} \qquad (A.38)$$

Using Edwards' (26) expressions for displacement,

$$u_{\alpha_4} = K_5 h p \bar{p} \cos\gamma \tag{A.39}$$

Prolate Spheroid: For a prolate spheroid, the following expression for K_5 is obtained

$$K_5 = \frac{1}{2G}\Big[(2q_o^2 - 1) + a_{24}\Big\{\Big(\frac{6q_o^2 - 3}{q_o}\Big)Q_o + \frac{2q_o^2 - 3}{q_o \bar{q}_o^2}\Big\} + 2a_{34}q_o\Big(3Q_o + \frac{1}{\bar{q}_o^2}\Big) + a_{44}\Big\{q_o\Big(Q_o - \frac{1}{\bar{q}_o^2}\Big) - \frac{\bar{q}_o^2}{q_o}(3 - 4\nu)\Big(Q_o + \frac{1}{\bar{q}_o^2}\Big)\Big\}\Big] \tag{A.40}$$

a_{24}, a_{34} and a_{44} are given by

$$a_{24} = a_{44}\{2(1-\nu)/3 - q_o^2\} \tag{A.41a}$$

$$a_{34} = a_{44}(1-\nu)/3 \tag{A.41b}$$

$$a_{44} = -q_o/\{Q_o(2 - \nu - 3q_o^2) + (1/\nu - q_o^2 + 2 - 2\nu)/\bar{q}_o^2\} \tag{A.41c}$$

Oblate Spheroid: For an oblate spheroid, the following expression for K_5 is obtained

$$K_5 = \frac{1}{2G}\Big[-(2\bar{q}_o^2 + 1) + ia_{24}\Big\{\Big(\frac{6\bar{q}_o^2 + 3}{\bar{q}_o}\Big)Q_o - \frac{2\bar{q}_o^2 + 3}{\bar{q}_o q_o^2}\Big\} +$$

$$i2a_{34}\bar{q}_o\ (3Q_o - \frac{1}{q_o^2}) + ia_{44}\{\bar{q}_o(Q_o + \frac{1}{q_o^2}) -$$

$$\frac{q_o^2}{\bar{q}_o}(3 - 4\nu)(Q_o - \frac{1}{q_o^2})\}] \qquad (A.42)$$

a_{24}, a_{34} and a_{44} are given by

$$a_{24} = a_{44}\{2(1-\nu)/3 + \bar{q}_o^2\} \qquad (A.43a)$$

$$a_{34} = a_{44}(1-\nu)/3 \qquad (A.43b)$$

$$a_{44} = -i\bar{q}_o/\{Q_o(2 - \nu + 3q_o^2) -$$

$$(1/\nu + \bar{q}_o^2 + 2 - 2\nu)/q_o^2\} \qquad (A.43c)$$

A.5 Volume Change Per Unit Strain, v^*

As stated in section A.2, in a spheroidal coordinate system a spheroidal pore is represented by a prototype spheroid that has the same shape as the pore, but the whose size, in general, cannot be the same as that of the pore. Hence, the change in volume per unit strain along the global z-axis, v^*, is obtained by the following relation.

$$v^* = v_p'(\frac{V_i}{V_i'})E \qquad (A.44)$$

in which v_p' is the change in volume of the spheroid per unit external stress along the global z-axis (i.e. for $\sigma_z' = 1$), V_i is the initial

volume of the pore, V_i' is the initial volume of the spheroid, and E is the elastic modulus of the medium. The stress components in the local coordinate system of the spheroid corresponding to $\sigma_z' = 1$ are given by Eq. A.22. In Eq. A.44, v_p' can be expressed as

$$v_p' = \int_A u_\alpha' dA \qquad (A.45)$$

in which the integral is taken over the surface area of the pore and u_α' is the displacement normal to area dA (Fig. A.3) such that when integrated over the surface of the spheroid it provides the volume change due to $\sigma_z' = 1$.

As explained in section A.4, the displacements corresponding to load case 2 ($\sigma_x = -\sigma_y = 1$) cause no change in the volume of the spheroid, and are ignored in obtaining u_α'. In section A.5.2, it is shown that load case 5 ($\tau_{yz} = 1$) also causes no change in the volume of a pore. Hence, the derivation of the expressions for v^* requires a combination of the displacement expressions for only load case 1 and load case 3. A cylindrical coordinate system (y, z, Y) is used in the following sections to take advantage of the symmetry of the spheroids.

A.5.1 General Expressions for Volume Change, v_p

In this section the expressions for the change the volume of the spheroid, v_p, are obtained for given displacements, u_α, on the surface of the spheroid. v_p can be written as

$$v_p = \int_A u_\alpha dA \tag{A.46a}$$

The expression for v_p is obtained by finding the corresponding expressions for dA using the cylindrical coordinate system. Eq. A.46a can also be written as

$$v_p = 2 \int_{\gamma=0}^{2\pi} \int_{z=0}^{a} u_\alpha ds\ y d\gamma \tag{A.46b}$$

in which, ds is an infinitesimal arc segment on the perimeter of a cross section passing through the poles of the spheroid (Fig. A.3), and $d\gamma$ is an infinitesimal angle about the polar or z-axis of the spheroid. ds can be expressed in terms of the polar and equatorial semi-axes, a and b respectively, and the z-coordinate of the centroid of dA. The equation of the perimeter of a cross section passing through the poles of the spheroid is

$$\frac{z^2}{a^2} + \frac{y^2}{b^2} = 1 \tag{A.47}$$

Differentiating Eq. A.47 with respect to z and rearranging

$$\frac{dy}{dz} = -\left(\frac{b^2}{a^2}\right)\frac{z}{y} \tag{A.48}$$

From Eq. A.47,

$$y = b\left(1 - \frac{z^2}{a^2}\right)^{1/2} \tag{A.49}$$

Substituting Eq. A.49 for y into the right hand side of Eq. A.48

$$\frac{dy}{dz} = -\frac{b}{a^2}\frac{z}{(1 - z^2/a^2)^{1/2}} \tag{A.50}$$

or
$$dy^2 = \frac{b^2}{a^4}\frac{z^2}{1 - z^2/a^2}\,dz^2 \tag{A.51}$$

ds (in Eq. A.46b) can be expressed as

$$ds = (dy^2 + dz^2)^{1/2} \tag{A.52}$$

Substituting Eq. A.51 for dy^2 into Eq. A.52 and simplifying,

$$ds = \left\{\frac{a^4\left(1 - \frac{z^2}{a^2}\right) + b^2z^2}{a\left(1 - \frac{z^2}{a^2}\right)}\right\}^{1/2} dz \tag{A.53}$$

Substituting Eq. A.49 for y and Eq. A.53 for ds into Eq. A.46b and simplifying,

$$v_p = 2\frac{b}{a}\int_o^{2\pi}\int_o^a u_\alpha\left(a^2 - \frac{a^2 - b^2}{a^2}z^2\right)^{\frac{1}{2}} dz d\gamma \tag{A.54}$$

Prolate Spheroid: Substituting Eq. A.5a into Eq. A.54,

$$v_p = 2\frac{b}{a}\int_0^{2\pi}\int_0^a u_\alpha\left(a^2 - \frac{z^2}{a^2}\right)^{\frac{1}{2}} dz d\gamma \qquad (A.55)$$

Oblate Spheroid: For an oblate spheroid Eq. A.54 is rearranged to give:

$$v_p = 2\frac{b}{a}\int_0^{2\pi}\int_0^a u_\alpha\left(a^2 + \frac{b^2 - a^2}{a^2}z^2\right)^{\frac{1}{2}} dz d\gamma \qquad (A.56)$$

Substituting Eq. A.7a into Eq. A.56,

$$v_p = 2\frac{b}{a}\int_0^{2\pi}\int_0^a u_\alpha\left(a^2 + \frac{z^2}{a^2}\right)^{\frac{1}{2}} dz d\gamma \qquad (A.57)$$

A.5.2 Volume Change due to Load Case 5, v_{p5}

The purpose of this section is to demonstrate that v_{p5}, the change in the volume of the spheroid due to load case 5 ($\tau_{yz} = 1$), is zero, and hence, load case 5 will not have to be considered further. As pointed out earlier (section A.4), displacement expressions for load case 4 are used for load case 5.

Prolate Spheroid: Substituting u_{α_4} (Eq. A.39) for u_α in Eq. A.55

$$v_{p5} = 2\frac{b}{a}K_s\int_0^{2\pi}\left[\int_0^a h\bar{p}\bar{p}\left(a^2 - \frac{z^2}{a^2}\right)^{\frac{1}{2}} dz\right]\cos\gamma d\gamma \qquad (A.58a)$$

In Eq. A.58a, the term inside the brackets is not a function of γ. Since $\int_0^{2\pi}\cos\gamma d\gamma = 0$,

$$v_{p5} = 0 \tag{A.58b}$$

Oblate Spheroid: Substituting u_{α_4} (Eq. A.39) for u_α in Eq. A.57

$$v_{p5} = 2\frac{b}{a}K_s \int_o^{2\pi} \left[\int_o^a hp\bar{p}\left(a^2 + \frac{z^2}{a^2}\right)^{\frac{1}{2}} dz\right]\cos\gamma d\gamma \tag{A.59a}$$

As demonstrated for Eq. A.58,

$$v_{p5} = 0 \tag{A.59b}$$

A.5.3 Expressions for v^*

In this section, the expressions for u'_α (Eq. A.45) are obtained by combining the displacement expressions for load cases 1 and 3. By substituting the expressions for u'_α in either Eq. A.55 (prolate) or Eq. A.57 (oblate), the corresponding expressions for v'_p are obtained. By substituting the expressions for v'_p into Eq. A.44, the expressions for v^* are obtained.

u'_α can be found by combining one half of the expression for load case 1 (Eq. A.25) and the expression for load case 3 (Eq. A.33) with Eqs. A.22a and A.22b for σ_y and σ_z, respectively.

$$u'_\alpha = u_{\alpha_1}\sin^2\psi/2 + u_{\alpha_3}\cos^2\psi \tag{A.60}$$

Substituting Eq. A.25 for u_{α_1} and Eq. A.33 for u_{α_2} in Eq. A.60 and rearranging

$$u'_\alpha = h\left(\frac{K_3}{2}\sin^2\psi + K_1\cos^2\psi\right) + hp^2\left(\frac{K_4}{2}\sin^2\psi + K_2\cos^2\psi\right) \quad (A.61)$$

Prolate Spheroid: Substituting Eqs. A.11 and A.14 for the intermediate variables p and h, respectively into Eq. A.61 gives:

$$u'_\alpha = \frac{a}{\sqrt{a^4 - z^2}}\left(\frac{K_3}{2}\sin^2\psi + K_1\cos^2\psi\right) + \frac{z^2}{a\sqrt{a^4 - z^2}}\left(\frac{K_4}{2}\sin^2\psi + K_2\cos^2\psi\right) \quad (A.62)$$

Substituting Eq. A.62 for u'_α in Eq. A.55 and integrating,

$$v'_p = 4\pi b\left\{\left(K_1 + \frac{K_2}{3}\right)\cos^2\psi + \left(\frac{K_3}{2} + \frac{K_4}{6}\right)\sin^2\psi\right\} \quad (A.63)$$

Substituting Eq. A.63 into Eq. A.44,

$$v^* = \frac{4\pi b V_i E}{V'_i}\left\{\left(K_1 + \frac{K_2}{3}\right)\cos^2\psi + \left(\frac{K_3}{2} + \frac{K_4}{6}\right)\sin^2\psi\right\} \quad (A.64)$$

in which, b is the equatorial semi-axis of the prototype spheroid used in the spheroidal coordinate system (Eq. A.5); V_i, V'_i, and E are as given for Eq. A.44 and K_i, i = 1, 4 are constants (Eqs. A.26-A.28

and Eqs. A.34-A.35) for given shape of the pore and elastic moduli of the medium.

Oblate Spheroid: Substituting Eqs. A.11 and A.19b for the intermediate variables p and h, respectively into Eq. A.61 gives

$$u'_\alpha = \frac{a}{i\sqrt{a^4 + z^2}}\left(\frac{K_3}{2}\sin^2\psi + K_1\cos^2\psi\right) + \frac{z^2}{ia\sqrt{a^4 + z^2}}\left(\frac{K_4}{2}\sin^2\psi + K_2\cos^2\psi\right) \qquad (A.65)$$

Multiplying both the numerator and the denominator of Eq. A.65 by the imaginary quantity i and then dropping the i in the numerator of the resulting expression (the displacement is real) (70) gives:

$$u'_\alpha = -\frac{a}{\sqrt{a^4 + z^2}}\left(\frac{K_3}{2}\sin^2\psi + K_1\cos^2\psi\right) - \frac{z^2}{a\sqrt{a^4 + z^2}}\left(\frac{K_4}{2}\sin^2\psi + K_2\cos^2\psi\right) \qquad (A.66)$$

Substituting Eq. A.66 for u'_α in Eq. A.57 and integrating,

$$v'_p = -4\pi b\left\{\left(K_1 + \frac{K_2}{3}\right)\cos^2\psi + \left(\frac{K_3}{2} + \frac{K_4}{6}\right)\sin^2\psi\right\} \qquad (A.67)$$

Substituting Eq. A.65 into Eq. A.44,

$$v^* = -\frac{4\pi b V_i E}{V'_i}\left\{\left(K_1 + \frac{K_2}{3}\right)\cos^2\psi + \left(\frac{K_3}{2} + \frac{K_4}{6}\right)\sin^2\psi\right\} \qquad (A.68)$$

in which, b is the equatorial semi-axis of the prototype spheroid used in the spheroidal coordinate system (Eq. A.7); V_i, V_i', and E are as given for Eq. A.44 and K_i, i = 1, 4 are constants (Eqs. A.29-A.31 and Eqs. A.36-A.37) for given shape of the pore and elastic moduli of the medium.

TABLE A.1

Direction Cosines Between Coordinate Axes of a Spheroid, X, Y, Z and the Coordinate Axes of the Medium, X', Y', Z'

	X'	Y'	Z'
X	1	0	0
Y	0	$\cos\psi$	$-\sin\psi$
Z	0	$\sin\psi$	$\cos\psi$

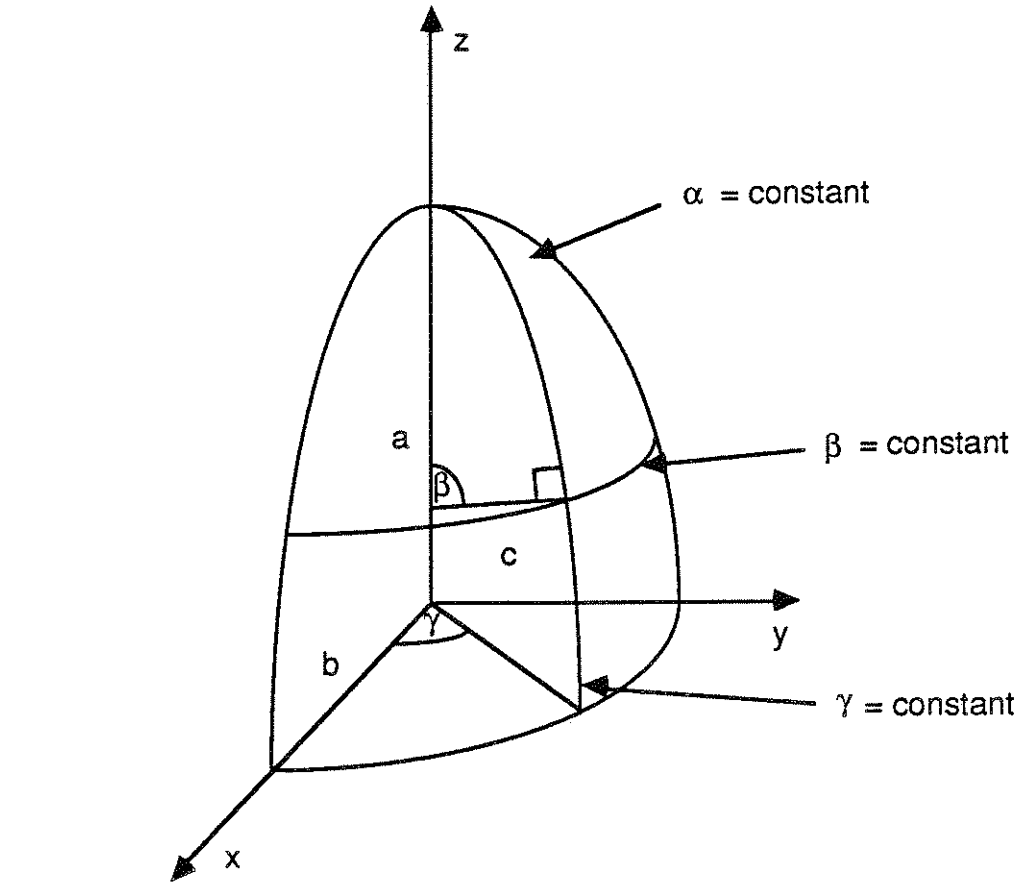

a)

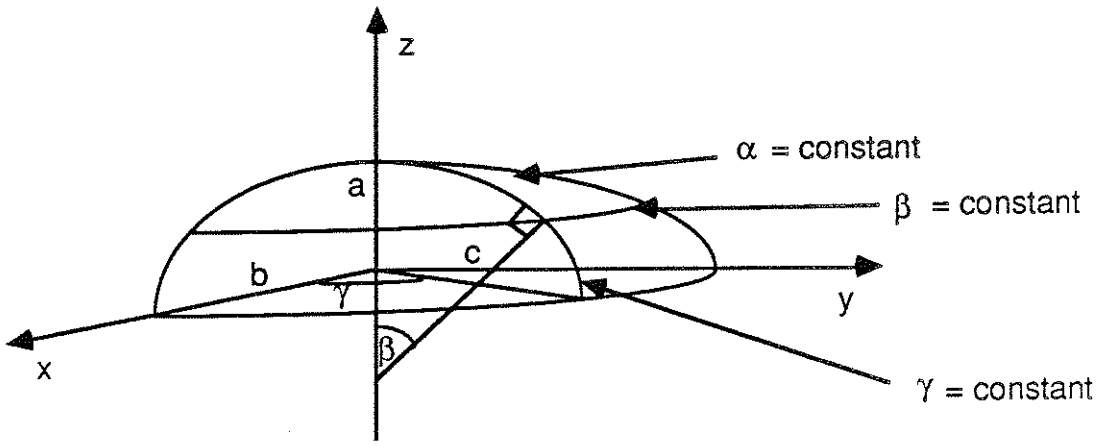

b)

Fig. A.1 Spheroidal Coordinate System for a) Prolate Spheroid b) Oblate Spheroid

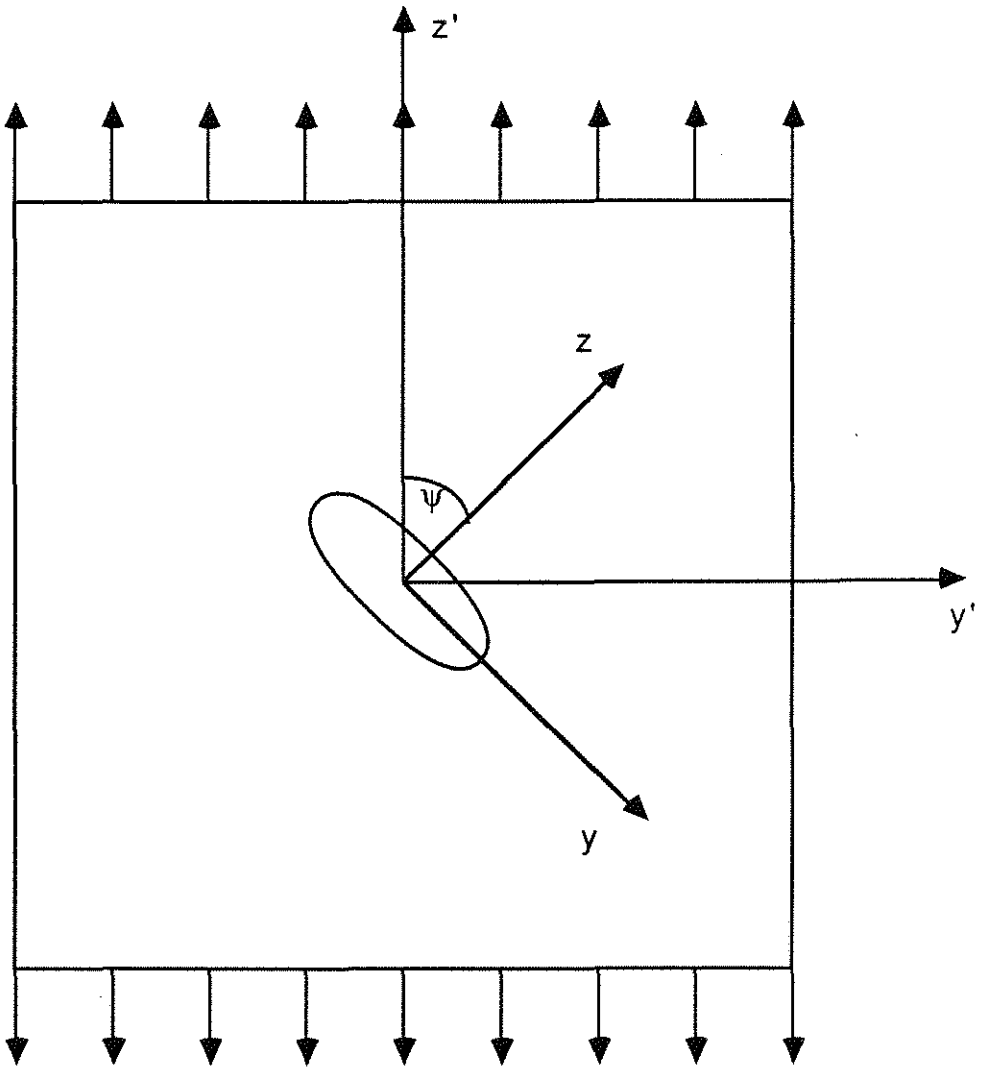

Fig. A.2 The Spheroid (Oblate) Oriented at an Angle ψ embedded in an Infinite Medium Subjected to Uniform Strain ε'_z

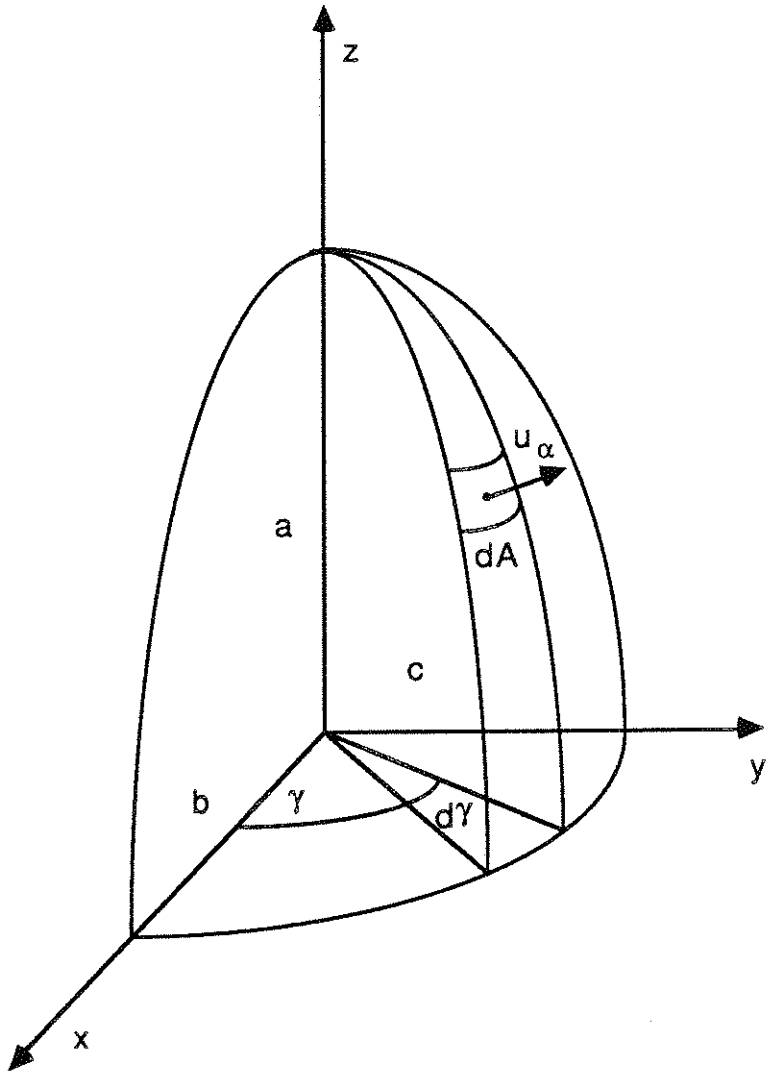

Fig. A.3 An Infinitesimal Area dA on the Surface of a Spheroid with a Normal Displacement u_α

APPENDIX B

COPRESSIBILITY OF A PORE IN AN INFINITE MEDIUM, C_{pp}

Consider an isolated spheroidal pore in an infinite homogeneous isotropic elastic medium. In the limiting cases, a spheroid can represent a spherical pore (a = b = c), a cylindrical pore (a prolate spheroid with a >> b = c), or a flat crack like pore (an oblate spheroid with a << b = c), in which a, b, and c are the axes of the spheroid.

If an internal hydrostatic stress, $\sigma_f(t)$, is applied on the wall of the pore (Fig. B.1), it causes a corresponding change in the volume of the pore, ΔV, which depends on the shape of the pore and the moduli of the medium. The compressibility of the pore, C_{pp}, can be defined as (101):

$$C_{pp} = \frac{\Delta V/V}{\sigma_f(t)} \tag{B.1}$$

Prolate Spheroidal Pore: Eq. B.1 for a prolate spheroidal pore can be expressed as (101)

$$C_{pp} = \frac{(2 - 4\nu)(1 + 2R) - (1 + 3R)\{1 - 2R + 4\nu R - 3q_o^2\}}{4G\{(1 + 3R)q_o^2 - (1 + R)(\nu + \nu R + R)\}} \tag{B.2}$$

in which ν is the Poisson's ratio of the medium, r is the aspect ratio (or the ratio of the polar to the equatorial semiaxis) of the pore ($r > 1.0$), $q_o^2 = \frac{r^2}{r^2 - 1}$, G is the shear modulus of the medium, and R is given by

$$R = (q_o^2 - 1)\left(1 + \frac{q_o}{2} \ln \frac{q_o - 1}{q_o + 1}\right) \tag{B.3}$$

Oblate Spheroidal Pore: In the case of an oblate spheroidal pore, the expression for C_{pp} is obtained by replacing q_o in Eq. (B.2) with the imaginary quantity $i\bar{q}_o$ (70, 101). Thus,

$$C_{pp} = \frac{(2 - 4\nu)(1 + 2R) - (1 + 3R)\{1 - 2R + 4\nu R + 3\bar{q}_o^2\}}{4G\{-(1 + 3R)\bar{q}_o^2 - (1 + R)(\nu + \nu R + R)\}} \tag{B.4}$$

in which $\bar{q}_o^2 = \frac{r^2}{1 - r^2}$, r is the aspect ratio ($r < 1.0$) and

$$R = -(1 + \bar{q}_o^2)[1 - \bar{q}_o \cot^{-1}(\bar{q}_o)] \tag{B.5}$$

For a spherical pore, the expression for oblate spheroidal pore (Eqs. B.4 and B.5) with $r = 0.9999$ can be used.

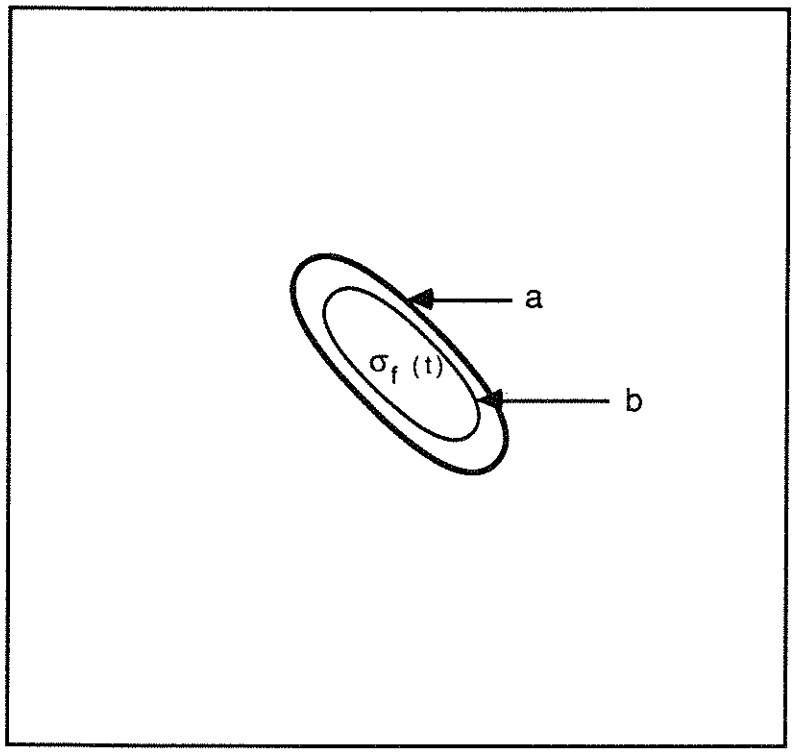

Fig. B.1 An Oblate Spheroidal Pore with an Internal Hydrostatic Stress $\sigma_f(t)$ embedded in an Infinite Medium. a = Pore Before Applying $\sigma_f(t)$, b = Pore After Applying $\sigma_f(t)$

APPENDIX C

RATE OF FLOW THROUGH AN ORIFICE, $q_{or}(t)$

Consider a saturated pore or cavity in a infinite homogeneous isotropic elastic medium. The medium is under uniform axial stress applied at the end (see Fig. C.1). The pore is connected to an unsaturated region via a circular cylindrical orifice of diameter d and length h. When the specimen is stressed uniaxially, there is a hydrostatic stress in the pore fluid causing a flow through the orifice. The flow through the orifice is assumed to be laminar, the fluid is assumed to be incompressible, and the velocity profile in the orifice is assumed to be fully developed (parabolic) for the entire length of the orifice. The orifice flow tends to relieve the hydrostatic stress in the pore. Problems like this are considered in the design and analysis of viscous dampers (35, 66). The case considered by Rao (66) is very similar to the present case. Rao (66) considered a dash pot consisting of a piston moving in a cylinder filled with liquid. The diameter of the piston was a little smaller than the inside diameter of the cylinder. The expression for the flow through the clearance between the piston and the cylinder was derived by equating the hydrostatic force at the bottom end of the clearance with the viscous force in the fluid flowing through the clearance. In the present case, the flow through the orifice is

considered in place of the flow through the clearance (66). The boundary conditions are changed accordingly.

The viscous force on an annular ring of pore fluid (Fig. C.2) of thickness dy at a distance y from the center line of the orifice is

$$F_1 = 2\pi h(\frac{d\tau}{dy})ydy \tag{C.1}$$

in which $\tau = -\mu\frac{dv}{dy}$ is the viscous force and v is the velocity of pore fluid at a distance y from the center line of the orifice.

Thus,

$$F_1 = -2\pi\mu h\frac{d^2v}{dy^2}ydy \tag{C.2}$$

The hydrostatic force at the end of the ring is

$$F_2 = (2\pi ydy)\sigma_f(t) \tag{C.3}$$

in which $\sigma_f(t)$ = hydrostatic stress in the pore pore fluid at time t. For the equilibrium of the ring we must have

$$F_1 = F_2 \tag{C.4}$$

or

$$\frac{d^2v}{dy^2} = -\frac{\sigma_f(t)}{\mu h} \tag{C.5}$$

Integrating Eq. C.5 twice and substituting the following boundary conditions,

$$\frac{dv}{dy} = 0 \text{ at } y = 0 \tag{C.6}$$

and

$$v = 0 \text{ at } y = d/2 \tag{C.7}$$

the following expression for v is obtained

$$v = \frac{\sigma_f(t)}{2\mu h}\left(\frac{d^2}{4} - y^2\right) \tag{C.8}$$

The rate of flow, $q_{or}(t)$, through the orifice can now be calculated by integrating the velocity over the cross section of the orifice.

$$q_{or}(t) = \int_o^{d/2} v\, 2\pi y\, dy \tag{C.9}$$

Substituting Eq. C.8 into Eq. C.9 and integrating,

$$q_{or}(t) = \frac{\pi d^4}{64\mu h}\sigma_f(t) \tag{C.10}$$

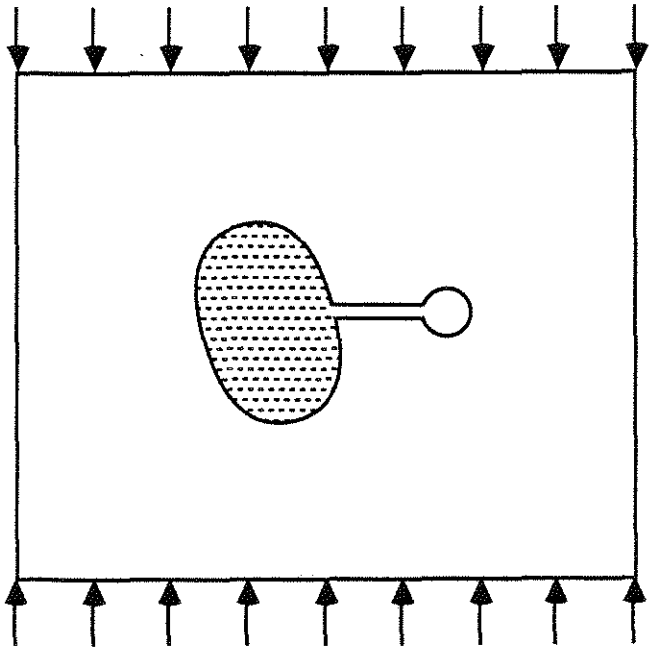

Fig. C.1 A Saturated Pore Embedded in an Infinite Medium Connected to an Unsaturated Region via an Orifice

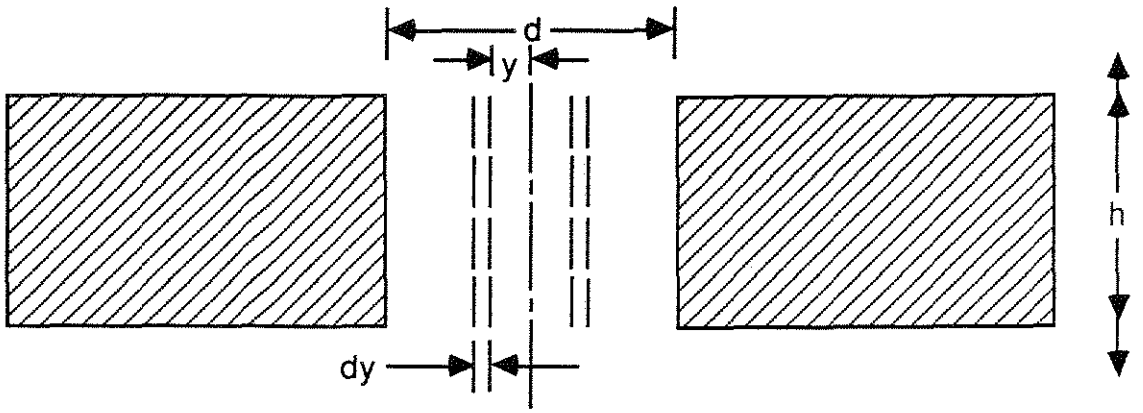

Fig. C.2 Enlarged View of the Orifice, with Diameter d and Length h, Showing an Annular Ring of Pore Fluid of Radius y and Thickness dy

APPENDIX D

EXPRESSIONS FOR COEFFICIENTS P^* and Q^*

Following Berryman (12)

$$P^* = \frac{1}{3}T_{iijj} \tag{D.1a}$$

$$Q^* = \frac{1}{5}(T_{ijij} - \frac{1}{3}T_{iijj}) \tag{D.1b}$$

in which T_{ijkl} is the tensor relating the applied uniform strain field, ε^o_{kl} away from a spheroidal pore, and the strain field, ε_{ij} at the pore, i.e.

$$\varepsilon_{ij} = T_{ijkl}\varepsilon^o_{kl} \tag{D.2}$$

T_{ijkl} consists of only two scalars, T_{iijj} and T_{ijij} used in the determination of P^* and Q^*, as expressed by Eq. (1). These scalars are given by

$$T_{iijj} = \frac{3F_1}{F_2} \tag{D.3a}$$

$$T_{ijij} = \frac{1}{3}T_{iijj} + \frac{2}{F_3} + \frac{1}{F_4} + \frac{F_4F_5 + F_6F_7 - F_8F_9}{F_2F_4} \tag{D.3b}$$

in which the F_i, $i = 1,9$ are given by

$$F_1 = 1 + A\left[\frac{3}{2}(f + \theta) - C\left(\frac{3}{2}f + \frac{5}{2}\theta - \frac{4}{3}\right)\right], \tag{D.4a}$$

$$F_2 = 1 + A\left[1 + \frac{3}{2}(f + \theta) - \frac{C}{2}(3f + 5\theta\right] + B(3 - 4C) + \frac{A}{2}(A + 3B)(3 - 4C)[f + \theta - C(f - \theta + 2\theta^2], \tag{D.4b}$$

$$F_3 = 1 + A\left[1 - \left(f + \frac{3}{2}\theta\right) + C(f + \theta)\right], \tag{D.4c}$$

$$F_4 = 1 + \frac{A}{4}[f + 3\theta - C(f - \theta)], \tag{D.4d}$$

$$F_5 = A\left[-f + C\left(f + \theta - \frac{4}{3}\right)\right] + B\theta(3 - 4C), \tag{D.4e}$$

$$F_6 = 1 + A[1 + f - C(f + \theta)] + B(1 - \theta)(3 - 4C), \tag{D.4f}$$

$$F_7 = 2 + \frac{A}{4}[3f + 9\theta - C(3f + 5\theta)] + B\theta(3 - 4C), \tag{D.4g}$$

$$F_8 = A\left[1 - 2C + \frac{f}{2}(C - 1) + \frac{\theta}{2}(5C - 3)\right] + B(1 - \theta)(3 - 4C) \tag{D.4h}$$

$$F_9 = A[(C - 1)f - C\theta] + B\theta(3 - 4C), \tag{D.4i}$$

in which A, B, and C are functions of the moduli of the constituents, K_i and G_i, and those of the composite, K^*, G^*, and ν^*.

$$A = \frac{G_i}{G^*} - 1, \tag{D.5a}$$

$$B = \frac{1}{3}\left(\frac{K_i}{K^*} - \frac{G_i}{G^*}\right), \tag{D.5b}$$

$$C = \frac{\frac{1}{2} - \nu^*}{1 - \nu^*} \tag{D.5c}$$

f and θ are functions of the aspect ratio of the pore, r. The pore could be a prolate spheroid ($r > 1$) or an oblate spheroid ($r <$

1), in which r is the ratio of the polar semiaxis to the equatorial semiaxis.

(i) For a prolate spheroidal pore,

$$\theta = \frac{r}{(r^2 - 1)^{\frac{3}{2}}} \left[r(r^2 - 1)^{\frac{1}{2}} - \cosh^{-1} r \right] \qquad \text{(D.6a)}$$

$$f = \frac{r}{r^2 - 1}(2 - 3\theta) \qquad \text{(D.6b)}$$

(ii) For an oblate spheroidal pore,

$$\theta = \frac{r^2}{(1 - r^2)^{\frac{3}{2}}} \left[\cos^{-1} r - r(1 - r^2)^{\frac{1}{2}} \right] \qquad \text{(D.7a)}$$

$$f = \frac{r^2}{1 - r^2}(3\theta - 2) \qquad \text{(D.7b)}$$

APPENDIX E

KEY TO SPECIMEN IDENTIFICATION

Each specimen has an identification number of the following form:

Specimen Identification: i-j/X-R/k

in which

i = batch number

j = specimen number

X = type of specimen

R = water cement ratio

k = strain rate number

Type of specimen - X

P = cement paste
MA = mortar A
MB = mortar B

Strain rate number - k

1 = 0.3 microstrain/sec
2 = 3 microstrain/sec
3 = 30 microstrain/sec
4 = 300 microstrain/sec
5 = 3000 microstrain/sec
6 = 30,000 microstrain/sec
7 = 300,000 microstrain/sec

Example: 3-6/MA-0.4/5

3000 microstrain/sec

mortar A with W/C = 0.4

6^{th} specimen of the 3^{rd} batch

APPENDIX G

NOTATION

C_{pp}	fractional volume change of a pore per unit internal hydrostatic stress (in pore fluid) or pore compressibility
C_i	volume concentration of the i^{th} phase of a composite
d	diameter of an orifice
E_i	the initial modulus of elasticity
E_i^*	converged value of the initial modulus of elasticity of a composite
E_s	modulus of elasticity of the solid phase
G^*	converged value of the shear modulus of a composite
G_1^*	initial estimate of G^* the shear modulus of a composite
G_{n+1}^*	estimated value of the shear modulus of a composite at the end of n+1 iterations
G_j	shear modulus of the j^{th} phase of a composite
G_s	shear modulus of the solid phase of a composite
h	length of an orifice
K^*	converged value of the bulk modulus of a composite
K_1^*	initial estimate of the bulk modulus of a composite
K_{n+1}^*	estimated value of the bulk modulus of a composite at the end of n+1 iterations
K_f^*	effective bulk modulus of a saturated pore
K_f	bulk modulus of the pore fluid
K_j^f	bulk modulus of the j^{th} phase of a composite
K_s	bulk modulus of the solid phase of a composite
M^*	shear or bulk modulus of a composite
M_i	shear or bulk modulus of the i^{th} phase of a composite

$q_{or}(t)$ the rate of flow of pore fluid through orifice at time t

r ratio of the polar semiaxis to the equatorial semiaxis of a spheroidal pore

R_{cv} the characteristic volume ratio of a saturated pore with an orifice

S/C sand to cement ratio (by weight)

T time at the end of the application of a given strain

t_i i^{th} value of time t

$V(t)$ volume of a pore at time t

V_i initial volume of a pore

v^* change in the volume of a pore per unit average applied strain on the material containing the pore

Δt_j small time interval = $t_{j+1} - t_j$

$\Delta V_c(T)$ small change in the volume of the pore fluid due to its compressibility in the presence of a hydrostatic stress

$\Delta V_{fp}(t)$ small change in the volume of pore fluid due to hydrostatic stress in it at time t

$\Delta V_o(T)$ small change the volume of the pore fluid due to flow of pore fluid through the orifice at time T

$\Delta V_{pe}(t)$ small change in the volume of empty pore due to external strain

$\Delta V_{pp}(t)$ small change in the volume of pore due to pressure in the pore fluid

ε applied axial strain

ε_L^* longitudinal strain of a composite at a given time

ε_p average strain at the peak stress

ε_{pp} average post peak strain at 90 percent of the peak stress

ε_T^* transverse strain of a composite at a given time

$\dot{\varepsilon}$ applied axial strain rate

$\dot{\varepsilon}_{0-100}$	average applied strain rate from zero stress to the peak stress
$\dot{\varepsilon}_{5-20}$	average applied strain rate from 5 percent to 20 percent of the peak stress
$\dot{\varepsilon}_{50-99}$	average applied strain rate from 50 percent to 99 percent of the peak stress (on the descending portion of the stress-strain curve)
μ	viscosity of pore fluid
$\mu\varepsilon$	microstrain or strain of 10^{-6} in./in.
ν_i	Poisson's ratio at stress of 20 percent of the strength
ν_i^*	converged value of the initial modulus of elasticity of a composite
ν_s	Poisson's ratio of the solid phase
$\sigma(t)$	applied stress at time t
$\sigma_f(t)$	hydrostatic stress in pore fluid at time t
$\dot{\sigma}_f(t)$	derivative of $\sigma_f(t)$ with respect to time
ψ	angle between the polar semiaxis of a spheroidal pore the horizontal plane
ψ_j	value of ψ at angle j